Title

Structural characterization of the functional amyloid protein Orb2A, and evaluation of structure-based inhibitors of amyloid assembly

Author

Bowler, Jeannette Teresa

Publication Date

2021

Peer reviewed|Thesis/dissertation

UNIVERSITY OF CALIFORNIA

Los Angeles

Structural characterization of the functional amyloid protein Orb2A, and evaluation of structure-based inhibitors of amyloid assembly

A dissertation submitted in partial satisfaction of the
requirements for the degree of Doctor of Philosophy
in Molecular Biology

by

Jeannette Teresa Bowler

2021

ABSTRACT OF THE DISSERTATION

Structural characterization of the functional amyloid protein Orb2A, and evaluation of structure-based inhibitors of amyloid assembly

by

Jeannette Teresa Bowler
Doctor of Philosophy in Molecular Biology
University of California, Los Angeles, 2021
Professor David S. Eisenberg, Chair

Amyloids are stable protein assemblies characterized by their β-sheet rich secondary structure and unbranched, fibrillar morphology. Whereas formation of amyloid is traditionally associated with neurodegenerative diseases such as Alzheimer's disease (AD), the amyloid fold has also been adapted for beneficial biological functions. These so-called functional amyloids exhibit similar structural characteristics to pathogenic amyloids, but are not toxic to their hosts. The study of functional amyloid structure and mechanisms may provide insight into amyloid disease pathogenesis, and aid in the development of therapeutics.

In chapter one, I present the atomic-resolution structure of the amyloid-driving N-terminal segment of the functional amyloid protein Orb2A. Using micro-electron diffraction (micro-ED), I determined the structure of this nine-residue segment, which I term M9I, and found that it forms a classical amyloid steric zipper structure, with phenylalanine side chains playing a critical role in the formation of the self-complementary dry interface. Using electron microscopy, x-ray diffraction, and Thioflavin-T binding assays I show that the M9I segment is sufficient to form amyloid-like fibrils, and replacement of phenylalanine residues with tyrosine

reduces fibril formation of the Orb2A prion-like domain (PLD). I also propose a structural model for full-length Orb2A that incorporates both this M9I steric zipper structure, and a previously published cryo-EM structure of the downstream glutamine/histidine (Q/H)-rich region from the related Orb2B isoform.

In chapters two and three, I evaluate amyloid aggregation inhibitors that were rationally designed using steric zipper structures of segments derived from full-length proteins. Chapter two describes the amyloidogenic and phase-separating behavior of the nucleocapsid (NCAP) protein of SARS-CoV-2, and the structure-based design of peptide inhibitors against steric zipper-forming segments from its central low-complexity domain (LCD). My contribution to this work included high-throughput screening of this inhibitor panel in a cell culture model of SARS-CoV-2 infection, and subsequent evaluation of inhibitor hits. I identified an inhibitor termed G12 that robustly reduced SARS-CoV-2 infection in a dose-dependent manner, and disrupted phase-separation of NCAP *in vitro;* other weaker inhibitors of SARS-CoV-2 infection had no effect on NCAP phase separation, thereby correlating disruption of NCAP condensation with reduced infection in cultured cells. This work demonstrates that amyloid fibrils formed by NCAP can be targeted for antiviral drug design, and the G12 peptide inhibitor is a prototype molecule that may be further optimized for the treatment of severe COVID-19 disease.

Chapter three describes the structure of the AD-associated protein amyloid-β (residues 16-26 D23N), and the design of peptide inhibitors that reduce cytotoxicity and aggregation of full-length Aβ(1-42) and cross-seeding of tau by Aβ. My contribution to this work was in evaluation of inhibitor panels for reduction of Aβ-induced cytotoxicity in N2a cells. I identified one inhibitor termed D1 that reduced cytotoxicity when co-incubated with Aβ(1-42) prior to exposure to cells; a second generation of inhibitors was designed based on D1, and I identified two (D1b and D1d) that reduced cytotoxicity both when co-incubated with Aβ, and when added to pre-formed Aβ fibers directly before exposure to N2a cells. These inhibitors may be considered as lead molecules that can be further optimized for treatment of AD.

The dissertation of Jeannette Teresa Bowler is approved.

Jeff Bronstein

Feng Guo

Kelsey C. Martin

David B. Teplow

David S. Eisenberg, Committee Chair

University of California, Los Angeles

2021

Dedicated to my parents, for their endless love and support on this journey,

and for trusting their seven-year-old with the antique microscope that started it all

TABLE OF CONTENTS

LIST OF FIGURES

Chapter 1

Chapter 2

LIST OF TABLES

ACKNOWLEDGEMENTS

First and foremost, I would like to thank my graduate advisor David Eisenberg, who made this work entirely possible. David has been endlessly supportive of me through the ups and downs of graduate school; he provided the freedom and resources to pursue any question I was interested in, and his guidance and mentorship have allowed me to develop into the scientist I am today.

Thank you to my committee members - Feng Guo, Kelsey Martin, David Teplow, Jeff Bronstein, and David Eisenberg – for guiding and supporting me throughout my time at UCLA, and always challenging me to think deeply about my research.

Thank you to all current and former Eisenberg lab members. I especially want to thank Einav Tayeb-Fligelman, who I worked with closely on the NCAP inhibitors project (chapter 2), and Sarah Griner, who I worked with on the amyloid-beta inhibitors project (chapter 3); they were and continue to be an incredible source of support and inspiration for me, both in the laboratory and outside of it. I also want to thank Rebecca Nelson-Villarama, who I worked with as a first-year rotation student, and all of my Boyer Hall 219B office mates over the years - Lorena Saelices-Gomez, Lisa Johnson, Shruti Sahay, Nicole Wheatley, Meng Zhang, Megan Bentzel, Ke Hou, and Hope Pan. I also had the opportunity to work with two fantastic undergraduate students – Manya Bali and Ainan Geng – who helped me hone my mentorship skills. Finally, thank you to all other Eisenberg lab members that I had the pleasure of interacting with during my time in the lab: Paul Seidler, Qin Cao, Alice Soragni, Boris Brumshtein, Lin Jiang, Jose Rodriguez, Melinda Balbirnie, Romany Abskharon, Alex Lisker, Lukasz Salwinski, Pascal Krotee, Elizabeth Guenther, Michael Hughes, Smriti Sangwan, Shannon Esswein, David Boyer, Kevin Murray, Jiahui Lu, Cindy Cheng, Sean Jiang, Greg Rosenberg, Binh Nguyen, Peter Yang, and Carolyn Hu.

The work described in this dissertation would not have been possible without the expertise of numerous scientists at UCLA. Our extraordinary crystallography team, Duilio Cascio and Michael Sawaya, spent long hours teaching me to solve crystal structures, and kept my spirits up at APS when my crystals turned out to be xylitol; also Michael Collazo and Genesis Falcon, for setting up countless crystallization trays (and some amazing 3D printing). Dan Anderson, our laboratory manager, for instrument guidance and maintenance of equipment and inventory to keep the lab running, particularly during the pandemic; Tamir Gonen and Michael Martynowycz for their expertise in micro-electron diffraction, without whom I could not have determined the M9I structure described in chapter 1; Wong Hoi Hui, Peng Ge, and Ivo Atanasov at EICN for help with electron microscopy, which I utilized in nearly every project I worked on. For the NCAP project (chapter 2), I would like to especially thank Robert Damoiseaux, Vaithilingaraja Arumugaswami, and Gustavo Garcia Jr., for their expertise that made this ambitious project possible. Additionally, thank you to Cindy Chau for administrative support, and the Molecular Biology Interdepartmental Program (MBIDP) and the Cellular and Molecular Biology (CMB) Training Grant for financial support.

I also want to thank all the friends I met at UCLA that made grad school fun, many of whom were mentioned above, and additionally - Jessica Ochoa, Prashansa Ratan, Meaghan Valliere, Henry Chan, and Sunny Chun. Everyone in the Guo, Yeates, Rodriguez, and Feigon labs, who made 3:30pm coffee time the best part of the day, and our Women in Science (WiSE) group, who have been incredible sources of strength and inspiration, particularly during the challenging pandemic year.

Finally, thank you to my family and friends outside of UCLA, for your continuous love and support, even when I seemed to fall off the face of the earth: J.S., M.B, D.J.B, D.T.B., D.C., M.C., M.A., H.M., C.A.

VITA

Education

B.S. Biochemistry - Department of Chemistry & Biochemistry, San Francisco State University. Honors: *summa cum laude* 2014

Research and Teaching Experience

Graduate Student Researcher - Molecular Biology Institute, University of California, Los Angeles (Advisor: Dr. David Eisenberg) 2014-present

Graduate Teaching Assistant - Department of Molecular, Cell and Developmental Biology, UCLA (Supervisors: Dr. Luisa Iruela-Arispe and Dr. Hilary Coller) 2015, 2017

Undergraduate Research Assistant – Department of Chemistry & Biochemistry, San Francisco State University (Advisor: Dr. Weiming Wu) 2012-2014

Undergraduate Teaching Assistant - Department of Chemistry & Biochemistry, SFSU (Supervisor: Dr. Elizabeth Runquist) 2013-2014

Publications

Bowler JT, Sawaya MR, Boyer DR, Cascio D, Bali M, Eisenberg DS. "Structure of the aggregation-driving N-terminus of Orb2A revealed by micro-electron diffraction." *Submitted to J Biol Chem.*

Tayeb-Fligelman E, **Bowler JT**, Tai C, Sawaya MR, Jiang YX, Griner S, Cheng X, Salwinski L, Seidler PM, Lu J, Rosenberg GM, Hou K, Garcia Jr G, Abskharon R, Pan H, Zee CT, Boyer DR, Li Y, Anderson DH, Murray KA, Falcon G, Cascio D, Saelices L, Damoiseaux R, Arumugaswami V, Guo F, Eisenberg DS. "Amyloid formation of the Nucleoprotein of SARS-CoV-2 as an antiviral target" *Submitted to ACS Nano*.

Murray KA, Hu CJ, Seidler PM, Griner SL, **Bowler JT**, Abskharon R, Rosenberg GM, Bentzel M, Eisenberg DS. "De novo designed protein inhibitors of amyloid aggregation and seeding." *Under revision, PNAS.*

Griner SL, Seidler P, **Bowler J**, Murray KA, Yang TP, Sahay S, Sawaya MR, Cascio D, Rodriguez JA, Hattne J, Philipp S, Sosna J, Glabe C, Gonen T, Eisenberg DS. "Structure based inhibitors of Amyloid Beta core suggest a common interface with Tau." *eLife,* e46924. 2019 Oct.

Manuscript in progress

Tai CE, Tayeb-Fligelman E, Griner S, Salwinski L, **Bowler JT**, Abskharon R, Cheng X, Seidler PM, Jiang YX, Guo F. "The SARS-CoV-2 Nucleocapsid preferentially binds long and structured RNAs".

Selected Presentations

Oral Presentation: "Structure of the Fiber Core of Orb2A, a Functional Amyloid, Revealed by Micro-electron Diffraction" Jeannette Bowler*, Michael Sawaya, David Boyer, Duilio Cascio, David Eisenberg. 70th Annual Meeting of the American Crystallographic Association. Aug 3 2020. Virtual Meeting

Oral Presentation: "Structure of the Fiber Core of Orb2A, a Functional Amyloid, Revealed by Micro-electron Diffraction." Jeannette Bowler*, Michael Sawaya, David Boyer, Duilio Cascio, David Eisenberg. UCLA Biological Chemistry Seminar Series. Feb 24, 2020, Los Angeles, CA

Lightening Talk & Poster Presentation: "Structural Studies of Orb2A: A Functional Amyloid Necessary for Long-Term Memory Formation in *Drosophila*." Jeannette Bowler*, Michael Sawaya, David Boyer, Duilio Cascio, David Eisenberg. FASEB SRC The Protein Aggregation Conference: From Structure to In Vivo Sequelae. June 2019, Snowmass, CO

Poster Presentation: "Structural Studies of a Functional Amyloid Necessary for Long-Term Memory Formation in *Drosophila*." Jeannette Bowler*, Michael Sawaya, David Boyer, Duilio Cascio, David Eisenberg. UCLA Glenn T. Seaborg Symposium. November 2018, Los Angeles, CA

Poster Presentation: "Secondary Nucleation of α-synuclein Oligomers as a Mechanism of Cytotoxicity." Jeannette Bowler*, David Eisenberg. FASEB SRC Protein Aggregation in Health and Disease. June 2017, Steamboat Springs, CO

Awards & Scholarships

Best Poster Award - Glenn T. Seaborg Symposium, UCLA — Oct 2018

Cellular & Molecular Biology Training Program — 2015-2017
(Ruth L. Kirschstein National Research Service Award)

OVERVIEW

Chapter 1 is a manuscript submitted to *J Biol Chem* that describes the structure of the amyloid-driving N-terminal segment of the functional amyloid Orb2A. Orb2 is a member of the cytoplasmic polyadenylation element binding (CPEB) family of proteins, and is expressed in *Drosophila* as two isoforms: the rare Orb2A isoform, and the abundant Orb2B isoform. Orb2 binds to and regulates translation of synaptic mRNA, the gene products of which facilitate long-term memory (LTM) maintenance. This project began with the observation by Kausik Si's group that a mutation of the fifth position phenylalanine of Orb2A to tyrosine (F5Y) dramatically reduced Orb2A aggregation, and expression of this mutant in *Drosophila* led to the impairment of LTM maintenance. To understand how addition of a single oxygen atom can affect LTM formation, we structurally characterized the isoform-specific, fibril-driving N-terminal segment of Orb2A, which we termed M9I.

I first show that the M9I segment is sufficient to form amyloid-like fibers, as demonstrated by transmission electron microscopy (TEM) imaging, x-ray diffraction analysis exhibiting a cross-β pattern, and binding to the amyloid-specific dye Thioflavin-T (ThT). I then grew crystals of M9I and solved the structure using the micro-electron diffraction (micro-ED) method, with the aid of crystallography experts Michael Sawaya, Duilio Cascio, and Tamir Gonen. I found that M9I forms parallel in-register β-sheets, with neighboring sheets interacting via a water-excluded self-complementary interface formed by residues 5-FVNFI-9. We used computational methods to show that the M9I steric zipper structure is predicted to be approximately as stable as pathogenic amyloid steric zippers. The fifth and eighth position phenylalanine residues stack in the dry interface, providing a structural hypothesis for how the F5Y mutation reduces aggregation and LTM: addition of the tyrosyl oxygen may cause a steric clash in the interface, thereby destabilizing Orb2A fibers. I then expressed and purified the

Orb2A PLD (residues 1-80) either as the wild-type sequence, or replacing either F5 or F8 with a tyrosine to sterically disrupt the dry interface. Using ThT assays and TEM imaging, I found that fibril formation was reduced upon replacing either phenylalanine residue, suggesting that F5 and F8 are important for driving Orb2A aggregation. Lastly I propose a possible structural model for full-length Orb2A, which integrates our M9I structure with the previously published cryo-EM structure of endogenous Orb2B fibers.

Chapter 2 is a manuscript submitted to *ACS Nano* that describes the amyloid-forming properties and design of structure-based inhibitors of the nucleocapsid (NCAP) protein from SARS-CoV-2. This project was started as a result of the COVID-19 pandemic, and was a collaborative effort between multiple labs, encompassing structural, biochemical, computational, and cultured cell experiments. Einav Tayeb-Fligelman led the project, and along with Sarah Griner, Sean Jiang, Cindy Cheng, and I, show that both full-length NCAP, and its central LCD segment, can form amyloid-like fibers and undergo liquid-liquid phase separation (LLPS) in the presence of a short viral RNA segment; Christen Tai prepared RNA samples and analyzed RNA-protein binding. Michael Sawaya led the x-ray crystallography work and determined three atomic resolution structures of short amyloid-driving segments of the LCD. These structures informed computational design of inhibitors of amyloid formation, which we hypothesized may disrupt the functional oligomerization of NCAP in the viral replication cycle.

My primary contribution to this project was to manage all cell culture work, including screening of over 100 inhibitor peptide candidates in a previously established cell culture model of SARS-CoV-2 viral infection. To accomplish this, I worked with virology expert Vaithilingaraja Arumugaswami and high-throughput screening expert Robert Damoiseaux to execute and analyze viral infectivity using immunofluorescence staining in HEK293 cells stably expressing human ACE2. I optimized the inhibitor preparation and assay conditions for compatibility with our low-solubility inhibitors, and used high-throughput confocal microscopy and image quantification to assess inhibitor effectiveness. I identified several peptides that reduced

infectivity in cells, and I found that the most effective inhibitor, called G12, reduced viral infection in a dose-dependent manner by ~50% at the highest dose, with no associated cytotoxicity. I also tested the effect of our top inhibitor hits on liquid-liquid phase separation (LLPS) of full-length NCAP protein, and found that G12 strongly disrupted phase separation, while the other inhibitors with weak anti-viral activity had little to no effect on NCAP LLPS. Taken together with all results in the paper, we correlated a disruption of NCAP LLPS and amyloid formation with a reduction in SARS-CoV-2 infectivity, and showed proof-of-concept for use of structure-based, rationally designed peptides for treatment of severe COVID-19 infection.

Chapter 3 is a reprint of a published paper (Griner, et al., 2019, *eLife* e46924) describing the development of structure-based peptide inhibitors of amyloid-beta (Aβ) that reduce cytotoxicity of exogenous Aβ(1-42) fibers, and seeding of tau protein by Aβ. This work was led by Sarah Griner, who crystallized and solved the Aβ 16-26 D23N structure. My contribution as third author was to perform and analyze the cytotoxicity assays of exogenously added Aβ(1-42) to N2a cells. I screened the initial panel of designed inhibitors following co-incubation with Aβ(1-42), and identified the inhibitor D1 as a robust inhibitor of cytotoxicity. D1 was further optimized by Kevin Murray to generate a second generation of inhibitors, of which I identified two inhibitors that performed slightly better than D1 when co-incubated with Aβ(1-42), and interestingly were also capable of reducing cytotoxicity of Aβ(1-42) pre-formed fibers, on which the original D1 peptide had no effect. Paul Seidler performed tau biosensor cell seeding assays, and in combination with Sarah's biochemical work, showed that D1, D1b, And D1d all reduced seeding of tau by Aβ. In a separate submitted manuscript, (Murray et al., *PNAS in revision*) in which I am 5th author, I performed a similar assay testing a different panel of mini-protein Aβ inhibitors, which I found rescued Aβ-induced cytotoxicity to N2a cells.

CHAPTER 1

Structure of the aggregation-driving N-terminus of Orb2A revealed by micro-electron diffraction

Jeannette T. Bowler[1,2*], Michael R. Sawaya[1,2], David R. Boyer[1,2], Duilio Cascio[1,2], Manya Bali[1,2], David S. Eisenberg[1,2*]

[1]*Molecular Biology Institute, University of California, Los Angeles*

[2]*Howard Hughes Medical Institute*

*for correspondence: **jbowler@ucla.edu** (JTB), **david@mbi.ucla.edu** (DSE)

Running title: Micro-ED structure of the Orb2A N-terminus

Keywords: Amyloid, cytoplasmic polyadenylation element binding (CPEB) protein, electron microscopy (EM), functional amyloid, intrinsically disordered protein, micro-electron diffraction (micro-ED), Orb2, protein aggregation, protein structure

Abstract

Amyloid protein aggregation is commonly associated with progressive neurodegenerative diseases, however not all amyloid fibrils are pathogenic. The neuronal cytoplasmic polyadenylation element binding (CPEB) protein is a regulator of synaptic mRNA translation, and has been shown to form functional amyloid aggregates that stabilize long-term memory. In adult *Drosophila* neurons, the CPEB homolog Orb2 is expressed as two isoforms, of which the Orb2B isoform is far more abundant, but the rarer Orb2A isoform is required to initiate Orb2 aggregation. The N-terminus is a distinctive feature of the Orb2A isoform and is critical for its aggregation, and intriguingly, replacement of phenylalanine in the 5th position of Orb2A with tyrosine (F5Y) in *Drosophila* impairs stabilization of long-term memory. The structure of endogenous Orb2B fibers was recently determined by cryo-EM, but the structure adopted by

fibrillar Orb2A is less certain. Here we use micro-electron diffraction to determine the structure of the first nine N-terminal residues of Orb2A, at a resolution of 1.05 Å. We find that this segment (which we term M9I) forms an amyloid-like array of parallel in-register β-sheets, which interact through side chain interdigitation of aromatic and hydrophobic residues. Our structure provides an explanation for the decreased aggregation observed for the F5Y mutant, and offers a hypothesis for how the addition of a single atom (the tyrosyl oxygen) affects long-term memory. We also propose a structural model of Orb2A that integrates our structure of the M9I segment with the published Orb2B cryo-EM structure.

Introduction

Amyloid protein aggregation is characterized by the formation of stable, self-propagating, β-sheet rich protein fibrils(1). Although amyloid formation is traditionally associated with neurodegenerative diseases such as Alzheimer's and Parkinson's, a growing number of functional proteins have been identified whose function in the amyloid state provides a biological benefit to their host(2, 3). These include components of bacterial biofilms(4–6) and fungal hydrophobins(7, 8) as well as scaffolding and signaling complexes(9–11), and several RNA-binding proteins (RBPs)(12–15). One such functional amyloid RBP is the cytoplasmic polyadenylation element binding (CPEB) protein, first shown to have functional amyloid properties in *Aplysia (Ap*CPEB*)*(16). *Ap*CPEB(17), as well as its mammalian homolog CPEB3(18, 19) and *Drosophila* homolog Orb2(20, 21), is localized at neuronal synapses and contains the canonical RNA-recognition motifs (RRM) found in all CPEB proteins, as well as a functional prion-like domain (PLD). As a monomer, CPEB is a repressor of mRNA translation, while synaptic activity promotes formation of stable amyloid-like aggregates of CPEB, resulting in activation of mRNA translation(22, 23). The mRNAs targeted by CPEB are transcripts of several genes that facilitate long-term memory (LTM) persistence(20, 23–25), and the ability of CPEB

to stably maintain an amyloid-like state is proposed as a biochemical mechanism for long-term, synapse-specific changes in protein expression(18, 22, 26).

The *Drosophila* homolog Orb2 has been well characterized, revealing an intriguing aggregation mechanism(25–32). Two protein isoforms are expressed from the *orb2* gene: Orb2A, which is highly aggregation-prone and kept at extremely low concentration in the resting-state synapse, and Orb2B, which is more soluble and makes up the majority of expressed Orb2 protein. Following synaptic stimulation, Orb2A forms stable aggregates that nucleate Orb2B amyloid formation, thereby switching Orb2 from a translation inhibitor to activator(27–29), possibly through recruitment of Orb2 monomer- or amyloid-specific binding partners that facilitate RNA degradation or translation, respectively(29, 30). Both Orb2 isoform sequences are nearly identical, consisting of a Q/H-rich region and C-terminal RRMs. The isoforms differ only at the N-terminus: whereas Orb2B has a 162-residue serine/glycine-rich N-terminus that is predicted to be intrinsically disordered and as of yet has unknown function, the Orb2A N-terminus is only 9-residues in length, but is nevertheless critical for its self-assembly(27) and function in initiating Orb2B aggregation(28).

The structure of endogenous Orb2 fibers was recently determined by cryo-EM(32), showing that the ordered fiber core is formed by the Q/H-rich region and is made up of three interwound protofilaments, each consisting of paired in-register β-sheets connected by a β-hairpin. Although the Orb2A isoform also contains this Q/H-rich region, several lines of evidence point towards a critical role for the isoform-unique N-terminus in Orb2A fiber formation. Deletion or mutation of the Orb2A N-terminal residues was found to reduce formation of insoluble Orb2 aggregates both *in vitro*(31) *and in vivo*, and a single point mutation of the 5th position phenylalanine to tyrosine (F5Y) impaired LTM formation in *Drosophila*(27). Additionally, solid-state NMR (ssNMR) experiments indicate that the N-terminal residues of Orb2A adopt a highly ordered, in-register parallel β-sheet, whereas the Q/H-rich region has more intermediate dynamics and was not required for fiber formation(33).

Here we characterized and determined the structure of the critical nine-residue Orb2A N-terminus (which we term M9I) by micro-electron diffraction, and find that this segment forms self-complementary β-sheets driven, at least in part, by hydrophobic aromatic residues F5 and F8.

Results

We initially characterized full-length Orb2A (Orb2A-FL), and the first 80 residues (Orb2A-PLD) containing both the M9I segment and the Q/H-rich region (Fig. S1A,E), following bacterial protein expression and purification under strong denaturing conditions. Purified Orb2A-FL rapidly precipitated upon dialysis or dilution into a physiological salt buffer containing mild denaturant (1M urea), and exhibited weak ThT fluorescence (Fig. S1B). TEM analysis showed Orb2A-FL forms a heterogenous mixture of fibrillar and amorphous aggregates, and x-ray diffraction patterns from aligned fibers revealed weak broad reflections at ~4.7 and 10 Å (Fig. S1C,D), indicating that Orb2A-FL can form amyloid-like structures, although this may be less efficient *in vitro* without native binding partners(32). Under the same incubation conditions, purified Orb2A-PLD formed more typical amyloid-like fibrils that exhibited a similar fiber diffraction pattern and higher ThT fluorescence, and fibril formation occurred over several days (Fig. S1F-H). We attempted to prepare Orb2A-PLD or Orb2A-FL fiber samples suitable for cryo-EM, but fibers remained highly bundled and heterogenous in a variety of buffer and fibrillation conditions.

We therefore chose to focus on the short but critical M9I segment for our high-resolution structural studies (Fig. 1A). When incubated in physiological salt buffer at room temperature, M9I forms amyloid fibrils within a few hours, reaching maximum ThT fluorescence within ~1-2 days (Fig. 1B, blue). TEM imaging shows that M9I forms twisting, unbranched fibers approximately 10 nm in width and up to several microns in length. Aligned M9I fibers exhibited

the amyloid-characteristic cross-β diffraction pattern, with sharp meridional reflections at 4.8 Å and equatorial reflections at 10.5 Å (Fig. 1C, top row).

We also tested the effect that the F5Y mutation has on M9I amyloid formation. When incubated under the same conditions, M9I-F5Y appears to initially bind similar levels of ThT as the wild-type peptide, but the signal drops after ~1 day and remains significantly lower than wild-type peptide by the end of 5 days incubation (Fig. 1B, purple). Examination by TEM at 20 hours shows that M9I-F5Y forms rod-like fibers which appear to be slightly wider than WT M9I fibers and significantly shorter (Fig. 1C, left). Fiber morphology remained similar after 5 days of incubation (Fig. 1C, right), and while individual WT fibrils tended to assemble into thicker rope-like helical filaments, M9I-F5Y formed clumps of short (~50-300 nM in length) rod-like fibrils. X-ray diffraction of M9I-F5Y fibers after 1 day incubation revealed powder diffraction-like rings (Fig. 1C middle), consistent with poor alignment of these short fibers. Additionally, lower resolution reflections differ significantly between WT and F5Y fibers (Fig. S2), which may indicate an altered arrangement of pairs of β-sheets within individual protofibrils. Taken together, these results show that the M9I segment is sufficient to rapidly and efficiently form typical amyloid-like fibers, and incorporation of the F5Y mutation results in an altered morphology that appears to preclude formation of typical elongated amyloid fibers.

We next determined the atomic structure of M9I in the fibrillar state at 1.05 Å resolution. Crystallization screening of the wild-type M9I peptide showed a propensity to form small fibrillar and needle-like crystals, but single crystals could not be grown large enough for traditional x-ray data collection (Fig. S3). However, examination of the hanging drop crystallization solution by TEM revealed microcrystals of an optimal size for micro-electron diffraction (micro-ED), which has previously been used to solve the structures of other amyloid spine segments(34–36). We grew microcrystals in batch by incubating equal volumes of peptide stock solution with crystallization solution, and prepared sample grids using a similar workflow to single-particle cryo-EM. M9I microcrystals diffracted to high resolution (resolution cutoff at

1.05 Å) and the phases were determined using direct methods (Fig. 2A, Table 1). Our structural model reveals that M9I forms an array of parallel, in-register β-sheets arranged in a face-to-back orientation, as defined by a class 4 steric zipper. Aromatic side chains (Y2, F5, F8) are stacked in an energetically favorable parallel-displaced orientation(37) along the fiber axis (Fig. 2B), and in addition to main chain hydrogen bonds, a hydrogen-bonded ladder forms parallel to the fibril axis between amide side chains of N7 (Fig. 2C). The C-terminal residues F5-I9 assemble into a water-excluded steric zipper, in which the F5 benzyl ring stacks in an edge-to-face orientation against F8 of the neighboring sheet. In contrast to the tightly packed interface formed by C-terminal residues, the N-terminal residues M1-K4 are more loosely packed and hydrated, with side chains interacting with a network of ordered water molecules (Fig. S4B). We predict that in full-length Orb2A fibers, these N-terminal residues are either solvent exposed or interact with polar residues further downstream of the M9I segment (Fig 4). The average solvation energy per residue upon assembly of the M9I dry interface was calculated to be -0.56 kcal/mol, on par with solvation energies of formation of pathogenic amyloid steric zippers(14). The dry interface buries relatively little surface area (128.2 $Å^2$) compared to steric zippers on average (~150-200 $Å^2$)(1), but the high calculated shape complementary (0.88) reflects the close packing and favorable van der Waals contacts formed by hydrophobic side chains (Fig. S4C).

Our structure offers a hypothesis for the effect of the F5Y replacement, as addition of a hydroxyl group would cause a steric clash with F8 on the neighboring sheet, potentially destabilizing the inter-sheet interface. We further explored the contribution of the F5-F8 interaction, as inter-sheet Phe-Phe interactions have been reported to play a role in driving fiber formation of other amyloidogenic proteins(38). We expressed and purified the OrbA-PLD (residues 1-80) with either F5 or F8 replaced by tyrosine (Y) to sterically disrupt the packing of these residues in the dry interface, and compared aggregation kinetics and fiber morphology to the wild-type (WT) Orb2A-PLD (Fig. 3). Whereas WT Orb2A-PLD formed abundant elongated fibrillar species, the F5Y variant formed short fibrils reminiscent of those formed by the M9I-

F5Y segment, and exhibited a corresponding reduction in ThT fluorescence. The F8Y variant appeared to form a heterogenous mixture of long and short fibers, although reduced ThT fluorescence indicates less efficient fibril formation. Taken together, these results show that the M9I segment of Orb2A adopts a parallel, in-register steric zipper structure with side chains of F5 and F8 stacked within the dry inter-sheet interface, and that replacement of either of these residues impairs formation of amyloid-like fibrils of the Orb2A-PLD.

In addition, we examined whether it is sterically possible for the Orb2A Q/H-rich region, which is connected to M9I via a 13-residue linker (Fig. 1), to adopt a protofilament structure of the form of the Orb2B cryo-EM structure(32). In both structures, individual strands are oriented in parallel in-register β-sheets, and extension of a pair of sheets from the M9I structure shows that the Q/H-rich region can potentially form a β-hairpin connected via the 13-residue linker (Fig. 4). The alternating up-down orientation of β-sheets in the M9I homo-zipper results in one sheet (colored grey) that can potentially form a heterozipper interaction between M9I and the exposed outer interface of the β1 strand of the Q/H-region. Note that in this model F5 would also be part of the potential heterozipper interface, and its interaction with residues downstream of M9I may also affect fibrillation. The Q/H-region extending from the mated strand (colored purple) can still form a β-hairpin, but the orientation would preclude a similar heterozipper formation. Homotypic seeding is the most common mechanism by which amyloid fibers grow(1, 39), and we predict that Orb2A may seed Orb2B by templating hydrogen-bonded stacking of their common Q/H-rich regions. This speculative model would be consistent with previous studies indicating that the Orb2A isoform is required for initiating aggregation, whereas Orb2B is required for maintaining stable aggregates over the long-term(25, 27, 28, 30).

Discussion

Prior structural studies of Orb2A indicate that the protein can adopt multiple conformations, but have left unclear the structure of the isoform-unique M9I segment. *In vitro*,

Orb2A is reported to form parallel in-register β-sheets over time(31, 33, 40), with one ssNMR study indicating that the M9I segment, but not the Q/H-rich region, forms the ordered fiber core(33). Orb2A can also undergo liquid-liquid phase separation and subsequent fiber formation, although analysis of immobile residues in that study did not clearly point to the presence of M9I segment(41). In a solution-state NMR study of the Orb2A PLD, the Q/H-rich region adopted varying degrees of α-helical secondary structure whereas the rest of the protein, including M9I, remained disordered(42), and in the presence of lipids the N-terminus was found to form an α-helix and Orb2A fibrillation was inhibited(43). The M9I segment was not observed in the endogenous Orb2 cryo-EM structure(32), but this may be expected given that the Orb2B isoform is predominantly expressed. Given the critical role of the M9I segment in initiating Orb2 aggregation, determining its fibrillar structure would improve our understanding of the early steps in Orb2 amyloid formation.

To this end, we used micro-ED to determine the atomic resolution structure of the M9I segment from Orb2A, and show that a hydrophobic stretch of residues (5-FVNFI-9) forms a self-complementary steric zipper core, consistent with ssNMR data of the Orb2A PLD(33). Phenylalanine residues (F5 and F8) of neighboring sheets stack closely within the dry interface, leading us to hypothesize that the previously characterized F5Y mutation(27, 31) may reduce Orb2A amyloid formation by sterically hindering proper assembly of β-sheets, instead forcing assembly through an alternative interface. Whereas our x-ray diffraction results indicate that strands formed by M9I-F5Y (Fig. 1) are likely still oriented in a cross-β arrangement (although not necessarily a class 4 zipper), ThT assays suggest that fibrillation is less efficient, and EM imaging of fiber assemblies show the mutation induces a distinct morphology relative to WT fibers. Screening crystallization conditions for M9I-F5Y yielded only amorphous aggregates or very small fibrous species (Fig. S3B), and we suspect that the F5Y mutation may preclude formation of a well-ordered crystalline lattice large enough to be useful for structure determination.

Examination of the M9I structure reveals stabilizing interactions that are common among amyloid-driving steric zipper segments. Aromatic residues, of which M9I has three, have been proposed to stabilize amyloid protein assembly (38, 44–49), and here we find in-register stacking of aromatic side chains produces favorable π-π interactions along the fiber axis (Fig. 2C). In addition, neighboring β-sheets interact through a self-complementary interface made up primarily of aromatic and hydrophobic side chains, and polar resides (2-YNK-4) interact with ordered water molecules. Only one polar residue, N7, is part of the dry interface, and forms a hydrogen-bonded ladder of stacked amide side chains along the fiber axis. Such polar ladders frequently form between stacked side chains parallel to the amyloid fiber axis (49–56), including in the endogenous Orb2B structure(32).

Additionally, energetic stability calculations reveal that the M9I steric zipper structure is of relatively similar energetic stability(14) and shape complementarity(1) to pathogenic amyloid zippers, which may in part explain the strong amyloid-forming propensity of this segment. *In vivo*, aberrant Orb2A aggregation may be avoided by regulation of protein expression levels, e.g. by post-translational modifications that affect protein stability(29) and variations in intron splicing(57). Orb2B fibers are also unstable under acidic conditions allowing for lysosomal degradation(32), and Orb2 fibrillation may also be modulated by lipid membranes(43) and divalent metal binding(40).

On the basis of our structure of M9I, we propose a structural model for full-length Orb2A. The M9I steric zipper structure we report here (residues 1-9) and that of the Orb2 Q/H-rich region(32) (residues 23-53) can theoretically be formed by a single Orb2A strand, with a 13-residue disordered linker connecting the two structured domains (Fig. 4). We predict that Orb2A aggregation may initially be driven by the hydrophobic, steric zipper-forming propensity of the isoform-unique M9I segment. Formation of the M9I steric zipper structure would orient multiple strands of the adjacent Q/H-rich region in close proximity, effectively increasing the local concentration and promoting conversion to a more stable β-sheet conformation.

Formation of such a multi-stranded complex would generate an Orb2A seed with an identical Q/H-rich region protofilament structure as found in endogenous Orb2B fibers, allowing for structurally-homotypic seeding. This hypothetical hetero-fiber complex is supported by prior studies showing a direct interaction between Orb2A and Orb2B mediated by their Q/H-rich regions(27, 28), and demonstrating that the more aggregation-prone Orb2A isoform induces the conversion of soluble monomeric Orb2B into stable aggregates(29, 30, 32). Although such a complex is structurally feasible it is highly speculative at this point, and further studies will be required to determine if it describes the Orb2 aggregation mechanism.

In conclusion, our results add to the growing literature on the functional amyloid activity of Orb2, and suggest a plausible structural mechanism for initiation of Orb2 aggregation. Ultimately, this work may aid in our understanding of LTM maintenance, and yield insights into the molecular mechanisms of amyloid formation and disease.

Experimental Procedures

Plasmids & cloning

Orb2A-FL plasmid was a gift from Dr. Ansgar Siemer (USC), expressing full-length Orb2A in a pET-28 vector with a C-terminal His-tag. The Orb2A-PLD construct was generated using overlap-extension PCR(58) and the F5Y and F8Y mutants were generated using the Quikchange II site-directed mutagenesis kit (Agilent Technologies Inc, Santa Clara, CA). All plasmid sequences were confirmed by Sanger sequencing (Laragen Inc, Culver City, CA).

Protein expression & purification

Recombinant protein was expressed and purified largely following previously established protocols(33). Plasmids were transformed into Bl21-Gold(DE3) cells (Agilent) and cultures grown at 37 °C in LB-kanamycin media until OD600 reached ~0.6, then expression induced with 1mM IPTG and cultures incubated either at 30 °C for 4-5 hours (Orb2A-FL) or 20 °C for 15-

18 hours (Orb2A-PLD constructs). Cell pellets were harvested at 4,000 rpm for 15 minutes at 4 °C and stored at -80 °C until use. Orb2A-FL and -PLD constructs were solubilized by different methods as follows: FL pellets were re-suspended in FL-lysis buffer (50 mM Tris pH 8.0, 100 mM NaCl, 0.5% Triton X-100, 0.05% 2-mercaptoethanol) supplemented with Halt protease inhibitor (ThermoFisher), and sonicated on ice for ~10 minutes, followed by centrifugation at 10,000 rpm for 15 minutes at 4 °C. The soluble fraction was discarded, and the insoluble fraction re-suspended in FL-extraction buffer (100 mM sodium phosphate pH 8.0, 250 mM NaCl, 6 M guanidine hydrochloride, 10% v/v glycerol, 1mM DTT), sonicated again then incubated overnight on an orbital shaker at room temperature; the next day, the soluble fraction was separated by centrifugation at 15,000 rpm for 30 minutes at 4 °C. PLD construct pellets were resuspended in PLD-lysis buffer (10 mM Tris pH 8.0, 8 M urea, 100 mM sodium phosphate, 0.05% 2-mercaptoethanol, Halt protease inhibitor) and sonicated on ice for ~15 minutes, followed by centrifugation at 15,000 rpm for 30 minutes at 4 °C. The remaining purification steps are the same for all constructs: the soluble cell lysate was filtered thru a 0.45-um high-particulate syringe-driven filter (HPF Millex-HV, Millipore, Billerica, MA). A 5-mL HisTrap-HP column (GE Healthcare) was equilibrated in Buffer A (10 mM Tris pH 8.0, 8M urea, 100 mM sodium phosphate, 1 mM DTT) and filtered lysate was loaded at 1 mL/min. The column was then washed with Buffer A + 0.5% Triton X-100, Buffer A + 500 mM NaCl, and Buffer A adjusted to pH 6.7, and finally Buffer A alone again. Orb2A protein was then eluted with a step gradient of Elution Buffer (Buffer A + 500 mM imidazole pH 8). Most protein eluted at ~100 mM imidazole. Purified protein was loaded into 6,000-8,000 molecular weight cutoff dialysis tubing (Fisher Scientific) and dialyzed at 4 °C against PBS pH 7.4, 4 M urea, 10% glycerol, 1 mM DTT, then filtered thru a 0.2-um spin filter (Millipore). Protein concentration was measured by A280 absorbance using a NanoDrop One (ThermoScientific) and the calculated extinction coefficient, and snap frozen in liquid nitrogen and stored at -80 °C.

Peptide preparation

Peptides were purchased from Genscript (Piscataway, NJ) at >98% purity and stored in lyophilized form at -20 °C.

Thioflavin-T assays

Thioflavin-T (ThT) assays were performed in black polystyrene 96-well plates (ThermoFisher cat. #265301) sealed with UV optical tape, with a total volume per well of 200 uL. ThT fluorescence was measured with an excitation/emission wavelength of 440/480 nm using a FLUOstar Omega plate reader (BMG LABTECH), and readings were taken every 15 minutes. Experiments were performed at 25 °C, without agitation except for a 5 second, 300 rpm shake every 15 minutes. ThT curves are averaged from three independent replicates with error bars showing standard deviation. For M9I (wild-type) and M9I-F5Y, peptides were dissolved in 100% DMSO (Fisher Bioreagents cat. #BP231100), then diluted in PBS pH 7.4 and filtered with a 0.2 uM spin filter (Millipore). Peptide solution was mixed with ThT stock solution (100 uM ThT in 1X PBS pH 7.4) in 96-well plates for a final concentration of 1 mg/mL peptide (~850 uM) in PBS pH 7.4 (1% DMSO) and 20 uM ThT. For Orb2A-FL and Orb2A-PLD (Fig. 1), protein stocks were diluted to 10 uM in PBS pH 7.4, 1 M urea, 1 mM EDTA, 5% glycerol, 1 mM DTT, and 10 uM ThT. For Orb2A-PLD mutant ThT assays (Fig. 3), protein stocks were diluted to 10 uM in 10 mM HEPES pH 7.6, 100 mM KCl, 1 M urea, 0.1 mM $CaCl_2$, 1 mM $MgCl_2$, 5% glycerol, 1 mM DTT, and 10 uM ThT.

Transmission electron microscopy analysis

Protein and peptide samples were prepared for TEM in 96-well plates as described above for ThT assays, except that ThT dye was not added (instead an equal volume of PBS pH 7.4 was added). Samples were spotted onto freshly glow-discharged carbon-coated formvar grids (Ted Pella Inc), and allowed to adsorb for 3-4 minutes before wicking off excess liquid with Whatman

filter paper. The grids were then washed twice with milliQ water, followed by staining with 2% uranyl acetate for 2 mins, wicked off and the grids allowed to fully dry before imaging. Grids were imaged using either a T12 or T20 electron microscope (FEI).

Fiber diffraction

Orb2A-FL and -PLD stocks were diluted to 10 uM in PBS pH 7.4, 1 M urea, 1 mM EDTA, 5% glycerol, 1 mM DTT, and incubated at room temperature without agitation; Orb2A-FL was incubated for 1 day, and Orb2A-PLD for 7 days. Fibrils were spun down in a tabletop microcentrifuge at 21,000 x g for 20 minutes. The supernatant was removed, and fibers were gently resuspended in water followed by centrifugation to remove salt from the sample. Fiber samples were concentrated 50X in water and suspended between two glass capillary ends, and let to dry overnight. Fiber diffraction images were taken with a RIGAKU R-AXIS HTC imaging plate detector using CuK_{α} radiation from a Rigaku FRE+ rotating anode generator with VARIMAX HR confocal optics (Rigaku, Tokyo, Japan). Radial profiles were calculated with a program written in-house that calculates the average intensity as a function of distance from the beam center.

M9I crystallization & structure determination by micro-ED

Micro-ED data collection and processing was performed essentially as described in previously established protocols(59, 60). Lyophilized M9I peptide was dissolved in 100% DMSO (ThermoFisher), followed by dilution with milliQ water to yield a 6 mg/mL peptide solution in 1% DMSO, then filtered using a 0.2-um spin filter (Millipore). The filtered solution was mixed in a 1:1 ratio with a 0.1 M sodium phosphate pH 4.6, 1.5 M NaCl solution, and allowed to incubate quiescently on the benchtop at room temperature, and microcrystals grew within 2-3 days. 4 uL of microcrystal solution was dispensed onto freshly glow-discharged Quantifoil Cu R1/4 300-mesh carbon grids, and allowed to adsorb for 4 minutes before wicking off excess liquid, and

grids were washed twice with milliQ water to remove excess salt. Grids were plunge frozen into liquid ethane using a Vitrobot Mark IV (FEI) and either stored in liquid nitrogen until use, or placed into a cryogenic autoloader for imaging. Images and diffraction data were collected using a Thermo Fisher Talos Arctica cryo-electron microscope operating at 200 kV and fitted with a Ceta-D CMOS 4k x 4k camera. Images were recorded as a movie in rolling shutter mode with 2 x 2 pixel binning(61), and an exposure time of 2 seconds per frame, while the stage was continuously rotated within the electron beam at a fixed rate of 0.3° per second, corresponding to a fixed angular wedge of 0.6° per frame. Datasets spanned a wedge of reciprocal space ranging from 40 to 90°. We used a selected area aperture with an illuminating spot size of ~1 uM, thereby equating to an electron dose rate of <0.01 $e^-/Å^2$ per second deposited onto our crystals. Diffraction movies were converted from SER files to SMV format using publicly available software (**https://cryoem.ucla.edu/pages/MicroED**)(59). Diffraction images were indexed and integrated with XDS and datasets scaled and merged with XSCALE(62) from 11 different crystals. Phases were determined by direct methods with SHELXD(63). Subsequent rounds of model building and refinement were performed using COOT(64) and REFMAC(65), respectively. Electron scattering factors were used for refinement. Data processing and refinement statistics are reported in Table 1.

Structure stability calculations

Surface area buried and shape complementarity (Sc) were calculated using AREAIMOL(66, 67) and Sc(68–70), respectively. Solvation energy was calculated based on previously published work(14, 44, 71, 72).

All graphs were made with GraphPad Prism version 9. Diffraction images were analyzed using the Adxv software package (Scripps). All M9I structure images were made using either PyMol or UCSF Chimera; hydrophobicity gradients were generated in Chimera based on the Kyte-

Doolittle scale(73). Atomic distances were measured using Chimera; for aromatic residues, the centroid of the benzene ring was used as the point of reference.

Data Availability

The atomic coordinates and structure factors have been deposited in the Protein Data Bank (**http://wwpdb.org/**) Accession code: 7SXN

This article contains supporting information: supplementary.docx (Supplementary Figs 1-4)

Acknowledgements

We thank Ansgar Siemer and Sandy Falk (USC) for the Orb2A plasmid, Daniel Anderson, Michael Collazo, Michael Martynowycz, and Ainan Geng for technical support, and Tamir Gonen, Jose Rodriguez, and Maria Flores for discussion. We thank the Electron Imaging Center for Nanomachines (EICN) at UCLA, the Advanced Photon Source (APS) at Argonne National Laboratory, and the UCLA-DOE X-ray Crystallization Core Technology Center for use of facilities.

Author contributions

J.T.B. and D.S.E designed the project. Cloning, expression and purification of Orb2A constructs, and Thioflavin-T assays were performed by J.T.B. and M.B. Fiber diffraction and analysis were performed by J.T.B, M.R.S. and D.C. TEM imaging and M9I crystallization was performed by J.T.B., and micro-ED sample prepared by J.T.B. and D.R.B. Micro-ED data was collected by J.T.B., and data processing and refinement by J.T.B., M.R.S., D.R.B, and D.C. Stability calculations were done by J.T.B., M.R.S., and M.B. The manuscript was written by J.T.B., M.R.S, and D.S.E. with input from all authors.

Funding and additional information

This work was funded by NSF MCB 1616265.

Conflict of interest

D.S.E. is a SAB member and equity holder in ADRx, Inc.

Abbreviations

CPEB, cytoplasmic polyadenylation element binding; LTM, long-term memory; micro-ED, micro-electron diffraction; PLD, prion-like domain; RBP, RNA-binding protein; RRM, RNA-recognition motif; ssNMR, solid-state nuclear magnetic resonance; TEM, transmission electron microscopy; ThT, Thioflavin-T

Table 1. Statistics of microED data collection and atomic refinement of M9I

Data collection	
Excitation voltage (kV)	200
Electron source	Field emission gun
Wavelength (Å)	0.0251
Space group	$P2_1$
Unit cell dimensions	
a, b, c (Å)	4.83, 23.1, 29.8
α, β, γ (°)	90.0, 92.0, 90.0
Resolution (Å)	18.26-1.05 (1.08-1.05)*
R_{merge} (%)	15.6 (71.2)
Measured reflections	36,014 (1,101)
Unique reflections	2,596 (153)
Completeness (%)	83.3 (69.9)
Multiplicity	13.9 (7.2)
I/σ	8.24 (1.79)
$CC_{1/2}$ (%)	99.4 (57.2)
Refinement	
Reflections in working set	2,336
Reflections in test set	260
R_{work} (%)	18.1
R_{free} (%)	20.1
RMSD bond length (Å)	0.01
RMSD angle (°)	1.84
Number of non-H atoms in refinement	87
Average B-factor (Å^2)	10.7
Ramachandran (%)	
Favored	100
Allowed	0
Outliers	0

*Highest resolution shell shown in parentheses

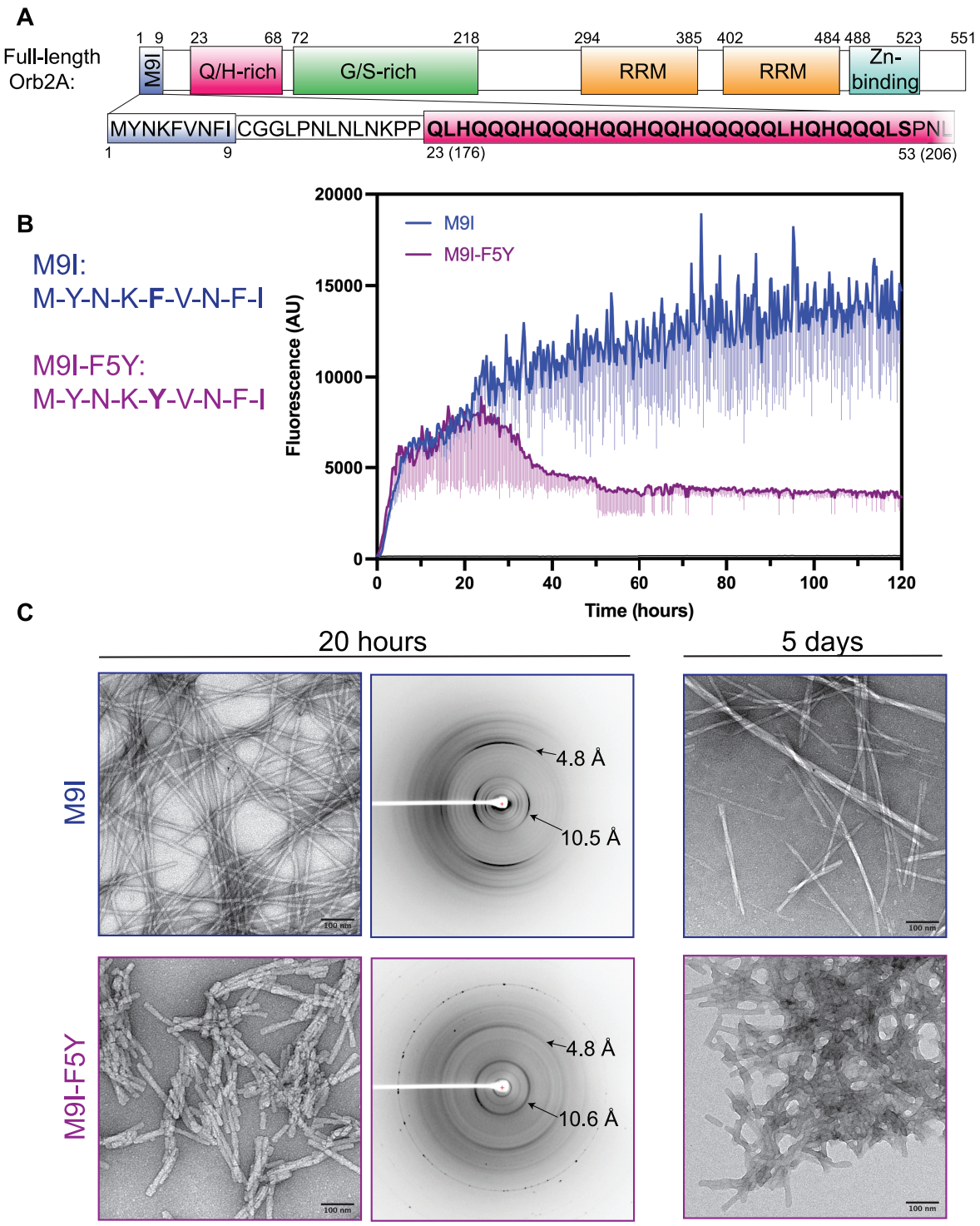

Figure 1: The hydrophobic nine-residue N-terminal segment of Orb2A (M9I) forms amyloid-like fibers

(**A**) Schematic of full-length Orb2A, showing the N-terminal sequence unique to the Orb2A isoform (M9I, blue), followed by a 13-residue linker (white), and the Q/H-rich domain (pink).

Both the linker and Q/H-rich domain are common to the Orb2A and Orb2B isoforms. The corresponding residue positions in the Orb2B isoform are in parentheses, and the segment forming the structured core of Orb2B fibers {Hervas et al, Science 2020} are indicated in bold. (**B**) Left: Segment sequences for wild-type M9I (blue) and M9I with the F5Y mutation (purple). Right: Kinetic Thioflavin T (ThT) assay comparing aggregation kinetics of wild-type M9I and M9I-F5Y at 1 mg/mL concentration (~850 uM). The darker line represents the average reading of three independent technical repeats, and the lighter vertical bars below represent 1 standard deviation. (**C**) Left: Negative-stain TEM analysis of fibers formed by M9I and M9I-F5Y after 20 hours of incubation under identical conditions as (panel B) but without added ThT. Middle: X-ray diffraction of aligned, dried fibers at 20 hours incubation. Right: Negative-stain TEM analysis of M9I and M9I-F5Y fibers after 5 days incubation

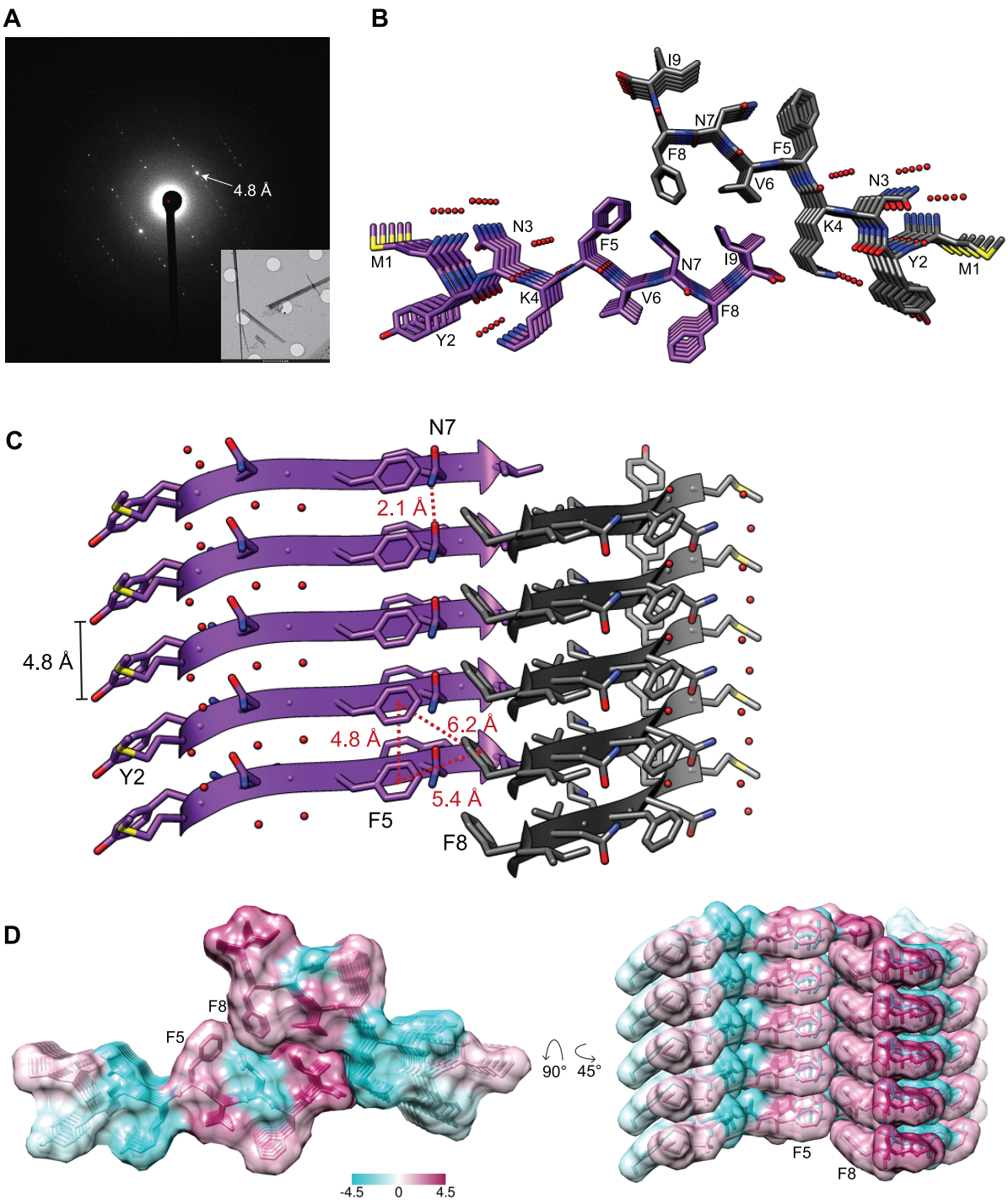

Figure 2: Structure of M9I segment as determined by micro-electron diffraction

(**A**) Representative electron diffraction pattern from micro-ED data collection on M9I microcrystals. Strong reflections at 4.8 Å (white arrow) correspond to inter-β-strand spacings. Inset: Electron micrograph of M9I microcrystals on Quantifoil grids with a hole diameter of 1

uM. (**B**) Structural model of M9I shows formation of in-register parallel β-sheets. Two sheets are viewed down the fibril axis, illustrating the water-excluded interface formed between sheets. Strands are related to each other via a 2_1-screw axis perpendicular to the fiber axis (class 4 steric zipper). Red spheres represent ordered water molecules. (**C**) View perpendicular to fibril axis, showing side chain stabilizing interactions along the fibril axis. Asparagine 7 (N7) side chain forms a ladder of hydrogen bonds, and aromatic residues (Y2, F5, F8) stack in a parallel-displaced fashion. F5 and F8 also interact closely in the dry interface. Atomic separations are indicated in red; distances between aromatic side chains were calculated using the benzyl ring centroid point (red stars). (**D**) Space-filling model of M9I colored according to the Kyte-Doolittle hydrophobicity scale (magenta-hydrophilic, teal-hydrophobic), showing tight packing of hydrophobic residues in the inter-sheet interface.

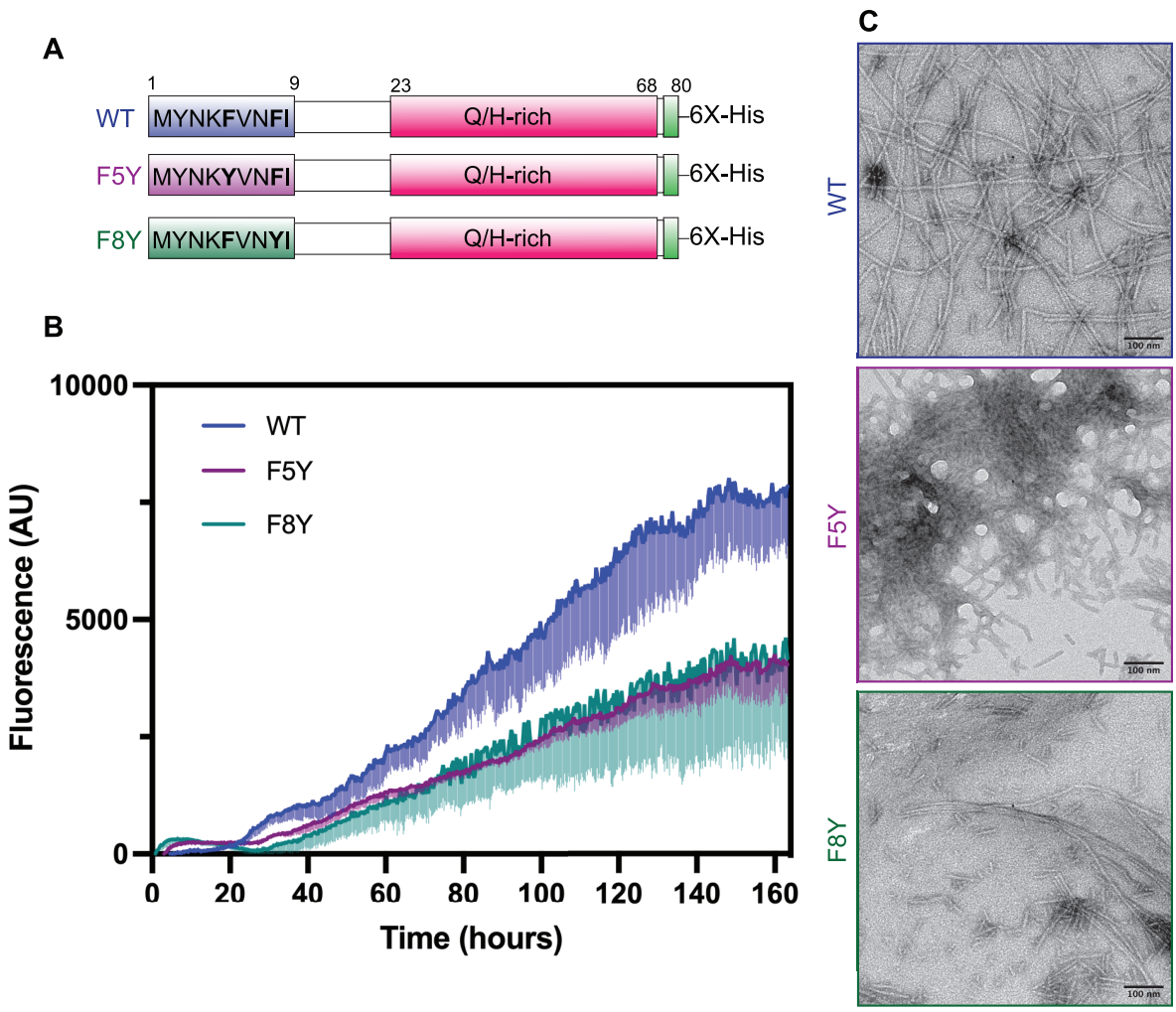

Figure 3: Phenylalanine replacements reduce fibrillation of Orb2A prion-like domain

(**A**) Schematic of Orb2A prion-like domain (PLD) constructs (residues 1-80) with either the fifth (F5Y) or eighth (F8Y) phenylalanine replaced by tyrosine. (**B**) ThT assay comparing aggregation of 10 uM wild-type PLD (blue) to the F5Y (purple) or F8Y (green) PLD constructs. Samples were incubated at 25 °C in HEPES-KCl-urea pH 7.4 buffer. The darker line represents the average reading of technical triplicates, and the lighter vertical bars represent 1 standard deviation. (**C**) Negative stain TEM imaging of WT, F5Y and F8Y Orb2A-PLD after 7 days incubation in identical conditions as above, but without ThT added.

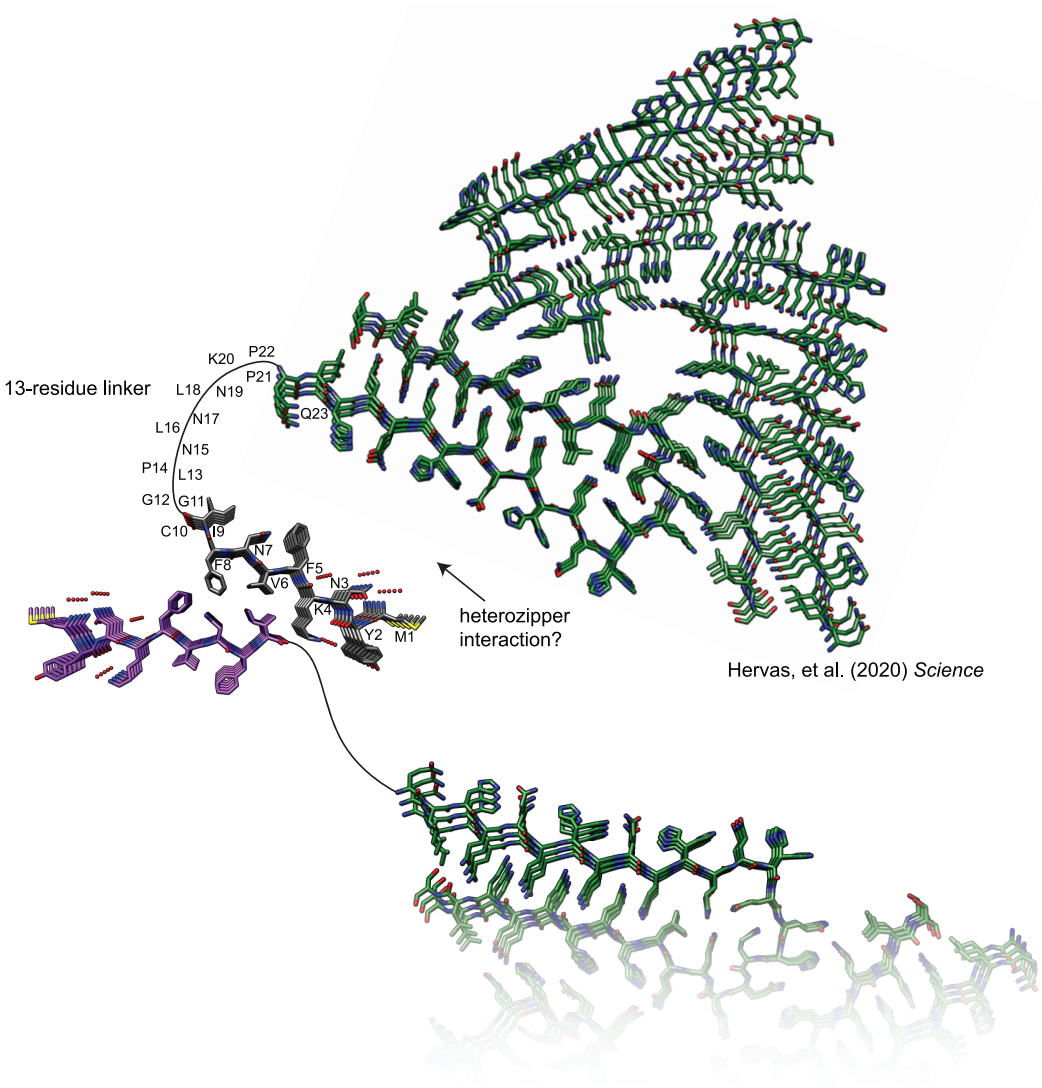

Figure 4: Speculative structural model of an Orb2A-Orb2B hetero-complex

Extension of a pair of sheets from the M9I homozipper structure (grey and purple) shows that the downstream Q/H-rich region (green) can adopt an identical β-hairpin structure as that formed by endogenous Orb2B fibers {Hervas et al, Science 2020}. Orb2A aggregation may initially be driven by homozipper formation of the hydrophobic M9I segment, which would then position the downstream Q/H-rich region in a favorable orientation to adopt an in-register β-sheet. Additionally, one of the paired M9I sheets (grey) could potentially interact with the Q/H-rich region via a heterozipper (black arrow). Formation of such an Orb2A protofibril could then initiate Orb2B fibrillation via structurally homotypic seeding of their identical Q/H-rich regions.

Supplementary Information

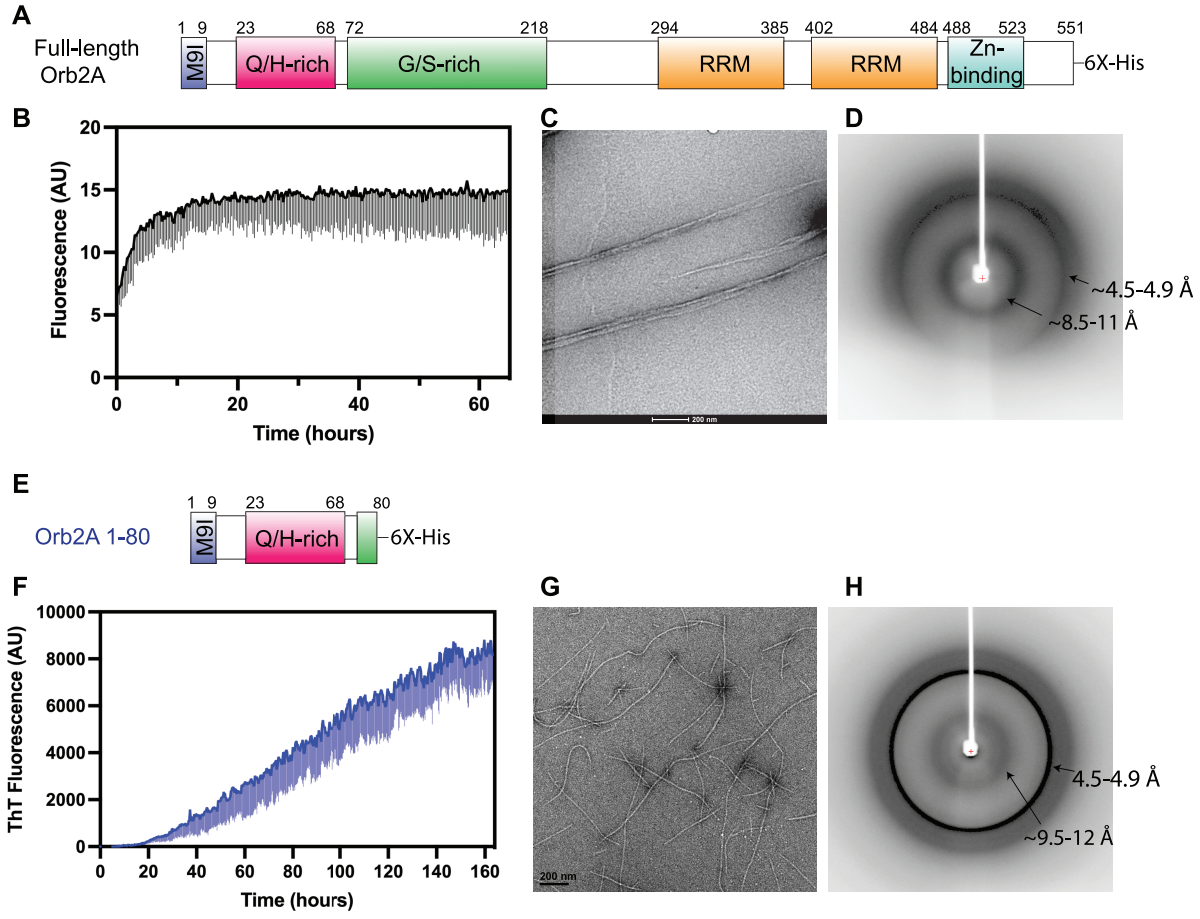

Supplemental Figure 1: Amyloid fibril formation of Orb2A-FL and Orb2A-PLD

(**A**) Schematic of recombinant Orb2A-FL construct (**B**) ThT assay of 10 uM Orb2A-FL at 25 °C. The darker line represents the average reading of technical triplicates, and the lighter vertical bars represent 1 standard deviation. (**C**) Negative stain TEM imaging of FL-Orb2A after 1 day incubation as in (panel B), but without ThT added. (**D**) Fiber diffraction on dried, aligned Orb2A-FL fibers prepared as in (panel C). (**E**) Schematic of recombinant Orb2A-PLD construct (**F**) ThT assay of 10 uM Orb2A-PLD at 25 °C. The darker line represents the average reading of technical triplicates, and the lighter bars represent 1 standard deviation. (**G**) Negative stain TEM of imaging Orb2A-PLD after 7 days incubation as in (panel F) but without ThT added. (**H**) Fiber diffraction on dried, aligned Orb2A-PLD fibers prepared as in (panel G).

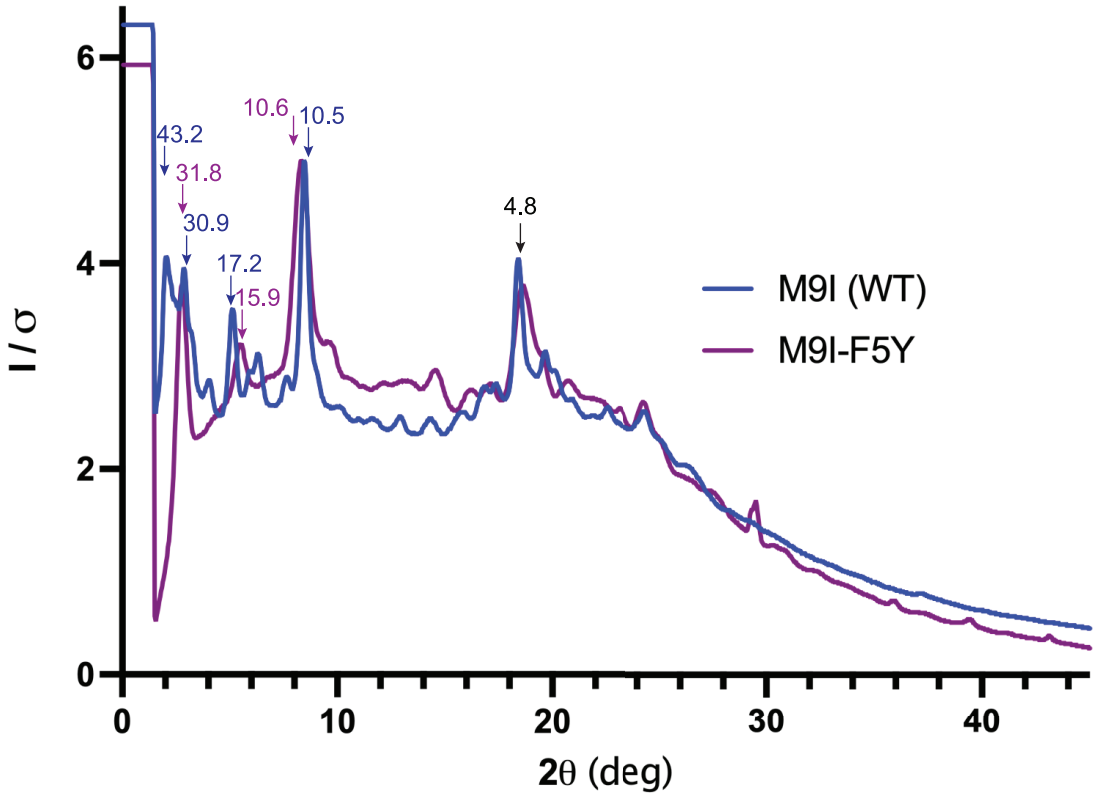

Supplementary Figure 2: Radial profile comparison of M9I and M9I-F5Y fiber diffraction

For M9I and M9I-F5Y fiber diffraction patterns (Fig. 1C) the average signal-to-noise ratio (I/σ) was plotted as a function of distance from beam center (2θ). Values indicated above reflection peaks indicate corresponding separations in real space (Å). Both M9I and M9I-F5Y exhibit reflection peaks at 4.8 Å and 10.5/10.6 Å respectively, indicative of an underlying parallel β-sheet structure, while lower resolution reflections (~11-45 Å) differ significantly, suggestive of altered packing between pairs of β-sheets.

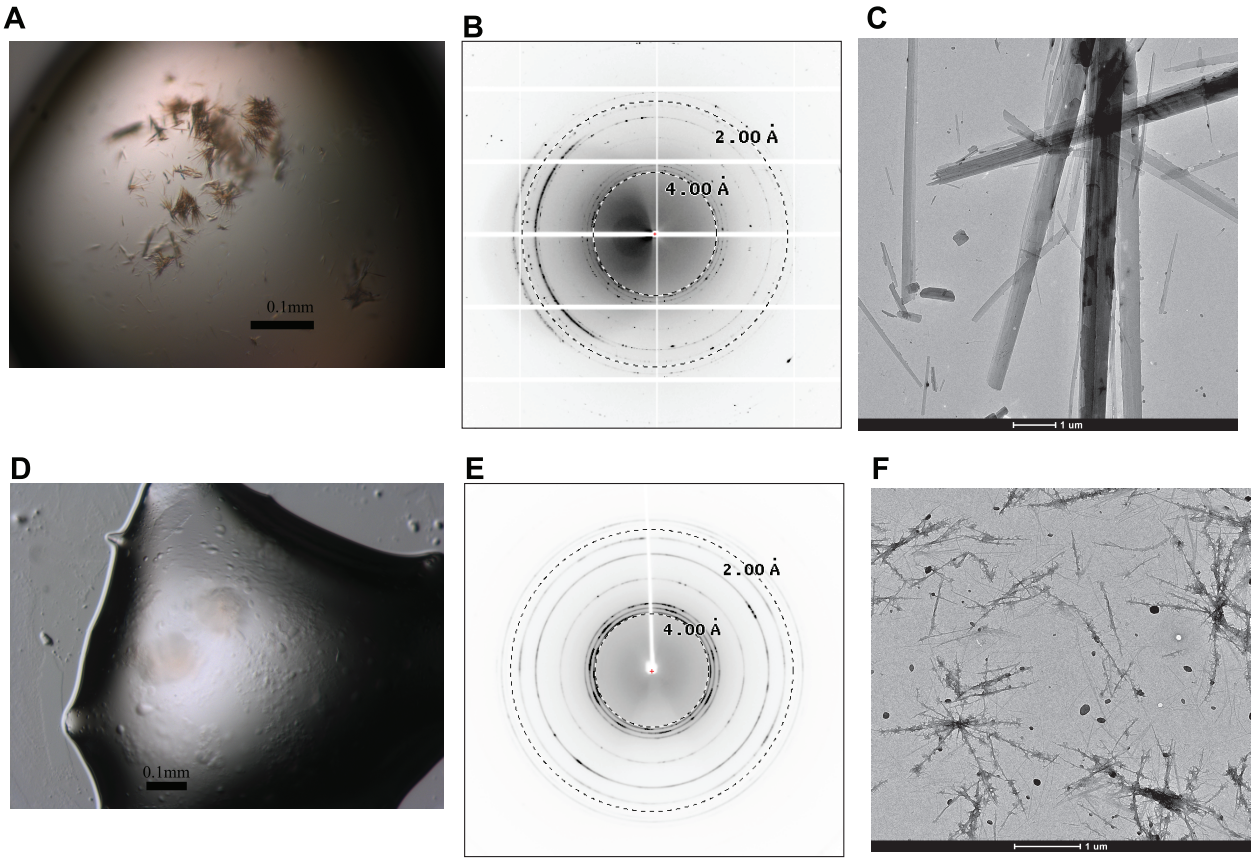

Supplementary Figure 3: Crystallization of M9I and M9I-F5Y

(**A**) M9I forms clusters of needle-like microcrystals that are visible by light microscopy in hanging drop vapor diffusion experiments, but could not be grown larger by optimization/seeding. Crystallization condition: 6 mg/mL M9I peptide dissolved in 1% DMSO (in milliQ water) mixed 1:1 with reservoir solution (100 mM sodium phosphate pH 4.6, 2.0 M NaCl) and incubated at 10 °C for 2 weeks. Crystals formed after 2-4 days incubation. (**B**) Microcrystals were looped and cryogenically frozen, and analyzed using the microfocus beamline (24-ID-E) at the Advanced Photon Source (APS). Individual crystals were difficult to find, and x-ray analysis showed no visible diffraction in the range typical for peptides (~5-30 Å)

(spots are due to ice contamination). (**C**) TEM imaging of M9I hanging drop experiments show abundant formation of microcrystals up to ~1 um in width and several um in length; larger microcrystals tended to contain multiple overlapping lattices when analyzed by micro-ED, and the best diffraction was obtained from smaller single microcrystals with a rectangular shape. (**D**) M9I-F5Y was set up in hanging drop crystallization trays under the same conditions as in (panel A) but formed only amorphous aggregates, even after extended (months) incubation. (**E**) M9I-F5Y aggregates were looped and analyzed using an in-house x-ray source; only ice diffraction was observed. (**F**) TEM imaging of M9I-F5Y aggregates from hanging drop experiments shows that the segment forms short, narrow fibrillar species, in contrast to the relatively large microcrystals formed by wild-type M9I in the same condition (panel C). Optimization around this condition, or other hits identified for M9I-F5Y in high-throughput screens, did not induce formation of ordered crystals.

A

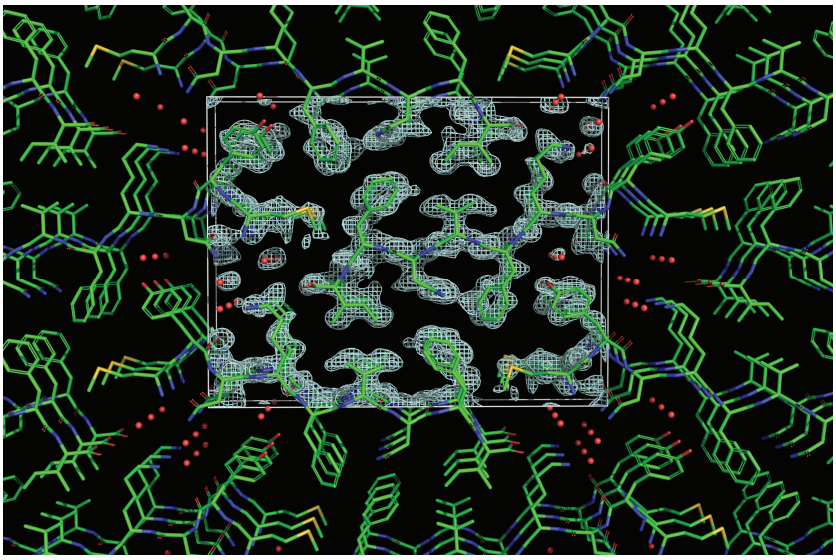

B

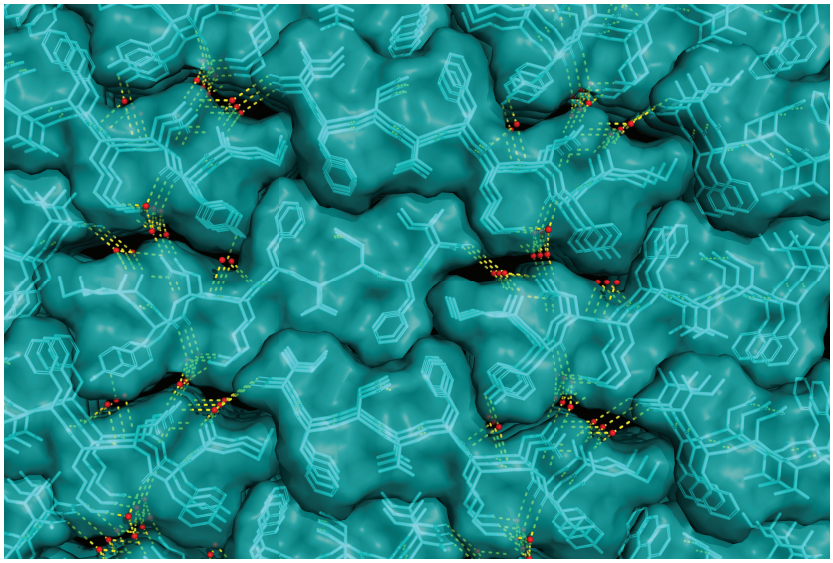

C

	Buried surface area (per strand)	Shape complementarity	Average solvation energy (ΔG°)/residue
M9I Dry interface	128.2 Å^2	0.880	-0.56 kcal/mol
M9I Hydrated interface	117.5 Å^2	0.314	-

Supplementary Figure 4: Crystal lattice formed by M9I

(**A**) Model of M9I crystal lattice, with one unit cell boxed and white mesh representing the $2F_o$-F_c density map contoured at 1σ. Red spheres represent ordered water molecules. Each unit cell

contains 2 asymmetric units, with 1 peptide molecule in each asymmetric unit. (**B**) Model of M9I crystal lattice with surface representation, showing self-complementary interdigitation of C-terminal side chains in a dry, tightly packed interface. In contrast, N-terminal side chains primarily form hydrogen-bonds (yellow dashed lines) with a network of ordered water molecules (red). (**C**) Calculated buried surface area and shape complementarity (Sc) for dry (C-terminal) and hydrated (N-terminal) interfaces, as well as the average solvation energy per residue of the dry interface.

References

1. Eisenberg, D. S., and Sawaya, M. R. (2017) Structural Studies of Amyloid Proteins at the Molecular Level. *Annual Review of Biochemistry*. **86**, 69–95

2. Otzen, D., and Riek, R. (2019) Functional Amyloids. *Cold Spring Harb Perspect Biol*. 10.1101/cshperspect.a033860

3. Sawaya, M. R., Hughes, M. P., Rodriguez, J. A., Riek, R., and Eisenberg, D. S. (2021) The expanding amyloid family: Structure, stability, function, and pathogenesis. *Cell*. **184**, 4857–4873

4. Chapman, M. R., Robinson, L. S., Pinkner, J. S., Roth, R., Heuser, J., Hammar, M., Normark, S., and Hultgren, S. J. (2002) Role of Escherichia coli curli operons in directing amyloid fiber formation. *Science*. **295**, 851–855

5. Bleem, A., Christiansen, G., Madsen, D. J., Maric, H., Strømgaard, K., Bryers, J. D., Daggett, V., Meyer, R. L., and Otzen, D. E. (2018) Protein Engineering Reveals Mechanisms of Functional Amyloid Formation in Pseudomonas aeruginosa Biofilms. *Journal of Molecular Biology*. **430**, 3751–3763

6. Deshmukh, M., Evans, M. L., and Chapman, M. R. (2018) Amyloid by Design: Intrinsic Regulation of Microbial Amyloid Assembly. *Journal of Molecular Biology*. **430**, 3631–3641

7. Macindoe, I., Kwan, A. H., Ren, Q., Morris, V. K., Yang, W., Mackay, J. P., and Sunde, M. (2012) Self-assembly of functional, amphipathic amyloid monolayers by the fungal hydrophobin EAS. *Proceedings of the National Academy of Sciences*. **109**, E804–E811

8. Pham, C. L. L., Rodríguez de Francisco, B., Valsecchi, I., Dazzoni, R., Pillé, A., Lo, V., Ball, S. R., Cappai, R., Wien, F., Kwan, A. H., Guijarro, J. I., and Sunde, M. (2018) Probing Structural Changes during Self-assembly of Surface-Active Hydrophobin Proteins that Form Functional Amyloids in Fungi. *Journal of Molecular Biology*. **430**, 3784–3801

9. Fowler, D. M., Koulov, A. V., Alory-Jost, C., Marks, M. S., Balch, W. E., and Kelly, J. W. (2005) Functional Amyloid Formation within Mammalian Tissue. *PLoS Biology*. **4**, e6

10. Mompean, M., Li, W., Li, J., Laage, S., Siemer, A. B., Bozkurt, G., Wu, H., and McDermott, A. E. (2018) The Structure of the Necrosome RIPK1-RIPK3 Core, a Human Hetero-Amyloid Signaling Complex. *Cell*. 10.1016/j.cell.2018.03.032

11. Do, H. Q., Hewetson, A., Myers, C., Khan, N. H., Hastert, M. C., M. Harsini, F., Latham, M. P., Wylie, B. J., Sutton, R. B., and Cornwall, G. A. (2019) The Functional Mammalian CRES (Cystatin-Related Epididymal Spermatogenic) Amyloid is Antiparallel β-Sheet Rich and Forms a Metastable Oligomer During Assembly. *Scientific Reports*. 10.1038/s41598-019-45545-w

12. Rayman, J. B., Karl, K. A., and Kandel, E. R. (2018) TIA-1 Self-Multimerization, Phase Separation, and Recruitment into Stress Granules Are Dynamically Regulated by Zn 2+. *Cell Reports*. **22**, 59–71

13. Saad, S., Cereghetti, G., Feng, Y., Picotti, P., Peter, M., and Dechant, R. (2017) Reversible protein aggregation is a protective mechanism to ensure cell cycle restart after stress. *Nat Cell Biol*. **19**, 1202–1213

14. Lu, J., Cao, Q., Hughes, M. P., Sawaya, M. R., Boyer, D. R., Cascio, D., and Eisenberg, D. S. (2020) CryoEM structure of the low-complexity domain of hnRNPA2 and its conversion to pathogenic amyloid. *Nat Commun*. **11**, 1–11

15. Murray, D. T., Kato, M., Lin, Y., Thurber, K. R., Hung, I., McKnight, S. L., and Tycko, R. (2017) Structure of FUS Protein Fibrils and Its Relevance to Self-Assembly and Phase Separation of Low-Complexity Domains. *Cell*. **171**, 615-627.e16

16. Si, K., Lindquist, S., and Kandel, E. R. (2003) A Neuronal Isoform of the Aplysia CPEB Has Prion-Like Properties. *Cell*. **115**, 879–891

17. Raveendra, B. L., Siemer, A. B., Puthanveettil, S. V., Hendrickson, W. A., Kandel, E. R., and McDermott, A. E. (2013) Characterization of prion-like conformational changes of the neuronal isoform of Aplysia CPEB. *Nature Structural & Molecular Biology*. **20**, 495–501

18. Fioriti, L., Myers, C., Huang, Y., Drisaldi, B., Pavlopoulos, E., Kandel, E. R., Fioriti, L., Myers, C., Huang, Y., Li, X., Stephan, J. S., Trifilieff, P., and Colnaghi, L. (2015) The Persistence

of Hippocampal-Based Memory Requires Protein Synthesis Mediated by the Prion- Article The Persistence of Hippocampal-Based Memory Requires Protein Synthesis Mediated by the Prion-like Protein CPEB3. *Neuron*. **86**, 1433–1448

19. Stephan, J. S., Fioriti, L., Lamba, N., Karl, K., Derkatch, I. L., Kandel, E. R., Stephan, J. S., Fioriti, L., Lamba, N., Colnaghi, L., Karl, K., and Derkatch, I. L. (2015) The CPEB3 Protein Is a Functional Prion that Interacts with the Actin Cytoskeleton Article The CPEB3 Protein Is a Functional Prion that Interacts with the Actin Cytoskeleton. *CellReports*. **11**, 1772–1785

20. Mastushita-Sakai, T., White-Grindley, E., Samuelson, J., Seidel, C., and Si, K. (2010) Drosophila Orb2 targets genes involved in neuronal growth, synapse formation, and protein turnover. *Proceedings of the National Academy of Sciences*. **107**, 11987–11992

21. Keleman, K., Krüttner, S., Alenius, M., and Dickson, B. J. (2007) Function of the Drosophila CPEB protein Orb2 in long-term courtship memory. *Nature Neuroscience*. **10**, 1587–1593

22. Si, K., Choi, Y. B., White-Grindley, E., Majumdar, A., and Kandel, E. R. (2010) Aplysia CPEB Can Form Prion-like Multimers in Sensory Neurons that Contribute to Long-Term Facilitation. *Cell*. **140**, 421–435

23. Ford, L., Ling, E., Kandel, E. R., and Fioriti, L. (2019) CPEB3 inhibits translation of mRNA targets by localizing them to P bodies. *Proc Natl Acad Sci USA*. **116**, 18078–18087

24. Stepien, B. K., Oppitz, C., Gerlach, D., Dag, U., Novatchkova, M., Krüttner, S., Stark, A., and Keleman, K. (2016) RNA-binding profiles of *Drosophila* CPEB proteins Orb and Orb2. *Proceedings of the National Academy of Sciences*. **113**, E7030–E7038

25. Krüttner, S., Traunmüller, L., Dag, U., Jandrasits, K., Stepien, B., Iyer, N., Fradkin, L. G., Noordermeer, J. N., Mensh, B. D., and Keleman, K. (2015) Synaptic Orb2A Bridges Memory Acquisition and Late Memory Consolidation in Drosophila. *Cell Reports*. **11**, 1953–1965

26. Kandel, E. R. (2012) The molecular biology of memory: cAMP, PKA, CRE, CREB-1, CREB-2, and CPEB. *Molecular Brain*. **5**, 14

27. Majumdar, A., Colon Cesario, W., White-Grindley, E., Huoqing, J., Ren, F., Khan, M. R., Li, L., Choi, E. M., Kannan, K., Guo, F., Unruh, J., Slaughter, B., and Si, K. (2012) Critical Role of Amyloid-like Oligomers of Drosophila Orb2 in the Persistence of Memory. *Cell*. **148**, 515–529

28. Krüttner, S., Stepien, B., Noordermeer, J. N., Mommaas, M. A., Mechtler, K., Dickson, B. J., and Keleman, K. (2012) Drosophila CPEB Orb2A Mediates Memory Independent of Its RNA-Binding Domain. *Neuron*. **76**, 383–395

29. White-Grindley, E., Li, L., Mohammad Khan, R., Ren, F., Saraf, A., Florens, L., and Si, K. (2014) Contribution of Orb2A Stability in Regulated Amyloid-Like Oligomerization of Drosophila Orb2. *PLoS Biology*. **12**, e1001786

30. Khan, M. R., Li, L., Pérez-Sánchez, C., Saraf, A., Florens, L., Slaughter, B. D., Unruh, J. R., and Si, K. (2015) Amyloidogenic Oligomerization Transforms Drosophila Orb2 from a Translation Repressor to an Activator. *Cell*. **163**, 1468–1483

31. Hervás, R., Li, L., Majumdar, A., Fernández-, M. C., Unruh, J. R., Slaughter, B. D., Galera-prat, A., Santana, E., Suzuki, M., Nagai, Y., Bruix, M., Casas-tintó, S., Menéndez, M., Laurents, D. V., Si, K., and Carrión-vázquez, M. (2016) Molecular Basis of Orb2 Amyloidogenesis and Blockade of Memory Consolidation. *PLoS Biology*. 10.1371/journal.pbio.1002361

32. Hervas, R., Rau, M. J., Park, Y., Zhang, W., Murzin, A. G., Fitzpatrick, J. A. J., Scheres, S. H. W., and Si, K. (2020) Cryo-EM structure of a neuronal functional amyloid implicated in memory persistence in Drosophila. *Science*. **367**, 1230–1234

33. Cervantes, S. A., Bajakia, T. H., Soria, M. A., Falk, A. S., Service, R. J., Langen, R., and Siemer, A. B. (2016) Identification and Structural Characterization of the N-terminal Amyloid Core of Orb2 isoform A. *Scientific Reports*. 10.1038/srep38265

34. Rodriguez, J. a., Ivanova, M. I., Sawaya, M. R., Cascio, D., Reyes, F. E., Shi, D., Sangwan, S., Guenther, E. L., Johnson, L. M., Zhang, M., Jiang, L., Arbing, M. a., Nannenga, B. L., Hattne, J., Whitelegge, J., Brewster, A. S., Messerschmidt, M., Boutet, S., Sauter, N. K., Gonen, T., and

Eisenberg, D. S. (2015) Structure of the toxic core of α-synuclein from invisible crystals. *Nature*. 10.1038/nature15368

35. Krotee, P., Griner, S. L., Sawaya, M. R., Cascio, D., Rodriguez, J. A., Shi, D., Philipp, S., Murray, K., Saelices, L., Lee, J., Seidler, P., Glabe, C. G., Jiang, L., Gonen, T., and Eisenberg, D. S. (2018) Common fibrillar spines of amyloid-β and human islet amyloid polypeptide revealed by microelectron diffraction and structure-based inhibitors. *Journal of Biological Chemistry*. **293**, 2888–2902

36. Griner, S. L., Seidler, P., Bowler, J., Murray, K. A., Yang, T. P., Sahay, S., Sawaya, M. R., Cascio, D., Rodriguez, J. A., Philipp, S., Sosna, J., Glabe, C. G., Gonen, T., and Eisenberg, D. S. (2019) Structure-based inhibitors of amyloid beta core suggest a common interface with tau. *eLife*. 10.7554/eLife.46924

37. McGaughey, G. B., Gagné, M., and Rappé, A. K. (1998) π-Stacking Interactions: ALIVE AND WELL IN PROTEINS*. *Journal of Biological Chemistry*. **273**, 15458–15463

38. Makwana, K. M., and Mahalakshmi, R. (2015) Implications of aromatic–aromatic interactions: From protein structures to peptide models. *Protein Science*. **24**, 1920–1933

39. O'Nuallain, B., Williams, A. D., Westermark, P., and Wetzel, R. (2004) Seeding Specificity in Amyloid Growth Induced by Heterologous Fibrils. *Journal of Biological Chemistry*. **279**, 17490–17499

40. Bajakian, T. H., Cervantes, S. A., Soria, M. A., Beaugrand, M., Kim, J. Y., Service, R. J., and Siemer, A. B. (2017) Metal Binding Properties of the N-Terminus of the Functional Amyloid Orb2. *Biomolecules*. **7**, 57

41. Ashami, K., Falk, A. S., Hurd, C., Garg, S., Cervantes, S. A., Rawat, A., and Siemer, A. B. (2021) Droplet and fibril formation of the functional amyloid Orb2. *J Biol Chem*. **297**, 100804

42. Oroz, J., Félix, S. S., Cabrita, E. J., and Laurents, D. V. (2020) Structural transitions in Orb2 prion-like domain relevant for functional aggregation in memory consolidation. *Journal of Biological Chemistry*. **295**, 18122–18133

43. Soria, M. A., Cervantes, S. A., Bajakian, T. H., and Siemer, A. B. (2017) The Functional Amyloid Orb2A Binds to Lipid Membranes. *Biophysical Journal*. **113**, 37–47

44. Hughes, M. P., Sawaya, M. R., Boyer, D. R., Goldschmidt, L., Rodriguez, J. A., Cascio, D., Chong, L., Gonen, T., and Eisenberg, D. S. (2018) Atomic structures of low-complexity protein segments reveal kinked b sheets that assemble networks. *Science*. **701**, 698–701

45. Krotee, P., Rodriguez, J. A., Sawaya, M. R., Cascio, D., Reyes, F. E., Shi, D., Hattne, J., Nannenga, B. L., Oskarsson, M. E., Philipp, S., Griner, S., Jiang, L., Glabe, C. G., Westermark, G. T., Gonen, T., and Eisen (2017) Atomic structures of fibrillar segments of hIAPP suggest tightly mated b -sheets are important for cytotoxicity. *eLIFE*. 10.7554/eLife.19273

46. Guenther, E. L., Cao, Q., Trinh, H., Lu, J., Sawaya, M. R., Cascio, D., Boyer, D. R., Rodriguez, J. A., Hughes, M. P., and Eisenberg, D. S. (2018) Atomic structures of TDP-43 LCD segments and insights into reversible or pathogenic aggregation. *Nature Structural & Molecular Biology*. **25**, 463–471

47. Stanković, I. M., Niu, S., Hall, M. B., and Zarić, S. D. (2020) Role of aromatic amino acids in amyloid self-assembly. *International Journal of Biological Macromolecules*. **156**, 949–959

48. Hee, J. S., Mitchell, S. M., Liu, X., and Leonhardt, R. M. (2017) Melanosomal formation of PMEL core amyloid is driven by aromatic residues. *Sci Rep*. **7**, 44064

49. Gallagher-Jones, M., Glynn, C., Boyer, D. R., Martynowycz, M. W., Hernandez, E., Miao, J., Zee, C.-T., Novikova, I. V., Goldschmidt, L., McFarlane, H. T., Helguera, G. F., Evans, J. E., Sawaya, M. R., Cascio, D., Eisenberg, D. S., Gonen, T., and Rodriguez, J. A. (2018) Sub-ångström cryo-EM structure of a prion protofibril reveals a polar clasp. *Nat Struct Mol Biol*. **25**, 131–134

50. Nelson, R., Sawaya, M. R., Balbirnie, M., Madsen, A. Ø., Riekel, C., Grothe, R., and Eisenberg, D. (2005) Structure of the cross-beta spine of amyloid-like fibrils. *Nature*. **435**, 773–778

51. Sawaya, M. R., Sambashivan, S., Nelson, R., Ivanova, M. I., Sievers, S. a, Apostol, M. I., Thompson, M. J., Balbirnie, M., Wiltzius, J. J. W., McFarlane, H. T., Madsen, A. Ø., Riekel, C., and Eisenberg, D. (2007) Atomic structures of amyloid cross-beta spines reveal varied steric zippers. *Nature*. **447**, 453–457

52. Wasmer, C., Lange, A., Van Melckebeke, H., Siemer, A. B., Riek, R., and Meier, B. H. (2008) Amyloid Fibrils of the HET-s(218–289) Prion Form a β Solenoid with a Triangular Hydrophobic Core. *Science*. **319**, 1523–1526

53. Tuttle, M. D., Comellas, G., Nieuwkoop, A. J., Covell, D. J., Berthold, D. a, Kloepper, K. D., Courtney, J. M., Kim, J. K., Barclay, A. M., Kendall, A., Wan, W., Stubbs, G., Schwieters, C. D., Lee, V. M. Y., George, J. M., and Rienstra, C. M. (2016) Solid-state NMR structure of a pathogenic fibril of full-length human α-synuclein. *Nature Structural & Molecular Biology*. 10.1038/nsmb.3194

54. Guerrero-Ferreira, R., Taylor, N. M., Arteni, A.-A., Kumari, P., Mona, D., Ringler, P., Britschgi, M., Lauer, M. E., Makky, A., Verasdonck, J., Riek, R., Melki, R., Meier, B. H., Böckmann, A., Bousset, L., and Stahlberg, H. (2019) Two new polymorphic structures of human full-length alpha-synuclein fibrils solved by cryo-electron microscopy. *eLife*. **8**, e48907

55. Ni, X., McGlinchey, R. P., Jiang, J., and Lee, J. C. (2019) Structural Insights into α-Synuclein Fibril Polymorphism: Effects of Parkinson's Disease-Related C-Terminal Truncations. *Journal of Molecular Biology*. **431**, 3913–3919

56. Kurt, T. D., Aguilar-Calvo, P., Jiang, L., Rodriguez, J. A., Alderson, N., Eisenberg, D. S., and Sigurdson, C. J. (2017) Asparagine and glutamine ladders promote cross-species prion conversion. *Journal of Biological Chemistry*. **292**, 19076–19086

57. Gill, J., Park, Y., McGinnis, J. P., Perez-Sanchez, C., Blanchette, M., and Si, K. (2017) Regulated Intron Removal Integrates Motivational State and Experience. *Cell*. **169**, 836-848.e15

58. Hansson, M. D., Rzeznicka, K., Rosenbäck, M., Hansson, M., and Sirijovski, N. (2008) PCR-mediated deletion of plasmid DNA. *Analytical Biochemistry*. **375**, 373–375

59. Hattne, J., Reyes, F. E., Nannenga, B. L., Shi, D., de la Cruz, M. J., Leslie, A. G. W., and Gonen, T. (2015) MicroED data collection and processing. *Acta Crystallogr A Found Adv*. **71**, 353–360

60. Shi, D., Nannenga, B. L., de la Cruz, M. J., Liu, J., Sawtelle, S., Calero, G., Reyes, F. E., Hattne, J., and Gonen, T. (2016) The collection of MicroED data for macromolecular crystallography. *Nature Protocols*. **11**, 895–904

61. Nannenga, B. L., Shi, D., Leslie, A. G. W., and Gonen, T. (2014) High-resolution structure determination by continuous-rotation data collection in MicroED. *Nat Methods*. **11**, 927–930

62. Kabsch, W. (2010) XDS. *Acta Cryst D*. **66**, 125–132

63. Sheldrick, G. M. (2008) A short history of SHELX. *Acta Cryst A*. **64**, 112–122

64. Emsley, P., Lohkamp, B., Scott, W. G., and Cowtan, K. (2010) Features and development of Coot. *Acta Cryst D*. **66**, 486–501

65. Murshudov, G. N., Vagin, A. A., and Dodson, E. J. (1997) Refinement of Macromolecular Structures by the Maximum-Likelihood Method. *Acta Cryst D*. **53**, 240–255

66. Project, C. C., and Number 4 (1994) The CCP4 suite: programs for protein crystallography. *Acta Cryst D*. **50**, 760–763

67. Lee, B., and Richards, F. M. (1971) The interpretation of protein structures: Estimation of static accessibility. *Journal of Molecular Biology*. **55**, 379-IN4

68. Connolly, M. L. (1983) Solvent-Accessible Surfaces of Proteins and Nucleic Acids. *Science*. **221**, 709–713

69. Lawrence, M. C., and Colman, P. M. (1993) Shape Complementarity at Protein/Protein Interfaces. *Journal of Molecular Biology*. **234**, 946–950

70. Richards, F. M. (1977) Areas, Volumes, Packing, and Protein Structure. *Annual Review of Biophysics and Bioengineering*. **6**, 151–176

71. Eisenberg, D., and McLachlan, A. D. (1986) Solvation energy in protein folding and binding. *Nature*. **319**, 199–203

72. Eisenberg, D., Wesson, M., and Yamashita, M. (1989) Interpretation of protein folding and binding with atomic solvation parameters. *Chemica Scripta*. **29**, 217–222

73. Kyte, J., and Doolittle, R. F. (1982) A simple method for displaying the hydropathic character of a protein. *Journal of Molecular Biology*. **157**, 105–132

CHAPTER 2

Amyloid Formation of the Nucleocapsid Protein of SARS-CoV-2 as an Antiviral Target

Einav Tayeb-Fligelman[1], Jeannette T. Bowler[1,5], Christen E. Tai[1,5], Michael R. Sawaya[6,10], Yi Xiao Jiang[1,5], Sarah Griner[1], Xinyi Cheng[1,5], Lukasz Salwinski[1,6], Paul M. Seidler[1], Jiahui Lu[1,5], Gregory M. Rosenberg[1,5], Ke Hou[1], Gustavo Garcia Jr[3], Romany Abskharon[1], Hope Pan[1,5], Chih-Te Zee[1,5], David R. Boyer[1,5], Yan Li[1,5], Daniel H. Anderson[1,10], Kevin A. Murray[1,5], Genesis Falcon[6], Duilio Cascio[6], Lorena Saelices[1,†], Robert Damoiseaux[3,4,7-9], Vaithilingaraja Arumugaswami[3,7-8], Feng Guo[1,5,9], David S. Eisenberg[1,2,5-7,10*]

Departments of [1]Biological Chemistry, [2]Chemistry and Biochemistry, [3]Molecular and Medical Pharmacology, and [4]Bioengineering, [5]Molecular Biology Institute, [6]UCLA-DOE Institute of Genomics and Proteomics, [7]California NanoSystems Institute, [8]Eli and Edythe Broad Center of Regenerative Medicine and Stem Cell Research, [9]Jonsson Comprehensive Cancer Center, and [10]Howard Hughes Medical Institute, University of California Los Angeles (UCLA), Los Angeles, California 90095, USA.

Keywords: sars-cov-2, covid-19, amyloid, peptide-based inhibitors, antiviral, low-complexity domain (LCD), liquid-liquid-phase separation (LLPS).

Abstract

The SARS-CoV-2 Nucleocapsid protein (NCAP) functions in RNA packaging during viral replication and assembly. Computational analysis of its amino acid sequence reveals low-complexity domains (LCDs) having sequence features akin to LCDs in other proteins known to function through liquid-liquid phase separation (LLPS) and amyloid formation. Previous reports have described NCAP's propensity to phase-separate in the presence of RNA, raising the question of whether NCAP forms amyloid as part of its function. Here we show that in the presence of viral RNA, NCAP, and particularly its central LCD segment, form amyloid-like fibrils when undergoing LLPS. Phase separated LCD transitions from liquid to solid-like states when incubated at body temperature, and the LCD fibrils exhibit an amyloid-typical X-ray diffraction pattern. Within the central LCD of NCAP we identified three 6-residue segments that drive amyloid formation and determined the atomic structure of fibrils formed by each. These structures informed the design of G12, a peptide-based inhibitor that interferes with NCAP fibril formation and LLPS, and demonstrates antiviral activity in SARS-CoV-2 infected cells. Our data therefore show that NCAP's LLPS and amyloid formation are correlated, and that NCAP's amyloid fibrils are targetable and may function in the viral life cycle.

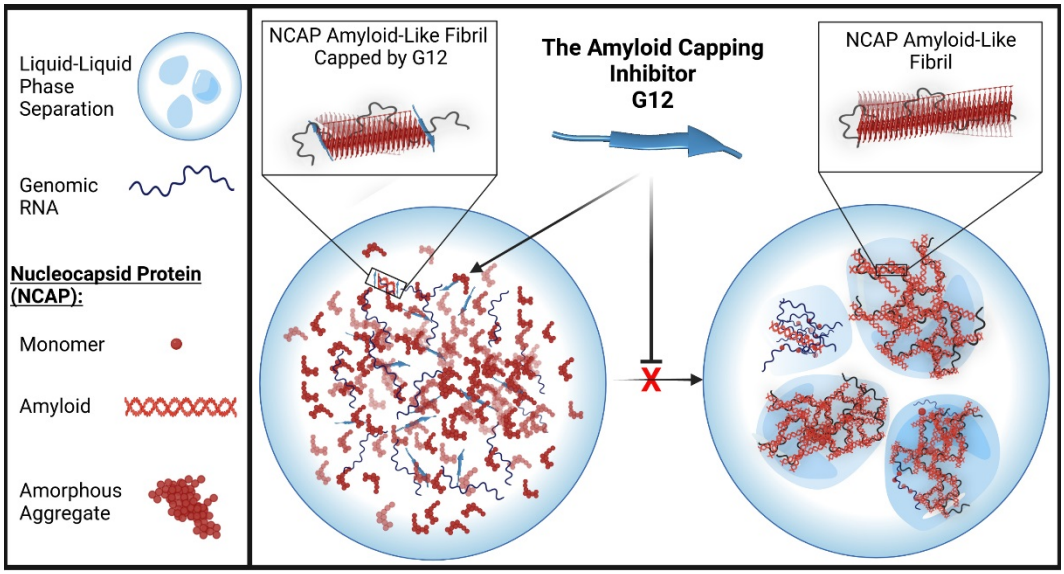

Introduction

The Nucleocapsid protein (NCAP) of Severe Acute Respiratory Syndrome Coronavirus 2 (SARS-CoV-2) is an RNA-binding protein that functions in viral replication by packaging the genomic viral RNA (vRNA) and aiding in virion assembly.[1–9] In the presence of RNA, intrinsically disordered regions of NCAP drive the formation of liquid-liquid phase separation (LLPS) droplets.[1,2,4–8,10,11] NCAP LLPS is enhanced in low salt buffers[4,5] and in the presence of zinc ions,[2] and these LLPS droplets may exist in a liquid or solid-like state.[1,2,4,8,10] The liquid state of the droplets is maintained by NCAP phosphorylation, and is presumed to allow vRNA processing in early stages of infection.[4,8] Non-phosphorylated NCAP, on the contrary, oligomerizes and forms solid-like droplets, probably to facilitate RNA packaging and nucleocapsid assembly in later stages.[4,8]

Based on analysis of its amino acid sequence as well as its functional similarities to other RNA-binding proteins, we hypothesized that NCAP acts as a functional amyloid within infected cells. In the sequence of NCAP, we identified two low complexity domains (LCDs). LCDs are sequences enriched in a small subset of amino acids[12] such as glycine and serine.[13] In RNA-binding proteins, LCDs are known to drive both LLPS and functional amyloid formation.[14,15] LLPS of RNA-binding proteins result in the creation of membraneless organelles such as stress granules and P-bodies that are involved in RNA metabolism, while a transition from liquid to solid-like states of the LLPS droplets often indicates droplet maturation and an underlying formation of amyloid fibrils.[14]

Amyloids are structured protein fibrils that can be either pathogenic or functional,[16] with an abundance of RNA-binding proteins encompassed in the functional amyloid category.[17] Functional amyloid fibrils, which are often reversible,[18,19] differ in structure and properties from irreversible pathogenic amyloid fibrils, although both form when proteins fold into mating β-sheets.[16] Specific examples of functional amyloid forming RNA-binding proteins are the memory

and emotion regulator FXR1 that exists as amyloid in the rat brain,[20] and the neuro-specific forms of the cytoplasmic polyadenylation element binding protein (CPEB) and its orthologs.[17] Several yeast RNA-binding proteins that function in mRNA processing also form fibrils, including the yeast protein Pub1 as well as its mammalian ortholog Tia1.[17] Generally, mRNA-protecting stress granules within mammalian cells appear as fibrillo-granular aggregates, while mRNA processing P-bodies form dense structures encompassing protein fibrils.[21] LCDs and LLPS formation are the common features of numerous functional amyloid forming- RNA-binding proteins,[14,17] and the NCAP of SARS-CoV-2 shares those features.

Experience shows that even efficient vaccines rarely eradicate viral diseases and their legacies of morbidity and mortality,[22] so COVID-19 therapies are needed. Along with others[23] we hold that NCAP of SARS-CoV-2 is a worthy drug target. NCAP is abundant in SARS-CoV-2 infected cells and its function is crucial for viral replication and assembly.[23] NCAP is also evolutionarily conserved in the coronavirus genus,[23] which may render it as a good target not only for COVID-19 treatments, but possibly also for future coronavirus pandemics. Better understanding of the structure and mechanism of action of NCAP will aid in drug development.

Results and Discussion

Analyzing the sequence of NCAP, we found that NCAP contains LCDs of the type that drive amyloid formation. In NCAP, two structured domains flank N-terminal, central, and C-terminal disordered regions (Figure 1). Using the SEG algorithm,[24] we identified a 75-residue LCD (residues 175-249) within the central intrinsically disordered region of NCAP, as well as a second, lysine-rich LCD of 19 residues (residues 361-379) within its C-terminal tail (CTT) (Figure 1). Those central and C-terminal LCDs coincide with regions previously shown to promote NCAP's LLPS,[4,10] and to drive distinct states of aggregation.[4,8] Consequently, we

hypothesized that the LCDs of NCAP also drive the formation of functional amyloid-like structures that may play a role in viral replication.

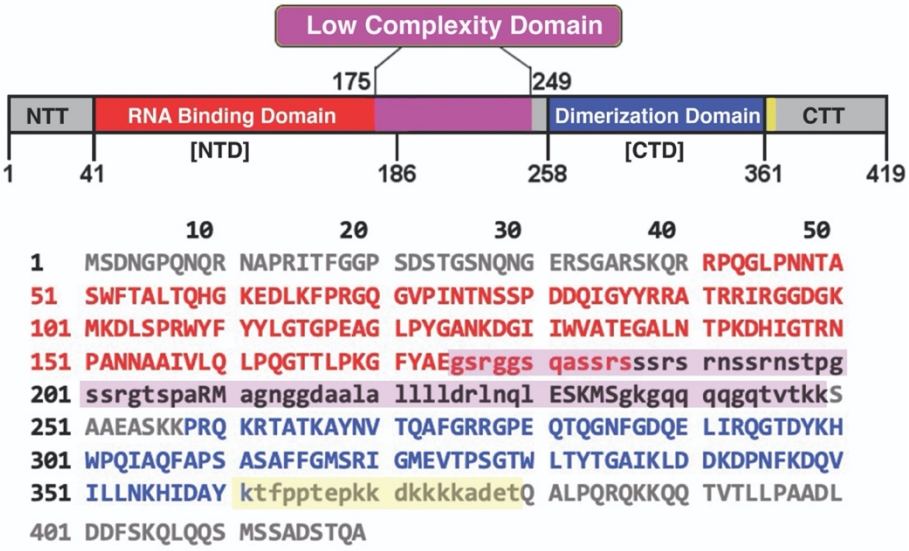

Figure 1. Organization of SARS-CoV-2 NCAP domains. Top: Domain definitions: N-terminal tail (NTT, gray), RNA-binding domain (RBD, red); the central low complexity domain (LCD, purple; residues 175-249), dimerization domain (DD, blue); C-terminal tail (CTT, gray). The C-terminal LCD is highlighted in yellow (residues 361-379). Bottom: Amino acid sequence of NCAP colored according to the domains presented in the top panel. LCDs are designated by lower-case letters.

NCAP LLPS is correlated with amyloid formation

First, we expressed and purified NCAP and studied its LLPS formation in low and physiological salt concentrations in the presence of a genomic vRNA segment. NCAP was recombinantly expressed and purified from bacteria, and only RNA-free NCAP fractions were used for subsequent experiments. To promote LLPS formation of NCAP *in vitro*, we included a 211-nucleotide long 5′- genomic vRNA segment, which we named hairpin-Site2 (S2hp), that comprises the single stranded segment Site2 (S2) and its flanking hairpins (Figure S1A, Table S1). S2 was previously shown to be a strong NCAP cross-linking site.[7] LLPS formation was then inspected in solutions containing different molar ratios of NCAP and S2hp vRNA (Figure 2A & Figure S1B), in the absence and presence of 20 μM $ZnCl_2$ (Figure 2A). Consistent with previous reports,[4,5] we found that vRNA was not essential to induce LLPS at low salt conditions (50 mM

NaCl; Figure 2A), however, was essential at a near physiological salt concentration (1X PBS buffer; Figure S1B). In both low and physiological salt, LLPS droplet diameter increased as a function of RNA concentration.

NCAP droplets stain positively by the amyloid-specific dye Thioflavin-S (ThS). As a positive control, Amyloid-β 1-42 (Aβ-42) fibrils[25] also stain with ThS (Figure 2A&B). Bright ThS fluorescence was evident in NCAP-LLPS droplets formed in the presence of S2hp vRNA, and in droplets formed in the presence of 20 μM $ZnCl_2$, with or without vRNA. In the absence of vRNA, zinc containing NCAP-LLPS droplets are rough and asymmetric, suggesting that zinc induces a more solid-like aggregation state (Figure 2A). Nevertheless, aggregation and ThS fluorescence depend on the presence of NCAP itself, since S2hp and $ZnCl_2$ alone produced neither (Figure 2B).

Maturation of the NCAP's LLPS droplets lead to NCAP fibril formation. After 2 weeks of incubation of LLPS droplets containing 30 μM NCAP with either $ZnCl_2$, vRNA, or both, fibrous and granular morphologies of NCAP assemblies are formed, as visualized by electron microscopy (Figure 2C). In the absence of vRNA, zinc-supplemented-NCAP forms thin, bundled filaments. Fibrils with better defined morphologies were observed in samples containing 0.75 μM S2hp (40:1 NCAP: vRNA molar ratio) and 20 μM $ZnCl_2$. The extended incubation required for the detection of fibrils by electron microscopy suggests that whereas ThS is a sensitive indicator of amyloid-like structures, fibrils grown in these conditions may be too short or too scarce to be visualized at earlier time points. Indeed, fibrils were scarce even after extended incubation. Nevertheless, more prominent fibril formation was detected in a sample of 50 μM NCAP, incubated for 3 days with 20 μM of $ZnCl_2$ at even lower ionic strength conditions (2 mM Tris pH 8.0, 30 mM NaCl; Figure 2D). Together, these results indicate that NCAP is capable of adopting amyloid-like structures within *in vitro* LLPS droplets, and that addition of vRNA and $ZnCl_2$ enhances the formation of granular and fibrillar NCAP assemblies.

Our observations reinforce the link between NCAP and other amyloid-forming RNA-binding proteins. Specifically, Mixed granular/fibrillar morphologies has been reported for pathological RNA-binding protein deposits[26] and for cellular stress granules containing functional-amyloids.[21,27] In addition, comparable to the effect of zinc on NCAP fibril formation, zinc enhances the amyloid-like formation of other RNA-binding proteins, such as TDP-43.[28] Finally, in line with the putative amyloid formation of NCAP, we detected NCAP puncta in SARS-CoV-2 infected human lung cells (A549-ACE2) (Figure 3), which may be indicative of NCAP phase separation,[4,7,10] and also of amyloid accumulation.[29–33]

The amyloid-like property of NCAP we observe here is apparently reversible since its formation is not as robust as irreversible pathogenic amyloids. Also, the amyloid-like form of NCAP is not likely to persist in assembled virions, in which the viral ribonucleoprotein complexes were shown to be distinct cylindrical structures.[34,35] NCAP amyloid-like fibrils should therefore be somehow regulated within host cells, and based on our correlation between LLPS and amyloid formation of NCAP, we think that similar factors may regulate both during the different stages of infection. Those factors may include, for example, post-translation modifications,[8,36,37] and interactions with other viral[4,38] and host proteins.[4,5,39–41] Our observation of the amyloid-like formation of NCAP may therefore direct future studies of NCAP amyloid regulation and function in SARS-CoV-2 infection.

Our study expands an emerging class of amyloid-forming viral proteins. In Influenza A virus, the full length and N-terminal segment of the PB1-F2 protein form cytotoxic amyloid fibrils when mixed with liposomes, whereas the C-terminal segment forms cytotoxic amyloid oligomers.[42] A 111-residue segment from the V protein of Hendra virus, a respiratory virus that may progress in humans to severe encephalitis, was shown to undergo a liquid to hydrogel transition of its LLPS droplets and to produce amyloid-like fibrils.[43] Other examples are of amyloid-forming peptide segments of avibirnavirus viral protease that contribute to protease self-assembly,[44] peptides from the fiber protein of adenovirus,[45,46] and a nine-residue peptide

from the C-terminus of the SARS-CoV envelope protein.[47] None of these previously studied viral amyloids were associated with NCAPs. Nevertheless, LCDs and prion-like sequences, such as those that exist in NCAP,[5] were identified in over two million eukaryotic viruses.[48] Therefore, our finding of a functional-amyloid-like viral RNA-binding protein may foreshadow a much wider field for investigation.

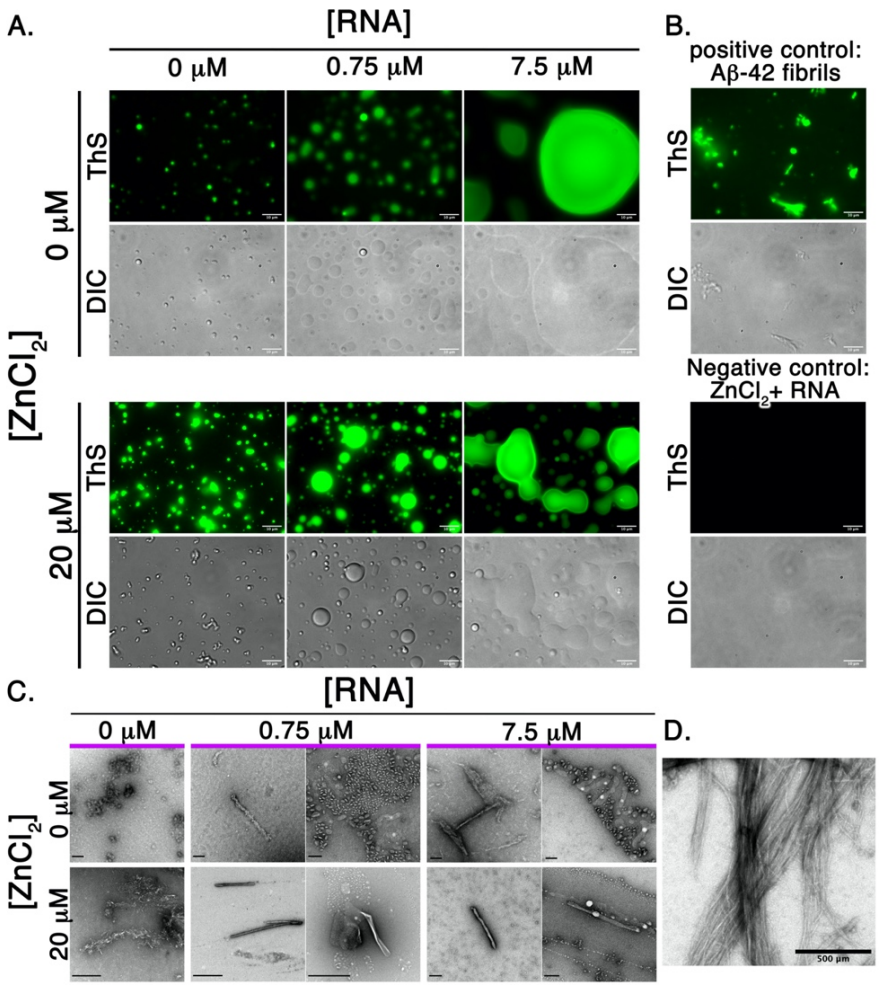

Figure 2. NCAP droplets formed by LLPS, stained with the amyloid dye ThS, exhibit smooth or rough, granular and fibrillar surfaces under transmission electron microscopy (TEM). A) 30 μM NCAP was incubated for 1 day at 37 °C in 20 mM Tris pH 8.0, 50 mM NaCl, in the absence or presence of indicated concentrations of S2hp vRNA and $ZnCl_2$. Typical amyloid-like structures were detected with ThS (green). B) Top: Preformed amyloid fibrils of Amyloid-β 1-42 (Aβ-42) used as a positive control. Bottom: The negative control (20 mM Tris pH 8.0, 50 mM NaCl buffer complemented with 7.5 μM S2hp and 20 μM $ZnCl_2$) shows no RNA/salt precipitation and no ThS binding. Similar observations were made for the blank solutions of all conditions shown in A. C) Negative stain TEM micrographs of NCAP mixtures

described in A, incubated for 2 weeks (without ThS). D) Fibrils formed with 50 μM NCAP, after 3 days of incubation at 37 ºC in 2 mM Tris pH 8.0, 30 mM NaCl and 20 μM $ZnCl_2$.

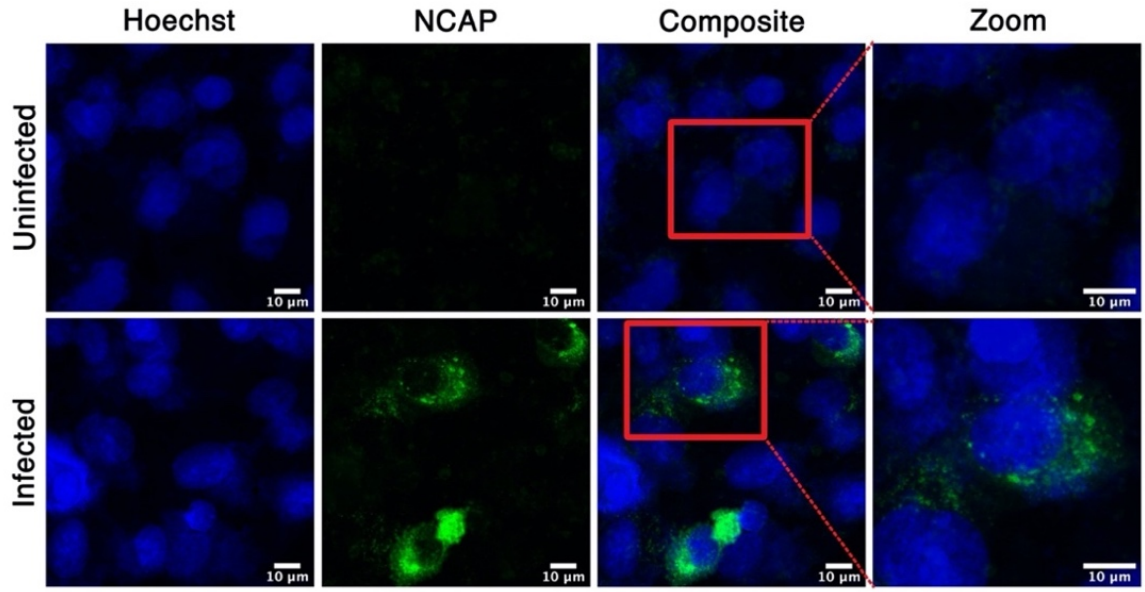

Figure 3: NCAP puncta in SARS-CoV-2 infected human lung cells, A549-ACE2. Cells were incubated with the virus for 24 h, then fixed and reacted with an anti-NCAP antibody, and with Hoechst 33342 nuclear stain. Uninfected cells were used as control. A 10 μm scale bar is shown on the bottom right.

Low-complexity domains drive NCAP amyloid formation

To elucidate the contribution of NCAP LCDs to amyloid formation, we generated truncation constructs with and without the central and C-terminal LCDs (Figure 4A), and learned that only protein segments containing at least one LCD are capable of amyloid formation. In PBS buffer, S2hp greatly stimulated amyloid formation of the central LCD, followed by the full-length NCAP, and to a lesser extent a segment containing the dimerization domain and C-terminal tail (named DD-C_{term}; Figure 4A) which includes the 19-residue LCD. In contrast, a segment containing only the N-terminal tail and RNA-binding domain (named N_{term}-RBD; Figure 4A) with no LCDs, produced no signal of Thioflavin-T (ThT) amyloid dye throughout the ~33h of measurement (Figure 4B).

These trends in aggregation propensity were echoed by a parallel set of experiments monitoring turbidity, which inform also on other forms of aggregation, including LLPS formation (Figure 4B). When mixing the central LCD segment with S2hp, the solution became turbid instantly, and thus the absorbance value of this sample was high already at time zero of measurement (Figure 4B, right). A reduction in the turbidity of the LCD-S2hp mixture was followed by a renewed increase after ~5.5 hours from the initial measurement, which matches the biphasic behavior of the same solution in the ThT assay (Figure 4B, left), and may mark a transition between different aggregation states, such as LLPS and amyloid formation.

Electron micrographs further support that NCAPs LCDs are the major contributors to NCAP's amyloid formation. Transmission electron microscopy images taken after 2 weeks of sample maturation revealed abundant, elongated, unbranched, amyloid-like LCD fibrils (Figure 4C). In agreement with the ThT and turbidity measurements, fewer fibrils of NCAP and the DD-C_{term} segment were observed, suggesting that non-LC sequences and folded domains can counteract amyloid formation. Nevertheless, unlike with the LCD only segment, the NCAP and the DD-C_{term} fibrils were morphologically altered by the addition of vRNA. Together, these observations indicate that LCDs drive NCAP amyloid formation.

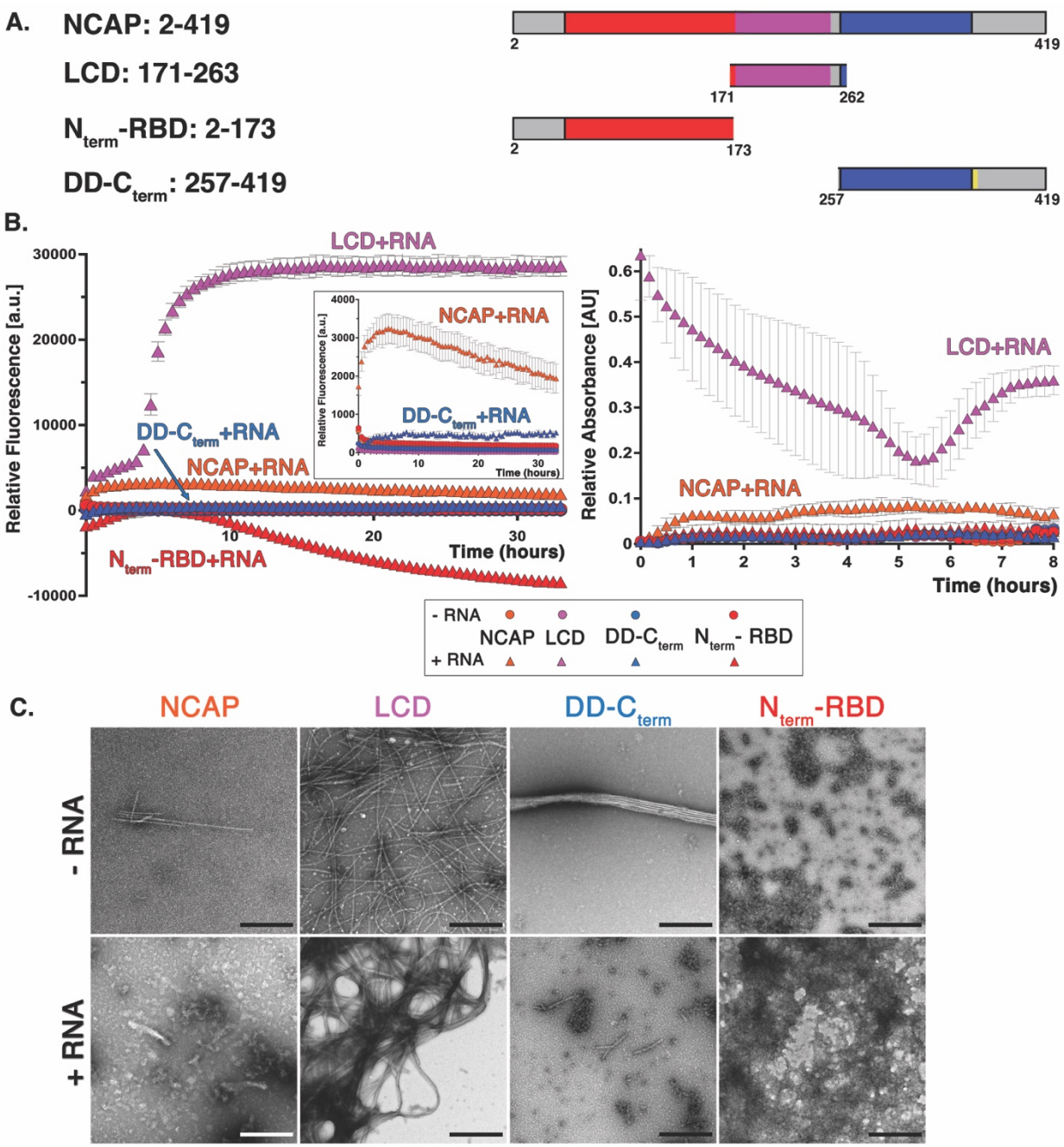

Figure 4. The amyloid-like fibril formation of NCAP and its segments is driven by the protein's LCDs, and is accelerated in the presence of S2hp vRNA. (A) Protein constructs used in this study are abbreviated NCAP, LCD, N_{term}-RBD and DD-C_{term}. (B) Left: ThT fibril formation kinetic assay of NCAP and its segments incubated with or without S2hp vRNA in 4 :1 NCAP: vRNA molar ratio. Protein only solutions (circles; all at ~y=0) show no increase in ThT signal

throughout measurements. S2hp addition (triangles) stimulates fibril formation of LCD-containing segments. The inset is an enlarged view of the low relative fluorescence region (a.u. 0-4000). The negative relative fluorescence signal of the N_{term}-RBD+ vRNA originates from the subtraction of the vRNA+ ThT blank signal. In the no protein (blank) solution, ThT binds to RNA and produces a flat but high signal (not shown); subtraction of this signal from that of the non-amyloid forming N_{term}-RBD+ vRNA mixture results in an overall negative signal, which may be explained by the vRNA now binding to the protein rather than the ThT dye. Right: Turbidity measurements (shape and color coded as on the left) also show that the central LCD and NCAP proteins are most strongly affected by S2hp vRNA addition. The relative absorbances (at 600 nm) for all proteins in the absence of vRNA, as well as for DD-C_{term}+ RNA, and N_{term}-RBD+ RNA, stay at baseline (~y=0). Both ThT and turbidity experiments were performed with triplicates and repeated three times on three different days. Error bars represent standard deviation (SD), calculated from triplicates. (C) Fibril formation of NCAP and its LCD and DD-C_{term} segments, but not N_{term}-RBD, at 2 weeks sample maturation, is observed by negative stain TEM. 500 nm scale bars are shown on the bottom right.

The central low-complexity domain of NCAP forms amyloid-like fibrils with steric zipper spines

The central LCD segment of NCAP demonstrates amyloid-like characteristics, similar to the amyloid-forming LCDs of FUS,[49,50] hnRNPA2,[51] TDP-43,[52] and other RNA-binding proteins.[13,19] The central NCAP-LCD segment undergoes a liquid to solid-like transition when incubated in PBS with S2hp vRNA (4: 1 LCD: S2hp molar ratio) at body temperature (Figure 5A). This liquid to solid-like transition may result from the formation of amyloid-like LCD fibrils (Figure 4C). Such LCD fibrils are also obtained in the presence of the shorter genomic vRNA segments, Site1 (S1), Site1.5 (S1.5) and S2, as well as with a non-specific RNA segment of a similar length (Table S1; Figure 5B), and even with no RNA (Figure 4C). This promiscuous LCD fibril formation is not necessarily due to the lack of vRNA- LCD interactions, since we validated the binding of LCD to

S2hp in a separate study (Tai, et al.*, manuscript in progress*). Furthermore, when the LCD was incubated for only one day with either vRNA segments S1 or S2, heavily-stained clusters with fibrils protruding from their edges were viewed by electron microscopy. These clusters dispersed after 4 days of incubation (Figure 5B), suggesting that LCD aggregation can undergo different states of maturation.

LCD fibrils formed in the absence of RNA, as well as fibrils formed with S2hp and with the non-specific RNA, all exhibit a typical amyloid diffraction pattern with a sharp reflection at 4.7 Å resolution, and a diffuse reflection at 10 Å (Figure 5C). This characteristic amyloid diffraction pattern indicates that fibrils grown with or without the different RNA types have a similar amyloid-like structure. Hence, we postulated that the LCD amyloid-like structure of NCAP is not influenced by interactions with RNA molecules within infected cells, and therefore this structure can guide the design of amyloid inhibitors.

To design inhibitors for NCAP fibril formation we required atomic-resolution structural information of NCAP amyloid. To gain this information we determined crystal structures of adhesive segments of NCAP. Formation of amyloid fibrils are stabilized by pairs of tightly mating β-sheets, with zipper-like interfaces termed steric zippers that can be predicted by a computer algorithm.[53] Within the central LCD, we identified and crystallized three such steric zipper forming segments: $_{179}$GSQASS$_{184}$, $_{217}$AALALL$_{222}$, and $_{243}$GQTVTK$_{248}$. X-ray structures confirmed that each segment forms β-sheets stabilized by steric zipper interfaces (Figure 6, Figure S2 & Table 1). GSQASS and GQTVTK segments both form parallel, in-register β-sheets, whereas the AALALL segment crystalized in two forms, both with antiparallel β-sheets.[54] The weaker zipper interface of the second form incorporates polyethylene glycol (Figure S2), and we do not consider it further. We then performed solvation energy calculations to estimate the stability of the four crystal structures (Table S2). The steric-zipper formed by AALALL is the most stable, which can be explained in part by its high composition of hydrophobic residues. GSQASS and GQTVTK, on the contrary, contain mostly polar residues, which may contribute to

the putative reversibility of NCAP fibrils, similarly to the highly polar reversible amyloid fibrils formed by the LCDs of FUS and hnRNPA2.[55]

Our LCD steric zipper segments coincide with reports of NCAP sequences important for LLPS formation, again pointing to LLPS and amyloid formation in NCAP as intertwined processes. Those previous reports include a region containing the GQTVTK segment,[10] as well as a sequence comprising the AALALL segment and the first four residues of GQTVTK.[4] This may suggest that the targeted inhibition of either LLPS or amyloid formation, may result in the inhibition of both. Of note, GSQASS is part of a region that is common with LCDs from the human proteome[56] and should not be considered as a drug target. Therefore, we proceeded with the steric zippers AALALL and GQTVTK as templets for the design of NCAP amyloid-formation inhibitors.

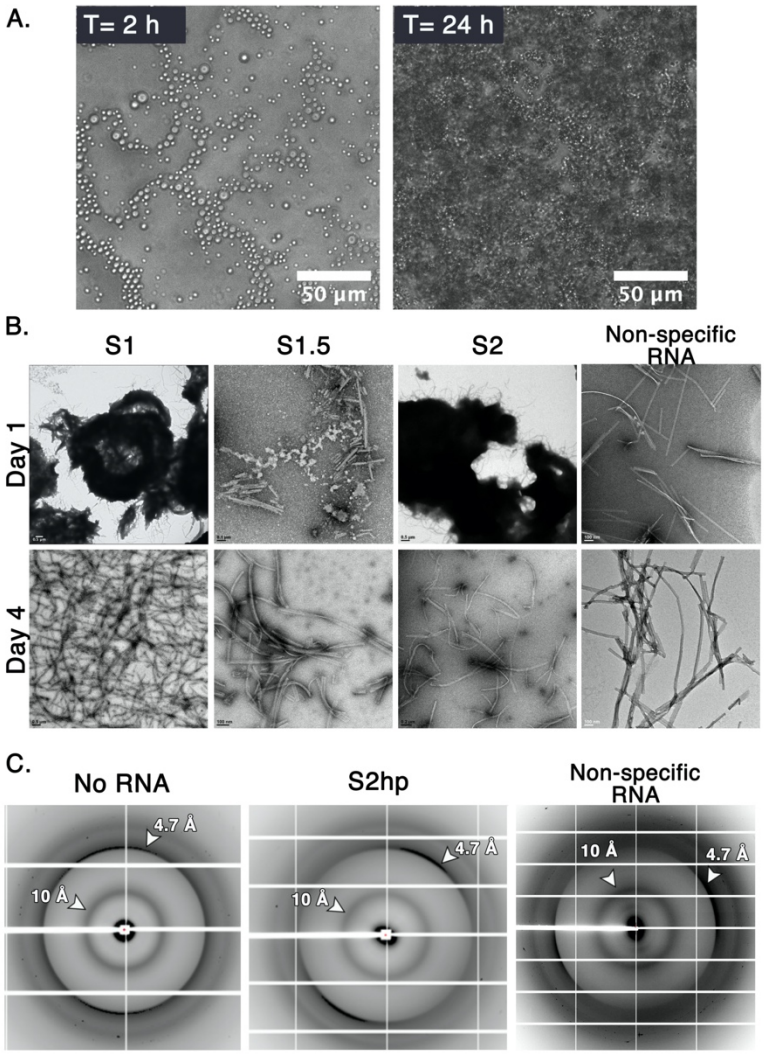

Figure 5. The central LCD segment of NCAP demonstrates amyloid-like characteristics. A) Light microscopy images revealing a liquid to solid-like transition in a mixture of 4: 1 LCD: S2hp molar ratio, incubated in PBS for 2 h (left) and 24 h (right) at 37 ºC. B) Negative stain TEM micrographs of LCD fibrils grown in the presence of the short vRNA segments S1 (11 nucleotides), S1.5 (22 nucleotides) and S2 (22 nucleotides), as well as with a non-specific RNA (Table S1) in 1: 2 LCD: RNA molar ratio in PBS at 37 ºC. The higher RNA concentration used here is due to the small size of those RNA segments. C) X-ray diffraction of LCD only fibrils (left), and LCD fibrils grown with S2hp vRNA (middle), or non-specific RNA (right) shows amyloid-characteristic 4.7 Å and 10 Å reflections, labeled by arrows.

Figure 6. Amyloid-like association of NCAP segments revealed by crystallography. The upper row shows the quality of the fit of each model to its corresponding simulated annealing composite omit maps. The maps are contoured at the 1.0 sigma level. All structural features are well defined by the density. The view is down the fibril axis. Each chain shown here corresponds to one strand in a β-sheet. Thousands of identical strands stack above and below the plane of the page making ~100 micron-long β-sheets. The face of each β-sheet of AALALL (PDB IDs: 7LTU, form 1) is symmetric with its back. However, GSQASS (PDB ID: 7LV2) and GQTVTK (PDB ID: 7LUZ) each reveal two distinct sheet-sheet interfaces: face-to-face and back-to-back. The tighter associated pair of sheets is shown here. The lower row shows 18 strands from each of the steric zippers at a view nearly perpendicular to the fibril axis. GSQASS and GQTVTK are parallel, in register sheets, mated with Class 1 zipper symmetry. The AALALL zippers are antiparallel, in register sheets, mated with Class 7 zipper symmetry. Trifluoroacetic acid (TFA) appears in the AALALL-form 1 steric zipper, and polyethylene glycol (PEG) binds form 2 (PDB ID: 7LUX; Figure S2).

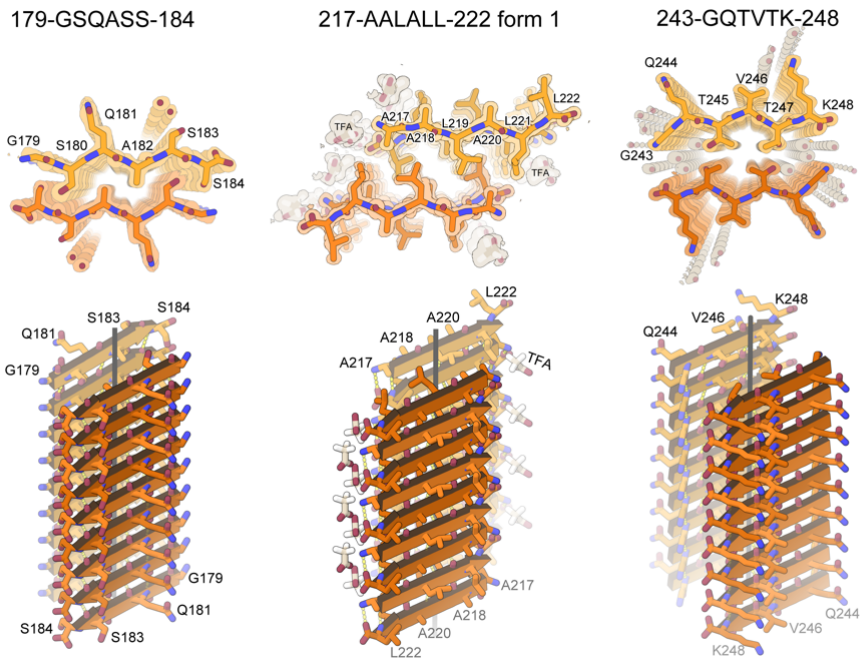

Segment	^{179}GSQASS^{184}	^{217}AALALL^{222} Form 1	^{217}AALALL^{222} Form 2	^{243}GQTVTK^{248}
Data Collection Beamline	APS 24-ID-E	APS 24-ID-E	APS 24-ID-E	APS 24-ID-E
Space group	$P2_12_12_1$	P1	$P2_12_12$	$P2_1$
Resolution (Å)	1.30 (1.39-1.30)*	1.12 (1.18-1.12)	1.30 (1.36-1.30)	1.10 (1.17-1.10)
Unit cell dimensions: a,b,c (Å)	4.77, 13.60, 42.44	9.45, 11.34, 20.27	44.46, 9.54, 10.95	19.57, 4.78, 22.03
Unit cell angles: α,β,γ (°)	90.0, 90.0, 90.0	74.9, 79.1, 67.8	90.0, 90.0, 90.0	90.0, 94.0, 90.0
Measured reflections	1833 (338)	5371 (323)	4666 (550)	4677 (344)
Unique reflections	809 (139)	2270 (136)	1234 (139)	1726 (170)
Overall completeness (%)	93.2 (95.9)	78.4 (31.1)	93.0 (84.8)	87.1 (50.9)
Overall redundancy	2.3 (2.4)	2.4 (2.4)	3.8 (4.0)	2.7 (2.0)
Overall R_{merge}	0.126 (1.04)	0.084 (0.397)	0.105 (0.808)	0.085 (0.446)
$CC_{1/2}$	99.7 (56.7)	98.5 (89.2)	99.7 (54.4)	99.5 (84.3)
Overall I/δ	3.5 (0.7)	5.9 (2.0)	5.9 (1.8)	6.0 (1.4)
Refinement R_{work} / R_{free}	0.259 / 0.253	0.158 / 0.197	0.217 / 0.248	0.133 / 0.177
RMSD bond length (Å)	0.015	0.009	0.010	0.009
RMSD angle (°)	1.4	1.3	1.6	1.5
Number of segment atoms	40	180**	40	93**
Number of water atoms	2	1	1	12
Number of other solvent atoms	0	21	14	0
Average B-factor of peptide (Å^2)	12.3	12.3	14.2	8.2

Average B-factor of water (Å^2)	19.9	12.8	26.6	24.7
Average B-factor other solvent (Å^2)	N/A	20.8	27.3	N/A
PDB ID code	7LV2	7LTU	7LUX	7LUZ

Table 1. Crystallographic data collection and refinement statistics from SARS-CoV-2 NCAP segments

*Numbers in parentheses report statistics in the highest resolution shell.

**Count includes hydrogen atoms.

Structure-based amyloid inhibitor diminishes NCAP fibril formation and LLPS *in vitro*, and demonstrates anti-viral activity in SARS-COV-2 infected cells

Our amyloid-spine structures offer atomic-resolution information about these fibril-driving, "homo-steric-zipper" segments, in which the two sequence segments that interdigitate to form the steric zipper have the same sequence. In contrast, in hetero-steric zippers the two segments that interdigitate have different sequences. In the near-atomic resolution cryo-EM structures of amyloid fibrils (e.g. [32,57]), both homo- and hetero-zippers are seen. Homo-zippers frequently stabilize the interaction of two identical protofilaments within a fibril. Hetero-zippers frequently stabilize the folds of individual protofilaments. In some cases, the stabilizing segment of a hetero-zipper of one of the sheets has also been found as a homo-zipper in a crystal structure. Of importance here, inhibitors designed based on template sequences of homo-zippers have been effective for inhibition of fibrils that contain that sequence in hetero-zippers.[58,59]

Based on our homo-zipper structures we designed and screened an array of peptide inhibitor candidates, aimed to cap the tips of the otherwise elongating steric zipper structures. We have found such capping inhibitors to be effective in inhibiting the aggregation and prion-like seeding of other amyloid-forming proteins.[58,60–65] To design NCAP amyloid capping inhibitors, we implemented two approaches: Sequence/Structure-based design and Rosetta-based modeling.[66]

Both approaches select for sequences that bind strongly to our steric zipper structure templates and contain bulky residues that block fibril extension by sterically interfering with the addition of NCAP proteins to the fibril tip. Our Sequence/Structure-based approach maintains high sequence identity with the parent steric zipper forming segment to exploit the homomeric tendency of amyloid aggregation, whereas the Rosetta-based approach explores the sequence space more exhaustively (Figure 7A). Our designed inhibitors range in length from 6 to 12 residues, and include both L- and D-amino acid sequences.

Screening of this inhibitor panel revealed that the inhibitor G12 significantly reduces NCAP fibril and LLPS formation *in vitro* (Figure 7). G12 is a D-amino acid peptide with the sequence d-(RRFFMVLV), designed against the AALALL steric zipper-forming segment. The Rosetta-calculated binding score of G12 to AALALL fibril tips was slightly better than that of an additional AALALL strand (Table S3). In the ThT assay, G12 reduced S2hp-stimulated fibril formation of NCAP with as little as a 1: 0.25 NCAP: G12 molar ratio, whereas an even greater reduction was evident at 1: 0.5 and 1: 1 ratios. A similar trend was observed for NCAP phase separation, where increased concentrations of G12 disrupted the formation of spherical NCAP droplets (Figure 7, Figures S3 & S4), and promoted formation of aggregates with reduced ThS-binding capacity (Figure S3).

In agreement with its *in vitro* inhibitory function, G12 exhibits dose-dependent antiviral activity, without inflicting cytotoxicity (Figure 7D, E & Figure 8). In these experiments, we first transfected peptide inhibitors to HEK293 cells that express the human ACE2 receptor (HEK293-ACE2 cells) to allow SARS-CoV-2 infection. Four hours post-transfection, SARS-CoV-2 viral stock was added and viral infection was detected by quantitative immunofluorescence labeling of the spike protein at 24 hours post-infection (Figure 7D, E & Figure 8). We considered spike protein expressing cells as infected, and calculated their percentage from the total number of cells in the culture. %Infected cells was then normalized to an infected culture that was treated with vehicle only. When evaluating multiple G12 concentrations in those cells, a clear

dose-dependent viral- inhibition trend was evident between ~6-16 μM (Figure 8), although some data points exhibited larger errors because of technical limitations of the assay (Figure S5). In addition, G12 is dissolved in dimethyl sulfoxide (DMSO) which precluded testing higher concentrations in this cell-based assay for a complete dose-response curve. Nevertheless, G12 is a promising anti-SARS-CoV-2 lead that can be optimized for increased solubility and potency.

Whereas G12 was designed against the AALALL structure, the inhibitor candidate P32 was rationally designed against the less stable steric zipper segment, GQTVTK and was accordingly less effective as an inhibitor. We therefore consider P32 as a negative control for G12. P32 is an L-peptide inhibitor candidate, with the amino acid sequence GWTVTK. P32 is able to partition into NCAP- LLPS droplets (Figure S4), however, it exhibits only moderate inhibition of fibril formation of NCAP, and shows no effect on NCAP LLPS formation and ThS binding (Figure 7 & Figure S3). In HEK293-ACE2 cells, transfection with a high concentration (16 μM) of P32 inhibited the virus only when cells were infected with a low viral titer (MOI: 0.02). At a five-fold higher viral titer (MOI: 0.1), P32 lost its inhibitory effect. In contrast, G12 (at 12 μM) shows a marked inhibitory effect against both low and high viral titers (Figure 7). Overall, these results with G12 and P32 correlate disruption of *in vitro* NCAP amyloid formation and phase separation with SARS-CoV-2 inhibition in cultured human cells.

G12 inhibitory activity validates design of inhibitors of SARS-CoV-2 replication based on steric-zipper structures of NCAP amyloid. Nevertheless, extensive refinement and mechanistic evaluation are still necessary. G12 requires high concentrations for effective results, as do other peptide-based drugs,[67] necessitating optimization. Despite the high required dosages and limited solubility of G12 in aqueous solutions, HEK293-ACE2 cells transfected with ~ 15 μM of FITC-labeled G12 showed that the inhibitor remained soluble and diffuse in the cytoplasm for at least 24 hours (Figure S6). Additionally, while a common drawback to peptide therapeutics is stability, G12 is a D-peptide, offering greater resistance to proteolytic degradation than L-peptides.[68] Worldwide, the use of peptide-based therapeutics is gaining momentum, with more

than 80 peptides already in the global market and hundreds in the clinical and pre-clinical pipelines,[69] including for the treatment of HIV. [67] To our knowledge, G12 is the first peptide-based prototype for the treatment of COVID-19.

Conclusions

The NCAP protein of SARS-CoV-2 belongs to the subclass of fibril-forming proteins that contains both an RNA-binding domain and LCDs (Figure 1), that undergo LLPS,[1–8] and as we show here, forms amyloid-like fibrils. LLPS and fibril formation of NCAP are stimulated by vRNA, and LLPS droplets are positive to the amyloid specific dye ThS (Figures 2 & 4). The central LCD of NCAP forms fibrils that produce the amyloid-characteristic diffraction pattern, and when incubated with RNA, LCD LLPS droplets mature into a solid-like material (Figure 5), similar to other functional amyloid-forming RNA-binding proteins.[13,19,49–52] In SARS-CoV-2 infected cells, NCAP forms puncta (Figure 3), which may be indicative of amyloid formation. [29–33] Finally, the amyloid and LLPS inhibitor (Figure 7), G12, designed based on LCD derived amyloid spine structures (Figure 6), diminishes SARS-CoV-2 infection in human cells in a dose-dependent manner (Figures 7 & 8). Those results associate NCAP with known amyloid-forming RNA-binding proteins, extend our knowledge of amyloidogenic viral proteins, and support our hypothesis that NCAP LLPS is correlated with its amyloid formation. The study of viral NCAPs as functional amyloid may therefore promote our understanding and treatment of viral infections, not only for SARS-CoV-2, but possibly also for other viruses that act via similar mechanisms.

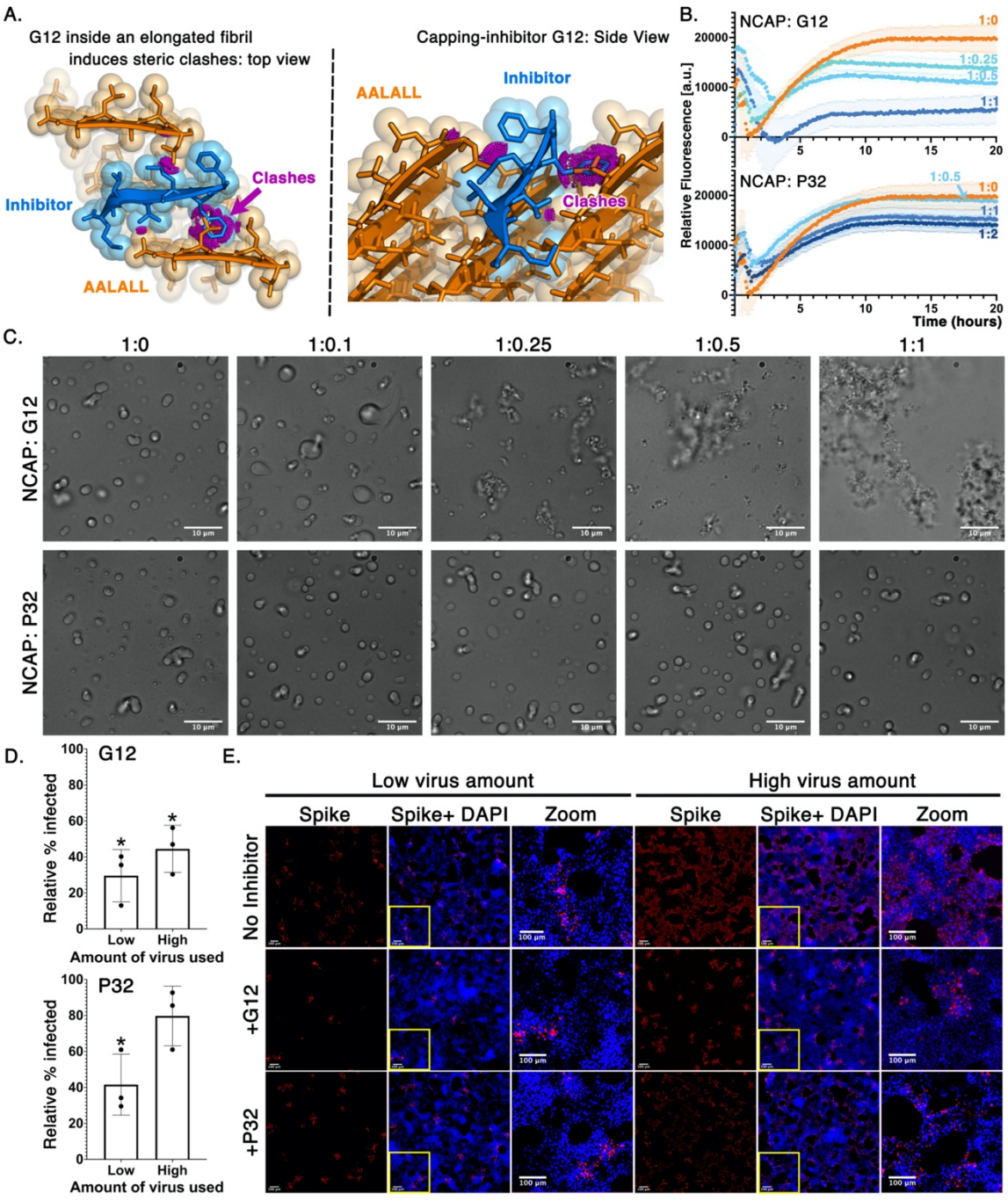

Figure 7. Design and evaluation of amyloid capping inhibitors for NCAP. A) The Rosetta-based design model of G12 capping-inhibitor, built against the AALALL X-ray crystal structure, form 1 (Figure 6, Table 1), which serves as a proxy for full-length NCAP amyloid. Views down the fibril axes (left) and tilted from the axis (right) of the inhibitor G12 (blue) capping an AALALL fibril (orange). Additional AALALL strands are shown adjacent to the bound inhibitor to illustrate

their steric clashes (magenta) with the inhibitor. B) ThT fibril formation kinetic assay of NCAP with S2hp (4:1 molar ratio) in the absence (1: 0) and presence of increasing concentrations of the inhibitor candidates G12 (top) and P32 (bottom). NCAP: inhibitor molar ratios are shown next to each curve. The fluorescence signals of the blank solutions (containing all components except NCAP protein) were subtracted from that of the corresponding samples to yield the relative fluorescence curves. Each experiment was repeated at least three times on three different days with triplicates. Error bars represent SD from triplicates. C) Light microscopy images of NCAP- S2hp mixtures (40: 1 NCAP: S2hp molar ratio), in the absence (1: 0) and presence of increasing concentrations of the inhibitor candidates G12 (top) and P32 (bottom) show dose-dependent LLPS disruption by G12, but not by P32. The NCAP: inhibitor molar ratios are depicted above the images, and 10 μm scale bars are shown on the bottom right. D) Relative % SARS-CoV-2 infected cells with low (MOI:0.02) and high (MOI:0.1) viral titers in HEK293-ACE2 cells pre-transfected with 12 μM of G12 or 16 μM of P32. Error bars represent SD calculated from triplicate wells. Statistical significance was calculated using an ordinary one-way ANOVA – Dunnett's relative to vehicle transfected cells (*$p < 0.05$). E) Representative immunofluorescence labeling images of SARS-CoV-2 spike protein (red), overlaid with a DAPI nucleus stain (blue) in HEK293-ACE2 cells from D. The zoomed in insets are of the regions in the yellow boxes of corresponding composite images. 100 μm scale bars appear on the bottom left of each image.

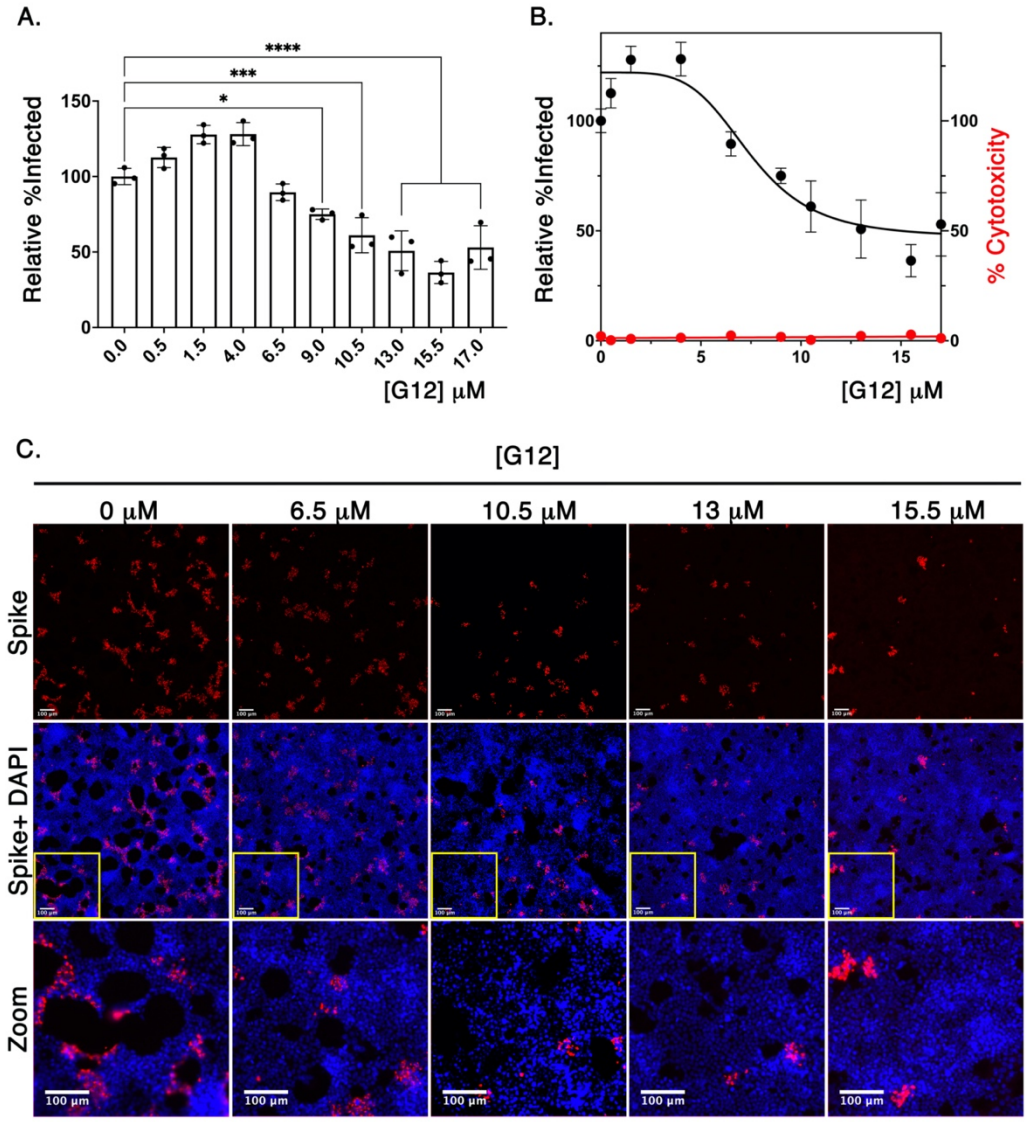

Figure 8. G12 inhibits SARS-CoV-2 infection in HEK293-ACE2 cells in a dose-dependent manner. A) Dose-response analysis of HEK293-ACE2 cells treated with 10 different concentrations of the G12 inhibitor (for additional concentrations see Figure S5). Bars indicate the mean of individual replicates, and error bars represent SD. Statistical significance was calculated using an ordinary one-way ANOVA – Dunnett's relative to leftmost column (*, $p < 0.05$; ***, $p < 0.0005$; ****, $p < 0.0001$). B) Dose-response data in (A), were fit with a nonlinear regression model (black line) and the 95% confidence interval of the IC50 for G12 was evaluated between 7-11 µM. Cytotoxicity of G12 at each concentration was measured by LDH release assay (red line), indicating that G12 is non-toxic. Error bars represent SD from triplicates and are too

small to be visualized on the cytotoxicity data points. C) Representative immunofluorescence images of infected HEK293-ACE2 cells at varying concentrations of G12, stained for SARS-CoV-2 spike protein (red) and cell nuclei (DAPI, blue). The zoomed in insets are of the yellow boxes on the left bottom side of the spike + DAPI images. Scale bars in all images are of 100 μm.

Methods

Molecular biology reagents. Phusion HF DNA polymerase, Quick Ligase and restriction enzymes were purchased from New England BioLabs. Custom DNA oligonucleotides were synthesized by IDT (Coralville, IA). RNA oligonucleotides, S1, S1.5, S2, and the non-specific RNA (siDGCR8-1, antisense strand) were synthesized by Horizon Discovery Biosciences.

Computational prediction of low-complexity sequences. The amino acid sequence of the Nucleocapsid protein of SARS-CoV-2 (UniProtKB[70] accession number: P0DTC9) was evaluated for low-complexity using SEG[24] with default settings: window length = 12, trigger complexity 2.2, extension complexity 2.5. LCDs were defined by strings of at least 10 low-complexity residues. Long LCDs, such as the central NCAP-LCD, were allowed no more than 5 interrupting non-low-complexity residues between strings of 10 or more low-complexity residues.[24]

Construct design. Full length SARS-CoV-2 Nucleocapsid protein gene and its fragments were PCR amplified from 2019-nCoV Control Plasmid (IDT Inc, Cat No 10006625) and spliced with N-terminal 6xHis-SUMO tag[71] using splicing by overlap extension (SOE) technique.[72] 5' KpnI and 3' SacI restriction sites introduced with the flanking primers were used to ligate resulting constructs into pET28a vector. When needed, an additional round of SOE was performed to generate internal Nucleocapsid protein deletion mutants. Construct sequences were confirmed by Sanger sequencing (Laragen, Culver City, CA). Primers used for cloning are given in Table S4.

Protein expression & purification: full-length NCAP and truncation constructs: All NCAP constructs were expressed as fusions to 6xHis-SUMO (6xHis-SUMO-NCAP). Plasmids were transformed into *Escherichia coli* Rosetta2 (DE3) strain (MilliporeSigma cat. no 71-397-4) and small-scale cultures were grown at 37 °C overnight in LB with 35 μg/mL kanamycin and 25 μg/mL chloramphenicol. TB with 35 μg/μL kanamycin was inoculated with overnight starter culture at a 1:100 ratio and large-scale cultures were grown at 37 °C with 225 rpm shaking until the OD600 reached ~0.6. Protein expression was induced with 1 mM IPTG and cultures were further incubated with shaking at 28 °C overnight, then harvested at 5000 *g* at 4 °C for 15 minutes. Bacterial pellets were either used right away or stored at -20 °C. Pellets from 2-4 L of culture were re-suspended in ~200 mL chilled Buffer A (20 mM Tris pH 8.0, 1 M NaCl) supplemented with Halt Protease Inhibitor Cocktail (ThermoScientific cat. no. 87785) and sonicated on ice at 80 % amplitude for a total sonication time of 15 minutes, with pauses at regular intervals so the sample does not exceed 15 °C. Cell debris was removed via centrifugation at 24,000 *g* at 4 °C for 30-60 minutes, filtered twice through 0.45-*μm* high particulate syringe filters (MilliporeSigma cat. no. SLCRM25NS), and imidazole added to 5 mM. Filtered clarified lysate was loaded onto HisTrap HP columns (GE Healthcare) and proteins were eluted over a step-gradient with Buffer B (20 mM Tris pH 8.0, 1 M NaCl, 500 mM imidazole), with extensive low-imidazole (<20 %) washes to improve purity. NCAP proteins generally eluted in 20-50 % Buffer B. Fractions were analyzed by SDS-PAGE, pooled and dialyzed against 20 mM Tris pH 8.0, 250 mM NaCl at 4 °C overnight. Following dialysis, the sample was concentrated using Amicon Ultra-Centrifugal filters (MilliporeSigma) and urea was added up to 1 M final concentration if protein precipitation was observed. Ulp1 protease (homemade) was added at a 1:100-1:200 w/w ratio to purified proteins, along with 1 mM DTT, and the sample was incubated at 30 °C with 195 rpm shaking for 1-2 hours. After cleavage, NaCl was added to 1M final concentration to reduce aggregation, and the sample was incubated with HisPur Ni-NTA resin (ThermoScientific cat. no. PI88222) equilibrated in Buffer A at 25 °C with 140 rpm shaking for

30 minutes. Cleaved NCAP proteins were eluted from the resin via gravity flow chromatography, then the resin was washed twice with Buffer A, twice with Buffer A + 5 mM imidazole, and finally with Buffer B. The flow-through and appropriate washes were concentrated and flash frozen for storage or further purified by gel filtration. Directly prior to gel filtration, the sample was centrifuged at 21,000 *g* for 30 minutes at 4 °C to remove large aggregates. Soluble protein was injected on a HiLoad Sephadex 16/600 S200 (for constructs larger than ~25 kDa) or S75 (for constructs smaller than ~25 kDa) (GE Healthcare) equilibrated in SEC buffer (20 mM Tris pH 8.0, 300 mM NaCl) and run at a flow rate of 1 mL/min. Elution fractions were assessed by SDS-PAGE for purity, and confirmed to have low RNA contamination as assessed by 260/280 nm absorbance ratio. Pooled fractions were concentrated and 0.2-*μm* filtered. Protein concentration was measured by A280 absorbance using a NanoDrop One (ThermoScientific) and calculated by the sequence-specific extinction coefficient, and aliquots were flash frozen and stored at -80 °C. Of note, the first N-terminal residue in all purified constructs (residue #1) is a threonine remaining from cleavage of the 6xHis-SUMO tag during protein purification. **Aβ42**. Amyloid-β 1-42 (Aβ42) was used as a control for Thioflavin-S binding (Figure 2). Aβ42 was purified as previously described.[73] After HPLC purification the protein was lyophilized, resuspended in 10 mM NaOH in 2 mg/mL concentration and incubated on ice for 30 min, then filtered with a 0.1-μm pore size centrifugal tube (Millipore Ultrafree-MC-VV cat. no. UFC30VV00). The protein was further purified via size exclusion chromatography using a Superdex® 200 Increase 10/300 GL column (cat. no. 28-9909-44) into PBS. Purified protein was then aliquoted and stored at -80 °C.

Rosetta-based peptide inhibitor design. Crystal structures of LCD segments GSQASS, GQTVTK and AALALL (form 1) were used as templates for the design of peptide inhibitors in Rosetta3 software.[66] 5 layers of the steric zipper structure was generated. A 6-residue peptide chain was placed at the top or bottom of the fibril-like structure. Rosetta Design was used to sample all amino acids and their rotamers on the sidechains of the fixed peptide backbone. The

lowest energy conformations of the sidechains were determined by minimizing an energy function containing terms for Lennard-Jones potential, orientation-dependent hydrogen bond potential, solvation energy, amino acid-dependent reference energies, and statistical torsional potential dependent on backbone and sidechain dihedral angles. Buried surface area and shape complementarity were scored by AREAIMOL[74] and Sc,[75] respectively, from the CCP4 suite of crystallographic programs.[76] Design candidates were selected based on their calculated binding energy to the top or bottom of the fibril-like structure, shape complementarity, and propensity for self-aggregation. The binding energy for an additional strand of the native sequence (i.e., AALALL) was computed for comparison with peptide inhibitor designs. The structural model of each candidate peptide was manually inspected in PyMOL.[77] Many computational designs produced sequences with high hydrophobic content, thus two arginine residues were added onto the N-terminal end to increase peptide solubility. The candidate G12 was the most effective inhibitor in preliminary screens, and therefore was chosen for further evaluation.

Peptide synthesis and purification. The NCAP steric zipper segments $_{179}$GSQASS$_{184}$ and $_{243}$GQTVTK$_{248}$ and inhibitor candidate G12 were synthesized by LifeTein. Inhibitor candidate P32 was synthesized by GenScript. The NCAP segment $_{217}$AALALL$_{222}$ was synthesized and purified in-house as H-AALALL-OH. Peptide synthesis was carried out at 0.1 mmol scale. A 2-chlorotrityl chloride resin (Advanced Chemtech) was selected as the solid support with a nominal loading of 1.0 mmol/g. Each loading of the first amino acid was executed by adding 0.1 mmol of Fmoc-Leu-OH (Advanced Chemtech FL2350/ 32771) and 0.4 mmol of diisopropylethylamine (DIPEA), dissolved in 10 mL of dichloromethane (DCM), to 0.5 grams of resin. This mixture was gently agitated by bubbling with air. After 30 minutes, the supernatant was drained, and the resin was rinsed twice with 15 mL aliquots of capping solution, consisting of 17:2:1 DCM/MeOH/DIPEA. With the first amino acid loaded, the elongation of each polypeptide was completed in a CEM Liberty Blue™ Microwave Peptide Synthesizer. A 1.0 M solution of N,N'-diisopropylcarbodiimide (DIC) in DMF was used as the primary activator, and a

1.0 M solution of ethyl cyanohydroxyiminoacetate (oxyma) in DMF, buffered by 0.1 M of DIPEA was used as a coupling additive. The Fmoc-L-Ala-OH used was also purchased from Advanced Chemtech (FA2100/ 32786). The microwave synthesizer utilizes 0.2 M solutions of each amino acid. For the deprotection of N-termini, Fmoc protecting groups, a 9% w/v solution of piperazine in 9:1 N-Methyl-2-Pyrrolidone to EtOH buffered with 0.1 M of oxyma was used. For 0.1 mmol deprotection reactions, 4 mL of the above deprotection solution was added to the resin. The mixture was then heated to 90 °C for 2 min while bubbled with nitrogen gas. The solution was drained, and the resin washed 4 times with 4 mL aliquots of DMF. For 0.1 mmol couplings, 2.5 mL of 0.2 M amino acid solution (0.5 mmol) was added to the resin along with 1 mL of the DIC solution (1.0 mmol) and 0.5 mL of oxyma solution (0.5 mmol). This mixture was agitated by bubbling for 2 min at 25 °C, then heated to 50 °C followed by 8 minutes of bubbling. After the last deprotection, the resin was washed with methanol, diethyl ether, dried over vacuum, and introduced to a cleavage cocktail consisting of: 20 mL of trifluoroacetic acid (TFA), 0.50 mL of water, 0.50 mL of triisopropylsilane (TIS). After 2 hours of vigorous stirring, the mixture was filtered, and the filtrate concentrated *in vacuo*. The residue was triturated with cold diethyl ether, and precipitated, crude peptide was collected by filtration. The crude peptide was then purified by RP-HPLC, using an Interchim puriFlashR 4125 Preparative Liquid Chromatography System equipped with a Luna (Phenomenex, C18(2), 5 µm, 100 Å, 30 x 100 mm) column. For purification, two buffer systems were utilized. Initial purifications and salt exchanges were executed with a 13 mM aqueous solution of trifluoroacetic acid (TFA; [A]) and a 2:3 water to acetonitrile solution, buffered by 13 mM of TFA ([B]). For better resolution of diastereomers and other impurities, ultrapure water, buffered by 14 mM of $HClO_4$, and a 2:3 water to acetonitrile solution, buffered by 5.6 mM of $HClO_4$, were selected as mobile phases A and B, respectively. The purity of the purified fractions was analyzed by RP-HPLC, using an Agilent 1100 Liquid Chromatography System equipped with a Kinetex (Phenomenex, C18, 5 µm, 100 Å, 4.6 x 250 mm) column. Ultrapure water with 0.1% TFA, and a 1:9 water to acetonitrile

solution with 0.095% TFA were selected as mobile phases [A] and [B], respectively. The flow rate was set at 1.0 mL/min and the gradient used is detailed in Table S5. The UV absorption at 214 nm was monitored. The resulting chromatogram is shown in Figure S7.

Preparation of inhibitor-candidate stock solutions. Lyophilized peptides of candidate inhibitors were dissolved in 100% DMSO (Sigma cat. no. D2650) to approximately 10 mM, centrifuged at 21,000 *g* for 30 minutes to remove large aggregates, then aliquoted and stored at -20 °C until use. To determine peptide concentrations accurately, stocks were diluted in UltraPure distilled water (ThermoFisher cat. no. 10977015), and the concentration was measured using the Pierce Quantitative Fluorometric Peptide Assay (ThermoFisher cat. no. 23290).

RNA in vitro transcription and purification. The nucleic acid sequence corresponding to S2hp (Table S1) was cloned from a gBlock (IDT) of the first 1000 nucleotides of the 5′-end of the SARS-CoV-2 genome into pUC19 vectors using the restriction sites EcoRI and KpnI. The clone was sequence-confirmed and the miniprep was used as a template for PCR. The forward primer for PCR containing the T7 promoter sequence was biotinylated on the 5′ end for removal of PCR template after transcription. The PCR product was purified by HiTrap column. The running buffer solutions (0.2-*μm* filtered) contained 2 M NaCl, 10 mM HEPES pH 7.0 (buffer A), and 10 mM NaCl, 10 mM HEPES pH 7.0 (buffer B). The purified PCR products were concentrated using Amicon Ultra centrifugal filter units (Millipore) and buffer-exchanged against 10 mM Na/HEPES pH 7.0. Transcription reactions ranging from 5 to 100 mL were set up. The transcription reaction was incubated at 37 °C with gentle shaking for one hour. After transcription, streptavidin beads (ThermoFisher) were added to the transcription and set on a rotator at room temperatures for an additional 15 minutes. The transcription reaction was centrifuged at 500 *g* for 10 minutes at 4 °C. The supernatant was decanted and pellet containing any PCR template remaining was discarded. The transcription reaction was then purified by 5 mL HiTrap Q HP column in several rounds, loading ~5 mL into the column each round. The

purified RNA was concentrated using Amicon Ultra-15 (Millipore) and buffer exchanged into 10 mM HEPES pH 7.0. The purity of the RNA was confirmed using denaturing polyacrylamide gels. The concentration was calculated by measuring OD260 and a conversion factor of 40 μg/mL/OD260.

LLPS assays: All solutions in this experiment were prepared using DNase/RNase-free water (ultrapure water), and were filtered twice using a 0.22-*μm* syringe filter. Preparations were done under sterile conditions and using sterile filter pipette tips to prevent RNA degradation. **LLPS of NCAP and LCD segment in PBS.** Purified NCAP and LCD protein solutions were centrifuged at 15,000 *g* for 15 minutes at 4 °C to remove large aggregates. The supernatant of each protein solution was recovered and separately diluted to 300 μM concentration in 20 mM Tris pH 8.0, 300 mM NaCl buffer, followed by further dilution in 1X PBS to 50 μM working solutions. S2hp RNA, stored at -20 °C, was thawed, then annealed by heating at 95 °C for 3 min and transferring quickly on ice. The RNA was diluted by its original buffer of 10 mM HEPES pH 7.0 to 187.5 μM and 18.75 μM stock solutions, then further diluted with 1X PBS to 25 μM and 2.5 μM working solutions. Respective protein and RNA blank solutions were prepared as controls. Proteins and RNA were then mixed in wells of a 384 black-well clear-bottom plate (Nunc) in final concentrations of 30 μM protein, and 0, 0.75, and 7.5 μM of S2hp RNA, to reach 1:0, 40:1 and 4:1 protein: RNA molar ratio. Blank mixtures were also prepared accordingly. The plate was immediately covered with an optical film (Corning Sealing Tape Universal Optical) and incubated in 37 °C with mild shaking. Images were obtained at indicated time points (Figures 5 & S1) using an ImageXpress XL (Molecular Devices, Sunnyvale) equipped with an 20x S Plan Fluor objective (NA 0.45) with Phase contrast and extra-long working distance (ELWD), environmental control module and transmitted light option with phase contrast light source. The imaging system was equilibrated to 37 °C for 2 hours before use. At least four sites were imaged for each well and each individual site was automatically focused using the IR laser autofocus of the ImageXpress. The plates were imaged in phase contrast channel with 2000ms

exposure time. All images were taken at full camera resolution without binning. The camera used was a Zyla scientific CMOS camera with 5.5 megapixels and a dual camera link interface. All images were recorded live into the MetaXpress Database and exported for downstream applications. **LLPS of NCAP in low salt buffer for ThS staining.** Experiments were carried out in 96-well black/clear glass-bottom plates (Cellvis glass-bottom plates cat. no. P96-1.5H-N). S2hp vRNA stock was annealed by heating at 95 ºC for 3 min and transferring quickly on ice. The RNA was diluted by its original buffer of 10 mM HEPES pH 7.0 to 750 μM and 75 μM stocks individually. 1 mM $ZnCl_2$ was prepared in ultrapure water and filtered twice with a 0.22-μm syringe filter. Fresh Thioflavin S (ThS) solution was prepared from powder (MP Biomedicals) in ultrapure water at 0.002 % w/v and was similarly filtered. Purified NCAP stock solution was centrifuged at 15,000 *g* for 15 minutes at 4 ºC to remove large aggregates. NCAP, S2hp vRNA and $ZnCl_2$ were mixed in 20 mM Tris pH 8.0, 50 mM NaCl (assay buffer) at final concentrations of 0, 0.75 or 7.5 μM S2hp, 0 or 20 μM $ZnCl_2$, and 30 μM NCAP, as indicated in Figure 2. ThS was diluted into the wells to a final concentration of 0.0002% w/v. Blank solutions containing everything but NCAP were prepared as controls. Premade, sonicated Aβ fibrils were used as a positive control for ThS binding. These Aβ42 fibrils were prepared by incubation of 11 μM Aβ42 solution in PBS at 37 ºC under quiescent conditions for 3 days. Fibril formation was verified using transmission electron microscopy and the sample was flash frozen and kept at -80 ºC. On the day of the experiment, Aβ42 fibrils were sonicated for 5 min in a Fisher Scientific solid state ultrasonic water bath with an operating frequency of 40 kHz. 40 μl of the sonicated fiber solution was added into the assay buffer that was complemented with 0.0002% w/v of ThS. After dispensing the samples, the plate was immediately covered with optical film (Corning Sealing Tape Universal Optical) and incubated in a plate reader (BMG LABTECH FLUOstar Omega) at 37 ºC for 1 day, with 700 rpm double orbital shaking during the first 30 min only. The plate was then imaged with ZEISS Axio Observer D1 fluorescence microscope, equipped with a 100x oil objective lens, using the 1,4- Diphenylbutadiene

fluorescence channel with a DAPI filter for ThS, as well as a DIC filter. Images were processed and rendered with FIJI (imageJ).[78] **LLPS of NCAP with G12 and P32 inhibitors:** Inhibitor-candidate stock solutions were prepared as described above. All LLPS assays with the inhibitors G12 and P32 were performed in 96-well black/clear glass-bottom plates (Cellvis glass-bottom plates cat. no. P96-1.5H-N) in 20 mM Tris pH 8, 50 mM NaCl, and 20 μM $ZnCl_2$. Directly prior to assay setup, purified NCAP protein was centrifuged at 15,000 *g* for 15 minutes at 4 °C to remove large aggregates. S2hp RNA was briefly annealed by heating at 95 °C for 3 min and transferring quickly on ice. The experiments were set as elaborated below and images were acquired using an Axio Observer D1 microscope (Zeiss) equipped with a 100x oil objective lens, using the 1,4- Diphenylbutadiene fluorescence channel with a DAPI filter for ThS or FITC, and/or a DIC filter. Images were processed and rendered with FIJI (imageJ).[78] **Dose-dependence LLPS inhibitor assays (Figure 7).** Peptide inhibitors were serially diluted in 10% DMSO and were added to wells of 96-well plates containing 10 μM NCAP protein and 0.25 μM S2hp RNA (1:40 molar ratio) in 20 mM Tris pH 8, 50 mM NaCl, and 20 μM $ZnCl_2$. NCAP: inhibitor (or vehicle control) molar ratios are as indicated in the figure, and the final DMSO concentration in all wells was 0.5%. The plate was covered with optical film (Corning Sealing Tape Universal Optical) and incubated for ~30 minutes at room temperature without shaking prior to imaging. **LLPS assay with inhibitors ThS (Figure S3).** Samples were added to 96-well plates for a final concentration of 30 μM NCAP and 0.75 μM S2hp RNA (1:40 molar ratio) in 20 mM Tris pH 8, 50 mM NaCl, and 20 μM $ZnCl_2$. Inhibitor were added from stock solutions to a final concentration of 30 μM. ThS (from 0.01% w/v stock solution made in ultrapure water) was added to a final concentration of 0.0002%. Final %DMSO in the wells was 0.8% for the P32 mixture, and 1.4% for the G12 mixture. The no inhibitor control (containing everything but the inhibitors) shown in the figure contained 1.4% DMSO (as in G12), however similar or somewhat smaller ThS-binding LLPS droplets were observed in no inhibitor wells containing 0.8% DMSO.

Samples were incubated for 30 minutes at room temperature without shaking prior to imaging that was proceeded as indicated above.

LLPS assay with FITC peptides (Figure S4). FITC-labeled peptide inhibitor stocks were added to non-labeled stocks at a 1:9 labeled: non-labeled ratio. The FITC-labeled peptides were added to 96-well plates to a final concentration of 10 μM NCAP, 0.25 μM S2hp RNA (1:40 molar ratio), and inhibitor samples (in 0.5% final DMSO concentration), in 20 mM Tris pH 8, 50 mM NaCl, and 20 μM $ZnCl_2$. The plate was covered with optical film (Corning Sealing Tape Universal Optical) and incubated at 37 °C without shaking for 24 hours prior to imaging.

Thioflavin-T fibrillation kinetic assays: All solutions in these experiments were prepared using DNase/RNase-free water (ultrapure water), and were filtered twice using a 0.22-*μm* syringe filter. Preparations were done under sterile conditions and using sterile filter pipette tips to ensure RNA preservation. Thioflavin T (ThT) stock solution was freshly prepared from powder (Sigma, CAS ID: 2390-54-7) at a concentration of 20 mM in DNase/RNase ultrapure water, followed by 0.22-*μm* filtration. **Evaluation of NCAP and its segments.** Purified NCAP protein and its segments were separately diluted into 20 mM Tris pH 8.0, 300 mM NaCl buffer at 235 μM concentration. S2hp RNA was diluted by 10 mM HEPES pH 7.0 buffer to 75 μM concentration. The proteins, RNA and ThT were then mixed to final concentrations of 300 μM ThT, 30 μM protein, and 0 or 7.5 μM RNA (as indicated in Figure 4), in 1X PBS pH 7.4. Blank samples containing everything but the protein were prepared. The reaction was carried out in a black 384-well clear-bottom plate (NUNC 384) covered with optical film (Corning Sealing Tape Universal Optical) and incubated in a plate reader (BMG LABTECH FLUOstar Omega) at 37 °C, with 700 rpm double orbital shaking for 30 seconds before each measurement. ThT fluorescence was measured with excitation and emission wavelengths of 430 and 485 nm, respectively. Measurements were made in triplicates for each sample. All triplicate values were averaged, and blank readings from samples without proteins were averaged and subtracted from

the values of corresponding protein mixtures. The results were plotted against time with calculated standard deviation (SD; from triplicates) shown as error bars. The experiment was repeated at least three times on different days. **Evaluation of peptide-based inhibitor candidates on NCAP fibril formation.** Inhibitor candidates were prepared as described above and added to 30 μM NCAP protein, complemented with 7.5 μM of S2hp RNA (4:1 NCAP: RNA molar ratio) in 1X PBS buffer, in 1:0, 1:0.25, 1:0.5, 1:1, or 1:2 NCAP: inhibitor molar ratios (as indicated in Figures 7) in a 384 black-well clear-bottom plate (Nunc). ThT was added to the well to 300 μM final concentration. Blank solutions containing everything but the protein were prepared. The final concentration of DMSO (from the inhibitor stocks) in each well was 2.7% v/v. The plates were immediately covered with optical film (Corning Sealing Tape Universal Optical) and a ThT fibril formation kinetic assay was performed and processed as described above.

Turbidity kinetic absorbance measurement assay for NCAP and its segments. All solutions were prepared using DNase/RNase-free water (ultrapure water), and were filtered twice using a 0.22-*μm* syringe filter. Preparations were done under sterile conditions and using sterile filter pipette tips to ensure RNA preservation. Protein and RNA working solutions were prepared as described above for the ThT experiment of NCAP and its segments. Each reaction sample contained 30 μM protein and 0 or 7.5 μM RNA, in 1X PBS pH 7.4. Blank samples contained everything but the protein. The reaction was carried out in a black 384-well clear-bottom plate (NUNC 384) covered with optical film (Corning Sealing Tape Universal Optical) and incubated in a plate reader (BMG LABTECH FLUOstar Omega) at 37 °C, with mixing before and between measurements. Turbidity was measured with absorbance (OD) at 600 nm. Measurements were made in triplicates for each sample. Triplicate values were averaged, and appropriate blank readings (samples without the protein) were averaged and subtracted from the corresponding readings. The results were plotted against time with calculated SD (from

triplicates) shown as error bars. The experiment was repeated at least three times on different days.

Negative stain transmission electron microscopy (TEM): Samples for negative staining TEM were prepared as described below. All solutions in these experiments were prepared using DNase/RNase-free water (ultrapure water), and were filtered twice using a 0.22-μm syringe filter. Preparations were done under sterile conditions and using sterile filter pipette tips to ensure RNA preservation. For grid preparation and screening, 4 μL of each sample was applied directly onto 400-mesh copper TEM grids with Formvar/Carbon support films (Ted Pella), glow discharged (PELCO easiGlowxs) for 45 seconds at 15 mA immediately before use. Grids were incubated with the samples for 2 minutes, then the samples were blotted off using filter paper. The grids were washed three times with water and once with 2 % uranyl acetate solution with blotting after each wash. The grids were then incubated with 6 μL of uranyl acetate solution for 30-45 seconds before blotting. Micrographs were imaged using a FEI Tecnai T12 microscope at room temperature with an accelerating voltage of 120 kV. Images were recorded digitally with a Gatan US 1000 CCD camera, using the Digital Micrograph® software, and processed in the ImageJ[79] software. **NCAP fibrils from LLPS droplets formed in low salt buffer.** NCAP samples with and without 0.75/ 7.5 μM S2hp and 20 μM $ZnCl_2$ (Figure 2) were prepared in 20 mM Tris pH 8.0, 50 mM NaCl as described in the LLPS method section, but without ThS. The samples were incubated for 14 days at 37 °C with shaking. Samples were transferred into 1.5 mL tubes and centrifuged at 14,000 *g* for 30 min at room temperature (RT). 4 μL from each sample was recovered from the bottom of the tube and applied on the EM grid as described above.

NCAP fibrils with $ZnCl_2$ in 2 mM Tris pH 8.0, 30 mM NaCl (low ionic strength conditions). Purified NCAP was diluted to 50 μM final concentration from its stock solution (made in 20 mM Tris pH 8.0, 300 mM NaCl buffer) into ultrapure water supplemented with $ZnCl_2$ in 20 μM final concentration. Samples were incubated for 3 days with acoustic resonance mixing at 37 °C using a custom-built 96-well plate shaker set to 40 Hz. The samples were then

recovered and applied on the EM grid as described above. **NCAP and its segments.** NCAP and its segments (Figure 4) were separately diluted to 235 μM concentration by 20 mM Tris pH 8.0, 300mM NaCl. The S2hp RNA was diluted to 250 μM by 10 mM HEPES, pH 7.0 buffer. Each reaction sample contained 100 μM protein and 0/ 25 μM RNA in 1X PBS pH 7.4. Fibril formation was carried out in parafilm-covered PCR tubes, incubated in a floor shaker (Torrey Pines Scientific Inc, Orbital mixing chilling/heating plate) at 37 °C, with fast mixing speed for 14 days. **LCD fiber formation with S1, S1.5, S2 and antisense siDGCR8-1 RNA.** RNA stock solutions were thawed, then annealed by heating at 95 °C for 3 min and transferring quickly on ice. The RNAs were diluted to 1 mM concentration by their original buffer of 10mM HEPES pH 7.0. LCD protein stock was freshly thawed and added together with the appropriate RNA solution into 1X PBS to reach 1:2 protein: RNA molar ratio at either 50 or 20 μM final concentration of NCAP, in 50 μL final volume in a black 384-well clear-bottom plate (NUNC 384). The plate was covered with optical film (Corning Sealing Tape Universal Optical) and incubated in a plate reader (BMG LABTECH FLUOstar Omega) at 37 °C with shaking. Samples were taken for TEM screening after 12 h (day1) or 4 days of incubation.

X-ray fiber diffraction: LCD with and without S2hp vRNA. 1.27 mM purified LCD stock solution was thawed and dialyzed in a dialysis cassette with a 3.5 kDa cutoff (Thermo Scientific cat. no. 87724) for 4 hours at RT in 20 mM Tris pH 7.4, 50mM NaCl buffer with or without the addition of S2hp vRNA in 4:1 LCD: S2hp molar ratio (955 μM protein and 236 μM RNA). After dialysis, the samples were added to a black 384-well clear-bottom plate (NUNC 384), covered with optical film (Corning Sealing Tape Universal Optical) and incubated in a plate reader (BMG LABTECH FLUOstar Omega) at 37 °C, with 30 seconds of 700 rpm double orbital shaking every 5 minute for 3 weeks. The fibrils were pelleted and washed three times in water by centrifugation at 13,000 *g* for 10 minutes at RT, then pelleted again and resuspended in 5 μL of deionized water. Fibrils were aligned by pipetting 2 μL of the fibril resuspension in a 3 mm gap between two fire-polished glass rods, positioned end-to-end. After 1 hour of drying at room

temperature, another 2 μL of the fibril suspension was applied, thickening the sample. After another hour of drying, the aligned fibril sample was transferred to the exterior of a standard crystal mounting loop. To glue the sample to the loop, the loop was wetted with 50% v/v ethylene glycol solution, then touched to the surface of the sample and immediately plunged in liquid nitrogen. The samples were shipped to the Advanced Photon Source, beamline24-ID-E at Argonne National Laboratory for remote data collection. The sample was kept at 100 K using a nitrogen cryo-stream. Diffraction patterns were collected on a Dectris Eiger 16 M pixel detector using a 2 second exposure at 100% transmission and 1-degree rotation. The X-ray beam wavelength was 0.9792 Å and impinged on the sample only, avoiding the loop and ethylene glycol, so these later materials do not contribute to the diffraction pattern. The detector was placed 350 mm from the sample. **LCD with non-specific RNA (antisense siDGCR8-1 RNA).** LCD stock solution was concentrated to 2.2 mM and the buffer was exchanged to 20 mM Tris pH 8.0, 150mM NaCl in a centrifugal filter with 3kDa cutoff (Millipore Sigma Amicon Ultra cat. no. C82301). Antisense siDGCR8-1 RNA stock solution, stored at −20 °C, was thawed and combined with the LCD solution in 1:3 LCD: RNA molar ratio. The solution was titrated to reach a final pH of ~ 5 as confirmed with pH paper. The final protein concentration was 283 μM and RNA concentration was 849 μM. The reaction mixture was incubated in a floor shaker (Torrey Pines Scientific Inc, Orbital mixing chilling/heating plate) at 37 °C, with rapid mixing speed for 7 days. The fibrils were prepared and mounted as described above except that the fibrils were aligned with a single application of 5 μL of the fibril suspension, rather than two smaller applications. Diffraction was measured at beamline24-ID-C, rather than 24-ID-E. Diffraction patterns were collected on a Dectris Eiger2 16 M pixel detector using a 1 second exposure at 90% transmission and 0.5-degree sample rotation. The X-ray beam wavelength was 0.9791 Å and impinged on the sample only, avoiding the loop and ethylene glycol, so these later materials do not contribute to the diffraction pattern. Exposures were collected at sample-to-detector distances of 200 and 500 mm.

Crystallization of NCAP peptide segments. The NCAP segment $_{217}$-AALALL-$_{222}$ crystallized in batch just before the purification by RP-HPLC. The peptide had been deprotected and cleaved from the resin, triturated with cold diethyl ether, and precipitated. Most of the product had been collected via filtration, but some residual peptide remained in the round bottom flask and we intended to use this residual peptide to check the peptide purity by analytical HPLC. We dissolved the residual peptide with water, acetonitrile, and TFA in a ratio of approximately 45:45:10 and transferred to a 1 mL glass vial for HPLC injection. The solution was left in the sample holder and needle-like crystals formed after a week. Some of these crystals were retained for crystal structure determination. The bulk of the peptide was further purified, as described above. The purified peptide was dissolved at 10 mg/mL concentration in 19.6 mM LiOH. Crystals were grown by the hanging drop vapor diffusion method. The UCLA Crystallization Facility set up crystallization trays with a Mosquito robot dispensing 200 nL drops. Needle shaped crystals of $_{217}$-AALALL-$_{222}$ grew at 20 ºC in a reservoir solution composed of 30 % w/v polyethylene glycol (PEG) 3000 and 0.1 M n-Cyclohexyl-2-aminoethanesulfonic acid (CHES), pH 9.5. The purified NCAP segment $_{179}$-GSQASS-$_{184}$ was dissolved in water at 100 mg/mL concentration. Hanging drop crystallization trays were set using 200 nL drops. Needle shaped crystals grew at 20 ºC using a reservoir solution composed of 1.0 M Na,K tartrate, 0.2 M Li_2SO_4, and Tris pH 7.0. Needle-shaped crystals appeared immediately after setting up the tray. The purified NCAP segment $_{243}$-GQTVTK-$_{248}$ was dissolved in water at 68 mg/mL concentration. Hanging drop crystallization trays were set using 200 nL drops. Needle-shaped crystals appeared within 1 day at 20 ºC using a reservoir solution composed of 2.0 M $(NH_4)_2SO_4$, 0.1 M sodium HEPES, pH 7.5, and 2 % v/v PEG 400.

Crystallographic structure determination of NCAP peptide segments. Microfocus X-ray beam optics were required to measure crystal diffraction intensities from our crystals since they were needle-shaped, and less than 5 microns thick. We used microfocus beamline 24-ID-E of the Advanced Photon Source located at Argonne National Laboratory. Crystals were cooled to

a temperature of 100 K. Diffraction data were indexed, integrated, scaled, and merged using the programs XDS and XSCALE.[80] Data collection statistics are reported in Table 1. Initial phases for AALALL and GSQASS were obtained by molecular replacement with the program Phaser[81] using a search model consisting of an ideal β-strand with sequence AAAAAA. Phases for GQTVTK were obtained by direct methods using the program ShelxD.[82] Refinement was performed using the program Refmac.[83] Model building was performed using the graphics program Coot.[84] Structure illustrations were created using PyMOL.[77]

Inhibitor candidate evaluation in HEK293-ACE2 cells infected with SARS-CoV-2: HEK293-ACE2 cells (ATCC CRL3216) stably over-expressing the human ACE2 receptor were established as previously described. [85] Cells were cultured in DMEM (Gibco cat no. 11995-065) supplemented with 10% FBS (Gibco cat no. 26140-079), 1% penicillin-streptomycin (Gibco cat no. 15140-122), 10 mM HEPES pH 7 (Gibco cat no. 15630106), 50 μM 2-mercaptoethanol (Sigma cat no. M3148), and 1 μg/mL puromycin (Gibco cat no. A1113803) for selection, at 37 °C, 5% CO_2. Cells were confirmed negative for mycoplasma by PCR using a Universal Mycoplasma Detection Kit (ATCC cat. no. 30-1012K). The HEK293-ACE2 cells were plated in a 96-well black/clear plates (Greiner Bio-One cat. no. 655090) at 2 x10^4 cells per well. The cells were incubated for 1-2 days at 37 °C, 5% CO_2, then exchanged into antibiotic-free media and incubated for an additional day. Cells were then transfected with the peptide-based inhibitors, either unlabeled (Figures 7,8 & Figure S5; Final peptide concentrations are detailed in the figures), or with ~15 μM of FITC-labeled G12 (Figure S6) by diluting stock solutions (made in 5% DMSO) into cell culture medium to a 10X concentration, and serially diluting from there for dose-response assays while maintaining similar DMSO concentration in all peptide dosages (Figure 8 &Figure S5). 10 μL of 10X peptide diluted in culture medium was added to 90 μL media in each well, for a final DMSO concentration of 0.5% in all wells. Finally, Endo-Porter (PEG-formulation) transfection reagent (GeneTools LLC, Philomath, OR) was added to each

well at a final concentration of 6 μM. Plates were incubated for 2-4 hours, then the cells were infected with SARS-CoV-2 in the UCLA BSL3 High-Containment Facility, as described previously.[85] Briefly, SARS-CoV-2 (Isolate USA-WA1/2020) (BEI Resources) was added in 200 μl final volume at a MOI of 0.02 or 0.1 for low and high viral titer screens with the inhibitor candidates P32 and G12 (Figure 7D, E) or 0.05 for evaluation of dose dependence antiviral activity with the inhibitor G12 (Figure 8 & Figure S5). The uninfected control received only the base media used for diluting the virus. The plates were incubated for an additional 24 hours at 37 °C, 5% CO_2 and fixed with 100% methanol for immunofluorescence assay. Fixed cells were washed with 3 times with PBS pH 7.4 (Gibco cat. no. 10010-023) and incubated with blocking buffer (2% BSA, 0.3% Triton X-100, 5% goat serum, 5% donkey serum, 0.01% NaN3 in PBS) for 2 hours at room temperature. Anti-Spike protein primary antibody was diluted into blocking buffer and incubated overnight at 4°C. Either of these primary antibodies was used: "BEI Resources, NIAID, NIH mouse monoclonal Anti-SARS-Related Coronavirus 2 Spike Glycoprotein S1 Domain (produced *in vitro*), cat. no. NR-53788" at a 1:300 dilution ratio, or "SinoBiological SARS-CoV-2 (2019-nCoV) Spike S1 Antibody, Rabbit Mab, cat. no. 40150-R007" at a 1:100 dilution ratio. Following overnight incubation, cells were washed with PBS and incubated with AlexaFluor-555 conjugated secondary antibody diluted at 1:1000 (Abcam cat. no. 150114 or 150078) for one hour at room temperature. Cells were then stained with 10 μg/mL DAPI (ThermoFisher cat. no. D1306) for 10 minutes, and stored in PBS for imaging. Plates were imaged using an ImageXpress confocal microscope (Molecular Devices, San Jose, CA) in widefield mode at 10X magnification. 9 sites per well were imaged, and the percentage of infected cells was quantified using the MetaXpress multiwavelength cell scoring module. We considered spike protein expressing cells as infected, and calculated their percentage from the total number of cells in the well. %Infected cells was then normalized to an infected culture that was treated with vehicle only. Statistical analysis was performed using one-way ANOVA in

GraphPad Prism, and IC_{50} values were estimated (Figure 8) using a four-parameter non-linear fit dose response curve.

Cytotoxicity assay in HEK293-ACE2 cells (Figure 8B): HEK293-ACE2 cells were plated and transfected with peptides following the same protocol as used for the viral assays, but following transfection were incubated at 37 °C and 5% CO_2 for 24 hours. Peptide cytotoxicity was then assessed using the CyQUANT LDH Cytotoxicity Assay (ThermoFisher cat no. C20300) following the manufacturer protocol.

NCAP immunofluorescence staining in A549-ACE2 cells (Figure 3): A549-ACE2 cells were plated at 10,000 cells/well in F12-K Nutrient Mixture (Gibco cat no. 21127-022) supplemented with 10% FBS (Gibco cat no. 26140-079), 1% penicillin-streptomycin (Gibco cat no. 15140-122), and 1 μg/mL puromycin (Gibco cat no. A1113803) and 6 μg/mL blasticidin (Gibco cat no. A1113903) for selection, on Corning BioCoat Poly-D-Lysine/Laminin 8-well culture slides (Corning cat. no. 354688) and incubated overnight at 37 ºC, 5% CO_2. Cells were then infected with SARS-CoV-2 virus as detailed above at a MOI of 0.025 for 24 hours at 37 ºC, 5% CO_2, then fixed with 4% paraformaldehyde for 30 minutes, washed with 3 times with 1X PBS pH 7.4 (Gibco cat. no. 10010-023) and stored at 4 ºC. Mock infection was performed at similarly treated as control. Cells were washed again in PBS, 3 times for 5 min each wash, immediately prior to staining. Cells were permeabilized with blocking buffer (2% BSA, 0.3% Triton X-100, 5% goat serum, 5% donkey serum, 0.01% NaN3 in PBS) for 1 hours at room temperature. The blocking solution was then replaced with a fresh blocking solution supplemented with 1:500 diluted primary monoclonal mouse anti- SARS-CoV-2 NCAP antibody (MyBioSource cat no. MBS8400155, clone no. 11D5). The cells were incubated with the antibody for overnight at 4 ºC, then washed twice for 10 min at RT with a TBST solution (Tris-buffered saline made of 50 mM Tris pH 7.4, 150 mM NaCl, supplemented with 0.1% Tween-20), followed by an additional 1 h TBST wash at RT. Washing solution was replaced with fresh TBST added with 1:500 diluted goat

anti-mouse IgG H&L, Alexa Fluor 647, preabsorbed secondary antibody (Abcam, cat no. ab150119). Cells were incubated with the secondary antibody with mild agitation for 1 hour at RT, followed by 3 washes of 15 min with TBST and 3 washes of 15 min with 1xPBS. Hoechst 33342 Nuclear Stain was added to the last 15 min PBS wash in 1:1000 dilution. The cells were finally washed again with PBS for 1 hour at RT and the slide was separated from the chambers and rinsed with ultrapure water. In the meantime, ProLong- glass antifade mountant (Invitrogen, cat no. P36980) was equilibrated to RT. Excessive water was blotted from the slide through the sides of the wells to allow dryness, and the mountant was applied to the slide. The slide was covered with a Slip-Rite cover glass #1.5 (Richard-Allan Scientific, cat. no. 152450) and placed in a dark box. The mountant was allowed to cure over weekend. Images were captured using Zeiss LSM 700 inverted confocal microscope equipped with a ×63 apochromatic oil objective. Images were processes and rendered with FIJI.[78]

ASSOCIATED CONTENT

Supporting information: PDF document containing: Scheme of S2hp vRNA (Figure S1A), Microscope images of NCAP phase separation *in vitro* (Figures S1B), Atomic structures of two forms of AALALL steric-zipper segment (Figure S2), LLPS of NCAP with G12 and P32 peptide inhibitors, stained with ThS (Figure S3), distribution of FITC labeled inhibitor candidates in *in vitro* NCAP solutions (Figure S4), extended dose-dependence antiviral activity curve for the inhibitor G12 (Figure S5), distribution of FITC labeled G12 in HEK293-ACE2 cells (Figure S6), Analytical HPLC traces (Figure S7) and mass-spectroscopy (Figure S8) for purified AALALL. Tables S1-S5.

Author Information

Corresponding author:

David S. Eisenberg- Departments of Chemistry and Biochemistry and Biological Chemistry, UCLA-DOE Institute, Molecular Biology Institute, and Howard Hughes Medical Institute, University of California Los Angeles (UCLA), Los Angeles, California 90095, USA; https://orcid.org/0000-0003-2432-5419. Email: **david@mbi.ucla.edu.**

Present addresses:

† Center for Alzheimer's and Neurodegenerative Diseases, Department of Biophysics, O'Donnell Brain Institute, University of Texas Southwestern Medical Center, Dallas, Texas 75390, USA.

Author Contributions

All authors have given approval to the final version of the manuscript. Protein constructs and cloning: P.M.S, Luk.S. Protein preparation and experimentation: E.T-F, J.T.B., S.G, X.C., R.A, J.L, Y.J. RNA preparation and experimentation: C.T., Y.L., Luk.S. Peptide preparation: C.T.Z. X-ray crystallography: M.R.S., C.T.Z, J.L, K.H, G.F, D.C. Fluorescence and electron Microscopy: E.T-F., J.T.B, X.C., D.B., R.A, Y.J, H.P, G.M.R, J.L. Computational analysis and inhibitor design: G.M.R., P.M.S., Y.J., E.T-F., Lor.S, K.A.M. In-cell assays: J.T.B, G.G jr., E.T-F. Writing and figure preparation: E.T-F., M.R.S., J.T.B, F.G., D.S.E. Technical support: D.H.A, Project management: E.T.F., M.R.S., R.D., V.A, F.G., D.S.E.

Funding Sources

E.T-F is supported by the Human Frontiers Science Project Organization (HFSPO) (LT000623/2018-L). Luk.S is supported by NIH NIGMS GM123126 grant. C.T.Z. is funded by the UCLA Dissertation Year Fellowship. We thank NIH AG AG048120, NSF MCB 1616265, and HHMI for support.

Acknowledgements

We thank Megan Bentzel, Jose Rodriguez, Meytal Landau, and Mark Arbing for discussions. We thank the staff at the Northeastern Collaborative Access Team, which is funded by the National

Institute of General Medical Sciences from the National Institutes of Health (P30 GM124165). The Eiger 16M detector on the 24-ID-E beam line is funded by a NIH-ORIP HEI grant (S10OD021527). The Advanced Photon Source, a U.S. Department of Energy (DOE) Office of Science User Facility operated for the DOE Office of Science by Argonne National Laboratory under Contract No. DE-AC02-06CH11357. Some of this work was also performed at the Stanford-SLAC Cryo-EM Center (S2C2), which is supported by the National Institutes of Health Common Fund Transformative High-Resolution Cryo-Electron Microscopy program (U24 GM129541). The content is solely the responsibility of the authors and does not necessarily represent the official views of the National Institutes of Health. The authors also acknowledge the use of instruments at the Electron Imaging Center for NanoMachines supported by NIH (1S10RR23057 to ZHZ) and CNSI at UCLA. This material is based upon work supported by the National Science Foundation under Grant No. (MCB 1616265), NIH/NIA R01 Grant AG048120, the U.S. Department of Energy (DOE) Contract No. DOE - DE-FC02-02ER63421, and by UCLA David Geffen School of Medicine – Eli and Edythe Broad Center of Regenerative Medicine and Stem Cell Research Award Program, Broad Stem Cell Research Center (BSCRC) COVID 19 Research Award (OCRC #20-73).

Competing interests

D.S.E. is an advisor and equity shareholder in ADRx, Inc. The remaining authors declare no competing interests.

Data availability

The atomic coordinates were deposited in the RCSB Protein Data Bank (PDB) under accession numbers 7LV2, 7LTU, 7LUX, and 7LUZ.All other data is available in the main and supplementary text and upon request.

Abbreviations

Aβ42, Amyloid-β 1-42; a.u., arbitrary unit; A.U., absorbance unit; COVID, coronavirus disease; CPEB, cytoplasmic polyadenylation element binding protein; cryoEM, electron cryogenic microscopy; CTT, C-terminal tail; DD, dimerization domain; DMSO, dimethyl sulfoxide; FUS, Fused in sarcoma; HIV, human immunodeficiency virus; hnRNP- heterogenous nuclear ribonucleoprotein; IC, inhibitory concentration; LC, low complexity; LCD, low complexity domain; LLPS, liquid-liquid-phase separation; NCAP, Nucleocapsid protein; NTT, N-terminal tail; PEG, polyethylene glycol; RBD, RNA-binding domain; SARS-CoV, severe acute reparatory syndrome coronavirus; SARS-CoV-2, severe acute reparatory syndrome coronavirus 2; SD, standard deviation; S2hp, hairpin S2; TDP-43, transactive response DNA-binding protein of 43 kDa; TEM, transmission electron microscopy; TFA, trifluoroacetic acid; ThS- Thioflavin-S; ThT, Thioflavin-T; vRNA, viral RNA.

Supporting Information

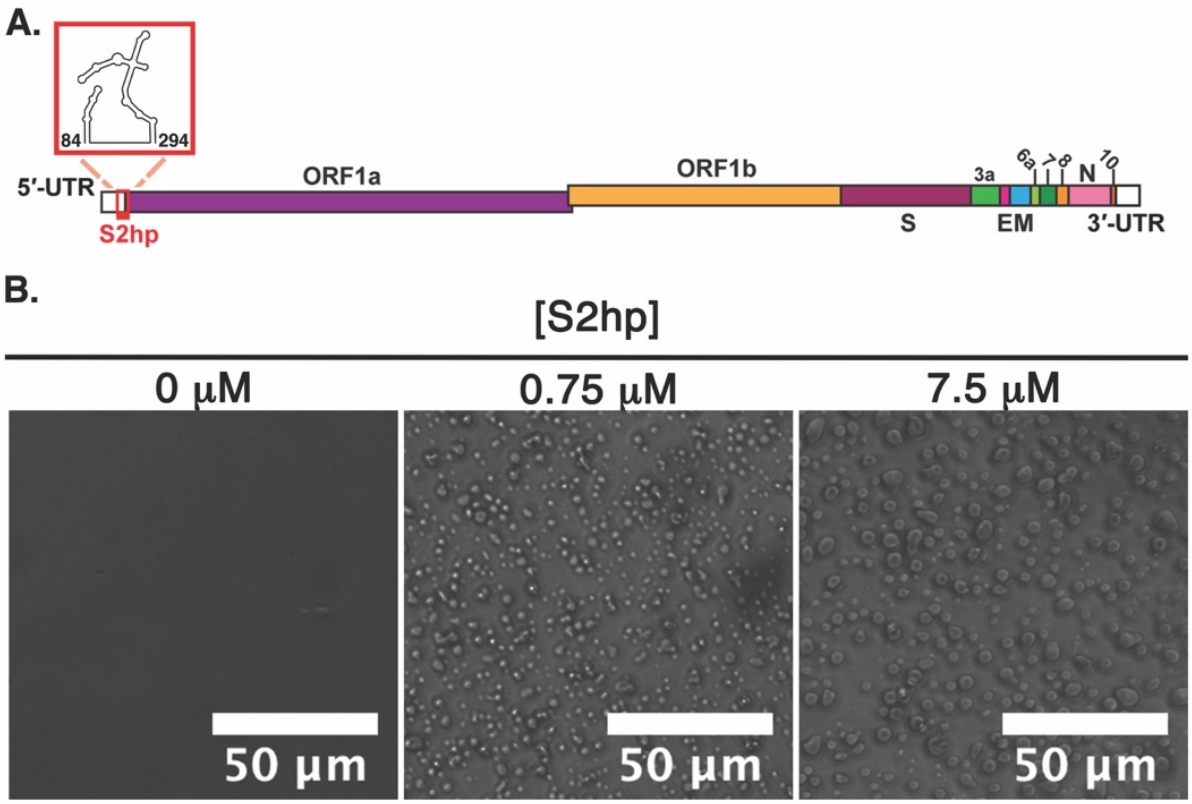

Figure S1: NCAP forms LLPS when incubated with hairpin-Site2 (S2hp) viral RNA (vRNA) under near physiological salt conditions. A) A schematic representation of SARS-CoV-2 genome and the location of S2hp vRNA used in this study. B) Phase separation droplets formed in PBS buffer after 1 day of incubation of 30 μM NCAP and 1: 0 (0 μM), 40: 1 (0.75 μM), and 4: 1 (7.5 μM) NCAP: S2hp molar ratio.

Figure S2: Expended version of Figure 6. Amyloid-like association of the NCAP segment AALALL revealed in two crystal forms. The upper row shows the quality of the fit of each model to its corresponding simulated annealing composite omit maps. The maps are contoured at the 1.0 sigma level. The structural features are well defined by the density. The view is directed down the fibril axis. Each chain shown here corresponds to one strand in a beta-sheet. Thousands of identical strands stack above and below the plane of the page making ~100 micron-long beta-sheets. The face of each beta-sheet of AALALL (PDB IDs: 7LTU, form 1; 7LUX form 2) is symmetric with its back. The lower row shows 18 strands from each of the steric zippers at a view nearly perpendicular to the fibril axis. The AALALL zippers are antiparallel, in register sheets, mated with Class 7 zipper symmetry. Trifluoroacetic acid (TFA) appear bound to the AALALL- form 1 steric zipper, and Polyethylene glycol (PEG) to form 2. As the PEG is incorporated into the zipper interface in form 2, we postulate that this form is less likely to occur in vivo.

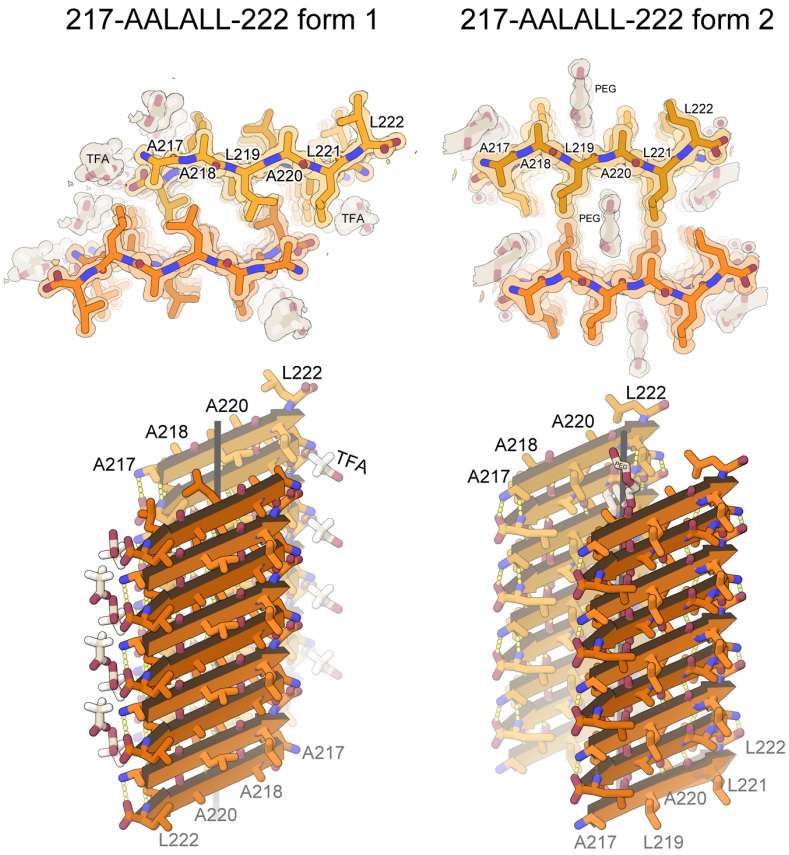

Figure S3: G12, but not P32, disrupt NCAP's phase separation and amyloid formation. 30 μM NCAP protein was mixed with 0.75 μM S2hp RNA (40: 1 molar ratio), and incubated in low salt conditions with zinc (20 mM Tris pH 8, 50 mM NaCl, 20 μM $ZnCl_2$). ThioflavinS (ThS) was added at a final concentration of 0.0002% w/v. Inhibitors were dissolved in DMSO according to their solubility limits and added to the appropriate mixtures in 1:1 NCAP : inhibitor molar ratio. The final DMSO concentration in the G12 and P32 containing mixtures were 1.4% and 0.8% respectively. "No inhibitor" NCAP controls were performed for each final DMSO concentration and a representative image is shown. Droplets were imaged after 30 min incubation at room temperature. Top row – LLPS droplets of NCAP with no inhibitors and a 1.4% final DMSO concentration show strong ThS binding (green). Similar to somewhat smaller ThS-binding LLPS droplets were observed with 0.8% final DMSO concentration. Middle row – addition of G12 completely disrupts NCAP's LLPS and induces formation of protein aggregates with reduced ThS binding capacity. Bottom row – addition of P32 to NCAP has no significant effect on NCAP LLPS or ThS binding.

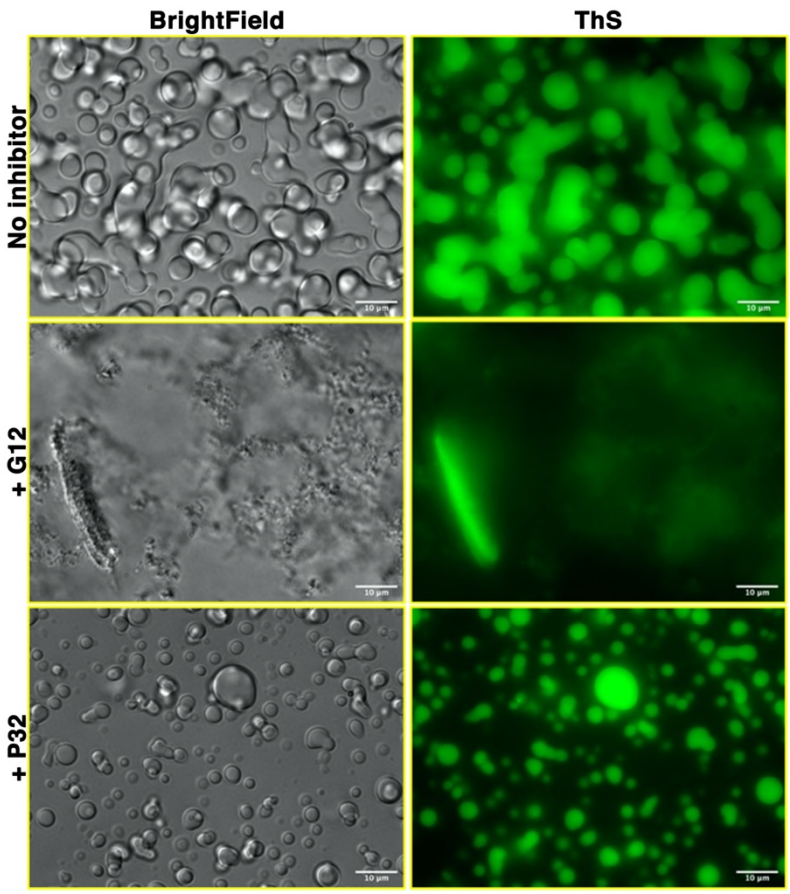

Figure S4:

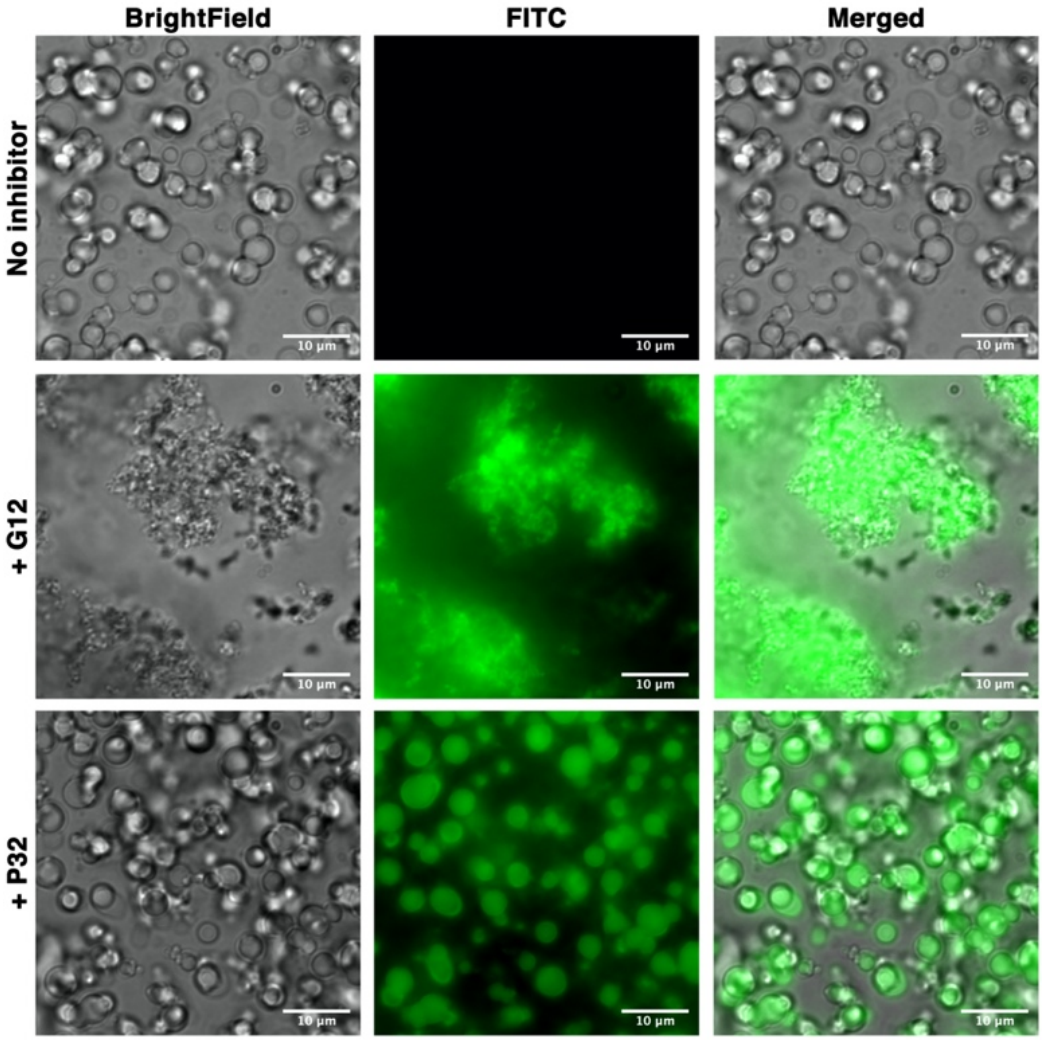

Localization of FITC-tagged G12 and P32 in NCAP LLPS droplets. 10 µM NCAP protein was mixed with 0.25 µM S2hp RNA (40: 1 molar ratio) in 20 mM Tris pH 8, 50 mM NaCl, 20 µM $ZnCl_2$. FITC-tagged peptide was mixed with untagged peptide at a 1: 9 ratio, and was then added to the samples at a final concentration of 10 µM (1: 1 molar ratio with NCAP). Samples were incubated at 37°C for 24 hours. Top row – NCAP LLPS without inhibitor show no fluorescence. Middle row - Addition of G12 induces formation of aggregates that contain the G12 peptide (green). Bottom row – P32 (green) partitions into NCAP's LLPS droplets, but has no effect on their morphology.

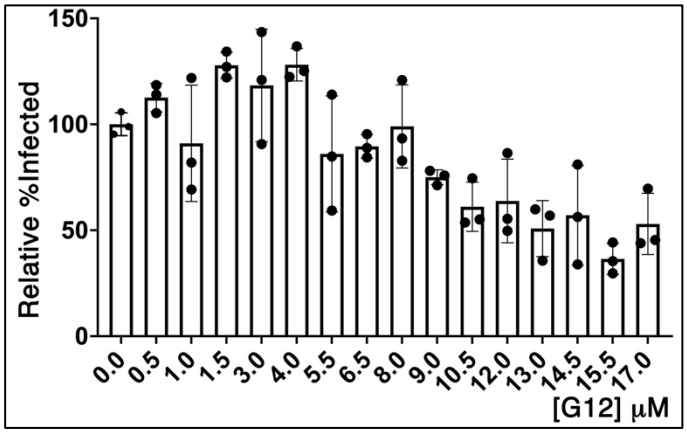

Figure S5: (Extended version of Figure 8A). A full dose-dependence analysis of G12 inhibition of SARS-CoV-2 infection in HEK293-ACE2 cells. Cells were transfected with indicated concentrations of G12, infected 3-4 hours later with the virus, and fixed at 24 hours post infection. The overall percentage of cells positive for infection in each sample were calculated via quantitative immunofluorescence labeling of the spike protein, relative to the number of nuclei in each sample. The relative % infected was then achieved by normalizing the percentage of positive cells to the vehicle control (0 µM G12). Bars indicate the mean of individual replicates and error bars represent SD from triplicates.

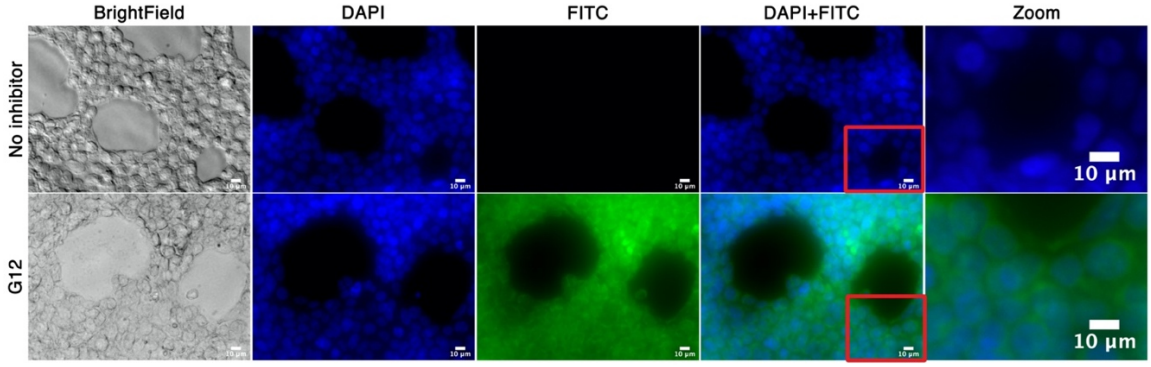

Figure S6: FITC-labeled G12 is diffused in transfected HEK293-ACE2 cells as visualized using fluorescence microscopy. FITC-tagged G12 (green) was transfected into HEK293-ACE2 cells, which were then incubated for 24 hours at 37 ºC, 5% CO_2, then fixed and stained with DAPI (blue). G12 peptide signal is detectable in the majority of cells, and appears to remain soluble and diffused within the cytoplasm. The "zoom" inset on the right is an enlarged view of the red boxes in the composite DAPI+ FITC images. A 10 µm scale bar is shown on the right bottom side of each image.

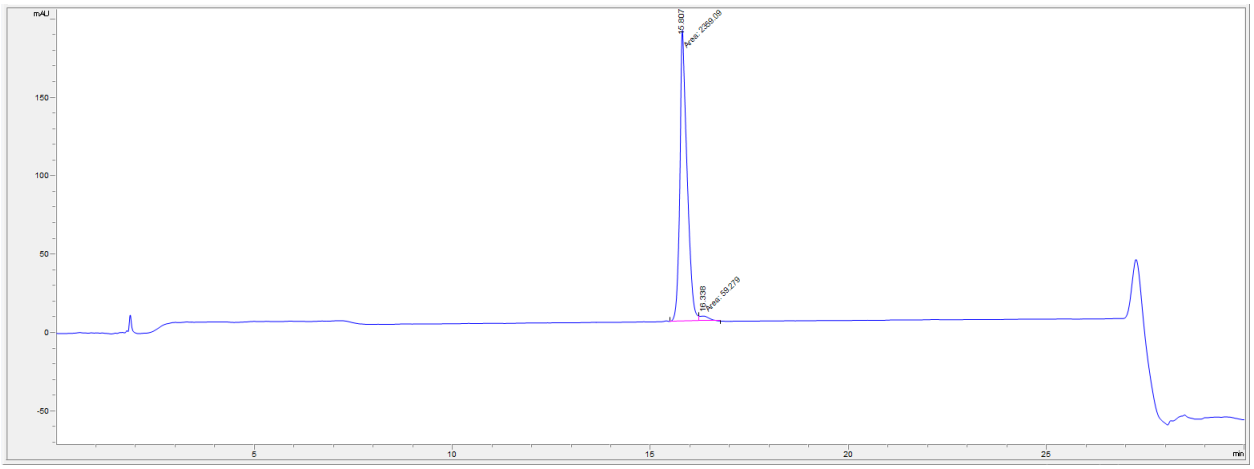

Figure S7. Analytical HPLC trace for purified AALALL. The analytes are detected by their absorbance (y-axis, mAU) at 214 nm as they pass through the flow cell over time (x-axis, minutes). Peak areas were manually integrated. **t_R 15.807**: 2359.1 mAU^2 (97.549%); **t_R 16.338**: 59.3 mAU^2 (2.451%). In addition to RP-HPLC analysis, the purified AALALL was also characterized by ESI-MS via direct injection into a Waters LCT Premier Mass Spectrometer (Figure S8**)**. The calculated monoisotopic mass for AALALL is 570.363 g/mol, m/z calculated: $[M+1H]^{1+}$ = 571.371; $[2M+1H]^{1+}$ = 1141.734. Observed: 571.191; 1141.383.

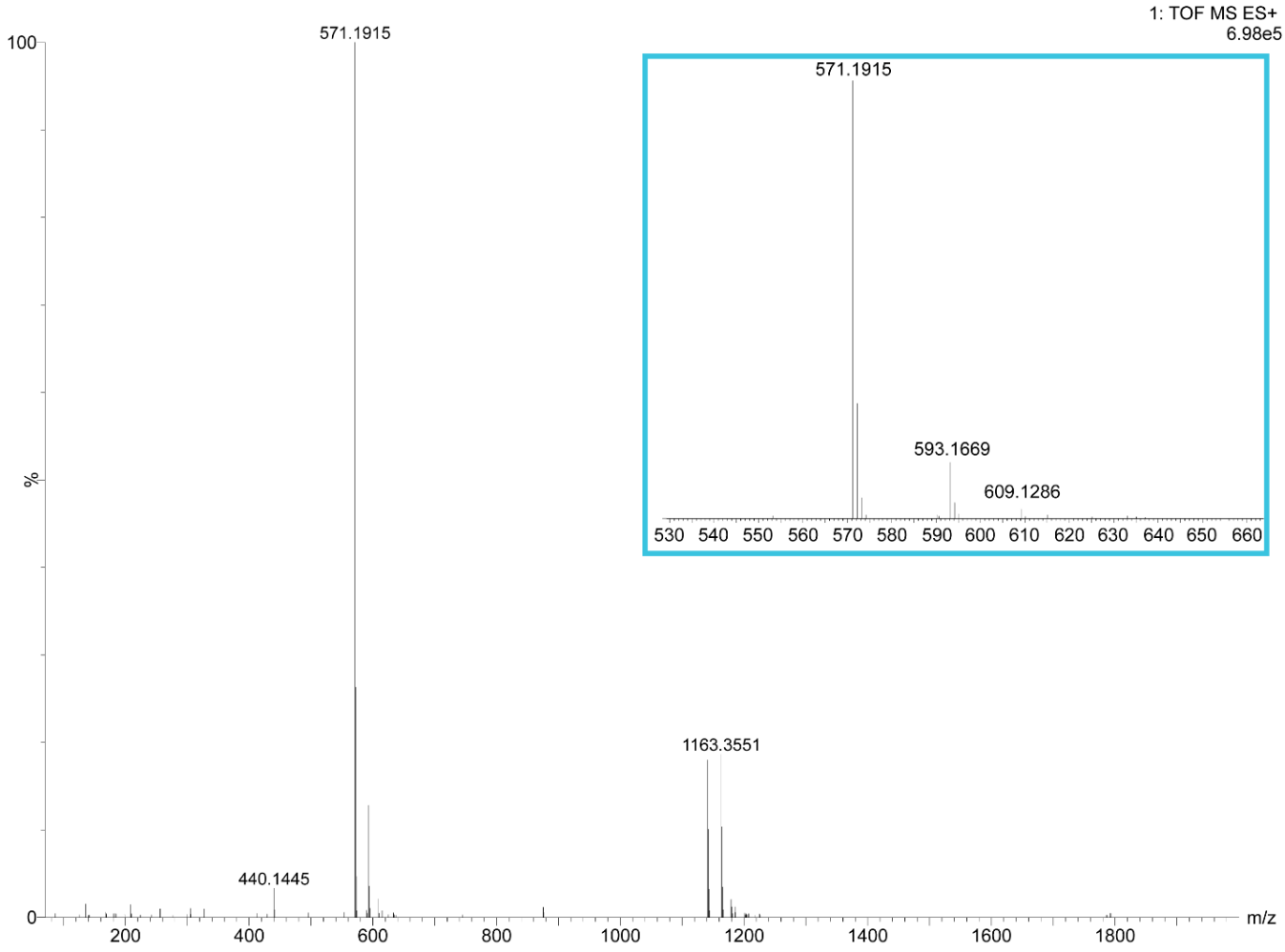

Figure S8. Broadband mass spectrum of purified AALALL collected by direct injection. The scan range was 100-2000 (m/z), and the population of each ion is represented by relative abundance.

RNA name	Origin	RNA sequence
Site1 (S1)	5'-end gRNA [34-44]*	5’-AACCAACUUUC-3’
Site1.5 (S1.5)	5'-end gRNA [60-83]	5’-UGUUCUCUAAACGAACUUUAAAAU-3’
Site2 (S2)	5'-end gRNA [128-149]	5’-UAUAAUUAAUAACUAAUUACUG-3’
Hairpin Site2 (S2hp)	5'-end gRNA [84-294]	5'-CTGTGTGGCTGTCACTCGGCTGCATGCTTAGTGCACTCACG CAGTATAATTAATAACTAATTACTGTCGTTGACAGGACACGAGT AACTCGTCTATCTTCTGCAGGCTGCTTACGGTTTCGTCCGTGTT GCAGCCGATCATCAGCACATCTAGGTTTCGTCCGGGTGTGACC GAAAGGTAAGATGGAGAGCCTTGTCCCTGGTTTCAACGA-3'
antisense siDGCR8-1[1]	human	5'-AUCACACUCUUGUCCGAUGUU-3'

Table S1. RNA sequences used in this work.

*Nucleotide sequence boundaries.

Peptide Structure	Area buried in zipper interface per chain (Å2)	Shape complementarity	ΔG°/chain (kcal/mol)	ΔG°/residue (kcal/mol)
179-GSQASS-184	164	0.89	-0.9	-0.2
217-AALALL-222 form 1	73	0.81	-6.2	-1.0
217-AALALL-222 form 2	155	0.78	-6.5	-1.1
243-GQTVTK-248	102	0.39	-1.4	-0.2

Table S2. Steric zipper structural stability statistics.

Inhibitor Name	Sequence	Target Structure	Design Approach	Rosetta Score[(a)]
P32	GWTVTK	GQTVTK	Sequence/Structure-based	
G12	d-(RRFFMVLM)	AALALL	Rosetta-based	-34.5 (fibril top) -35.7 (fibril bottom)*

Table S3. Sequences and Rosetta scores of peptide-based inhibitor-candidates presented in this manuscript.

(a) An arbitrary energetic score calculated for the binding of the designed peptide inhibitor to the fibril tip.[2] These scores were calculated without the terminal arginine chain that was added to increase peptide solubility (in the case of G12).

*The Rosetta score for the binding of additional AALALL strand for comparison is -30.78 (fibril top) and -34.57 (fibril bottom).

Primer	Sequence	Constructs	Description
NCAP-1	gatataccatgggcagcagccatcatcatc	NCAP	5' flanking (His-SUMO), NcoI
NCAP-2	tcgacggagctcctattaggcctgagttgagtcagcact	NCAP, DD-C_{term}	3' flanking, SacI
NCAP-3	gacggagctcctattatgcgtagaagccttttggcaa	N_{term}-RBD	3' flanking, SacI
NCAP-4	tcgacggagctcctattaacgtttttgccgaggcttctt	LCD	3' flanking, SacI
NCAP-5	attggtggtacctctgataatggaccccaaaatcagcga	NCAP, N_{term}-RBD	SUMO/NCAP SOE (forward), KpnI
NCAP-6	gtccattatcagaggtaccaccaatctgttctctgtgagcctc	NCAP, N_{term}-RBD	SUMO/NCAP SOE (reverse), KpnI
NCAP-7	gccataggtaccttctacgcagaagggagcaga	LCD	5' flanking, KpnI
NCAP-8	tggtggtaccaagcctcggcaaaaacgtact	DD-C_{term}	5' flanking, KpnI

Table S4. PCR Primers.

AALALL QC Analysis		
Time	[A]	[B]
(min)	(%)	(%)
0	90	10
5	80	20
25	60	40
26	0	100
30	0	100

Table S5. Gradient utilized for AALALL peptide purity analysis shown in Figures S7 & S8.

References for experimental procedures

(1) Han, J.; Lee, Y.; Yeom, K. H.; Kim, Y. K.; Jin, H.; Kim, V. N. The Drosha-DGCR8 Complex in Primary MicroRNA Processing. *Genes Dev*. **2004**, *18* (24), 3016–3027. https://doi.org/10.1101/gad.1262504.

(2) Leaver-Fay, A.; Tyka, M.; Lewis, S. M.; Lange, O. F.; Thompson, J.; Jacak, R.; Kaufman, K.; Renfrew, P. D.; Smith, C. A.; Sheffler, W.; Davis, I. W.; Cooper, S.; Treuille, A.; Mandell, D. J.; Richter, F.; Ban, Y. E. A.; Fleishman, S. J.; Corn, J. E.; Kim, D. E.; Lyskov, S.; Berrondo, M.; Mentzer, S.; Popović, Z.; Havranek, J. J.; Karanicolas, J.; Das, R.; Meiler, J.; Kortemme, T.; Gray, J. J.; Kuhlman, B.; Baker, D.; Bradley, P. Rosetta3: An Object-Oriented Software Suite for the Simulation and Design of Macromolecules. *Methods Enzymol.* **2011**, *487* (C), 545–574. https://doi.org/10.1016/B978-0-12-381270-4.00019-6.

References

(1) Savastano, A.; Ibáñez de Opakua, A.; Rankovic, M.; Zweckstetter, M. Nucleocapsid Protein of SARS-CoV-2 Phase Separates into RNA-Rich Polymerase-Containing Condensates. *Nat. Commun.* **2020**, *11* (1), 1–10. https://doi.org/10.1038/s41467-020-19843-1.

(2) Chen, H.; Cui, Y.; Han, X.; Hu, W.; Sun, M.; Zhang, Y.; Wang, P. H.; Song, G.; Chen, W.; Lou, J. Liquid–Liquid Phase Separation by SARS-CoV-2 Nucleocapsid Protein and RNA. *Cell Res.* **2020**, *30* (12), 1143–1145. https://doi.org/10.1038/s41422-020-00408-2.

(3) Cubuk, J.; Alston, J. J.; Incicco, J. J.; Singh, S.; Stuchell-Brereton, M. D.; Ward, M. D.; Zimmerman, M. I.; Vithani, N.; Griffith, D.; Wagoner, J. A.; Bowman, G. R.; Hall, K. B.; Soranno, A.; Holehouse, A. S. The SARS-CoV-2 Nucleocapsid Protein Is Dynamic, Disordered, and Phase Separates with RNA. *Nat. Commun.* **2021**, *12* (1), 1936. https://doi.org/10.1038/s41467-021-21953-3.

(4) Lu, S.; Ye, Q.; Singh, D.; Cao, Y.; Diedrich, J. K.; Yates, J. R.; Villa, E.; Cleveland, D. W.; Corbett, K. D. The SARS-CoV-2 Nucleocapsid Phosphoprotein Forms Mutually Exclusive Condensates with RNA and the Membrane-Associated M Protein. *Nat. Commun.* **2021**, *12* (1), 502. https://doi.org/10.1038/s41467-020-20768-y.

(5) Perdikari, T. M.; Murthy, A. C.; Ryan, V. H.; Watters, S.; Naik, M. T.; Fawzi, N. L. SARS-CoV-2 Nucleocapsid Protein Phase-separates with RNA and with Human HnRNPs. *EMBO J.* **2020**, *39* (24). https://doi.org/10.15252/embj.2020106478.

(6) Cascarina, S. M.; Ross, E. D. A Proposed Role for the SARS-CoV-2 Nucleocapsid Protein in the Formation and Regulation of Biomolecular Condensates. *FASEB J.* **2020**, *34* (8), 9832–9842. https://doi.org/10.1096/fj.202001351.

(7) Iserman, C.; Roden, C. A.; Boerneke, M. A.; Sealfon, R. S. G.; McLaughlin, G. A.; Jungreis, I.; Fritch, E. J.; Hou, Y. J.; Ekena, J.; Weidmann, C. A.; Theesfeld, C. L.; Kellis, M.; Troyanskaya, O. G.; Baric, R. S.; Sheahan, T. P.; Weeks, K. M.; Gladfelter, A. S. Genomic

RNA Elements Drive Phase Separation of the SARS-CoV-2 Nucleocapsid. *Mol. Cell* **2020**, *80* (6), 1078-1091.e6. https://doi.org/10.1016/j.molcel.2020.11.041.

(8) Carlson, C. R.; Asfaha, J. B.; Ghent, C. M.; Howard, C. J.; Hartooni, N.; Safari, M.; Frankel, A. D.; Morgan, D. O. Phosphoregulation of Phase Separation by the SARS-CoV-2 N Protein Suggests a Biophysical Basis for Its Dual Functions. *Mol. Cell* **2020**, *80* (6), 1092-1103.e4. https://doi.org/10.1016/j.molcel.2020.11.025.

(9) Ye, Q.; West, A. M. V.; Silletti, S.; Corbett, K. D. Architecture and Self-Assembly of the SARS-CoV-2 Nucleocapsid Protein. *Protein Sci.* **2020**, *29* (9), 1890–1901. https://doi.org/10.1002/pro.3909.

(10) Jack, A.; Ferro, L. S.; Trnka, M. J.; Wehri, E.; Nadgir, A.; Nguyenla, X.; Fox, D.; Costa, K.; Stanley, S.; Schaletzky, J.; Yildiz, A. SARS-CoV-2 Nucleocapsid Protein Forms Condensates with Viral Genomic RNA. *PLOS Biol.* **2021**, *19* (10), e3001425. https://doi.org/10.1371/journal.pbio.3001425.

(11) Wu, Y.; Ma, L.; Cai, S.; Zhuang, Z.; Zhao, Z.; Jin, S.; Xie, W.; Zhou, L.; Zhang, L.; Zhao, J.; Cui, J. RNA-Induced Liquid Phase Separation of SARS-CoV-2 Nucleocapsid Protein Facilitates NF-KB Hyper-Activation and Inflammation. *Signal Transduct. Target. Ther.* **2021**, *6* (1), 1–13. https://doi.org/10.1038/s41392-021-00575-7.

(12) Cascarina, S. M.; Elder, M. R.; Ross, E. D. Atypical Structural Tendencies among Low-Complexity Domains in the Protein Data Bank Proteome. *PLOS Comput. Biol.* **2020**, *16* (1), e1007487. https://doi.org/10.1371/JOURNAL.PCBI.1007487.

(13) Kato, M.; Han, T. W.; Xie, S.; Shi, K.; Du, X.; Wu, L. C.; Mirzaei, H.; Goldsmith, E. J.; Longgood, J.; Pei, J.; Grishin, N. V.; Frantz, D. E.; Schneider, J. W.; Chen, S.; Li, L.; Sawaya, M. R.; Eisenberg, D.; Tycko, R.; McKnight, S. L. Cell-Free Formation of RNA Granules: Low Complexity Sequence Domains Form Dynamic Fibers within Hydrogels. *Cell* **2012**, *149* (4), 753–767. https://doi.org/10.1016/J.CELL.2012.04.017.

(14) Lin, Y.; Protter, D. S. W.; Rosen, M. K.; Parker, R. Formation and Maturation of Phase-

Separated Liquid Droplets by RNA-Binding Proteins. *Mol. Cell* **2015**, *60* (2), 208–219. https://doi.org/10.1016/J.MOLCEL.2015.08.018.

(15) Furukawa, Y.; Nukina, N. Functional Diversity of Protein Fibrillar Aggregates from Physiology to RNA Granules to Neurodegenerative Diseases. *Biochim. Biophys. Acta - Mol. Basis Dis.* **2013**, *1832* (8), 1271–1278. https://doi.org/10.1016/j.bbadis.2013.04.011.

(16) Eisenberg, D.; Jucker, M. The Amyloid State of Proteins in Human Diseases. *Cell* **2012**, *148* (6), 1188–1203. https://doi.org/10.1016/j.cell.2012.02.022.

(17) Nizhnikov, A. A.; Antonets, K. S.; Bondarev, S. A.; Inge-Vechtomov, S. G.; Derkatch, I. L. Prions, Amyloids, and RNA: Pieces of a Puzzle. *Prion* **2016**, *10* (3), 182–206. https://doi.org/10.1080/19336896.2016.1181253.

(18) Cereghetti, G.; Saad, S.; Dechant, R.; Peter, M. Reversible, Functional Amyloids: Towards an Understanding of Their Regulation in Yeast and Humans. *Cell Cycle* **2018**, *17* (13), 1545–1558. https://doi.org/10.1080/15384101.2018.1480220.

(19) Hughes, M. P.; Sawaya, M. R.; Boyer, D. R.; Goldschmidt, L.; Rodriguez, J. A.; Cascio, D.; Chong, L.; Gonen, T.; Eisenberg, D. S. Atomic Structures of Low-Complexity Protein Segments Reveal Kinked β Sheets That Assemble Networks. *Science* **2018**, *359* (6376), 698–701. https://doi.org/10.1126/science.aan6398.

(20) Sopova, J. V.; Koshel, E. I.; Belashova, T. A.; Zadorsky, S. P.; Sergeeva, A. V.; Siniukova, V. A.; Shenfeld, A. A.; Velizhanina, M. E.; Volkov, K. V.; Nizhnikov, A. A.; Kachkin, D. V.; Gaginskaya, E. R.; Galkin, A. P. RNA-Binding Protein FXR1 Is Presented in Rat Brain in Amyloid Form. *Sci. Rep.* **2019**, *9* (1), 1–14. https://doi.org/10.1038/s41598-019-55528-6.

(21) Souquere, S.; Mollet, S.; Kress, M.; Dautry, F.; Pierron, G.; Weil, D. Unravelling the Ultrastructure of Stress Granules and Associated P-Bodies in Human Cells. *J. Cell Sci.* **2009**, *122* (20), 3619–3626. https://doi.org/10.1242/JCS.054437.

(22) Roush, S. W.; Murphy, T. V.; Basket, M. M.; Iskander, J. K.; Moran, J. S.; Seward, J. F.; Wasley, A. Historical Comparisons of Morbidity and Mortality for Vaccine-Preventable

Diseases in the United States. *J. Am. Med. Assoc.* **2007**, *298* (18), 2155–2163. https://doi.org/10.1001/jama.298.18.2155.

(23) Bai, Z.; Cao, Y.; Liu, W.; Li, J. The SARS-CoV-2 Nucleocapsid Protein and Its Role in Viral Structure, Biological Functions, and a Potential Target for Drug or Vaccine Mitigation. *Viruses* **2021**, *13* (6). https://doi.org/10.3390/V13061115.

(24) Wootton, J. C.; Federhen, S. Analysis of Compositionally Biased Regions in Sequence Databases. *Methods Enzymol.* **1996**, *266*, 554–571. https://doi.org/10.1016/s0076-6879(96)66035-2.

(25) Bussière, T.; Bard, F.; Barbour, R.; Grajeda, H.; Guido, T.; Khan, K.; Schenk, D.; Games, D.; Seubert, P.; Buttini, M. Morphological Characterization of Thioflavin-S-Positive Amyloid Plaques in Transgenic Alzheimer Mice and Effect of Passive Aβ Immunotherapy on Their Clearance. *Am. J. Pathol.* **2004**, *165* (3), 987. https://doi.org/10.1016/S0002-9440(10)63360-3.

(26) Murakami, T.; Qamar, S.; Lin, J. Q.; Schierle, G. S. K.; Rees, E.; Miyashita, A.; Costa, A. R.; Dodd, R. B.; Chan, F. T. S.; Michel, C. H.; Kronenberg-Versteeg, D.; Li, Y.; Yang, S. P.; Wakutani, Y.; Meadows, W.; Ferry, R. R.; Dong, L.; Tartaglia, G. G.; Favrin, G.; Lin, W. L.; Dickson, D. W.; Zhen, M.; Ron, D.; Schmitt-Ulms, G.; Fraser, P. E.; Shneider, N. A.; Holt, C.; Vendruscolo, M.; Kaminski, C. F.; St George-Hyslop, P. ALS/FTD Mutation-Induced Phase Transition of FUS Liquid Droplets and Reversible Hydrogels into Irreversible Hydrogels Impairs RNP Granule Function. *Neuron* **2015**, *88* (4), 678–690. https://doi.org/10.1016/J.NEURON.2015.10.030.

(27) Rayman, J. B.; Kandel, E. R. TIA-1 Is a Functional Prion-Like Protein. *Cold Spring Harb. Perspect. Biol.* **2017**, *9* (5). https://doi.org/10.1101/CSHPERSPECT.A030718.

(28) Garnier, C.; Devred, F.; Byrne, D.; Puppo, R.; Roman, A. Y.; Malesinski, S.; Golovin, A. V.; Lebrun, R.; Ninkina, N. N.; Tsvetkov, P. O. Zinc Binding to RNA Recognition Motif of TDP-43 Induces the Formation of Amyloid-like Aggregates. *Sci. Rep.* **2017**, *7* (1), 1–10.

https://doi.org/10.1038/s41598-017-07215-7.

(29) Shin, W. S.; Di, J.; Murray, K. A.; Sun, C.; Li, B.; Bitan, G.; Jiang, L. Different Amyloid-β Self-Assemblies Have Distinct Effects on Intracellular Tau Aggregation. *Front. Mol. Neurosci.* **2019**, *0*, 268. https://doi.org/10.3389/FNMOL.2019.00268.

(30) Kaufman, S. K.; Sanders, D. W.; Thomas, T. L.; Ruchinskas, A.; Vaquer-Alicea, J.; Sharma, A. M.; Miller, T. M.; Diamond, M. I. Tau Prion Strains Dictate Patterns of Cell Pathology, Progression Rate, and Regional Vulnerability in Vivo. *Neuron* **2016**, *92* (4), 796. https://doi.org/10.1016/J.NEURON.2016.09.055.

(31) Seidler, P. M.; Boyer, D. R.; Murray, K. A.; Yang, T. P.; Bentzel, M.; Sawaya, M. R.; Rosenberg, G.; Cascio, D.; Williams, C. K.; Newell, K. L.; Ghetti, B.; DeTure, M. A.; Dickson, D. W.; Vinters, H. V.; Eisenberg, D. S. Structure-Based Inhibitors Halt Prion-like Seeding by Alzheimer's Disease-and Tauopathy-Derived Brain Tissue Samples. *J. Biol. Chem.* **2019**, *294* (44), 16451–16464. https://doi.org/10.1074/jbc.RA119.009688.

(32) Li, B.; Ge, P.; Murray, K. A.; Sheth, P.; Zhang, M.; Nair, G.; Sawaya, M. R.; Shin, W. S.; Boyer, D. R.; Ye, S.; Eisenberg, D. S.; Zhou, Z. H.; Jiang, L. Cryo-EM of Full-Length α-Synuclein Reveals Fibril Polymorphs with a Common Structural Kernel. *Nat. Commun.* **2018**, *9* (1), 3609. https://doi.org/10.1038/s41467-018-05971-2.

(33) Johnston, J. A.; Ward, C. L.; Kopito, R. R. Aggresomes: A Cellular Response to Misfolded Proteins. *J. Cell Biol.* **1998**, *143* (7), 1883–1898. https://doi.org/10.1083/JCB.143.7.1883.

(34) Klein, S.; Cortese, M.; Winter, S. L.; Wachsmuth-Melm, M.; Neufeldt, C. J.; Cerikan, B.; Stanifer, M. L.; Boulant, S.; Bartenschlager, R.; Chlanda, P. SARS-CoV-2 Structure and Replication Characterized by in Situ Cryo-Electron Tomography. *Nat. Commun.* **2020**, *11* (1), 2020.06.23.167064. https://doi.org/10.1038/s41467-020-19619-7.

(35) Yao, H.; Song, Y.; Chen, Y.; Wu, N.; Xu, J.; Sun, C.; Zhang, J.; Weng, T.; Zhang, Z.; Wu, Z.; Cheng, L.; Shi, D.; Lu, X.; Lei, J.; Crispin, M.; Shi, Y.; Li, L.; Li, S. Molecular

Architecture of the SARS-CoV-2 Virus. *Cell* **2020**, *183* (3), 730. https://doi.org/10.1016/J.CELL.2020.09.018.

(36) Wang, S.; Dai, T.; Qin, Z.; Pan, T.; Chu, F.; Lou, L.; Zhang, L.; Yang, B.; Huang, H.; Lu, H.; Zhou, F. Targeting Liquid–Liquid Phase Separation of SARS-CoV-2 Nucleocapsid Protein Promotes Innate Antiviral Immunity by Elevating MAVS Activity. *Nat. Cell Biol.* **2021**, *23* (7), 718–732. https://doi.org/10.1038/s41556-021-00710-0.

(37) Cai, T.; Yu, Z.; Wang, Z.; Liang, C.; Richard, S. Arginine Methylation of SARS-Cov-2 Nucleocapsid Protein Regulates RNA Binding, Its Ability to Suppress Stress Granule Formation, and Viral Replication. *J. Biol. Chem.* **2021**, *297* (1). https://doi.org/10.1016/J.JBC.2021.100821.

(38) Zhao, D.; Xu, W.; Zhang, X.; Wang, X.; Ge, Y.; Yuan, E.; Xiong, Y.; Wu, S.; Li, S.; Wu, N.; Tian, T.; Feng, X.; Shu, H.; Lang, P.; Li, J.; Zhu, F.; Shen, X.; Li, H.; Li, P.; Zeng, J. Understanding the Phase Separation Characteristics of Nucleocapsid Protein Provides a New Therapeutic Opportunity against SARS-CoV-2. *Protein Cell* **2021**, *12* (9), 734–740. https://doi.org/10.1007/s13238-021-00832-z.

(39) Wang, J.; Shi, C.; Xu, Q.; Yin, H. SARS-CoV-2 Nucleocapsid Protein Undergoes Liquid–Liquid Phase Separation into Stress Granules through Its N-Terminal Intrinsically Disordered Region. *Cell Discov.* **2021**, *7* (1), 1–5. https://doi.org/10.1038/s41421-020-00240-3.

(40) Huang, W.; Ju, X.; Tian, M.; Li, X.; Yu, Y.; Sun, Q.; Ding, Q.; Jia, D. Molecular Determinants for Regulation of G3BP1/2 Phase Separation by the SARS-CoV-2 Nucleocapsid Protein. *Cell Discov.* **2021**, *7* (1), 1–5. https://doi.org/10.1038/s41421-021-00306-w.

(41) Luo, L.; Li, Z.; Zhao, T.; Ju, X.; Ma, P.; Jin, B.; Zhou, Y.; He, S.; Huang, J.; Xu, X.; Zou, Y.; Li, P.; Liang, A.; Liu, J.; Chi, T.; Huang, X.; Ding, Q.; Jin, Z.; Huang, C.; Zhang, Y. SARS-CoV-2 Nucleocapsid Protein Phase Separates with G3BPs to Disassemble Stress Granules

and Facilitate Viral Production. *Sci. Bull.* **2021**, *66* (12), 1194–1204. https://doi.org/10.1016/J.SCIB.2021.01.013.

(42) Vidic, J.; Richard, C. A.; Péchoux, C.; Da Costa, B.; Bertho, N.; Mazerat, S.; Delmas, B.; Chevalier, C. Amyloid Assemblies of Influenza a Virus PB1-F2 Protein Damage Membrane and Induce Cytotoxicity. *J. Biol. Chem.* **2016**, *291* (2), 739–751. https://doi.org/10.1074/jbc.M115.652917.

(43) Salladini, E.; Gondelaud, F.; Nilsson, J. F.; Pesce, G.; Bignon, C.; Murrali, M. G.; Fabre, R.; Pierattelli, R.; Kajava, A. V.; Horvat, B.; Gerlier, D.; Mathieu, C.; Longhi, S. Identification of a Region in the Common Amino-Terminal Domain of Hendra Virus P, V, and W Proteins Responsible for Phase Transition and Amyloid Formation. *Biomolecules* **2021**, *11* (9), 1324. https://doi.org/10.3390/biom11091324.

(44) Zheng, X.; Jia, L.; Hu, B.; Sun, Y.; Zhang, Y.; Gao, X.; Deng, T.; Bao, S.; Xu, L.; Zhou, J. The C-Terminal Amyloidogenic Peptide Contributes to Self-Assembly of Avibirnavirus Viral Protease. *Sci. Rep.* **2015**, *5*. https://doi.org/10.1038/srep14794.

(45) Luckey, M.; Hernandez, J. F.; Arlaud, G.; Forsyth, V. T.; Ruigrok, R. W. H.; Mitraki, A. A Peptide from the Adenovirus Fiber Shaft Forms Amyloid-Type Fibrils. *FEBS Lett.* **2000**, *468* (1), 23–27. https://doi.org/10.1016/S0014-5793(00)01184-4.

(46) Papanikolopoulou, K.; Schoehn, G.; Forge, V.; Forsyth, V. T.; Riekel, C.; Hernandez, J. F.; Ruigrok, R. W. H.; Mitraki, A. Amyloid Fibril Formation from Sequences of a Natural β-Structured Fibrous Protein, the Adenovirus Fiber. *J. Biol. Chem.* **2005**, *280* (4), 2481–2490. https://doi.org/10.1074/jbc.M406282200.

(47) Ghosh, A.; Pithadia, A. S.; Bhat, J.; Bera, S.; Midya, A.; Fierke, C. A.; Ramamoorthy, A.; Bhunia, A. Self-Assembly of a Nine-Residue Amyloid-Forming Peptide Fragment of SARS Corona Virus E-Protein: Mechanism of Self Aggregation and Amyloid-Inhibition of HIAPP. *Biochemistry* **2015**, *54* (13), 2249–2261. https://doi.org/10.1021/acs.biochem.5b00061.

(48) Tetz, G.; Tetz, V. Prion-like Domains in Eukaryotic Viruses. *Sci. Rep.* **2018**, *8* (1), 1–10. https://doi.org/10.1038/s41598-018-27256-w.

(49) Luo, F.; Gui, X.; Zhou, H.; Gu, J.; Li, Y.; Liu, X.; Zhao, M.; Li, D.; Li, X.; Liu, C. Atomic Structures of FUS LC Domain Segments Reveal Bases for Reversible Amyloid Fibril Formation. *Nat. Struct. Mol. Biol.* **2018**, *25* (4), 341–346. https://doi.org/10.1038/s41594-018-0050-8.

(50) Murray, D. T.; Kato, M.; Lin, Y.; Thurber, K. R.; Hung, I.; McKnight, S. L.; Tycko, R. Structure of FUS Protein Fibrils and Its Relevance to Self-Assembly and Phase Separation of Low-Complexity Domains. *Cell* **2017**, *171* (3), 615-627.e16. https://doi.org/10.1016/j.cell.2017.08.048.

(51) Lu, J.; Cao, Q.; Hughes, M. P.; Sawaya, M. R.; Boyer, D. R.; Cascio, D.; Eisenberg, D. S. CryoEM Structure of the Low-Complexity Domain of HnRNPA2 and Its Conversion to Pathogenic Amyloid. *Nat. Commun.* **2020**, *11* (1), 4090. https://doi.org/10.1038/s41467-020-17905-y.

(52) Guenther, E. L.; Cao, Q.; Trinh, H.; Lu, J.; Sawaya, M. R.; Cascio, D.; Boyer, D. R.; Rodriguez, J. A.; Hughes, M. P.; Eisenberg, D. S. Atomic Structures of TDP-43 LCD Segments and Insights into Reversible or Pathogenic Aggregation. *Nat. Struct. Mol. Biol.* **2018**, *25* (6), 463–471. https://doi.org/10.1038/s41594-018-0064-2.

(53) Goldschmidt, L.; Teng, P. K.; Riek, R.; Eisenberg, D. Identifying the Amylome, Proteins Capable of Forming Amyloid-like Fibrils. *Proc. Natl. Acad. Sci. U. S. A.* **2010**, *107* (8), 3487–3492. https://doi.org/10.1073/pnas.0915166107.

(54) Sawaya, M. R.; Sambashivan, S.; Nelson, R.; Ivanova, M. I.; Sievers, S. A.; Apostol, M. I.; Thompson, M. J.; Balbirnie, M.; Wiltzius, J. J. W.; McFarlane, H. T.; Madsen, A. Ø.; Riekel, C.; Eisenberg, D. Atomic Structures of Amyloid Cross-β Spines Reveal Varied Steric Zippers. *Nature* **2007**, *447* (7143), 453–457. https://doi.org/10.1038/nature05695.

(55) Cao, Y.; Adamcik, J.; Diener, M.; Kumita, J. R.; Mezzenga, R. Different Folding States from the Same Protein Sequence Determine Reversible vs Irreversible Amyloid Fate. *J. Am. Chem. Soc.* **2021**, jacs.1c03392. https://doi.org/10.1021/JACS.1C03392.

(56) Gruca, A.; Ziemska-Legiecka, J.; Jarnot, P.; Sarnowska, E.; Sarnowski, T. J.; Grynberg, M. Common Low Complexity Regions for SARS-CoV-2 and Human Proteomes as Potential Multidirectional Risk Factor in Vaccine Development. *BMC Bioinformatics* **2021**, *22* (1), 1–18. https://doi.org/10.1186/s12859-021-04017-7.

(57) Fitzpatrick, A. W. P.; Falcon, B.; He, S.; Murzin, A. G.; Murshudov, G.; Garringer, H. J.; Crowther, R. A.; Ghetti, B.; Goedert, M.; Scheres, S. H. W. Cryo-EM Structures of Tau Filaments from Alzheimer's Disease. *Nature* **2017**, *547* (7662), 185–190. https://doi.org/10.1038/nature23002.

(58) Sievers, S. A.; Karanicolas, J.; Chang, H. W.; Zhao, A.; Jiang, L.; Zirafi, O.; Stevens, J. T.; Münch, J.; Baker, D.; Eisenberg, D. Structure-Based Design of Non-Natural Amino-Acid Inhibitors of Amyloid Fibril Formation. *Nature* **2011**, *475* (7354), 96–100. https://doi.org/10.1038/nature10154.

(59) Seidler, P. M.; Boyer, D. R.; Murray, K. A.; Yang, T. P.; Bentzel, M.; Sawaya, M. R.; Rosenberg, G.; Cascio, D.; Williams, C. K.; Newell, K. L.; Ghetti, B.; DeTure, M. A.; Dickson, D. W.; Vinters, H. V.; Eisenberg, D. S. Structure-Based Inhibitors Halt Prion-like Seeding by Alzheimer's Disease-and Tauopathy-Derived Brain Tissue Samples. *J. Biol. Chem.* **2019**, *294* (44), 16451–16464. https://doi.org/10.1074/jbc.RA119.009688.

(60) Neddenriep, B.; Calciano, A.; Conti, D.; Sauve, E.; Paterson, M.; Bruno, E.; A. Moffet, D. Short Peptides as Inhibitors of Amyloid Aggregation. *Open Biotechnol. J.* **2012**, *5* (1), 39–46. https://doi.org/10.2174/1874070701105010039.

(61) Soragni, A.; Janzen, D. M.; Johnson, L. M.; Lindgren, A. G.; Thai-Quynh Nguyen, A.; Tiourin, E.; Soriaga, A. B.; Lu, J.; Jiang, L.; Faull, K. F.; Pellegrini, M.; Memarzadeh, S.; Eisenberg, D. S. A Designed Inhibitor of P53 Aggregation Rescues P53 Tumor

Suppression in Ovarian Carcinomas. *Cancer Cell* **2016**, *29* (1), 90–103. https://doi.org/10.1016/j.ccell.2015.12.002.

(62) Seidler, P. M.; Boyer, D. R.; Rodriguez, J. A.; Sawaya, M. R.; Cascio, D.; Murray, K.; Gonen, T.; Eisenberg, D. S. Structure-Based Inhibitors of Tau Aggregation. *Nat. Chem.* **2018**, *10* (2), 170–176. https://doi.org/10.1038/nchem.2889.

(63) Saelices, L.; Chung, K.; Lee, J. H.; Cohn, W.; Whitelegge, J. P.; Benson, M. D.; Eisenberg, D. S. Amyloid Seeding of Transthyretin by Ex Vivo Cardiac Fibrils and Its Inhibition. *Proc. Natl. Acad. Sci. U. S. A.* **2018**, *115* (29), E6741–E6750. https://doi.org/10.1073/pnas.1805131115.

(64) Griner, S. L.; Seidler, P.; Bowler, J.; Murray, K. A.; Yang, T. P.; Sahay, S.; Sawaya, M. R.; Cascio, D.; Rodriguez, J. A.; Philipp, S.; Sosna, J.; Glabe, C. G.; Gonen, T.; Eisenberg, D. S. Structure-Based Inhibitors of Amyloid Beta Core Suggest a Common Interface with Tau. *Elife* **2019**, *8*. https://doi.org/10.7554/eLife.46924.

(65) Sangwan, S.; Sahay, S.; Murray, K. A.; Morgan, S.; Guenther, E. L.; Jiang, L.; Williams, C. K.; Vinters, H. V; Goedert, M.; Eisenberg, D. S. Inhibition of Synucleinopathic Seeding by Rationally Designed Inhibitors. *Elife* **2020**, *9*. https://doi.org/10.7554/eLife.46775.

(66) Leaver-Fay, A.; Tyka, M.; Lewis, S. M.; Lange, O. F.; Thompson, J.; Jacak, R.; Kaufman, K.; Renfrew, P. D.; Smith, C. A.; Sheffler, W.; Davis, I. W.; Cooper, S.; Treuille, A.; Mandell, D. J.; Richter, F.; Ban, Y. E. A.; Fleishman, S. J.; Corn, J. E.; Kim, D. E.; Lyskov, S.; Berrondo, M.; Mentzer, S.; Popović, Z.; Havranek, J. J.; Karanicolas, J.; Das, R.; Meiler, J.; Kortemme, T.; Gray, J. J.; Kuhlman, B.; Baker, D.; Bradley, P. Rosetta3: An Object-Oriented Software Suite for the Simulation and Design of Macromolecules. *Methods Enzymol.* **2011**, *487* (C), 545–574. https://doi.org/10.1016/B978-0-12-381270-4.00019-6.

(67) Shi, S.; Nguyen, P. K.; Cabral, H. J.; Diez-Barroso, R.; Derry, P. J.; Kanahara, S. M.; Kumar, V. A. Development of Peptide Inhibitors of HIV Transmission. *Bioact. Mater.*

2016, *1* (2), 109–121. https://doi.org/10.1016/j.bioactmat.2016.09.004.

(68) Xi, W.; Hansmann, U. H. E. The Effect of Retro-Inverse D-Amino Acid Aβ-Peptides on Aβ-Fibril Formation. *J. Chem. Phys.* **2019**, *150* (9). https://doi.org/10.1063/1.5082194.

(69) Muttenthaler, M.; King, G. F.; Adams, D. J.; Alewood, P. F. Trends in Peptide Drug Discovery. *Nat. Rev. Drug Discov.* **2021**, *20* (4), 309–325. https://doi.org/10.1038/s41573-020-00135-8.

(70) Consortium, T. U.; Bateman, A.; Martin, M.-J.; Orchard, S.; Magrane, M.; Agivetova, R.; Ahmad, S.; Alpi, E.; Bowler-Barnett, E. H.; Britto, R.; Bursteinas, B.; Bye-A-Jee, H.; Coetzee, R.; Cukura, A.; Da Silva, A.; Denny, P.; Dogan, T.; Ebenezer, T.; Fan, J.; Castro, L. G.; Garmiri, P.; Georghiou, G.; Gonzales, L.; Hatton-Ellis, E.; Hussein, A.; Ignatchenko, A.; Insana, G.; Ishtiaq, R.; Jokinen, P.; Joshi, V.; Jyothi, D.; Lock, A.; Lopez, R.; Luciani, A.; Luo, J.; Lussi, Y.; MacDougall, A.; Madeira, F.; Mahmoudy, M.; Menchi, M.; Mishra, A.; Moulang, K.; Nightingale, A.; Oliveira, C. S.; Pundir, S.; Qi, G.; Raj, S.; Rice, D.; Lopez, M. R.; Saidi, R.; Sampson, J.; Sawford, T.; Speretta, E.; Turner, E.; Tyagi, N.; Vasudev, P.; Volynkin, V.; Warner, K.; Watkins, X.; Zaru, R.; Zellner, H.; Bridge, A.; Poux, S.; Redaschi, N.; Aimo, L.; Argoud-Puy, G.; Auchincloss, A.; Axelsen, K.; Bansal, P.; Baratin, D.; Blatter, M.-C.; Bolleman, J.; Boutet, E.; Breuza, L.; Casals-Casas, C.; de Castro, E.; Echioukh, K. C.; Coudert, E.; Cuche, B.; Doche, M.; Dornevil, D.; Estreicher, A.; Famiglietti, M. L.; Feuermann, M.; Gasteiger, E.; Gehant, S.; Gerritsen, V.; Gos, A.; Gruaz-Gumowski, N.; Hinz, U.; Hulo, C.; Hyka-Nouspikel, N.; Jungo, F.; Keller, G.; Kerhornou, A.; Lara, V.; Le Mercier, P.; Lieberherr, D.; Lombardot, T.; Martin, X.; Masson, P.; Morgat, A.; Neto, T. B.; Paesano, S.; Pedruzzi, I.; Pilbout, S.; Pourcel, L.; Pozzato, M.; Pruess, M.; Rivoire, C.; Sigrist, C.; Sonesson, K.; Stutz, A.; Sundaram, S.; Tognolli, M.; Verbregue, L.; Wu, C. H.; Arighi, C. N.; Arminski, L.; Chen, C.; Chen, Y.; Garavelli, J. S.; Huang, H.; Laiho, K.; McGarvey, P.; Natale, D. A.; Ross, K.; Vinayaka, C. R.; Wang, Q.; Wang, Y.; Yeh, L.-S.; Zhang, J.; Ruch, P.; Teodoro, D. UniProt: The

Universal Protein Knowledgebase in 2021. *Nucleic Acids Res.* **2021**, *49* (D1), D480–D489. https://doi.org/10.1093/NAR/GKAA1100.

(71) Seidler, P. M. Structural and Biochemical Studies of the Hsp90 Chaperone Proteins, State University of New York at Buffalo, 2014.

(72) Heckman, K. L.; Pease, L. R. Gene Splicing and Mutagenesis by PCR-Driven Overlap Extension. *Nat. Protoc.* **2007**, *2* (4), 924–932. https://doi.org/10.1038/nprot.2007.132.

(73) Krotee, P.; Griner, S. L.; Sawaya, M. R.; Cascio, D.; Rodriguez, J. A.; Shi, D.; Philipp, S.; Murray, K.; Saelices, L.; Lee, J.; Seidler, P.; Glabe, C. G.; Jiang, L.; Gonen, T.; Eisenberg, D. S. Common Fibrillar Spines of Amyloid-β and Human Islet Amyloid Polypeptide Revealed by Microelectron Diffraction and Structure-Based Inhibitors. *J. Biol. Chem.* **2018**, *293* (8), 2888–2902. https://doi.org/10.1074/jbc.M117.806109.

(74) Saff, E. B.; Kuijlaars, A. B. J. J. Distributing Many Points on a Sphere. *Math. Intell.* **1997**, *19* (1), 5–11. https://doi.org/10.1007/BF03024331.

(75) Lawrence, M. C.; Colman, P. M. Shape Complementarity at Protein/Protein Interfaces. *J. Mol. Biol.* **1993**, *234* (4), 946–950. https://doi.org/10.1006/jmbi.1993.1648.

(76) Winn, M. D.; Ballard, C. C.; Cowtan, K. D.; Dodson, E. J.; Emsley, P.; Evans, P. R.; Keegan, R. M.; Krissinel, E. B.; Leslie, A. G. W.; McCoy, A.; McNicholas, S. J.; Murshudov, G. N.; Pannu, N. S.; Potterton, E. A.; Powell, H. R.; Read, R. J.; Vagin, A.; Wilson, K. S. Overview of the *CCP* 4 Suite and Current Developments. *Acta Crystallogr. Sect. D Biol. Crystallogr.* **2011**, *67* (4), 235–242. https://doi.org/10.1107/S0907444910045749.

(77) The PyMOL Molecular Graphics System, Version 1.2r3pre, Schrödinger, LLC.

(78) Schindelin, J.; Arganda-Carreras, I.; Frise, E.; Kaynig, V.; Longair, M.; Pietzsch, T.; Preibisch, S.; Rueden, C.; Saalfeld, S.; Schmid, B.; Tinevez, J. Y.; White, D. J.; Hartenstein, V.; Eliceiri, K.; Tomancak, P.; Cardona, A. Fiji: An Open-Source Platform for Biological-Image Analysis. *Nat. Methods* **2012**, *9* (7), 676–682.

https://doi.org/10.1038/nmeth.2019.

(79) Schneider, C. A.; Rasband, W. S.; Eliceiri, K. W. NIH Image to ImageJ: 25 Years of Image Analysis. *Nat. Methods* **2012**, *9* (7), 671–675. https://doi.org/10.1038/nmeth.2089.

(80) Kabsch, W. XDS. *Acta Crystallogr. Sect. D Biol. Crystallogr.* **2010**, *66* (2), 125–132. https://doi.org/10.1107/S0907444909047337.

(81) McCoy, A. J.; Grosse-Kunstleve, R. W.; Adams, P. D.; Winn, M. D.; Storoni, L. C.; Read, R. J. Phaser Crystallographic Software. *J. Appl. Crystallogr.* **2007**, *40* (4), 658–674. https://doi.org/10.1107/S0021889807021206.

(82) Sheldrick, G. M. Experimental Phasing with SHELXC/D/E: Combining Chain Tracing with Density Modification. *Acta Crystallogr. Sect. D Biol. Crystallogr.* **2010**, *66* (4), 479–485. https://doi.org/10.1107/S0907444909038360.

(83) Murshudov, G. N.; Skubák, P.; Lebedev, A. A.; Pannu, N. S.; Steiner, R. A.; Nicholls, R. A.; Winn, M. D.; Long, F.; Vagin, A. A. REFMAC5 for the Refinement of Macromolecular Crystal Structures. *Acta Crystallogr. Sect. D Biol. Crystallogr.* **2011**, *67* (4), 355–367. https://doi.org/10.1107/S0907444911001314.

(84) Emsley, P.; Lohkamp, B.; Scott, W. G.; Cowtan, K. Features and Development of Coot. *Acta Crystallogr. Sect. D Biol. Crystallogr.* **2010**, *66* (4), 486–501. https://doi.org/10.1107/S0907444910007493.

(85) Garcia, G.; Sharma, A.; Ramaiah, A.; Sen, C.; Purkayastha, A.; Kohn, D. B.; Parcells, M. S.; Beck, S.; Kim, H.; Bakowski, M. A.; Kirkpatrick, M. G.; Riva, L.; Wolff, K. C.; Han, B.; Yuen, C.; Ulmert, D.; Purbey, P. K.; Scumpia, P.; Beutler, N.; Rogers, T. F.; Chatterjee, A. K.; Gabriel, G.; Bartenschlager, R.; Gomperts, B.; Svendsen, C. N.; Betz, U. A. K.; Damoiseaux, R. D.; Arumugaswami, V. Antiviral Drug Screen Identifies DNA-Damage Response Inhibitor as Potent Blocker of SARS-CoV-2 Replication. *Cell Rep.* **2021**, *35* (1), 108940. https://doi.org/10.1016/J.CELREP.2021.108940.

CHAPTER 3

Structure based inhibitors of Amyloid Beta core suggest a common interface with Tau

Sarah L. Griner[1], Paul Seidler[1], Jeannette Bowler[1], Kevin A. Murray[1], Tianxiao Peter Yang[1] Shruti Sahay[1], Michael R. Sawaya[1], Duilio Cascio[1], Jose A. Rodriguez[1], Stephan Philipp[3], Justyna Sosna[3], Charles G. Glabe[3,4], Tamir Gonen[2], David S. Eisenberg[1]

[1]Howard Hughes Medical Institute, UCLA-DOE Institute, Departments of Biological Chemistry and Chemistry & Biochemistry, Molecular Biology Institute, University of California, Los Angeles, California, USA

[2]Howard Hughes Medical Institute, Janelia Research Campus, 19700 Helix Drive, Ashburn, Virginia 20147, USA. Present address: Department of Physiology, David Geffen School of Medicine, University of California, Los Angeles, California 90095

[3]Department of Molecular Biology and Biochemistry, University of California, Irvine, California, USA [4]Biochemistry Department, Faculty of Science and Experimental Biochemistry Unit, King Fahd Medical Research Center, King Abdulaziz University, Jeddah, Saudi Arabia

*To whom correspondence should be addressed: David S. Eisenberg, Howard Hughes Medical Institute, Los Angeles, CA 90095-1570, USA; fax: (310) 206-3914; email: david@mbi.ucla.edu

Running title: Inhibitors of Amyloid Beta and Tau

Keywords: amyloid, amyloid-β (Aβ), tau, inhibitor, electron diffraction, cross-seeding

Abstract

Alzheimer's disease (AD) pathology is characterized by plaques of amyloid beta (Aβ) and neurofibrillary tangles of tau. Aβ aggregation is thought to occur at early stages of the disease,

and ultimately gives way to the formation of tau tangles which track with cognitive decline. Here, we report the crystal structure of an Aβ core segment determined by MicroED and in it, note characteristics of both fibrillar and oligomeric structure. Using this structure, we designed peptide-based inhibitors that reduce Aβ aggregation and toxicity of already-aggregated species. Unexpectedly, we also found that these inhibitors reduce the efficiency of Aβ-mediated tau aggregation, and moreover reduce aggregation and self-seeding of tau fibrils. The ability of these inhibitors to interfere with both Aβ and tau seeds suggests these fibrils share a common epitope, and supports the hypothesis that cross-seeding is one mechanism by which amyloid is linked to tau aggregation and could promote cognitive decline.

Introduction

Although Alzheimer's disease (AD) is the most prevalent form of dementia, there are limited treatments to alleviate symptoms and none that halt its progression. Histological features of AD are extracellular senile plaques of amyloid beta (Aβ) and intracellular neurofibrillary tangles of tau (1, 2). While Aβ aggregation is thought to occur at the early stages of AD, tau aggregation correlates better to disease progression, with characteristic spreading along linked brain areas, and severity of symptoms correlating to the number of observed inclusions (3–8) . Structural information about the aggregated forms of Aβ and tau is accumulating, but to date this knowledge has not led to successful chemical interventions (9)

A link between the appearance of Aβ and tau pathologies has been noted in transgenic mouse models generated by crossing or co-expressing mutant Aβ and mutant tau, but the mechanism is not yet understood at the molecular level (10). By injecting Aβ seeds derived from synthetic peptide, transgenic mouse or AD patient tissue, tau pathology can be found both at the site of injection, and also in functionally connected brain areas (11–13). Tau aggregation has also been reported to follow Aβ seeding in 3D neuronal stem cell cultures that express early onset hereditary mutations to drive overproduction and aggregation of Aβ (14). In spite of these

observations, the molecular linkage of Aβ to tau remains unresolved. Proposed hypotheses include Aβ causing downstream cellular changes that trigger tau phosphorylation and eventual aggregation, and/or a direct interaction and seeding of tau by aggregated Aβ (15–17).

Several lines of evidence support the direct interaction model, although questions still remain; for example, how such an interaction could occur since Aβ plaques deposit extracellularly, while tau neurofibrillary tangles are intracellular. One possible model for intracellular aggregation could be that Aβ is cleaved from APP inside endosomes, and then exported (18). Another model proposes that smaller diffusible Aβ oligomers are the toxic species (19–21); indeed oligomers of Aβ isolated from AD serum are sufficient to induce tau aggregation (22). Aβ has also been found co-localize intra-neuronally with tau as well as at synaptic terminals, with increased interactions correlating with disease progression (5). Furthermore, soluble and insoluble complexes of Aβ bound to tau have been detected in AD tissue extracts (5, 23). *In vitro*, soluble complexes of Aβ and tau have been found to promote aggregation of tau(23), while another study found that Aβ fibrils can seed tau (24). Taking the evidence together, we hypothesize that cross-seeding of tau by Aβ promotes tangle formation in AD, which could be prevented not only by inhibiting Aβ aggregation, but also by disrupting the binding site of Aβ with tau.

A number of interaction sites have been proposed on both proteins. In Aβ, both the amyloid core KLVFFA, along with region spanning the carboxy terminal residues were found to bind tau (23). Conversely peptides from regions of tau in exons 7 and 9, well as aggregation prone sequences VQIINK and VQIVYK located at the beginning of repeat 2 (R2) and repeat 3 (R3) of the microtubule domain (K18), respectively, were found to bind Aβ (23). A computational seeding model predicts that the amyloid core of Aβ can form intermolecular β-sheet interactions with VQIINK or VQIVYK (25).

On this basis, we hypothesized that an inhibitor capable of targeting the amyloid core, which itself is an important sequence for Aβ aggregation (26–28), might block both Aβ

aggregation and tau seeding by Aβ. However, this segment has been observed in multiple conformations in steric zipper structures (29) and fiber models (30–34), impeding structure-based inhibitor design. In an effort to characterize a toxic conformation of this sequence, we focused our efforts on determining the structure of the segment 16-26, containing the Iowa early onset hereditary mutation, D23N (35). Based on this structure, we designed several inhibitors and found that they indeed blocked aggregation of Aβ, prevented cross-seeding of tau by Aβ, and surprisingly, also blocked tau homotypic seeding. We suggest that the efficacy of these structure-based inhibitors against both proteins, but not other amyloid fibrils, implies there is a similar binding interface displayed on both Aβ and tau aggregates, supporting the cross-amyloid cascade hypothesis in AD.

Results

Atomic structure of $A\beta_{16-26}$ D23N determined using MicroED

With crystals only a few hundred nanometers thick, we used micro-electron diffraction (MicroED) to determine the structure of Aβ residues 16-26 containing the hereditary mutation D23N, (Figure 1A), KLVFFAENVGS. The structure revealed pairs of anti-parallel β-sheets each composed of ~4000 strands, stacked into a fibril that spans the entire length of the crystal. Neighboring sheets are oriented face to back (Figure 1B, Table 1) defining a Class 7 steric zipper motif. In addition, the three C-terminal residues adopt an extended, non-β conformation which stabilizes the packing between steric zippers (Figure 1—Supplement 1). The sheet-sheet interface is strengthened by interdigitating side chains, Lys 16, Val18, Phe20, Glu22 from the face of one strand, and Leu17, Phe19, and the N-terminus from the back of the other. The zipper has an extensive interface with a high shape complementarity of 0.76 and a total buried solvent accessible surface area of 258 Å2.

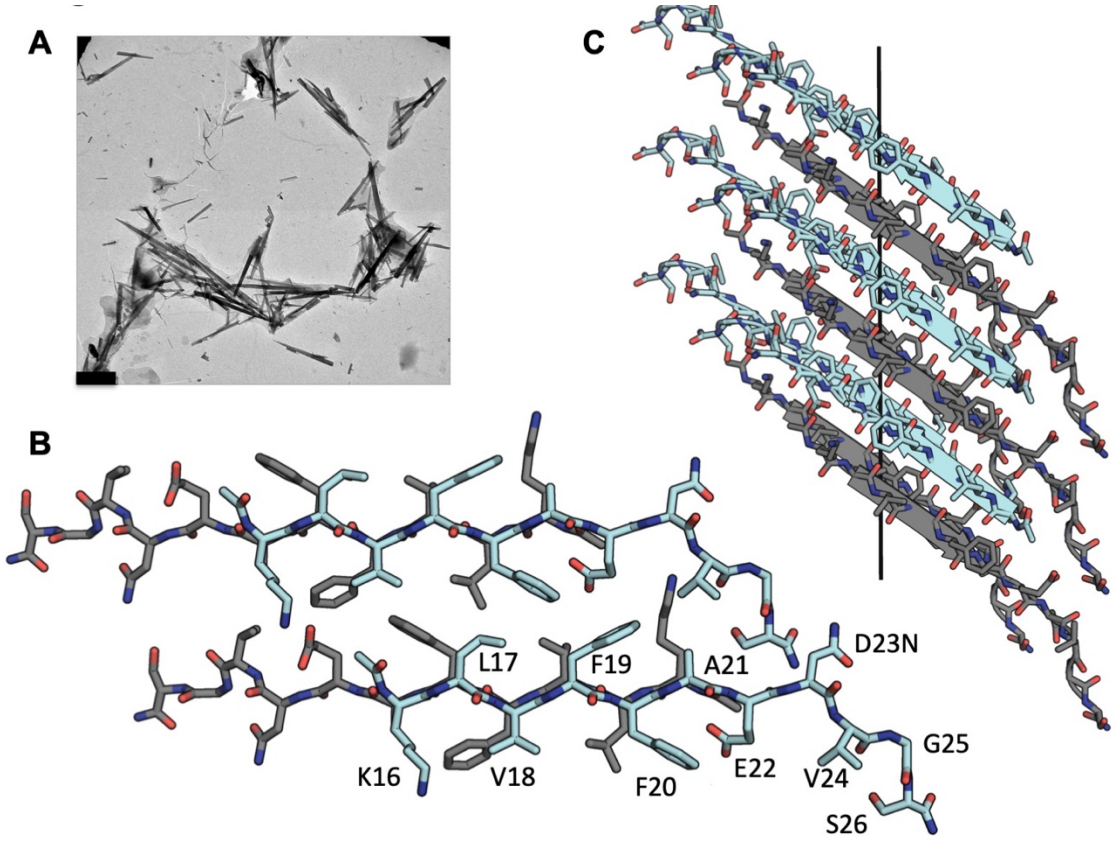

Figure 1. MicroED structure of segment Aβ 16-26 D23N from microcrystals. **A**. Electron micrograph of 3D crystals used for data collection, scale bar is 1μm. **B**. The crystal structure reveals tightly mated pairs of anti-parallel β-sheets with opposing sheets in grey and cyan. The side-chains interdigitate to form a dry interface. Two neighboring sheets are viewed perpendicular to the β-sheets. **C**. View of 6 layers perpendicular to the fibril axis (black line). The β-sheets stack out of register along the fibril axis.

Table 1. Statistics of MicroED data collection and atomic refinement.

	KLVFFAENVGS
Excitation Voltage (kV)	200
Electron Source	field emission gun
Wavelength (Å)	0.0251
Total dose per crystal (e^-/ Å^2)	2.7
Frame rate (frame/s)	0.3-0.5
Rotation rate (°/s)	0.3
#crystals used	13
Total angular rotation collected (°)	941
Merging Statistics	
Space group	$P2_1$
Cell dimensions	
a, *b*, *c* (Å)	11.67, 51.91, 12.76
α, β, γ (°)	90, 114.18, 90
Resolution (Å)	11.64-1.4 (1.44-1.40)*
R_{merge}	24.0% (65.2%)
No. Reflections	47,598 (1966)
Unique Reflections	2355 (163)
Completeness (%)	86.2% (78.0%)
Multiplicity	21 (12)
I/σ	9.06 (2.88)
$CC_{1/2}$	99.5% (69.7%)
Refinement Statistics	
No. reflections	2354
Reflections in test set	236
R_{work}	23.7%
R_{free}	28.3%
R.m.s. deviations	
Bond lengths (Å)	0.014
Bond angles (°)	1.5
Avg. B factor (Å^2)	9.46
Wilson B factor (Å^2)	7.2
Ramachandran (%)	
Favored	100%
Allowed	0%
Outliers	0

*Highest resolution shell shown in parenthesis.

This structure is partly identical to that of a shorter peptide segment, Aβ16-21, KLVFFA (crystal form-I) (29), which we used successfully as a search model for molecular replacement. Both the longer and shorter segments have class 7 symmetry. However, the two segments differ in registry. The shorter segment maintains an in-register hydrogen bonding pattern while the longer segment is out-of-register. That is, the strands of Aβ16-26 are tilted away from perpendicular to the fibril axis—a departure from canonical cross-β architecture. This elongated beta strand from residues 16-22 has also been observed in the full length *in vitro* fibrillar structure determined by cryoEM (Figure 1—Supplement 2) (81).

The antiparallel architecture and lack of registration of Aβ16-26 suggest this crystalline "fibrillar"-like assembly has some characteristics of an amyloid oligomer. Structural studies of amyloid oligomers most frequently reveal anti-parallel β sheet architecture (36–38), whereas fibril structures have revealed parallel β sheets (30, 31, 34, 39), with the exception of some short segments of Aβ (40) and in $A\beta_{1-40}$ containing the early onset hereditary mutation D23N which leads to in-register anti-parallel fiber deposition in plaques (32, 41). The out-of-register stacking of anti-parallel β strands has been proposed to be the defining trait of toxic oligomers (37, 42). The segment Aβ16-22 has been proposed to be able to form such oligomers in silica (43). The structures of Aβ16-21, Aβ16-26, and the full length fibrils may offer clues to designing inhibitors that impede both fibrillar and oligomeric assemblies.

Efficacy of inhibitors of Aβ aggregation designed against Aβ 16-26 D23N

As the zipper motif observed in the atomic structure of $A\beta_{16-26}$ D23N may be relevant to a variety of amyloid beta assemblies, we sought to use it to develop structure-based peptide inhibitors of $A\beta_{1-42}$. Our laboratory has developed a Rosetta based design strategy using steric zipper structures to design capping peptide inhibitors for a number of amyloid proteins implicated in disease (44–48). We chose to truncate our structure to residues 16-22 for the search model, omitting the residues not in the β strand. We threaded amino acids onto a

capping β strand and minimized energies of sidechains. From our first round of design we chose 6 distinct inhibitor candidates; those that were identified as good candidates but containing strong amino acid similarities to other top inhibitors were discarded. Our initial pool of inhibitors contained four L-form peptides, 2 each of 6 and 8 amino acids length, termed L1-L4, and two D-peptides 6 amino acids long, termed D1 and D2.

We assessed the efficacy of the inhibitors at a 10 molar excess by testing if they prevented $A\beta_{1-42}$ toxicity on Neuro-2a (N2a) cells, a mouse neuroblastoma cell line, (49). We measured cytotoxicity using 3-(4,5-dimethylthiazol-2-yl)-2,5-diphenyltetrazolium bromide (MTT) dye reduction (50, 51). Our toxicity assay revealed one inhibitor, D1 with the sequence (D)-LYIWVQ, that was able to eliminate the toxic effect of $A\beta_{1-42}$ (Figure 2A, Table S1); none of the inhibitors were toxic to N2a cells alone (Figure 2—Supplement 1A). In our molecular model of the inhibitor, smaller hydrophobic residues of D1 mimic interactions with the fibril interface on one side of the peptide, which promotes recognition, (Figure 2B), while the other side of the peptide positions large aromatic residues between Aβ residues, blocking possible further interactions (Figure 2C).

We focused on these key features of the inhibitor sequence for our second round of design and aimed to improve efficacy. We lengthened our peptides to extend over more of our available structure towards the carboxy-terminus and made conservative residue changes to the face containing smaller hydrophobic residues. We selected and tested 6 new designs. Of the six, four were eight amino acids long such that the inhibitor would extend over more of our crystal structure, which we called D1a-D1d. The additional two, termed D1e and D1f, were six amino acids long featuring slight sequence perturbations from D1 (Table S1- source data). We identified 2 of the 8 amino acid long inhibitors, D1b and D1d, that were also effective at reducing AB_{1-42} toxicity at both a tenfold excess and at an equimolar ratio (Figure 2—Supplement 1B, C). We then tested these two inhibitors, as well as D1, across a range of concentrations with final concentrations ranging from 100 nM to 10 μM (Figure 2D, E). We found that all inhibitors

elicited a dose dependent response, with all having an estimated IC_{50} of less than 1uM. The 6 residue long inhibitors, D1e and D1g, also had a similar effect on toxicity reduction as D1, however they did not perform as well as D1 in additional characterization and were not explored further (Figure 3—Supplement 1B). The cognate negative peptide control, LC, the L-form peptide of inhibitor D1, did not reduce toxicity (Figure 2E).

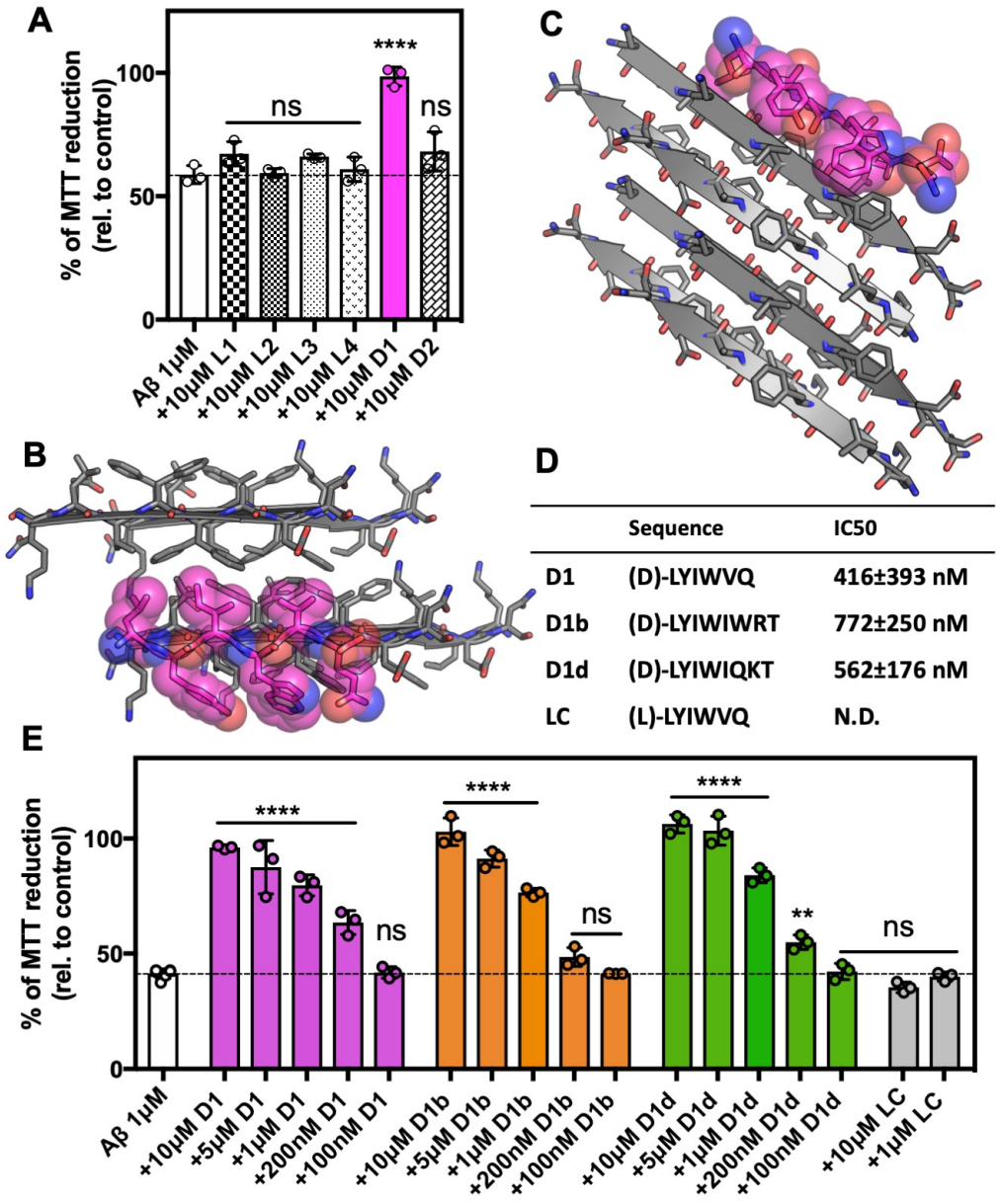

Figure 2. Development of inhibitors of Aβ fibril formation using structure-based design against Aβ 16-26 D23N **A**. Identification of Aβ1-42 inhibitor. 10 μM Aβ1-42 was incubated alone or with

100 μM of each candidate peptide inhibitor for 12 hours at 37 °C and then diluted 1:10 with pre-plated N2a cells. Cytotoxicity was quantified using MTT dye reduction Bars represent mean with individual technical replicates, error bars display one standard deviation (n = 3; ns = not significant; ****, $p < 0.0001$ using an ordinary one-way ANOVA- Dunnett's relative to leftmost column) **B, C.** Segment KLVFFAEN, derived from the Aβ 16-26 D23N crystal structure, was used as the design target. Model of peptide inhibitor D1(magenta) bound to the design target, KLVFFAEN (gray). Smaller hydrophobic residues of D1 mimic interactions with the fibril interface on one side of the peptide (**B)**, whereas the other side of the peptide positions large aromatic residues between Aβ residues, breaking possible further interactions (**C**). **D.** Overview of peptide inhibitors in D and L amino acid conformations, as indicated, used in this study and their sequences. Peptide LC is the L-form cognate peptide of D-form peptide D1 and is the negative control for peptide inhibitor D1 and its derivatives D1b and D1d. IC_{50} values were determined using 4 parameter nonlinear fit for half maximal inhibition. N.D., not determined. **E.** Peptide inhibitors D1, D1b, and D1d reduce the cytotoxicity of Aβ1-42 in a dose dependent manner, whereas control peptide LC does not. 10 μM Aβ1-42 was incubated alone or with various concentrations of each peptide inhibitor for 12 hours at 37 °C and then diluted 1:10 with pre-plated N2a cells. Cytotoxicity was quantified using MTT dye reduction. Bars represent mean with individual technical replicates, error bars display one standard deviation (n = 3-6; ns = not significant; **, $p < 0.002$; ****, $p < 0.0001$ using an ordinary one-way ANOVA Dunnett's relative to leftmost column).

Reduction of toxicity by designed inhibitors is explained by a reduction of $A\beta_{1-42}$ aggregation

We next sought to understand the mechanism by which our peptide inhibitors reduce the toxic effect of $A\beta_{1-42}$. We therefore assayed fibril formation to discern if this reduction of toxicity could be explained by reduced aggregation. We incubated $A\beta_{1-42}$ with our inhibitors at 10:1, 1:1, and 1:10 molar ratios and monitored fibril formation by thioflavin-T (ThT) fluorescence at 37 °C under quiescent conditions. We observe that all of our inhibitors reduce fibril formation in a dose dependent manner, while the negative control peptide, LC, does not (Figure 3A, Figure 3—Supplement 1A). The longer inhibitors, D1b and D1d, appear effective at an equimolar ratio. However, when assayed at higher concentrations, the inhibitors appear to self-assemble, but remain effective at reducing $A\beta_{1-42}$ toxicity (Figure 3—Supplement 1C, Figure 2E). After 72 hours, samples were taken for negative-stain TEM analysis, which confirmed the reduced abundance of Aβ1-42 fibrils. D1b and D1d were more effective at reducing fibril formation than D1, although all three inhibitors showed near equal efficiency in reducing toxicity. Fibrils were observed in the equimolar ratio sample of $A\beta_{1-42}$ with D1, whereas the comparable samples with D1b and D1d did not contain fibrils. Inhibitors that were not efficient at preventing toxicity, such as D1a and D1c, were also less effective at blocking fiber formation (Figure 2—Supplement 1C, Figure 3—Supplement 1A).

Since oligomers, and not fibrils, are considered to be the more toxic species of Aβ (19–22), we then investigated if our inhibitors affect the formation of oligomers or other cytotoxic $A\beta_{1-42}$ species. We used conformational antibodies to probe samples of $A\beta_{1-42}$ incubated with a 10-molar excess of inhibitor overnight at 37°C. Binding by oligomer specific conformational antibody A11 and A11-O9, a monoclonal variant of A11, was reduced by all of our inhibitors (Figure 3C, Figure 3—Supplement 1C, Figure 3—Supplement 2). While we have not determined the exact oligomeric assemblies the inhibitors are reducing, our antibody binding data coupled with the results of our toxicity assays suggest that the formation of a toxic oligomeric assembly is

decreased. Additionally, the inhibitors reduced the abundance of Aβ conformations recognized by antibodies mOC24, mOC64, mOC104, and mOC116. These antibodies bind fibrillar plaques from patient derived AD tissue and/or 3xTg-AD mouse tissue (52). Overall, these results indicate that our inhibitors may reduce oligomers, as well as disease relevant fibrillar conformations.

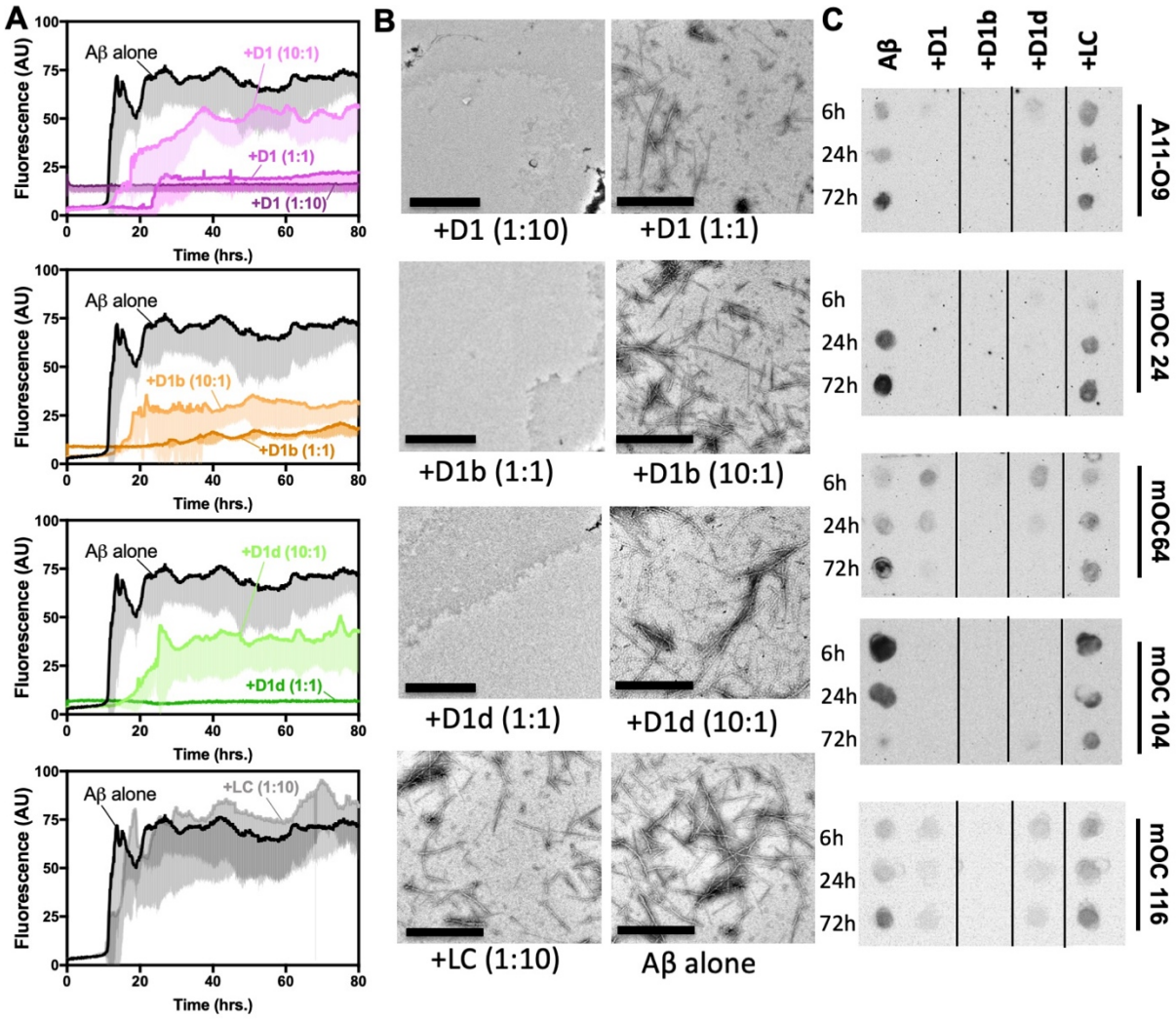

Figure 3. Designed inhibitors reduce aggregation of Aβ1-42 A. Peptide inhibitors D1, D1b, and D1d reduce fibril formation of Aβ1-42, while negative control peptide LC does not. 10 μM of Aβ1-42 was incubated alone or at a 1:10, 1:1, or 10:1 molar ratio to each inhibitor under quiescent conditions at 37 °C. Fibril formation was monitored using ThT fluorescence. Curves show the

average of three technical replicates with one standard deviation below. **B.** Negative-stain TEM analysis confirms the results of the ThT assays in Figure 3A. Samples were prepared as above and incubated for 72 hours before TEM analysis. Images of Aβ1-42 to D1 (1:10), D1b (1:1) and D1d (1:1) were captured at 3,200x; scale bars are 2μm. All other images were captured at 24,000x; scale bars are 500 nm. **C**. Peptide inhibitors reduce the formation of Aβ1-42 assemblies recognized by conformational monoclonal antibodies, while negative control peptides do not. 10 μM Aβ1-42 was incubated alone (left-most column) or with 10-fold molar excess of each peptide-based inhibitor. Aliquots of the reaction were tested for antibody-binding at 6 h, 24 h, and 72 h. Membranes were spliced as indicated for clarity.

Inhibitors bind and reduce toxicity of Aβ aggregates

As AD is only diagnosable long after Aβ aggregation has initiated, we wondered if these inhibitors would not only prevent amyloid aggregates from forming, but also if they can reduce the toxic effect of already formed aggregates. First, we incubated 10 μM Aβ at 37°C for 12hours to form oligomers (Figure 4—Supplement 1A), and then added inhibitors at various concentrations just prior to addition to N2a cells and assayed toxicity by MTT dye reduction. We found that adding the inhibitor to monomeric $A\beta_{1-42}$ prior to incubation had a marked difference from adding inhibitor to pre-formed $A\beta_{1-42}$ oligomers. When co-incubated with monomeric Aβ, the shorter D1 inhibitor was as effective as D1b and D1d at reducing toxicity; however, when added to pre-formed Aβ assemblies, only the longer inhibitors D1b and D1d were effective at reducing toxicity (Figure 4A). Both of the longer inhibitors could fully ameliorate toxicity of aggregates at 10 μM, but D1d is more potent, with effective reduction of toxicity to 1 μM. D1b differs from D1d only at amino acid positions 6 and 7. We suspect the difference in efficacy is conferred from residue 6, because both inhibitors contain positively charged residues at position

7, but at position 6 D1b contains a Gln while D1d has a much bulkier Trp. Our results indicate that while peptide inhibitors can both prevent aggregation initiation and block toxicity of aggregated assemblies, the latter appears to be more sensitive to slight perturbations in inhibitor composition.

We next performed TEM to determine if our inhibitors could disaggregate fibers, or if the fibers are being capped, as our inhibitor design would predict. We aggregated 10 μM $A\beta_{1-42}$ for 72 hours at 37°C under shaking conditions, then added inhibitors at 100 μM and incubated overnight. As the fibers are still present, we presume that our inhibitors are indeed capping or coating the fibers at toxicity inducing interfaces, thus preventing further seeding or toxic effects (Figure 4B). To investigate the capping ability of our inhibitors, we added the inhibitors to $A\beta_{1-42}$ during the exponential phase of fibril growth (Figure 4—Supplement 1B). We found that even at the lowest concentration of inhibitor, 10 μM Aβ: 1 μM inhibitor, we see minimal increase of signal for inhibitors D1b and D1d. Additionally, we observed a slight lowering of Tht signal samples with a 1:1 inhibitor addition, possibly due to inhibitors displacing ThT molecules bound to the fibrils. As the inhibitors do prevent monomer aggregation as well (Figure 3 A), we are cautious to overinterpret the result of this experiment, as the inhibitor could feasibly be sequestering free monomer or small assemblies from adding to the fibrils.

We performed SPR to verify that our inhibitors bind to fibers. We find that the most potent inhibitor of aggregated assemblies, D1d, binds to $A\beta_{1-42}$ fibrils with an apparent K_d of 52 μM (Figure 4C, Figure 4—Supplement 2). We used a one-inhibitor-to-one-protein substrate model to fit the data; however, the true K_d may be lower due to the complication of D1d self-interaction and polymorphic Aβ fibrils. Thus, we have shown that inhibitors D1b and D1d not only prevent aggregation of monomeric Aβ, but also bind aggregated states.

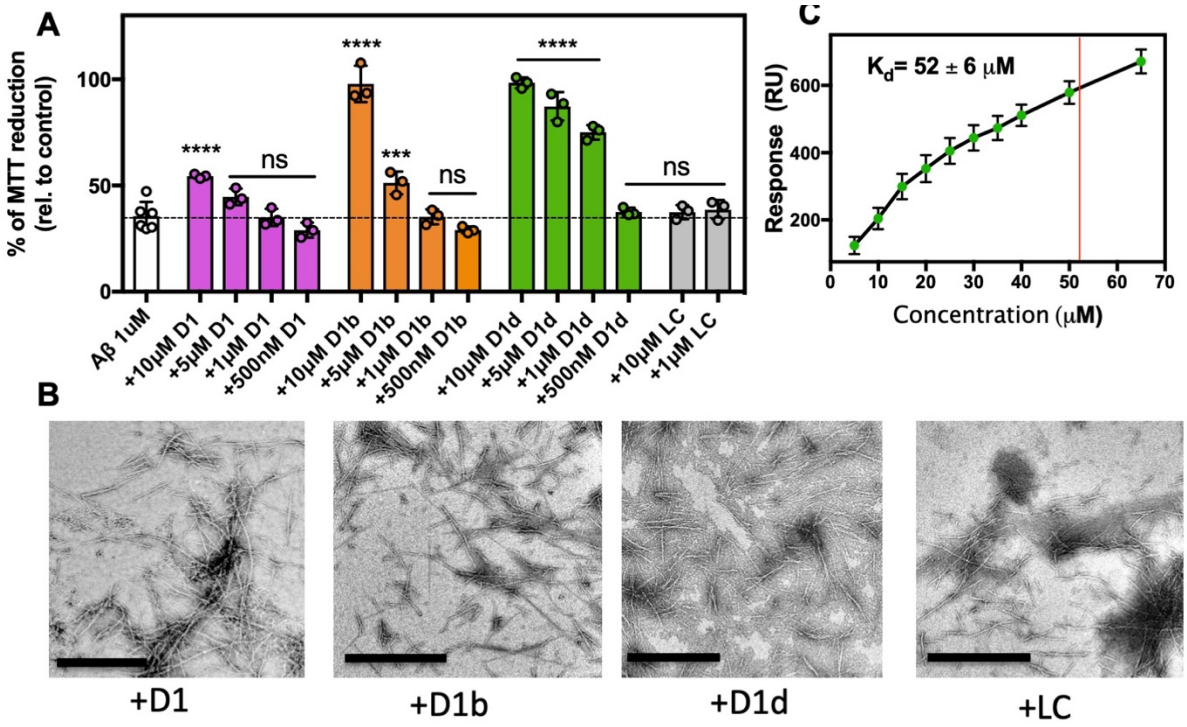

Figure 4. Inhibitors bind and block toxicity of aggregated Aβ1-42. **A.** The toxicity of already formed Aβ1-42 aggregates is lessened by peptide inhibitors. 10 μM Aβ1-42 was incubated alone for 12 hours at 37 °C. Indicated molar ratio of inhibitor was added to the incubated Aβ1-42 and then diluted 1:10 with pre-plated N2a cells. Cytotoxicity was quantified using MTT dye reduction. Bars represent mean with individual technical replicates (n = 3-6; ns = not significant; ***, $p < 0.0005$; ****, $p < 0.0001$ using an ordinary one-way ANOVA- Dunnett's relative to leftmost column). **B, C.** Inhibitors bind to Aβ1-42 fibrils. **B.** Peptide inhibitors do not disaggregate Aβ. 10 μM Aβ1-42 was incubated alone for 72 hours at 37 °. Peptide inhibitors were added at 10-fold molar excess and incubated at RT for 24 hours before TEM analysis. Images were captured at 24,000; scale bars are 500 nm. **C.** Binding isotherm of inhibitor D1d to fibrillar Aβ1-42. The maximal response (RU_{max}) was derived by fitting sensorgrams obtained over a range of D1d concentrations to the binding model with a K_d of 52 ± 6 μM, displayed as a red line. These RU_{max} values are plotted (mean ± SD, n = 3) as a function of concentration and fitted to a one to one binding model, displayed as a black line.

Inhibitors reduce seeding of tau by aggregated $A\beta_{1-42}$

Having demonstrated that our inhibitors block a toxic interface on Aβ, we next questioned if this interface could also be involved in cross seeding tau. First, we sought to validate the direct seeding mechanism that has been reported by others (23, 25, 53). We tested seeding of the microtubule binding domain of tau, K18+ (244-380) in a ThT assay at 37 °C under shaking conditions and found that fibrils of $A\beta_{1-42}$ and $A\beta_{16-26}$ D23N seeded aggregation, though not as efficiently as fibrils of K18 (Figure 5A, Figure 5—Supplement 1A). This seeding affect was also observed on full length tau in the presence of heparin (Figure 5—Supplement 1B). Conversely, K18 was unable to seed Aβ (Figure 5—Supplement 1C).

Next, we tested seeding in a well-established HEK293 biosensor cell line, tau-K18 (P301S) EYFP, which stably expresses the microtubule binding domain of tau P301S mutant. This cell line, referred to hereafter as tau-K18 biosensor cells, has been used to demonstrate prion like seeding from transfected tau fibrils to cells and has been used as a model system to test tau inhibitors (45, 54). We transfected biosensor cells with tau40 or Aβ fibrils (Figure 4—Figure Supplement 1A) to a final concentration of 250 nM. We found that Aβ was able to produce intracellular aggregates significantly greater than the vehicle alone, but only at around 2.5% efficiency of tau40. It is not altogether surprising that Aβ has such a low efficiency of cross-seeding; this mirrors a previous result in a similar system (24). It is possible that tau fibrils contain multiple polymorphs and interfaces capable of homotypic seeding, whereas Aβ may have a more limited number of tau seeding-competent conformations. Additionally, in vitro Aβ aggregation may create disproportionate ratios of assemblies compared to those present in AD. Regardless, it remains that some Aβ species is tau-seeding competent. The finding that Aβ is indeed able to seed aggregation in tau-K18 expressing cell lines suggests that the cross-interacting region of tau is located on this microtubule binding domain. We found other amyloid protein fibrils and non-fibrillar Aβ are not seeding-competent in this system (Figure 5—Supplement 1D), indicating the

biosensor cell assay can faithfully differentiate between fibrils of amyloid proteins, which differ in their underlying structures and sequences.

If our inhibitors block the interface responsible for seeding, we would expect Aβ treated with inhibitors to no longer to be seeds for tau. To test this hypothesis, we treated 250 nM Aβ fibers with indicated concentrations of inhibitor for 1 hour and transfected these into the biosensor cell line. All of our inhibitors were able to reduce seeding at 20 μM final concentration, while D1b showed a reduction in seeding at a concentration as low as1 μM (Figure 5DE). While both D1b and D1d reduced Aβ aggregate toxicity on N2a cells, D1d was the more effective inhibitor of Aβ toxicity, whereas D1b is the more effective inhibitor at reducing tau seeding.

We next sought to verify that the region of Aβ used to design inhibitors is important in seeding tau, and could be targeted by inhibitor D1b. We created two mutants of $A\beta_{1-42}$, with residues on either size of our steric zipper interface disrupted: $A\beta_{1-42}$ L17R/F19R and $A\beta_{1-42}$ K16A/V18A/E22A. We chose not to mutate residue Phe20, as it has been observed on both buried and solvent accessible interface in full length structures (30,31,81). We formed fibrils of each mutant construct and wild type, then incubated these fibrils with the indicated concentration of D1b, and used this to seed tau-K18 biosensor cells, as described previously (Figure 5—Supplement 2). We found that the fibrils of $A\beta_{1-42}$ L17R/F19R were able to seed similarly to WT $A\beta_{1-42}$, while no seeding was detected from $A\beta_{1-42}$ K16A/V18A/E22A. Seeding by $A\beta_{1-42}$ L17R/F19R was inhibited by D1b, suggesting that residues K16, V18 and E22 create the seeding interface which is targeted by inhibitor D1b.

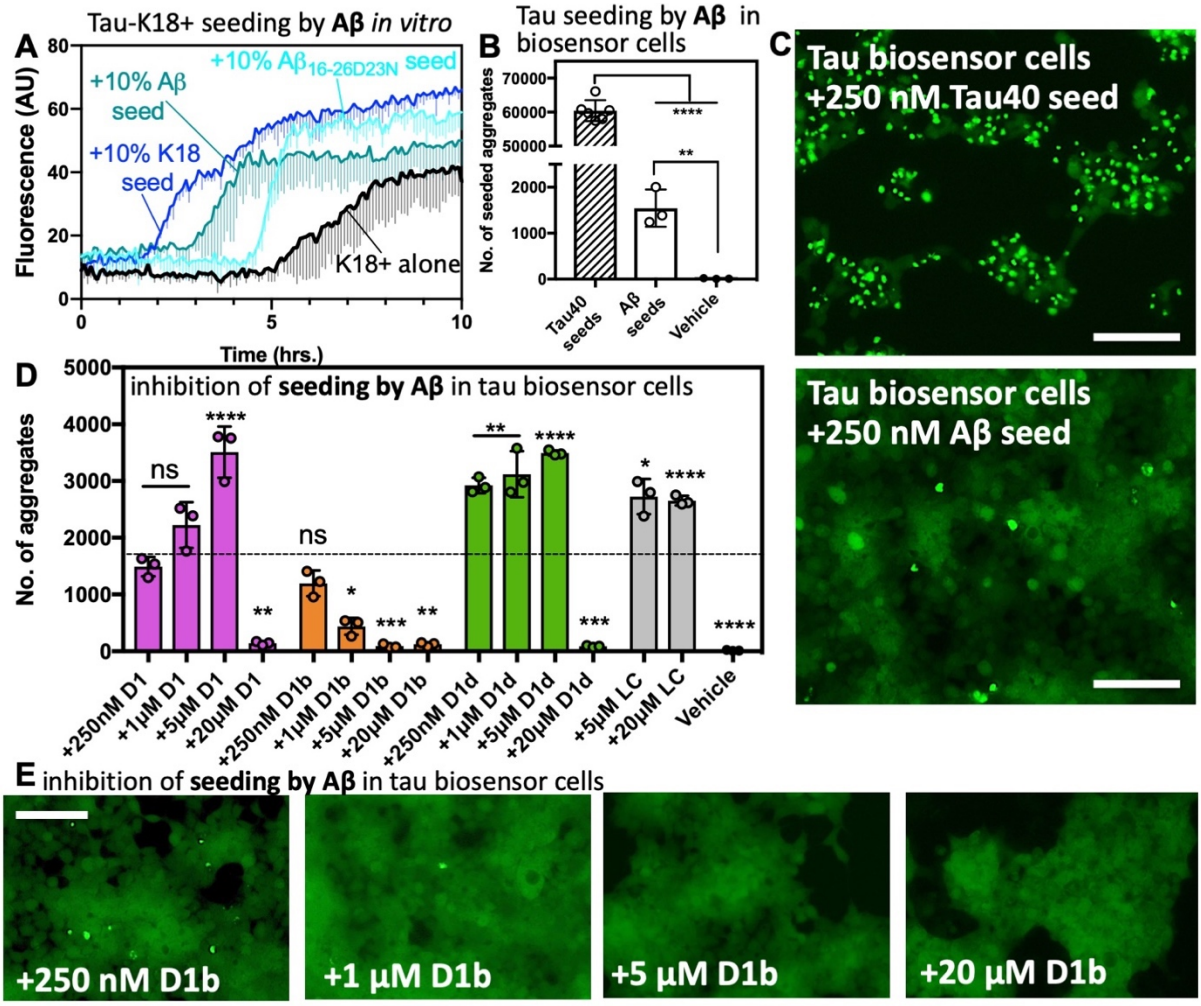

Figure 5. Tau aggregation is seeded by Aβ **and reduced by structure-based inhibitors.** **A.** 50 μM tau-K18+ was seeded with 10% monomer equivalent of pre-formed fibrils of Aβ1-42, $A\beta_{16\text{-}26}$ D23N or tau-K18 under shaking conditions at 700 RPM at 37 °C in PBS. Fibril formation was monitored using ThT fluorescence. Error bars below show the standard deviation of the average of three technical replicates. **B.** The number of intracellular aggregates present in tau-K18CY biosensor cells normalized to cell confluence seeded by the addition of 250 nM tau40 or 250 nM Aβ1-42 fibrils. Error bars show the standard deviation of the mean of technical replicates (n = 3; ****, p = 0.0001 using an ordinary one-way ANOVA- Dunnett's relative to leftmost column, and **, p= 0.0028 in unpaired t test of Aβ vs. vehicle) **C.** Representative images of seeded cells from B at 10x magnification, scale bar 100 μm. **D and E.**

Concentration dependent inhibition of Aβ1-42 induced seeding of tau aggregation in tau-K18CY biosensor cells. **D.** Average seeding by Aβ as a function of indicated inhibitor concentration. Error bars show the standard deviation of the mean of technical replicates (n = 3; ns = not significant; *, $p < 0.02$; **, $p < 0.005$; ***, $p < 0.001$; ****, $p < 0.0001$ using an ordinary one-way ANOVA- Dunnett's relative to leftmost column), and the dotted line shows the mean number of aggregates from untreated Aβ1-42 fibrils. **E.** Representative images of tau-K18CY biosensor cells showing the concentration dependent effect of D1b on seeding. Cells are shown at 10X magnification, scale bar 100 μm.

Inhibitors reduce tau aggregation and seeding

Our data support previous studies that suggest the tau binding surface on Aβ is localized to the segment whose structure we determined and targeted for design of inhibitors against Aβ aggregation and Aβ-mediated seeding of tau (23, 25). We hypothesized that the tau fibril could contain a similar self-complementary surface and would also be susceptible to treatment with our inhibitors. We first asked if the Aβ inhibitors, D1, D1b, and D1d could prevent monomeric tau from aggregating. We performed a ThT assay on 10 μM tau40, at 37 °C with shaking and 0.5 mg/mL heparin and found that all inhibitors function in a dose dependent manner similar to our results with Aβ monomer, while the control inhibitor LC does not reduce tau aggregation (Figure 6A, Figure 6—Supplement 1A). The peptide inhibitors are not able to block aggregation of the amyloid forming proteins hIAPP or alpha-synuclein, indicating that these inhibitors are specific for Aβ and tau, and are not general amyloid inhibitors (Figure 6—Supplement 1B).

Because we had observed differences in inhibitor efficacy on monomer versus aggregated species of Aβ, we next tested if the inhibitor was effective against the seeding ability of tau40 fibrils. We formed tau40 fibrils, treated them with indicated inhibitor concentration and transfected into tau-K18 biosensor cells to measure seeding inhibition. We found that similar to our Aβ-mediated tau biosensor seeding experiment, D1b was the best inhibitor, with an IC_{50} of 4.5 μM. D1 was slightly effective, while D1d showed seeding reduction only when increased to 75 μM (Figure 6B, C). It could be that D1b plays a dual role to inhibit both Aβ and tau, and this combined effect could explain the drastically reduced seeding from Aβ fibrils in our prior experiment (Figure 5D).

Next, we sought to determine potential binding sites on tau for D1b. We postulated that regions know to be drivers of tau aggregation could share structural features with the Aβ core, and thus be inhibited by D1b. We designed mutants of tau40 that disrupt key interactions in steric zipper interfaces determined from crystal structures of VQIINK(45) and VQIVYK (55), and cryoEM models of AD tau fibrils (56). In total we tested 6 different constructs, each

designed to block all but one aggregation interface of tau. The first 3 mutants were engineered to block the VQIVYK aggregation interfaces in addition to all but 1 of the 3 different known VQIINK interfaces. Mutant 1 (Q276W, L282R, I308P) leaves only interface A of VQIINK available for aggregation, mutant 2 (Q276W, I277M, I308P) leaves only interface B for aggregation, and mutant 3 (I277M, L282R, I308P) leaves only interface C accessible for aggregation. Constructs 4 and 5 were designed to test the effect of blocking VQIINK and all but 1 of the VQIVYK surfaces. Mutant 4 (Q276W, I277M, L282R, Q307W, V309W) leaves only the dry interface of VQIVYK available for aggregation and mutant 5 (Q276W, I277M, L282R, I308W) leaves only the solvent accessible surface for aggregation. In addition, we tested the effect of D1b on blocking seeding by 3R tau, which lacks the VQIINK aggregation segment and leaves the VQIVYK interface intact (Figure 6D, Figure 6—Supplement 2C-E).

To test if specific interfaces are inhibited by D1b, fibrils were formed from all of the different mutants, and then each was incubated with the indicated concentration of D1b and used to seed wild type tau-K18 biosensor cells, as described previously with wild type tau fibrils (Figure 6—Supplement 3A, B). We found that D1b was most effective at inhibiting seeding by fibrils of mutants that left intact: interface A of VQIINK which is thought to involve aggregation at site I277 of tau, the solvent accessible interface of VQIVYK as well as 3R (Figure 6D). D1b also showed moderate inhibition of several other tau mutants, but required high concentrations to inhibit seeding (Figure 6—Supplement 2C). As a control, we tested seeding by a mutant of tau40 that combined all of the different mutations, and found this mutant did not induce any seeding in tau-K18 biosensor cells (Figure 6—Supplement 1E), despite forming fibrils when incubated with heparin, indicating that at least one of the known interfaces is needed for seeding. Control inhibitor LC has little to no effect on seeding from any construct (Figure 6—Supplement 1F). Taken together, these data show that both the VQIINK and VQIVYK aggregation segments of tau are inhibited by D1b, and suggest that each may share common structural features with the Aβ core that could allow for cross-seeding of tau by Aβ.

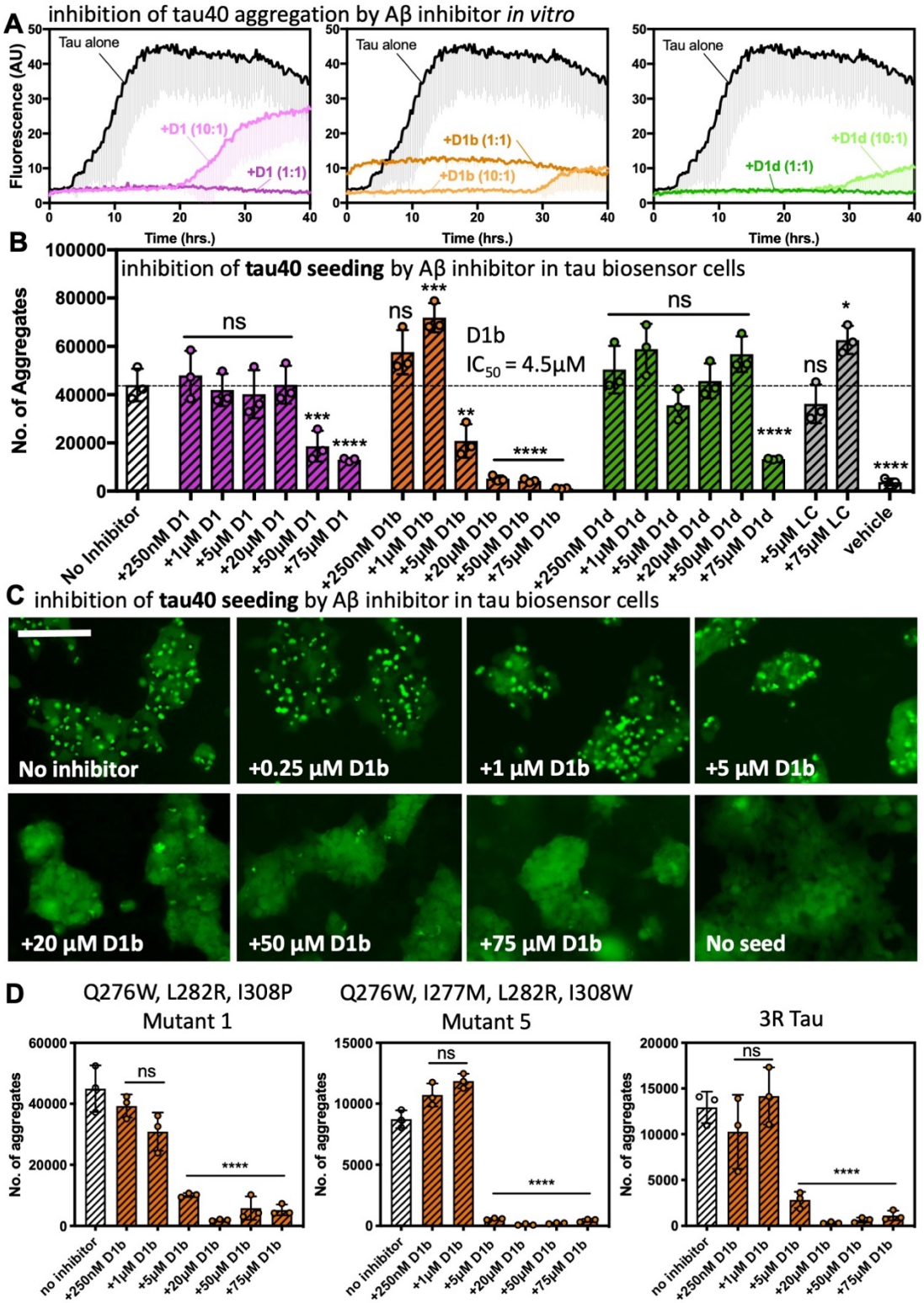
A
inhibition of tau40 aggregation by Aβ inhibitor *in vitro*
Fluorescence (AU)
Tau alone
+D1 (10:1)
+D1 (1:1)
+D1b (1:1)
+D1b (10:1)
+D1d (10:1)
+D1d (1:1)
Time (hrs.)
B
inhibition of **tau40 seeding** by Aβ inhibitor in tau biosensor cells
No. of Aggregates
D1b
IC50 = 4.5µM
ns
No Inhibitor
+250nM D1
+1µM D1
+5µM D1
+20µM D1
+50µM D1
+75µM D1
+250nM D1b
+1µM D1b
+5µM D1b
+20µM D1b
+50µM D1b
+75µM D1b
+250nM D1d
+1µM D1d
+5µM D1d
+20µM D1d
+50µM D1d
+75µM D1d
+5µM LC
+75µM LC
vehicle
C
inhibition of **tau40 seeding** by Aβ inhibitor in tau biosensor cells
No inhibitor
+0.25 µM D1b
+1 µM D1b
+5 µM D1b
+20 µM D1b
+50 µM D1b
+75 µM D1b
No seed
D
Q276W, L282R, I308P
Mutant 1
Q276W, I277M, L282R, I308W
Mutant 5
3R Tau
No. of aggregates
no inhibitor
+250nM D1b
+1µM D1b
+5µM D1b
+20µM D1b
+50µM D1b
+75µM D1b

Figure 6. Aβ inhibitors also reduce fibril formation and seeding by tau40. A. Peptide inhibitors D1, D1b, and D1d reduce fibril formation of tau40. 10 μM tau40 monomer was incubated at a 1:10, 1:1, or 10:1 molar ratio to each inhibitor with 0.5mg/ml heparin under shaking conditions at 700 RPM at 37 °C. Fibril formation was monitored using ThT fluorescence. Plots show the average of three technical replicates with one standard deviation below. **B**, **C**. The effects of the inhibitors on seeding by tau40 fibrils in tau-K18CY biosensor cells. The cells were seeded with 250 nM tau40 fiber (final concentration); in samples with inhibitor, tau40 fibers were incubated with indicated final concentrations of peptide inhibitor for one hour prior to addition to cells. **B.** Average number of aggregates at the indicated inhibitor concentrations, Bars represent mean with individual technical replicates, error bars display one standard deviation (n = 3; ns = not significant; *, $p < 0.03$; **, $p < 0.023$; ***, $p < 0.0008$; ****, $p < 0.0001$ using an ordinary one-way ANOVA- Dunnett's relative to leftmost column). dotted line represents number of aggregates from untreated tau40 fibrils. IC_{50} value was calculated from the dose–response plot of inhibitor D1b. **C**. Representative images of effect of D1b on seeding. Cells are shown at 10X magnification, scale bar 100 μm. **D.** Seeding from tau interface mutation fibrils in tau-K18CY biosensor cells is reduced by D1b. Experiment was performed as above. Average number of aggregates at the indicated inhibitor concentrations, Bars represent mean with individual technical replicates, error bars display one standard deviation (n = 3; ns = not significant; ****, $p < 0.0001$ using an ordinary one-way ANOVA- Dunnett's relative to leftmost column).

Designed inhibitor D1b targets disease relevant conformations

Amyloid polymorphs may differ depending on whether they were aggregated *in vitro* or extracted from human brain tissue (57). We sought to determine if our inhibitors are capable of blocking pathological forms of either tau, or Aβ. As suggested previously in our conformational antibody assay and structural alignment (Figure 3C), we hypothesized that our inhibitors would block disease-relevant amyloid polymorphs. Since we also found that our inhibitors blocked both homotypic and heterotypic tau seeding by aggregated tau and Aβ, we tested our inhibitor series on crude lysate from AD donor patient brain tissue.

We homogenized tissue from three different brain regions of a single AD patient brain, the hippocampal region, affected early as classified by Braak staging, and frontal and occipital lobe regions, which are affected later in disease progression (7,8). We also prepared samples from patient tissue with progressive supranuclear palsy (PSP), which is a tau aggregation disease that displayed no Aβ aggregation by immunostaining. We prepared samples from tissue of a non-diseased patient, as well as tau-immunodepleting PSP tissue. We transfected brain lysates into the biosensor cells; samples with inhibitor were treated with 10 μM D1, D1b, or D1d.

We found that treating the brain-derived lysates with D1b significantly reduced seeding by all tested brain tissue samples (Figure 7). The tau aggregate load from the different tissues has not been controlled, and this is likely the reason for different seeding efficiencies that are observed from different tissue types. Although our inhibitor D1b showed reduction of seeding in the hippocampal sample, the fibril load of this region may have been too great to have been efficiently halted by the dose used. Interestingly, the PSP tauopathy tissue was also responsive to treatment with each of the inhibitors, with D1b displaying the most pronounced inhibition. We surmise that D1b recognizes a common toxic epitope found in both Aβ, and in a variety of tau polymorphs.

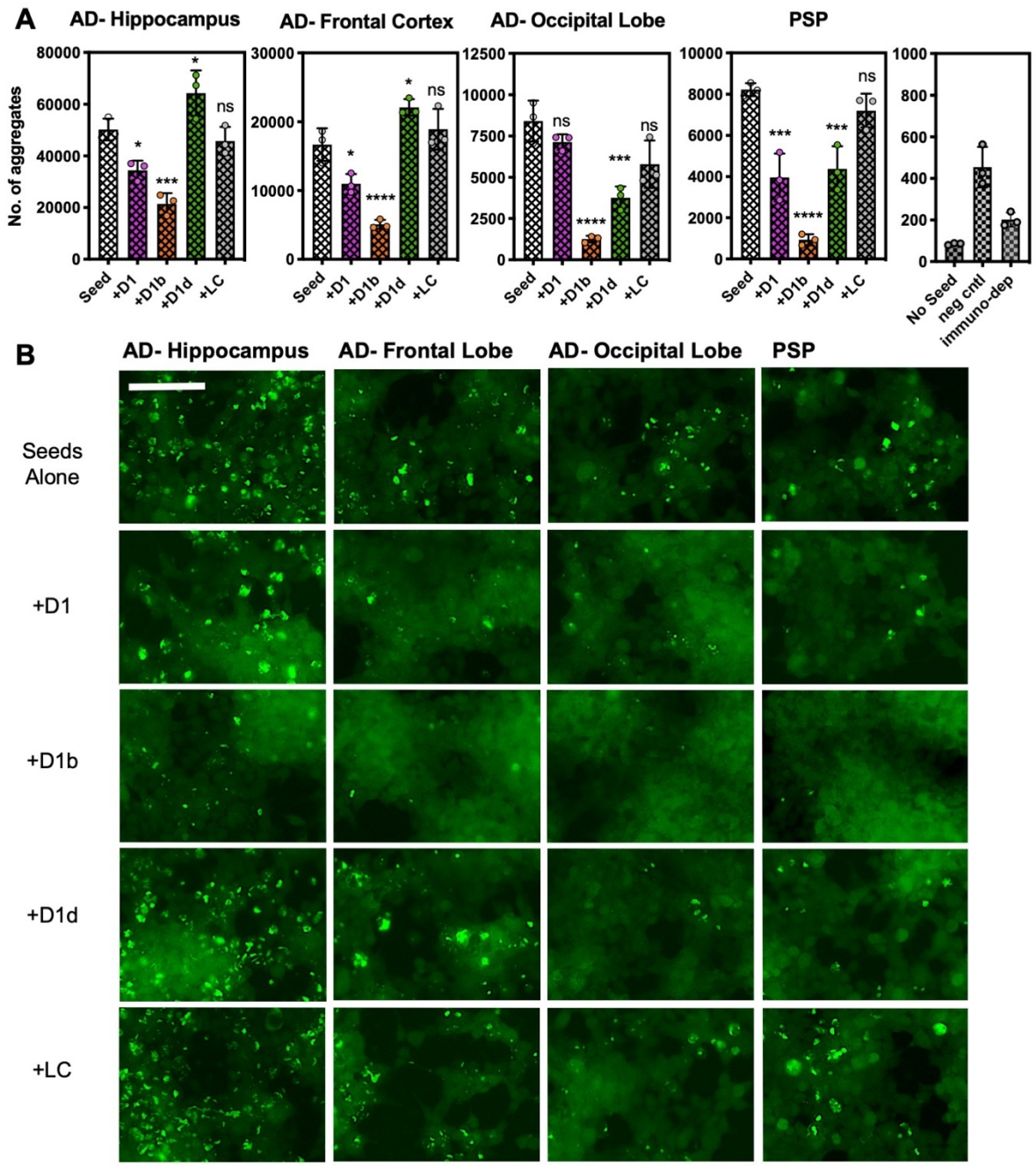

Figure 7. Peptide inhibitors reduce seeding by crude brain-extract from tauopathy donor tissue. Brain lysate was prepared in TBS buffer from 3 brain regions of one AD patient, and from a one sample of a PSP patient lacking Aβ plaques. Brain lysate from a non-disease patient (neg cntl) and a tau immunodepleted sample from PSP tissue are in right panel. Cells were seeded with a 1/400 dilution of brain tissue lysate; for samples with inhibitor, lysates were

incubated with inhibitor overnight prior to addition to cells. A concentration of 10 μM peptide was used for all of the experiments shown. **A.** The average number of aggregates seeded by lysate from each respective brain region, with or without addition of inhibitors. Bars represent mean with individual technical replicates (n = 3; ns = not significant; *, $p < 0.05$; ***, $p < 0.0005$; ****, $p < 0.0001$ using an ordinary one-way ANOVA- Dunnett's relative to leftmost column). **B**. Representative images of seeded biosensor cells from A shown at 10X magnification, scale bar 100 μm. Extended ANOVA data included as a supplementary file.

Discussion

The search for druggable targets in AD is muddied by the numerous proteins involved and incomplete understanding of whether or not the two histological protein hallmarks, Aβ and tau, interact directly with each other. On top of this, Aβ, the apparent initiator of the disease, aggregates into a wide variety of species, from soluble oligomers ranging from dimers to those that contain dozens of copies, to polymorphic fibril deposits. While there may be numerous toxic assemblies, targeting a specific sequence or structure of a toxic motif that is present in a variety of these assemblies could be an effective strategy for designing pharmaceuticals.

We targeted the amyloid core segment of Aβ due to its defined amyloidogenicity, and putative interaction with the late-stage aggregating protein, tau. We focused our efforts on the $A\beta_{16\text{-}26}$ segment with a hereditary mutation D23N, whose structure we determined by MicroED. Although the crystalline structure of this segment is fibril-like, and resembles a previously observed zipper interface as well as an interface in full length fibrils, the out-of-register interface

of the β-strands suggests that portions of this conformation may be present in a number of toxic oligomeric intermediates as well as in fibrils. We successfully used this structure to design a series of related inhibitors that reduce toxicity of Aβ in model N2a cells.

Our biochemical and toxicity studies indicate that these inhibitors function in two ways. The first is by preventing monomeric Aβ from aggregating. The second is by reducing toxicity of pre-formed oligomeric Aβ, possibly by binding to and blocking a surface that is responsible for conferring toxicity or seeding. While all of our designed inhibitors prevent monomeric Aβ from aggregating, only the longer D1b and D1d versions are effective at reducing toxicity of preformed assemblies. These two peptides were designed by extending the C-terminus. D1b and D1d could conceivably act by obscuring resides important for conferring toxicity, as supported by early onset hereditary mutations clustering at residues 21-23 (58–60).

Our data implicate an extended Aβ core in the spread of the disease, because targeting inhibitors to this region appears to block the templating interface needed to cross-seed tau. Aβ fibers treated with D1b showed a dramatic reduction of cross seeding in tau-K18 biosensor cells. Tau fibers treated with D1b showed similarly inhibited seeding in biosensor cells. The dual efficacy of the inhibitor D1b designed against the 16-23 region of Aβ suggests that these two pathological aggregates, Aβ and tau, share a common structural motif in AD. Indeed, we find that solvent accessible residues K16, V18, and E22 of Aβ are important for tau seeding. Conversely, by using mutant constructs of tau with only one available amyloid interface, we were able to determine two interfaces on tau where seeding was highly reduced by D1b. Both the R2 and R3 amyloid-prone regions of tau contain a D1b sensitive interface. Of note, the surface of R2 blocked by D1b contains residue I277, which previously has been shown to be critical for tau aggregation (61).

We find that overlaying our Aβ segment crystal structure with structures of tau R2 and R3 reveals a high degree of structural similarity both in the backbone, and also apparently in the complementarity of sidechains from each to intrinsically interdigitate (Figure 6—Supplement

3). Interestingly, Aβ overlays well with these regions of tau in both parallel and anti-parallel orientations, suggesting that either fiber or smaller oligomers could be capable of cross seeding on the ends of fibrils. Another mode of seeding could be facilitated along the side of the Aβ fibril using the solvent accessible interface from residues 16-22 (Figure 6—Supplement 4). While the modeled interface with tau is calculated to form with a favorable energy, burying of polar and charged residues (TauQ307/AβK16) could cause this interaction to be transient. Additionally, the differences in overall structure and stacking twists of the two fibrils could also explain why fibrils incorporating both proteins or fibril bundles containing both Aβ and tau fibrils are not observed. On this basis, we suggest that the amyloid core of Aβ and the regions VQIINK and VQIVYK can form similar structures in AD that are biochemically capable of cross-seeding.

Consistent with our finding that regions of Aβ and tau share structural similarities, we found that the Aβ inhibitor D1b is able to reduce seeding from brain homogenates, indicating that the inhibitor is recognizing a disease-related structural motif, while D1 and D1d are much less effective. It is curious that seeding by both AD and PSP is greatly reduced by the inhibitor D1b, as PSP pathology does not include Aβ aggregates. It is thought that different disease phenotypes, which display distinct fiber morphologies commonly referred to as strains, are determined by the formation of different steric zipper cores (62). Thus, PSP fibers may contain a different core than our in vitro aggregated tau or AD derived tau. However, our tau mutagenesis results suggest that inhibitor D1b can recognize at least 2 unique core interfaces, and thus could be able to act on multiple strains of tau fibers. There may exist other fibril polymorphs with different structural conformations which are not sensitive to D1b. Furthermore, it is unknown how different co-factors and post-translational modifications, such as tau phosphorylation, could affect the ability of Aβ to seed tau, and thus efficacy of D1b on tau seeding. Aβ cross-seeding may represent one of many possible stimuli of tau aggregation.

Similar to other peptide-based amyloid inhibitors, the effective dose to reduce toxicity of aggregated species is higher than to delay aggregation of monomeric species. This is emphasized by the differing efficacies of our related inhibitor series, where some inhibitors were able to prevent initial aggregation, but not toxicity or seeding from various assemblies. It appears that inhibitors to prevent an aggregation nucleus are much more promiscuous than those that ameliorate toxicity by binding to a distinct structure. This trend was observed in both Aβ and tau, suggesting a common inhibitory mechanism for both proteins, and highlights the need for multiple experimental measures to validate inhibitor efficacy.

In summary, our results suggest that a direct interaction between the Aβ core and the amyloid-prone regions of tau facilitates cross seeding. Our inhibitors designed for the Aβ core segment prevent cross seeding of tau, as well as tau homotypic seeding. The entwined nature of these two proteins in AD suggests it is necessary to control aggregation of both in order to treat the disease. Early detection is still crucial, but these data provide a platform on which further inhibitors can be designed for optimized inhibition of amyloid seeding in Alzheimer's disease.

Experimental Procedures

Recombinant Amyloid Beta Peptide purification- Aβ, and interface mutants, were purified as described in Krotee et. Al (48) After purification, the protein was lyophilized. Dried peptide powders were stored in desiccant jars at -20°C.

Peptide Preparation- Candidate inhibitors were custom made and purchased from Genscript (Piscataway, NJ). Lyophilized candidate inhibitors were dissolved at 10mM in 100% DMSO. 10mM stocks were diluted as necessary. All stocks were stored frozen at -20°C. Amyloid Beta was prepared by dissolving lyophilized peptide in 100% DMSO or 100mM NH_4OH. Next, the sample was spin-filtered and the concentration was assessed by BCA assay

(Thermo Scientific, Grand Island, NY). The DMSO or NH_4OH peptide stocks were diluted 100-fold in filter-sterilized Dulbecco's PBS (Cat. # 14200-075, Life Technologies, Carlsbad, CA).

Crystallization- 16-Ac-KLVFFAENVGS-NH_3-26 (Aβ 16-26 D23N) was dissolved at 4.5 mg/ml in 20% DMSO. Micro crystals were grown in batch in 0.2M magnesium formate, 0.1M Tris base pH 8.0, and 15% isopropanol at room temperature under quiescent conditions. Crystals grew within 4 days to a maximum of 2 weeks.

MicroED data collection- The procedures for MicroED data collection and processing largely follow published procedures (63, 64). Briefly, a 2-3 μl drop of crystals in suspension was deposited onto a Quantifoil holey-carbon EM grid then blotted and vitrified by plunging into liquid ethane using a Vitrobot Mark IV (FEI, Hillsboro, OR). Blotting times and forces were optimized to keep a desired concentration of crystals on the grid and to avoid damaging the crystals. Frozen grids were then either immediately transferred to liquid nitrogen for storage or placed into a Gatan 626 cryo-holder for imaging. Images and diffraction patterns were collected from crystals using FEI Tecnai 20 TEM with field emission gun (FEG) operating at 200 kV and fitted with a bottom mount TVIPS TemCam-F416 CMOS-based camera. Diffraction patterns were recorded by operating the detector in a video mode using electronic rolling shutter with 2 x 2 pixel binning (65). Exposure times for these images were either 2 or 3 seconds per frame. During each exposure, crystals were continuously unidirectionally rotated within the electron beam at a fixed rate of 0.3 degrees per second, corresponding to a fixed angular wedge of 0.6 or 0.9 degrees per frame.

Crystals that appeared visually undistorted produced the best diffraction. Datasets from individual crystals were merged to improve completeness and redundancy. Each crystal dataset spanned a wedge of reciprocal space ranging from 40-80°. We used a selected area aperture with an illuminating spot size of approximately 1 μm. The geometry detailed above equates to an electron dose rate of less than 0.01 $e^-/Å^2$ per second being deposited onto our crystals.

Measured diffraction images were converted from TIFF format into SMV crystallographic format, using publicly available software (available for download at **http://cryoem.janelia.org/downloads**).

We used XDS to index the diffraction images and XSCALE (66) for merging and scaling together datasets originating from thirteen different crystals.

Structure determination- We determined the structure of Aβ 16-26 D23N using molecular replacement. KLVFFA (pdb 2Y2A) led us to our atomic model. The solution was identified using Phaser (67). Subsequent rounds of model building and refinement were carried out using COOT and Phenix, respectively (68, 69). Electron scattering factors were used for refinement. Some reflections extended to 1.40 Å resolution. Calculations of the area buried and Sc were performed with AREAIMOL (70, 71)) and Sc (72–74), respectively.

Computational structure-based design- Computational designs were carried out using the RosettaDesign software as described previously (75). The atomic structure of the 16-KLVFFAENVGS-26 Aβ segment was used as a starting template for computational design. An extended L-peptide (or D-peptide, six to eight residues) was first placed at the end of the starting template of atomic structure. The design procedure then built side-chain rotamers of all residues onto the nine-residue peptide backbone placed at growing end of fibril. The optimal set of rotamers was identified as those that minimize an energy function containing a Lennard-Jones potential, an orientation-dependent hydrogen bond potential, a solvation term, amino acid-dependent reference energies, and a statistical torsional potential that depends on the backbone and side-chain dihedral angles. Area buried and shape complementarity calculations were performed with areaimol and Sc, respectively, from the CCP4 suite of crystallographic programs (70). The solubility of each peptide was evaluated by hydropathy index (76). The designed peptides were selected based on calculated binding energy of top or bottom binding mode, shape complementarity and peptide solubility. Each structural model of selected peptides went through human inspection using Pymol, where those peptides with sequence

redundancy and fewer binding interactions were omitted. Finally, select peptides were synthesized and tested experimentally.

Sample preparation for electron microscopy- Aβ1-42 was dissolved and diluted as previously described. Inhibitor stocks were prepared in 100% DMSO and were added such that the sample contained 10 μM monomeric Aβ1-42 the indicated ratio of inhibitor with final concentration of 1% DMSO. Samples were incubated for 72 hours at 37°C under quiescent conditions. Aβ1-42 fibrils were formed as described, and then treated with indicated ration of inhibitor for 24 hours at 37°C under quiescent conditions. Fibril abundance was checked using electron microscopy. Transmission electron microscopy-Samples were spotted onto non-holey grids and left for 160 to 180 seconds. Remaining liquid was wicked off and then left to dry before analyzing. Samples for negative-stain TEM were treated with 2% uranyl acetate after sample was wicked off the grid. After 1 minute, the uranyl acetate was wicked off. The grids were analyzed using a T12 Electron Microscope (FEI, Hillsboro, OR). Images were collected at 3,200 or 24,000x magnification and recorded using a Gatan 2kX2k CCD camera.

Thioflavin-T (ThT) kinetic assays- Thioflavin-T (ThT) assays were performed in black polystyrene 96-well plates (Nunc, Rochester, NY) or black polypropylene 96 well plates (Greiner Bio-One, Austria), as indicated, and sealed with UV optical tape. The total reaction volume was 150 μL per well. Aβ1-42 was prepared as described. Inhibitors were added at indicted concentrations, with a final concentration of 1%DMSO. ThT fluorescence was recorded with excitation and emission of 444 nm and 482 nm, respectively, using a Varioskan Flash (Thermo Fisher Scientific, Grand Island, NY). Experiments were performed at 37°C without shaking in triplicate and readings were recorded every 5 minutes. Seeding assay included 10% monomer equivalent of preformed fibrils, aggregated in LoBind polypropylene tubes, and sonicated for 10 minutes prior to addition. Inhibitor interruption assays were prepared as above in polypropylene plates. At approximal $T_{1/2}$, readings were paused and inhibitors were added as indicated, and plated were resealed with new UV optical tape.

ThT assays with tau40 were prepared as above with the following exceptions. 0.5mg/mL heparin (Sigma cat. no. H3393) was added to the reaction mixture and experiments were performed at 37°C with double orbital shaking at 700 rpm. ThT assays with K18+ were prepared as above with the following exceptions. Experiments were performed at 37°C with double orbital shaking at 700 rpm, in polypropylene plates. Seeding assays included 10% monomer equivalent of preformed fibrils, sonicated for 10 minutes prior to addition.

Cell culture- Neuro2a (N2a) cells (ATCC cat# CCL-131) were cultured in MEM media (Cat. # 11095-080, Life Technologies) plus 10% fetal bovine serum and 1% pen-strep (Life Technologies). Cells were cultured at 37°C in 5% CO2 incubator. Cells were authenticated by COX I gene analysis (Laragen), and mycoplasma negative by MycoAlert PLUS Detection Kit (Lonza, cat# LT07-701).

3-(4,5-dimethylthiazol-2-yl)-2,5-diphenyltetrazolium bromide (MTT) dye reduction assay for cell viability- N2a cells were plated at 5,000 cells per well in 90 µL of culture media, in clear 96-well plates (Cat. # 3596, Costar, Tewksbury, MA). Cells were allowed to adhere to the plate for 20-24 hours. Aβ1-42 samples were incubated at 10µM with or without inhibitors at varying ratios for 12 hours at 37°C and then applied to N2a cells. 10 µL of sample was added to cells. By doing this, samples were diluted 1/10 from in vitro stocks. Experiments were done in triplicate.

After a 24-hour incubation, 20 µL of Thiazolyl Blue Tetrazolium Bromide MTT dye (Sigma, St. Louis, MO) was added to each well and incubated for 3.5 hours at 37°C under sterile conditions. The MTT dye stock is 5 mg/mL in Dulbecco's PBS. Next, the plate was removed from the incubator and the MTT assay was stopped by carefully aspirating off the culture media and adding 100 µL of 100% DMSO to each well. Absorbance was measured at 570 nm using a SpectraMax M5. A background reading was recorded at 700 nm and subsequently subtracted from the 570 nm value. Cells treated with vehicle alone (PBS+0.1%DMSO) were designated at 100% viable and cells treated with 100% DMSO designated as 0% viable, and cell viability of all other treatments was

calculated accordingly. We employed one-way ANOVA as our statistical test for significance. Extended ANOVA data included as a supplementary file. IC_{50} values were estimated using a four-parameter non-linear fit dose-response curve in Graphpad Prism.

Dot Blot Assay- Aβ1-42 samples were incubated at 10 μM with or without inhibitors for 6, 24, and 72 hours at 37°C, and spotted onto a nitrocellulose membrane (Cat. # 162–0146, BioRad, Hercules, CA). 20μL was loaded for each condition; 2μL was spotted at a time and allowed to dry between application. The membranes were blotted as previously described (77), with the exception of the primary antibodies used. The antibodies used in the assay were previously generated and characterized (52). Blots were quantified with ImageJ.

Surface Plasmon Resonance (SPR)- SPR experiments were performed using BiacoreT200 instrument (GE Healthcare). Aβ42 fibrils/tau K18 fibrils were immobilized on a CM5 sensor chip. The fibrils of Aβ42 were prepared by placing a sample of 50 μM Aβ42 in PBS pH 7.4 in two wells of a Nunc 96-well optical bottom plate (Thermo Scientific), 150 μl/well and incubating the plate in a microplate reader (FLUOstar Omega, BMG Labtech) at 37 °C with double orbital shaking at 600 rpm overnight. Sample from the two wells were pooled together and Aβ42 fibrils were isolated from the incubation mixture by centrifuging it at 13,000 xG, 4°C for 45 minutes. The supernatant was removed and the pellet was re-dissolved in an equal volume of PBS as that of supernatant. The isolated fibrils were sonicated using a probe sonicator for 1-2 minutes at 18% amplitude with 2 sec on, 5 sec off pulses. The sonicated fibrils were filtered through a 0.22 μ filter to remove large aggregates. The sonicated and filtered fibrils were diluted to 60 μg/ml in 10 mM NaAc, pH 3 and then, immobilized immediately on a CM5 sensor chip using standard amine coupling chemistry. Briefly, the carboxyl groups on the sensor surface were activated by injecting 100 ul of 0.2 M EDC and 0.05 M NHS mixture over flow cells 1–2. The fibrils were then injected at a flow rate of 5 μl/min over flow cell 2 of the activated sensor surface for 900 seconds. The remaining activated groups in both the flow cells were blocked by injecting 120 μl of 1 M ethanolamine-HCl pH 8. 5.. For the binding assay each

peptide inhibitor was dissolved in 100 % DMSO at a concentration of 1 mM and diluted in PBS pH 7.4+1.2% DMSO to concentrations ranging from 5 μM to 260 μM. Each peptide was injected at a flow rate of 30 μl/min over both flow cells (1 and 2) at increasing concentrations (in running buffer, PBS, pH 7.4+1.2% DMSO) at 25°C. For each sample the contact time and dissociation time were 120 seconds and 160 seconds, respectively. 3 M NaCl was used as regeneration buffer. The data were processed and analyzed using Biacore T200 evaluation software 3.1. The data of flow cell 1 (blank control) was subtracted from the data of flow cell 2 (with immobilized fibrils/monomers). The equilibrium dissociation constant (Kd) was calculated by fitting the plot of steady-state peptide binding levels (Req) against peptide concentration (C) with 1:1 binding model (Eq 1).

Eq 1. $$Req = \frac{CR_{max}}{Kd + C} + RI$$

R_{max} = Analyte binding capacity of the surface
RI = Bulk refractive index contribution in the sample

Recombinant Tau purification- K18, K18+, Human Tau40 (residues 1-441) WT, 3R and mutants: interface A (Q276W, L282R, I308P), interface B (Q276W, I277M, I308P), interface C (I277M, L282R, I308P)interface 1 (Q276W, I277M, L282R, Q307W, V309W), interface 2 (Q276W, I277M, L282R, I308W), were expressed in pET28b with a C-terminal His-tag in BL21-Gold E. coli cells grown in TB to an OD600 = 0.8. Cells were induced with 0.5 mM IPTG for 3 hours at 37°C and lysed by sonication in 50 mM Tris (pH 8.0) with 500 mM NaCl, 20 mM imidazole, 1 mM beta-mercaptoethanol, and HALT protease inhibitor. Cells were lysed by sonication, clarified by centrifugation at 15,000 rpm for 15 minutes, and passed over a 5 ml HisTrap affinity column. The column was washed with lysis buffer and eluted over a gradient of imidazole from 20 to 300 mM. Fractions containing purified Tau40 were dialyzed into 50 mM MES buffer (pH 6.0) with 50 mM NaCl and 1 mM beta-mercaptoethanol and purified by cation exchange. Peak fractions were polished on a HiLoad 16/600 Superdex 200 pg in 1X PBS (pH 7.4), and concentrated to ~20-60 mg/ml by ultrafiltration using a 10 kDa cutoff.

Fibril incubation with inhibitors for tau biosensor cell-seeding assays. Aβ fibrils were prepared at 200 μM at 37°C for 72 hours before diluting to 50 μM in PBS buffer (pH 7.4) for seeding experiments. Tau40 WT and interface mutation fibrils were prepared by shaking 50 μM tau40 in PBS buffer (pH 7.4) with 0.5 mg/ml heparin (Sigma cat. no. H3393) and 1 mM dithiothreitol (DTT) for 3–6 days. Fibrillization was confirmed with an endpoint ThT reading, and fibrils were then diluted 20-fold to 1.25 μM in OptiMEM (Life Technologies, cat. no. 31985070). Inhibitors dissolved in DMSO were added to 20 μl of diluted fibrils at a concentration 20-fold greater than the final desired concentration. Fibrils were incubated for ~16 h with the inhibitor, and subsequently were sonicated in a Cup Horn water bath for 3 min before seeding the cells. The resulting 'pre-capped fibrils' were mixed with one volume of Lipofectamine 2000 (Life Technologies, cat. no. 11668027) prepared by diluting 1 μl of Lipofectamine in 19 μl of OptiMEM. After 20 min, 10 μl of fibrils were added to 90 μl of the tau-K18CY biosensor cells to achieve the final indicated ligand concentration. Cells were verified by STR profiling and confirmed mycoplasma negative (Laragen). Quantification of seeding was determined by imaging the entire well of a 96-well plate seeded in triplicate and imaged using a Celigo Image Cytometer (Nexcelom) in the YFP channel. Aggregates were counted using ImageJ (78) by subtracting the background fluorescence from unseeded cells and then counting the number of peaks with fluorescence above background using the built-in Particle Analyzer. We employed one-way ANOVA as our statistical test for significance. Extended ANOVA data included as a supplementary file. Dose-response curves were constructed for inhibitor peptides exhibiting concentration dependence by fitting to a nonlinear regression model in Graphpad Prism. High resolution images were acquired using a ZEISS Axio Observer D1 fluorescence microscope.

Preparation of Brain lysate. Human brain tissue was obtained from the Neuropathology Laboratory at UCLA Medical Center. AD and PSP cases were confirmed by the Neuropathology Laboratory by immunostaining autopsied brain tissue sections, and the PSP donor was

confirmed to be free of amyloid immunoreactivity. Tissue sections from the indicated brain regions were manually homogenized using a disposable ultra-tissue grinder (Thermo Fisher) in TBS (pH 7.4) supplemented with 1X HALT protease inhibitor. Homogenized tissue was aliquoted to several PCR tubes and prepared for seeding in biosensor cells by sonication as described by Kaufman et al. (79), except tissue sections were sonicated twice as long, for a total of 2 h, in an ice cooled circulating water bath with individual sample tubes stirring to ensure each tube received the same sonication energy. Subsequently, seeding was measured by transfection into biosensor cells and quantified as described above. We employed one-way ANOVA as our statistical test for significance. Extended ANOVA data included as a supplementary file.

Immunodepletion of Brain lysate- Lysate was prepared as above. 2ug (0.2µL at 11µg/uL) Tau antibody (Dako A0024) was conjugated to 0.75mg ProteinG Dynabeads (25µL of 30mg/mL). Antibody was mixed with beads and nutated for 10 min, washed with 200µL Citrate-phosphate wash buffer pH 5.0, and then resuspended in a minimal volume of was buffer. 200 µL of brain lysate diluted 1/20 in OptiMEM was added to antibody-bead suspension and Nutated for 30 min. Supernatant was removed and used for transfection into biosensor cells, as previously described.

Aggregation Inhibition Assay with α-synuclein- α-synuclein was expressed and purified as described previously in Rodriguez, *et al.* with the following exceptions to the expression protocol. An overnight starter culture was grown in 15 mL instead of 100 mL, 7 mL of which was used to inoculate 1 L. After induction, cells were allowed to grown for 3-4 hours at 34 °C (instead of 4-6 hours at 30 °C). Cells were then harvested by centrifuging at 5,000 x g.

ThT assays with α-synuclein were performed in black 96-well plates (Nunc, Rochester, NY) sealed with UV optical tape. The total reaction volume was 180 µL per well. ThT fluorescence was recorded with excitation and emission of 444 nm and 482 nm, respectively, using a Varioskan Flash (Thermo Fisher Scientific, Grand Island, NY). Experiments were

performed at 37°C, shaking at 600 rpm with a teflon bead, in triplicate and readings were recorded every 15 minutes. Alpha synuclein at 105 μM in PBS was diluted to a final concentration of 50 μM in 25 μM Thioflavin-T and PBS. Inhibitors were added at the specified concentration by diluting 10 mM stocks in 100% DMSO 1 to 40 in the same manner. Thus, inhibitors were tested at 5:1 molar excess of α-synuclein.

Aggregation Inhibition Assay with IAPP- Human IAPP1-37NH_2 (hIAPP) was purchased for Innopep (San Diego, CA). Peptides were prepared by dissolving lyophilized peptide in 100% 1,1,1,3,3,3-Hexafluoro-2-propanol (HFIP) at 250μM for 2 hours. Next, the sample was spin-filtered and then HFIP was removed with a CentriVap Concentrator (Labconco, Kansas City, MO). After removal of the HFIP, the peptide was dissolved at 1mM or 10mM in 100% DMSO (IAPP alone) or 100% DMSO solutions containing 1mM or 10mM inhibitor. The DMSO peptide stocks were diluted 100-fold in filter-sterilized Dulbecco's PBS (Cat. # 14200-075, Life Technologies, Carlsbad, CA). Thioflavin-T (ThT) assays with hIAPP were performed in black 96-well plates (Nunc, Rochester, NY) sealed with UV optical tape. hIAPP1-37NH_2 and mIAPP1-37NH_2 were prepared as described. The total reaction volume was 150 μL per well. ThT fluorescence was recorded with excitation and emission of 444 nm and 482 nm, respectively, using a Varioskan Flash (Thermo Fisher Scientific, Grand Island, NY). Experiments were performed at 25°C without shaking in triplicate and readings were recorded every 5 minutes.

Atomic structure overlay- A structural superposition of Aβ 16-26 and tau (5V5B, 6HRE) was performed using LSQ from coot (68). We calculated root mean square deviation (RMSD) of main chains for parallel orientations fitting 6-8 residues. Anti-parallel LSQ computation of Aβ 16-22 and tau 275-281 (5V5B) of C_α atoms was calculated, and side chain rotamers optimized with Foldit (80)over 2000 iterations to minimize energy to -603 REU. For side seeding model, residues 16-21 of Aβ (5OQV) were superimposed on 304-309 of Tau (6HRF). Tau was then manually moved perpendicular to the fibril axis to make a complementary surface with 5OQV. Backbone and side chain rotamers were optimized with Foldit to minimize energy to -1517REU.

Acknowledgements

We thank M. Diamond for gifting the monoclonal biosensor HEK293 cell-line that expressed tau-K18 (P301S) EYFP for our inhibitor assay. We thank Dr. Vinters and Christopher K. Williams for supplying patient tissue and immunohistological summaries of tissues. We thank Dan Anderson for general support in the laboratory. We thank Lorena Saelices for providing TTR fibers and Qin Cao for providing TDP-43 fibers. We thank Lin Jiang for helpful conversation regarding Aβ toxicity. We thank the UCLA-DOE X-ray Crystallography Core Technology Center; the Janelia Research Campus visitor program and Ivo Atanasov and the Electron Imaging Center for NanoMachines (EICN) of California NanoSystems Institute (CNSI) at UCLA for the use of their electron microscopes. We thank Johan Hattne for assistance processing MicroED data. The UCLA-DOE X-ray Crystallization Core Technology Center is supported in part by the Department of Energy grant DE-FC0302ER63421. The Gonen laboratory is funded by the Howard Hughes Medical Institute.

Competing Interests

DSE is a SAB member and equity holder in ADRx, Inc.

Author Contributions

SLG conceived and designed this study, interpreted results and wrote the manuscript. SLG crystallized, solved and analyzed Aβ 16-26 D23N, purified Aβ1-42, performed the ThT aggregation assays, prepared Aβ samples for toxicity, biosensor cell, and dot blot assays, and performed TEM experiments and structural overlays. PS performed and interpreted tau biosensor cell experiments, prepared brain extracts, and purified tau constructs. JB cultured cells, executed and analyzed toxicity experiments, and purified alpha synuclein. KM designed inhibitors for Aβ 16-26 D23N and performed biosensor seeding controls. SS preformed and

analyzed the SPR experiment. TPY performed tau interface mutant biosensor experiments. JAR screened crystals and collected MicroED data of Aβ16-26 D23N. MRS helped solve and analyze the Aβ 16-26 D23N structure, and calculate structural overlays. DC helped solve and analyze the Aβ 16-26 D23N structure. TG acquired and analyzed MicroED diffraction data. JS, SP and CGG generated essential material for experiments and performed and analyzed the dot blot assay. DSE conceived the idea for the project, secured funding, interpreted results and revised the manuscript. All authors reviewed the results and approved the final version of the manuscript.

Footnotes

This project was supported by the National Institutes of Health (NIH) (R01 AG029430) and (R56 AG061847).

The abbreviations used are: AD, Alzheimer's disease; Aβ, amyloid-β; MicroED, Microcrystal Electron Diffraction; N2a, Neuro-2a; ThT, thioflavin- T; MTT, 3-(4,5-dimethylthiazol-2- yl)-2,5-diphenyltetrazolium bromide; R2, repeat 2; R3, repeat 3.

The atomic coordinates and associated structure factors have been deposited in the Protein Data Bank 6O4J.

Supplementary Information

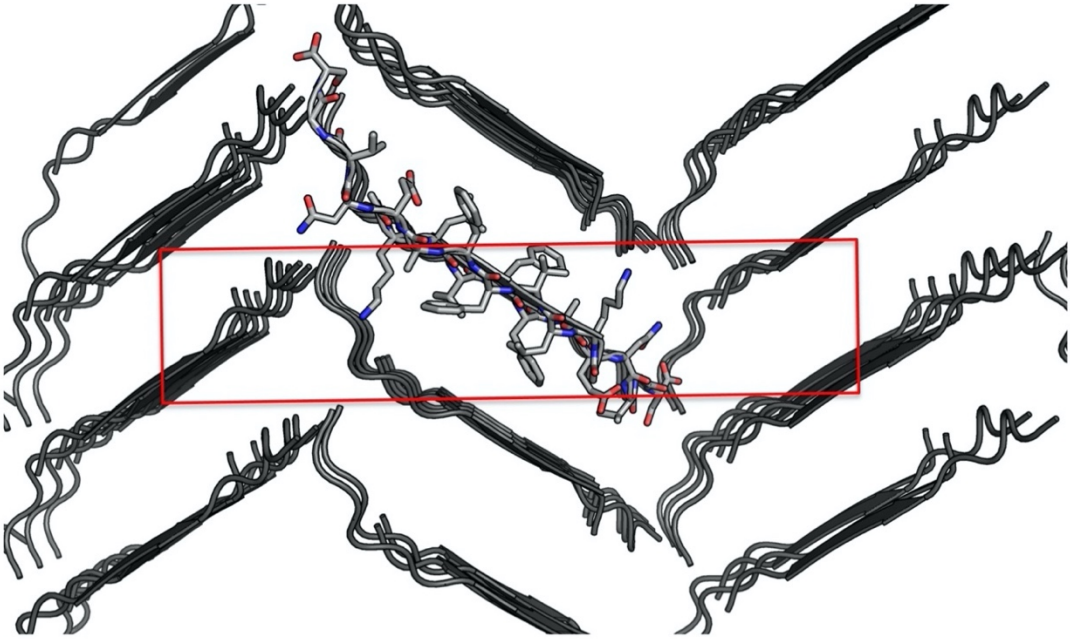

Figure Supplement 1-1. Crystal packing of the Aβ 16-26 D23N atomic structure. View down the 'a' axis of the unit cell, outlined in red.

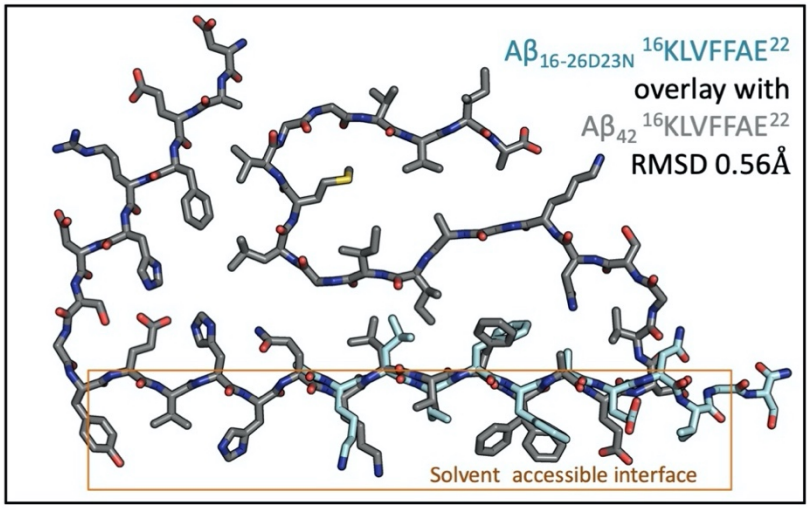

Figure Supplement 1-2. The spines of Aβ 16-26 D23N and $A\beta_{1-42}$ fibrils (5OQV) are structurally similar. 32 backbone atoms differ from each other by 0.57 Å RMSD. RMSD values were calculated using LSQ in Coot.

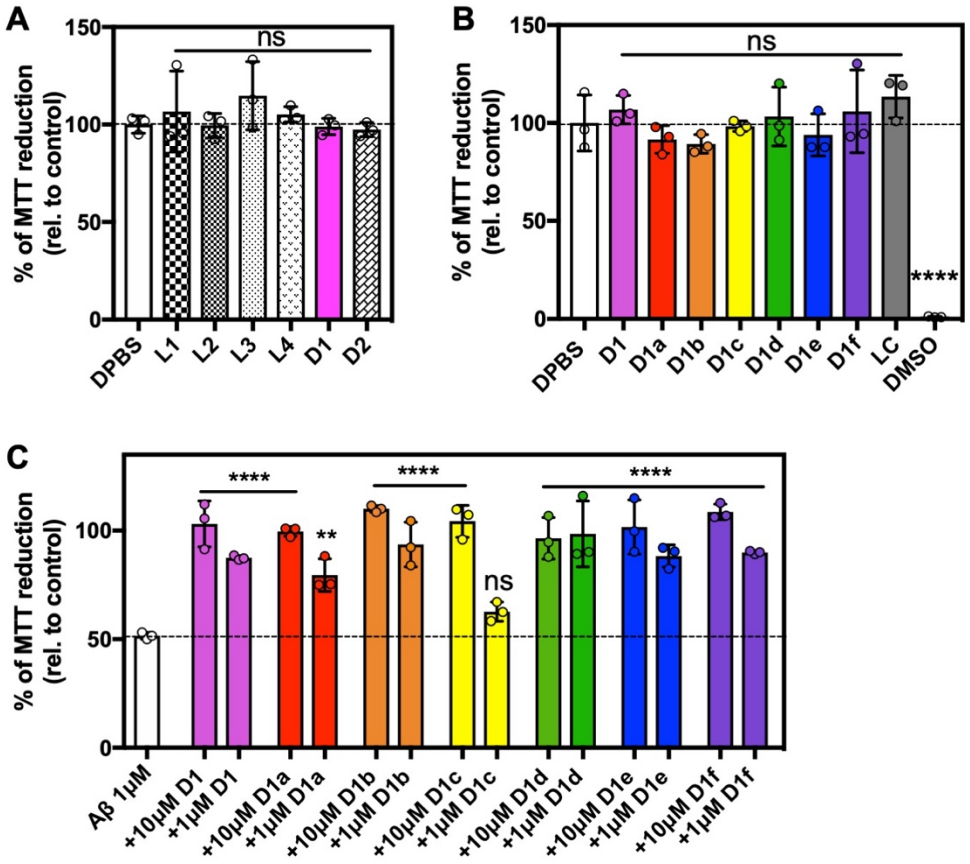

Figure Supplement 2-1. Extended Toxicity data **A, B.** Peptide inhibitors are not toxic. 100 μM of each peptide inhibitor was incubated for 12 hours at 37 °C and then diluted 1:10 with pre-plated N2a cells. Cytotoxicity was quantified using MTT dye reduction. Bars represent mean with individual technical replicates, error bars display one standard deviation. **C.** Second generation peptide inhibitors reduce the cytotoxicity of Aβ1-42. 10 μM Aβ1-42 was incubated alone or with 10 μM and 100 μM of each peptide inhibitor for 12 hours at 37 °C and then diluted 1:10 with pre-plated N2a cells. Cytotoxicity was quantified using MTT dye reduction. Bars represent mean with individual technical replicates, error bars display one standard deviation (n = 3; ns = not significant; ****, $p < 0.0001$ using an ordinary one-way ANOVA- Dunnett's relative to leftmost column).

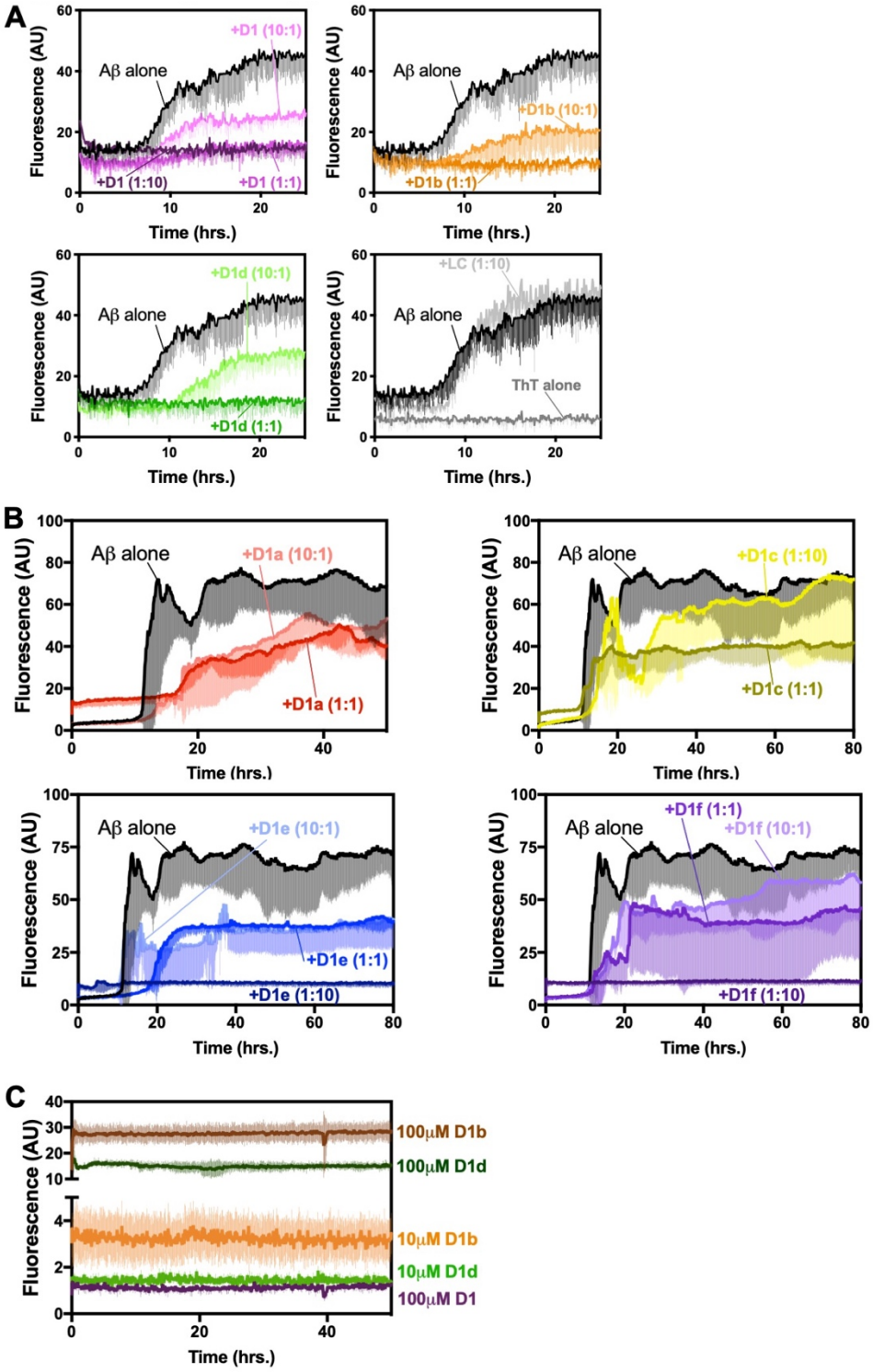

Figure Supplement 3-1. A. Peptide inhibitors D1, D1b, and D1d reduce fibril formation of Aβ1-42, while negative control peptide LC does not. 10 μM of Aβ1-42 was incubated alone or at a 1:10, 1:1, or 10:1 molar ratio to each inhibitor under quiescent conditions at 37 °C in

polypropylene plates. Fibril formation was monitored using ThT fluorescence. Curves show the average of three technical replicates with one standard deviation below.

B. Peptide inhibitors D1a, D1c, D1e, and D1f are less effective ate reducing fibril formation of Aβ1-42, 10 μM of Aβ1-42 was incubated alone or at a 1:10, 1:1, or 10:1 molar ratio to each inhibitor under quiescent conditions at 37 °C. Fibril formation was monitored using ThT fluorescence. Lines show the average of three technical replicates with one standard deviation below. Inhibitors D1a and D1c are not shown at (1:10) ratio due to high ThT signal from peptide self-association. **C.** Peptide inhibitors D1b and D1d self-associate at high concentrations. Peptide inhibitors were incubated at 10 μM and 100 μM under quiescent conditions at 37 °C. Fibril formation was monitored using ThT fluorescence. Lines show the average of three technical replicates with one standard deviation displayed below. .

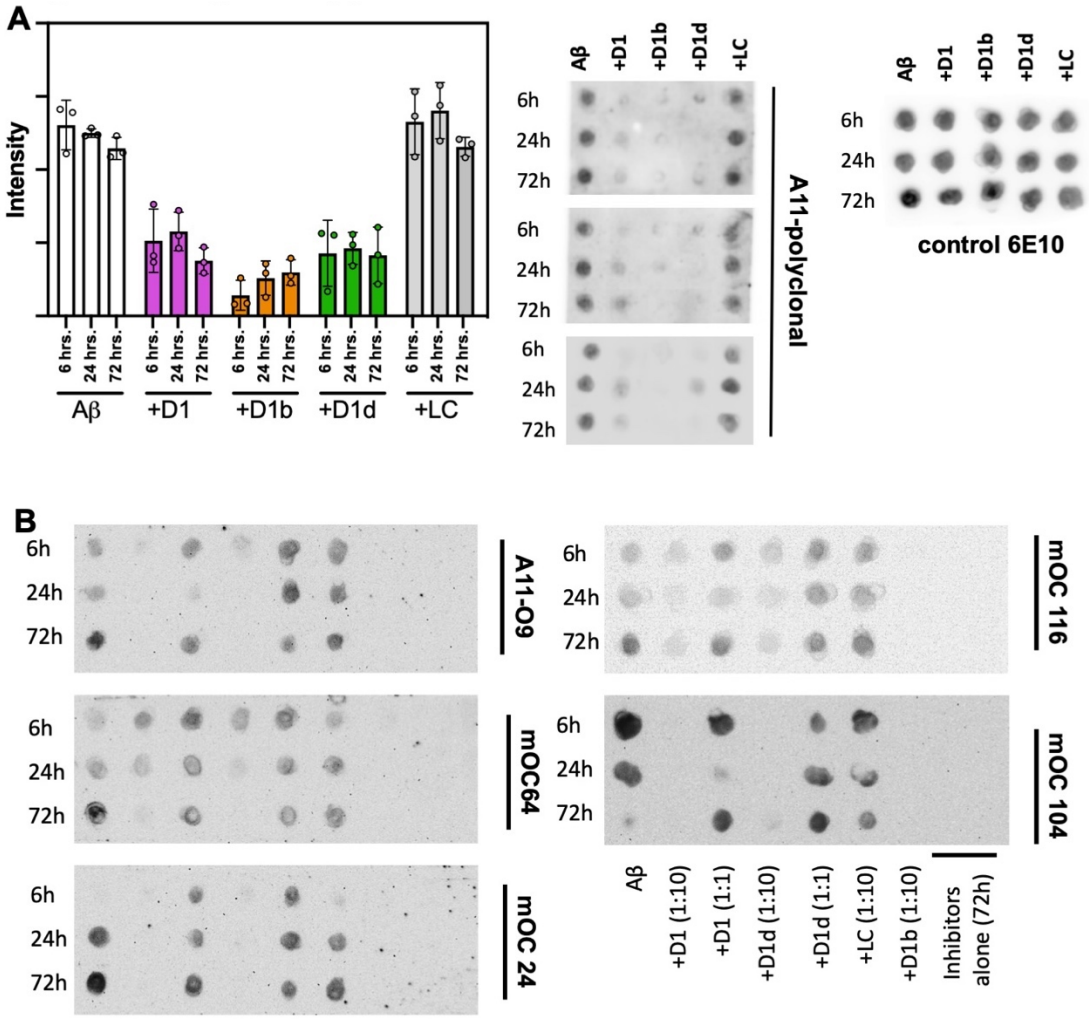

Figure Supplement 3-2. **A**. Peptide inhibitors reduce the formation of oligomeric Aβ1-42 recognized by polyclonal A11 antibody, while negative control peptide does not. 10 μM Aβ1-42 was incubated alone (left-most column) or with 10-fold molar excess of each peptide-based inhibitor. Aliquots of the reaction were tested for antibody-binding at 6 h, 24 h, and 72 h. 6E10 anti-amyloid beta (3-8) was used as a loading control. Blots were quantified using ImageJ. **B.** Unspliced dot blots from figure 4C. Column key displayed at lower right is representative of all displayed blots in B.

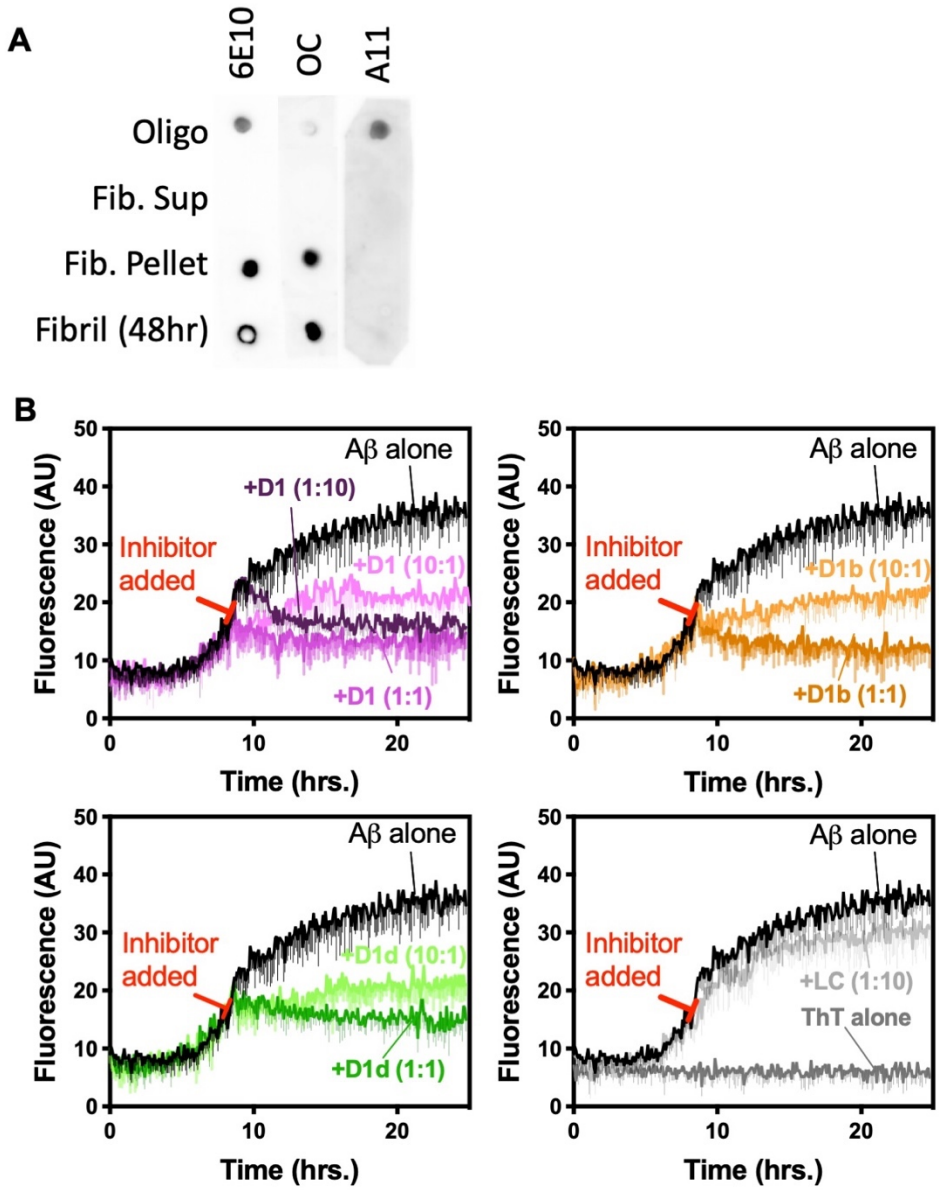

Figure Supplement 4-1 A. Conformation testing of Aβ preparations. 10 μM Aβ1-42 was incubated for 12hr at 37°C in oligomer preparation, or 48 hr. at 37°C with shaking for fibril conditions Fibrils were spun down at 50,000 rpm for 30 minutes. Samples were spotted on nitrocellulose membranes and probed with A11, OC and 6E10 antibodies. **B**. Peptide inhibitors D1, D1b, and D1d reduce fibril elongation of Aβ1-42, while negative control peptide LC does not. 10 μM of Aβ1-42 was incubated alone until approximately half maximal ThT (19 A.U.) was observed under quiescent conditions at 37 °C in polypropylene plates. Inhibitors were added at a 1:10, 1:1, or 10:1 molar ratio to Aβ1-42 reactions at 8.5 hours as indicated by red bar. Fibril

formation was monitored using ThT fluorescence. Curves show the average of three technical replicates with one standard deviation below.

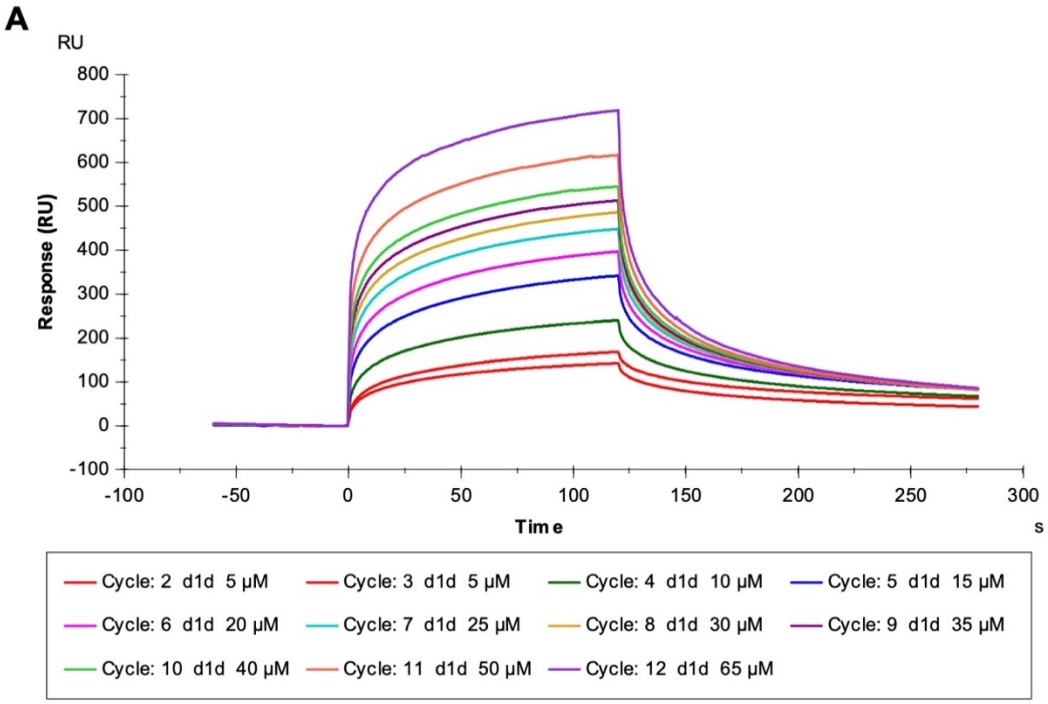

Figure Supplement 4-2. Representative Sensorgram obtained when D1d solutions at the indicated concentrations were flowed across the Aβ1-42 sensor chip. The data of flow cell 1 (blank control) was subtracted from the data of flow cell 2.

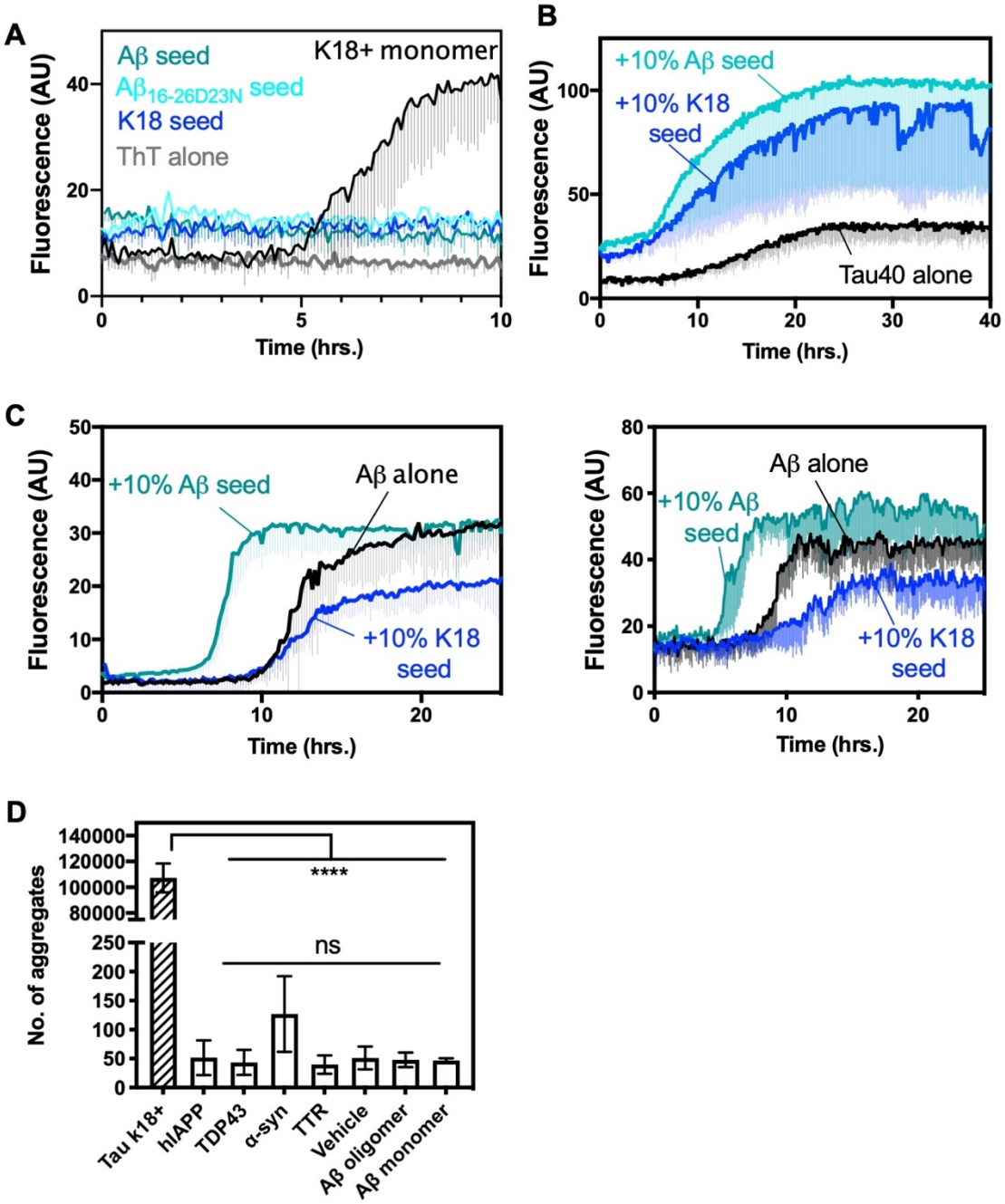

Figure Supplement 5-1. A. Extended ThT data of Tau seeding experiment. K18+ and Aβ1-42 seeds have some baseline ThT signal **B.** 20 μM tau40 was seeded with 10% monomer equivalent of pre-formed fibrils of Aβ1-42 or tau-K18 under shaking conditions at 700 RPM at 37 °C in buffer containing 0.5mg/ml heparin. Fibril formation was monitored using ThT fluorescence. Aβ1-42 or tau-K18 seeds showed reduced lag times (9.4 and 10.2 hr., respectively) than

unseeded tau40 (14.0 hr.). Error bars show the standard deviation of the average of three technical replicates. $T_{1/2}$ lag times were calculated using a four-parameter non-linear fit. **C.** 10 μM Aβ1-42 was seeded with 10% monomer equivalent of pre-formed seed of Aβ1-42 or K18, under quiescent conditions at 37 °C. Fibril formation was monitored using ThT fluorescence. Lines show average of three technical replicates. Left panel was performed in polystyrene plates, right panel was performed in polypropylene plates. **D.** Tau-K18+ versus amyloid fibrils of other proteins, and non-fibrillar Aβ efficiency of seeding the HEK293 biosensor that stably expresses K18 yellow fluorescent protein (YFP) fusion. The cells were seeded with 250 nM final concentration of protein. Bars represent mean with individual technical replicates, error bars display one standard deviation (n = 3; ns = not significant; ****, p < 0.0001 using an ordinary one-way ANOVA- Tukey's relative to leftmost column or against all columns excluding leftmost, as indicated). Amyloid fibrils were confirmed by endpoint ThT or Electron Microscopy. Non-fibrillar Aβ was used fresh (monomeric) or incubated for 12 hrs. 37 °C (oligomer).

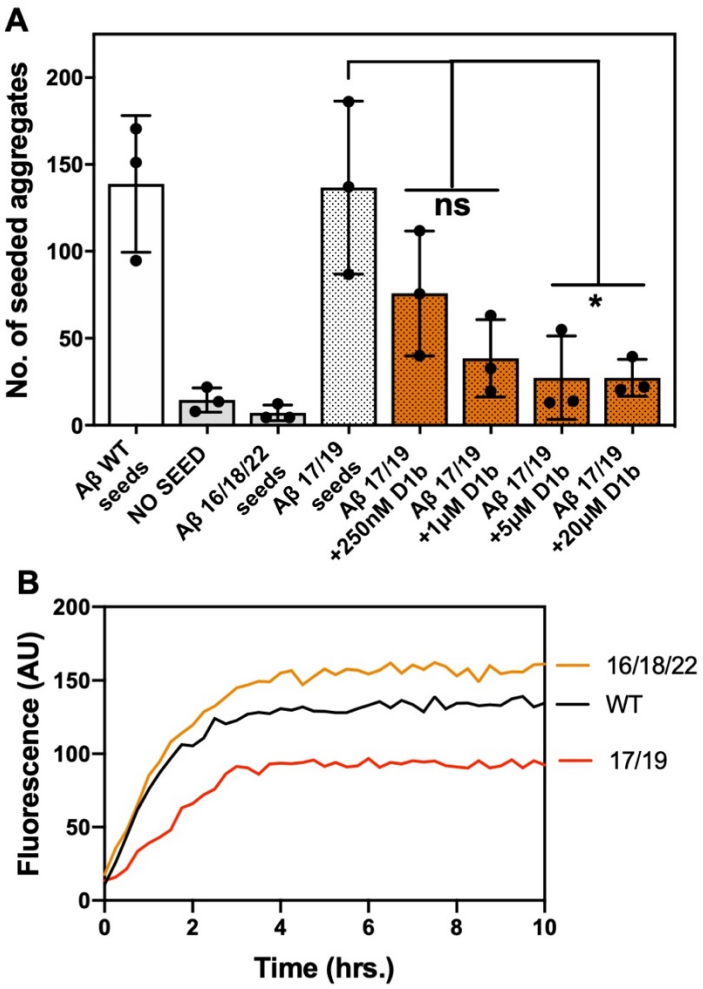

Figure Supplement 5-2. A. Aβ interface mutant constructs form fibrils. 25 μM of each Aβ constructs was incubated under quiescent conditions at 37 °C. Fibril formation was monitored using ThT fluorescence. Lines show the average of three technical replicates. **B.** Average seeding by Aβ mutant constructs and effect of indicated inhibitor concentration. Error bars show the standard deviation of the mean of technical replicates (n = 3; ns = not significant; *, p < 0.04 using an ordinary one-way ANOVA- Dunnett's relative to Aβ 17/19 seeds)

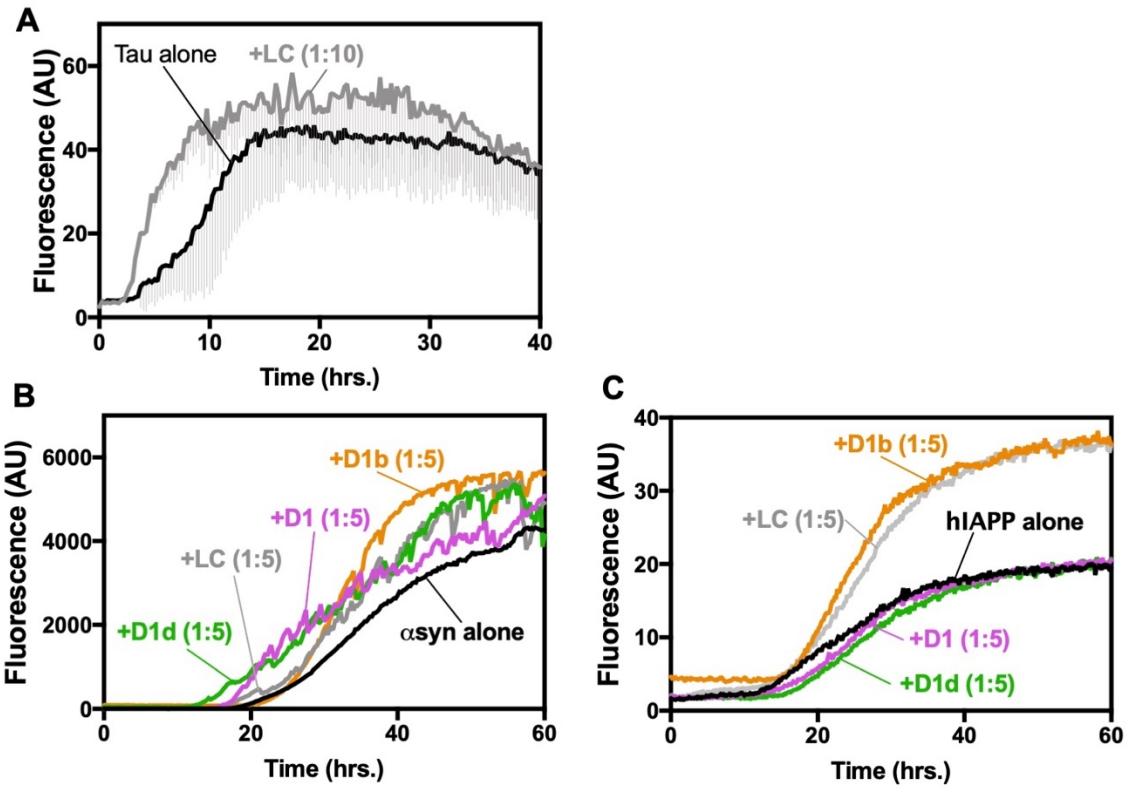

Figure Supplement 6-1. A. Control peptide inhibitor LC does not reduce fibril formation of tau40. 10 μM of tau40 was incubated at a 1:10 molar ratio to LC with 0.5mg/ml heparin under shaking conditions at 700 RPM at 37 °C. Fibril formation was monitored using ThT fluorescence. Lines show the average of three technical replicates with one standard deviation below. **B, C.** Designed inhibitors are not general amyloid inhibitors. **B**. 50 μM of α-synuclein was incubated at a 1:5 molar ratio to peptide inhibitors under shaking conditions at 700 RPM at 37 °C. Lines show the average of three technical replicates. **C.** 10 μM hIAPP was incubated at a 1:5 molar ratio to peptide inhibitors under quiescent conditions at 37 °C. Lines show the average of three technical replicates.

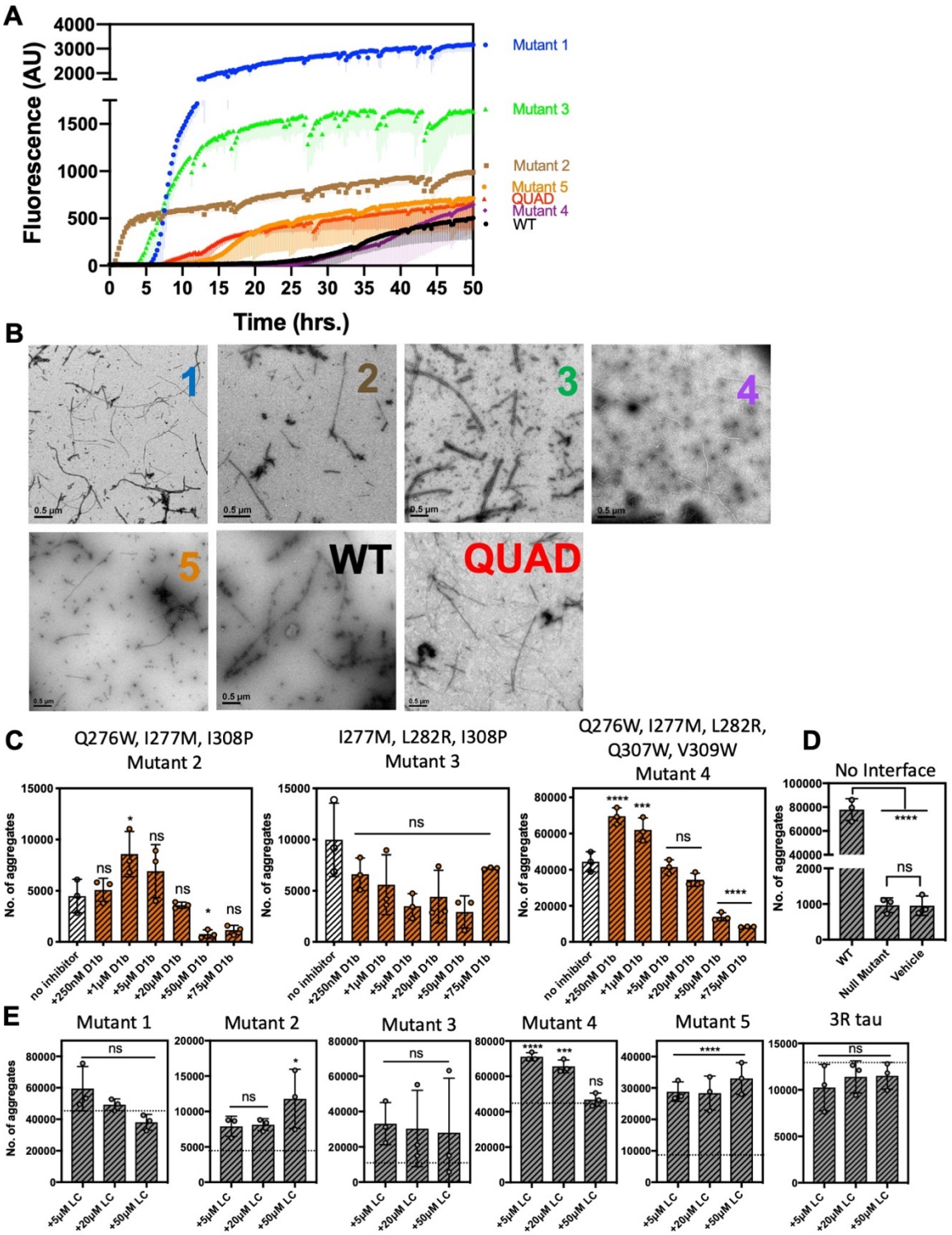

Figure Supplement 6-2. A, B. Tau 40 interface mutant constructs form fibrils. **A.** 10 μM of each tau40 constructs was incubated with 0.5mg/ml heparin under shaking conditions at 700 RPM at 37 °C. Fibril formation was monitored using ThT fluorescence. Lines show the average

of three technical replicates. **B. B.** Negative-stain TEM analysis confirms the results of the ThT assays in **A**. Scale bars are 0.5µm. **C, D, E.** Extended data of seeding by tau interface mutation fibrils in tau-K18CY biosensor cells. The cells were seeded with 250 nM tau40 fiber (final concentration); in samples with inhibitor, tau40 fibers were incubated with indicated final concentrations of peptide inhibitor for one hour prior to addition to cells. Average number of aggregates at the indicated inhibitor concentrations, Bars represent mean with individual technical replicates, error bars display one standard deviation ($n = 3$; ns = not significant; *, $p < 0.05$; ***, $p < 0.0005$; ****, $p < 0.0001$ 0001 using an ordinary one-way ANOVA- Dunnett's in **C, E**, relative to leftmost column (C**) or dotted line (E)**. Panel D was calculated using ANOVA-Tukey's, relative to leftmost column and between Null mutant and vehicle columns). **C**. Interface mutations less affected by D1b. **D.** Construct containing all interface mutations is seeding incompetent. **E.** Seeding interface mutants are not reduced by control inhibitor LC. Extended ANOVA data included as a supplementary file.

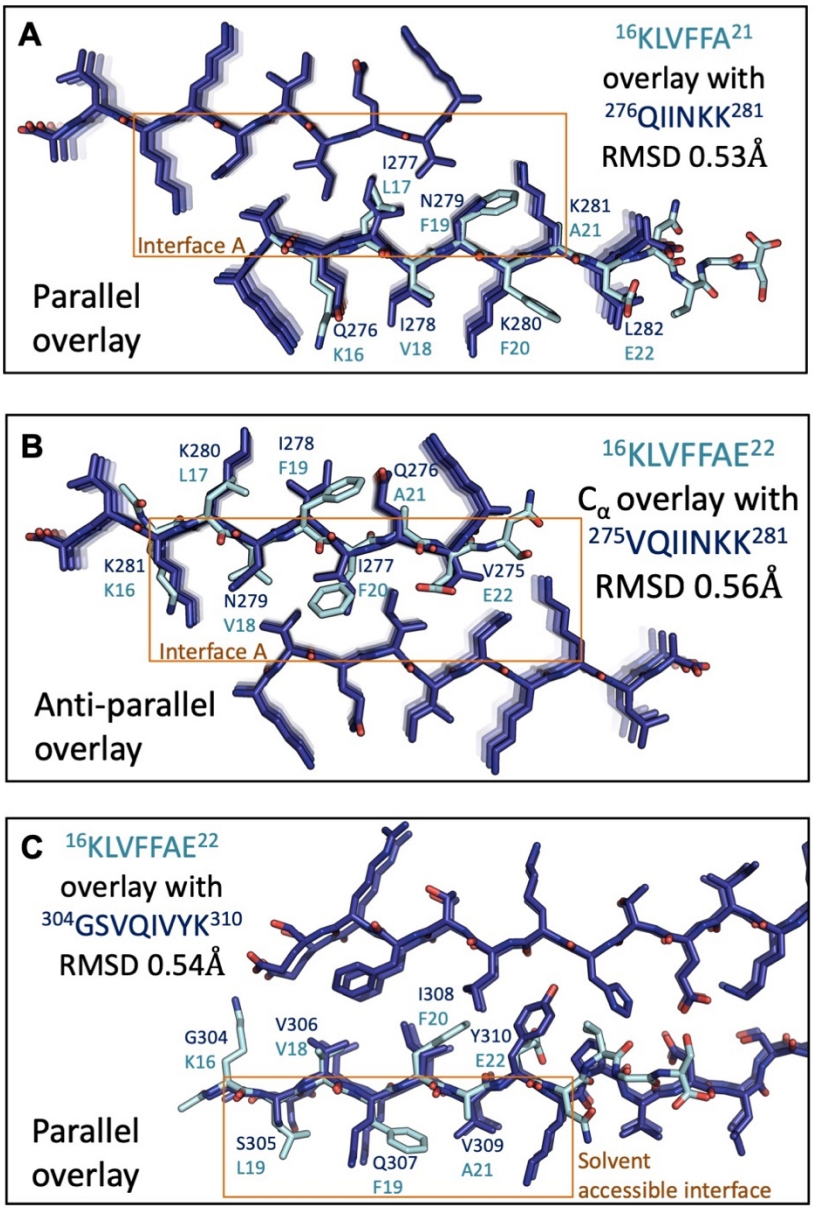

Figure Supplement 6-3. The spines of Aβ 16-26 D23N and tau are structurally similar. **A, B.** Aβ 16-26 D23N overlay with tau 274-283 in parallel and antiparallel orientations. **A.** 32 backbone atoms differ from each other by 0.53 Å RMSD. RMSD values were calculated using LSQ in Coot. **B.** The C_α atoms differ from each other by 0.56 Å RMSD. Backbone and side chain rotamers were optimized with Foldit over 2000 iterations to minimize energy to -603 REU. **C.** Aβ 16-22 overlay with tau 304-310 in parallel, backbone atoms differ from each other by 0.54 Å RMSD. RMSD values were calculated using LSQ in Coot.

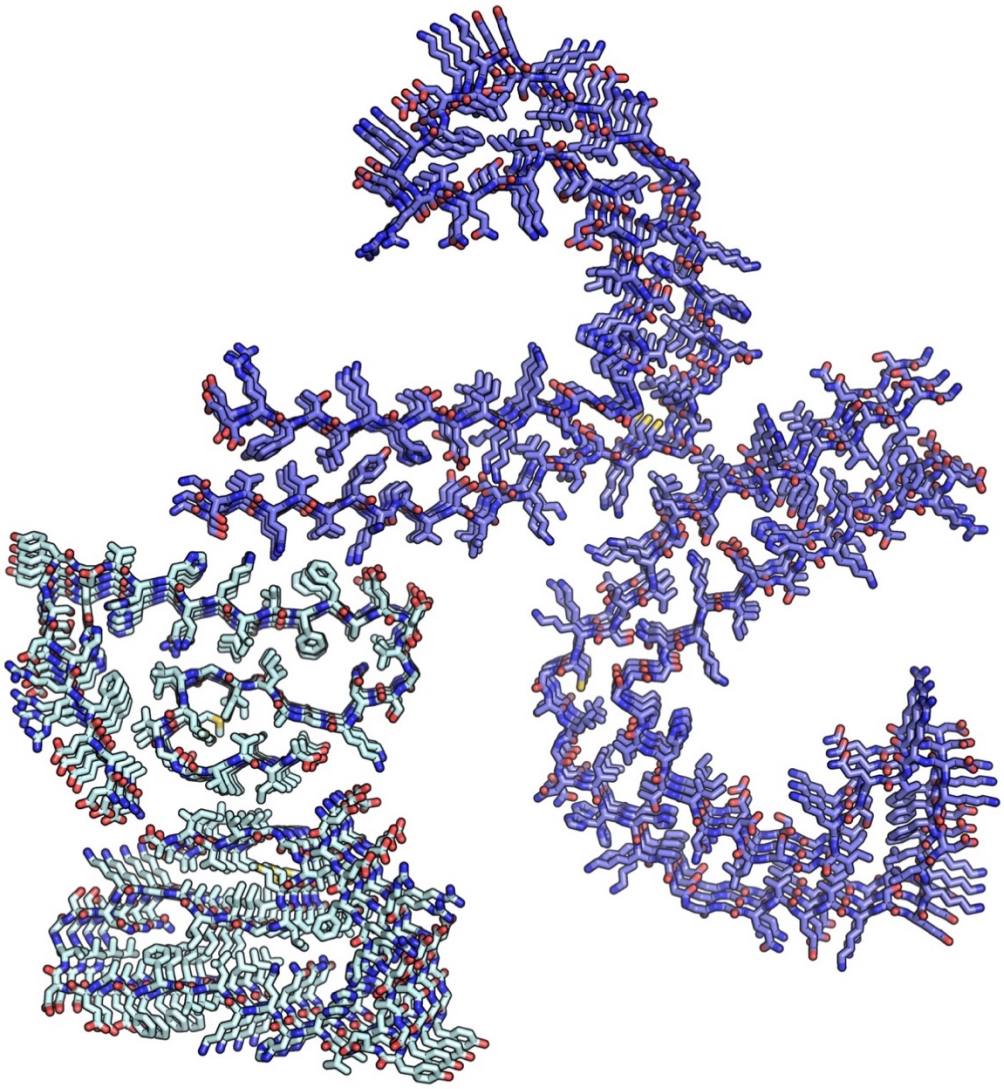

Figure Supplement 6-4. Hetero-seeding model from side of Aβ fibril. Residues 16-21 of Aβ (5OQV) were superimposed on 304-309 of Tau (6HRF). Tau was then manually moved perpendicular to the fibril axis to make a complementary surface with 5OQV. Backbone and side chain rotamers were optimized with Foldit to minimize energy to -1517REU.

Supplemental Table 1. Computed binding properties of designed inhibitors to amyloid-beta $_{16}$KLVFFAEN$_{23}$

Peptide Name	Sequence	MW (g/mol)	Hydropathicity (GRAVY)	Binding Energy (R.E.U.)	SA Buried (Å^2)	Shape Complementarity
L1	KWYFIE	885	-0.38	-4.41	760	0.76
L2	NLYVRE	793	-0.80	-5.02	761	0.73
L3	ERLYHFME	1124	-0.94	-4.69	1016	0.79
L4	QRVYRTWQ	1136	-1.84	-4.75	1026	0.75
LC	LYIWVQ	821	1.13	-4.25	719	0.75
D1	D-LYIWVQ	821	1.13	-4.92	771	0.70
D1a	D-LYIWIQMQ	1094	0.69	-5.33	1149	0.71
D1b	D-LYIWIWRT	1150	0.56	-6.11	1235	0.72
D1c	D-LYIWIWFS	1127	1.46	-5.95	1215	0.71
D1d	D-LYIWIQKT	1064	0.31	-5.25	1140	0.70
D1e	D-MYIWVQ	839	0.82	-4.94	776	0.70
D1f	D-MYIWRQ	896	-0.63	-4.40	802	0.70
D2	D-MLIVRN	745	1.07	-4.17	760	0.70

References

1. Glenner, G. G., Wong, C. W., Quaranta, V., and Eanes, E. D. (1984) The amyloid deposits in Alzheimer's disease: their nature and pathogenesis. *Appl. Pathol.* **2**, 357–369

2. Goedert, M., Eisenberg, D. S., and Crowther, R. A. (2017) Propagation of Tau Aggregates and Neurodegeneration. *Annu. Rev. Neurosci.* **40**, 189–210

3. Tanzi, R. E. (2012) The genetics of Alzheimer disease (7). *Cold Spring Harb. Perspect. Med.* **2**, a006296-

4. Hardy, J., and Selkoe, D. J. (2002) The amyloid hypothesis of Alzheimer's disease: progress and problems on the road to therapeutics. *Science.* **297**, 353–356

5. Manczak, M., and Reddy, P. H. (2014) Abnormal interaction of oligomeric amyloid-β with phosphorylated tau: implications to synaptic dysfunction and neuronal damage. *J Alzheimers Dis.* **36**, 285–295

6. Seward, M. E., Swanson, E., Norambuena, A., Reimann, A., Cochran, J. N., Li, R., Roberson, E. D., and Bloom, G. S. (2013) Amyloid- signals through tau to drive ectopic neuronal cell cycle re-entry in Alzheimer's disease. *J. Cell Sci.* **126**, 1278–1286

7. Brier, M. R., Gordon, B., Morris, J. H., Benzinger, T. L. S., and Ances, B. M. (2016) Tau and Aß imaging, CSF measures, and cognition in Alzheimer' s disease. *Sci. Transl. Med.* **8**, 1–10

8. Schwarz, A. J., Yu, P., Miller, B. B., Shcherbinin, S., Dickson, J., Navitsky, M., Joshi, A. D., Devous, M. D., and Mintun, M. S. (2016) Regional profiles of the candidate tau PET ligand18F-AV-1451 recapitulate key features of Braak histopathological stages. *Brain.* **139**, 1539–1550

9. Chen, G., Xu, T., Yan, Y., Zhou, Y., Jiang, Y., Melcher, K., and Xu, H. E. (2017) Amyloid beta : structure , biology and structure-based therapeutic development. *Nat. Publ. Gr.* **38**, 1205–1235

10. Oddo, S., Caccamo, A., Shepherd, J. D., Murphy, M. P., Golde, T. E., Kayed, R., Metherate, R., Mattson, M. P., Akbari, Y., and LaFerla, F. M. (2003) Triple-transgenic model of Alzheimer's Disease with plaques and tangles: Intracellular Aβ and synaptic dysfunction. *Neuron.* **39**, 409–421

11. Bolmont, T., Clavaguera, F., Meyer-Luehmann, M., Herzig, M. C., Radde, R., Staufenbiel, M., Lewis, J., Hutton, M., Tolnay, M., and Jucker, M. (2007) Induction of tau pathology by intracerebral infusion of amyloid-β-containing brain extract and by amyloid-β deposition in APP x tau transgenic mice. *Am. J. Pathol.* **171**, 2012–2020

12. Gotz, J. (2001) Formation of Neurofibrillary Tangles in P301L Tau Transgenic Mice Induced by Abeta 42 Fibrils. *Science (80-.).* **293**, 1491–1495

13. Morales, R., Bravo-Alegria, J., Duran-Aniotz, C., and Soto, C. (2015) Titration of biologically active amyloid-β seeds in a transgenic mouse model of Alzheimer's disease.

Sci. Rep. **5**, 9349

14. Choi, S. H., Kim, Y. H., Hebisch, M., Sliwinski, C., Lee, S., D'Avanzo, C., Chen, H., Hooli, B., Asselin, C., Muffat, J., Klee, J. B., Zhang, C., Wainger, B. J., Peitz, M., Kovacs, D. M., Woolf, C. J., Wagner, S. L., Tanzi, R. E., and Kim, D. Y. (2014) A three-dimensional human neural cell culture model of Alzheimer's disease. *Nature*. **515**, 274–278

15. Ittner, L. M., and Götz, J. (2011) Amyloid-β and tau - A toxic pas de deux in Alzheimer's disease. *Nat. Rev. Neurosci.* **12**, 67–72

16. Stancu, I. C., Vasconcelos, B., Terwel, D., and Dewachter, I. (2014) Models of β-amyloid induced Tau-pathology: the long and "folded" road to understand the mechanism. *Mol. Neurodegener.* **9**, 51

17. Morales, R., Moreno-Gonzalez, I., and Soto, C. (2013) Cross-Seeding of Misfolded Proteins: Implications for Etiology and Pathogenesis of Protein Misfolding Diseases. *PLoS Pathog*. **9**, 1–4

18. Rajendran, L., Honsho, M., Zahn, T. R., Keller, P., Geiger, K. D., Verkade, P., and Simons, K. (2006) Alzheimer's disease beta-amyloid peptides are released in association with exosomes. *Proc. Natl. Acad. Sci.* **103**, 11172–11177

19. Lesné, S., Ming, T. K., Kotilinek, L., Kayed, R., Glabe, C. G., Yang, A., Gallagher, M., and Ashe, K. H. (2006) A specific amyloid-β protein assembly in the brain impairs memory. *Nature*. **440**, 352–357

20. Lambert, M. P., Barlow, A. K., Chromy, B. A., Edwards, C., Freed, R., Liosatos, M., Morgan, T. E., Rozovsky, I., Trommer, B., Viola, K. L., Wals, P., Zhang, C., Finch, C. E., Krafft, G. A., and Klein, W. L. (1998) Diffusible, nonfibrillar ligands derived from Aβ 1-42 are potent central nervous system neurotoxins. *Proc. Natl. Acad. Sci.* **95**, 6448–6453

21. Benilova, I., Karran, E., and De Strooper, B. (2012) The toxic Aβ oligomer and Alzheimer's disease: an emperor in need of clothes. *Nat. Neurosci.* 10.1038/nn.3028

22. Jin, M., Shepardson, N., Yang, T., Chen, G., Walsh, D., and Selkoe, D. J. (2011) Soluble amyloid -protein dimers isolated from Alzheimer cortex directly induce Tau hyperphosphorylation and neuritic degeneration. *Proc. Natl. Acad. Sci.* **108**, 5819–5824

23. Guo, J.-P., Arai, T., Miklossy, J., and McGeer, P. L. (2006) Abeta and tau form soluble complexes that may promote self aggregation of both into the insoluble forms observed in Alzheimer's disease. *Proc. Natl. Acad. Sci. U. S. A.* **103**, 1953–8

24. Vasconcelos, B., Cosmin, I., Arjan, S., Matthew, B., Wang, P., Vanoosthuyse, A., Kolen, K. Van, Verheyen, A., Kienlen, P., Jean, C., Octave, N., Baatsen, P., and Moechars, D. (2016) Heterotypic seeding of Tau fibrillization by pre - aggregated Abeta provides potent seeds for prion - like seeding and propagation of Tau - pathology in vivo. *Acta Neuropathol.* **131**, 549–569

25. Miller, Y., Ma, B., and Nussinov, R. (2011) Synergistic interactions between repeats in tau

protein and Aβ amyloids may be responsible for accelerated aggregation via polymorphic States. *Biochemistry*. **50**, 5172–5181

26. Tjernberg, L. O., Callaway, D. J., Tjernberg, a, Hahne, S., Lilliehöök, C., Terenius, L., Thyberg, J., and Nordstedt, C. (1999) A molecular model of Alzheimer amyloid beta-peptide fibril formation. *J. Biol. Chem.* **274**, 12619–12625

27. Bernstein, S. L., Wyttenbach, T., Baumketner, A., Shea, J. E., Bitan, G., Teplow, D. B., and Bowers, M. T. (2005) Amyloid β-protein: Monomer structure and early aggregation states of Aβ42 and its Pro19alloform. *J. Am. Chem. Soc.* **127**, 2075–2084

28. Marshall, K. E., Vadukul, D. M., Dahal, L., Theisen, A., Fowler, M. W., Al-Hilaly, Y., Ford, L., Kemenes, G., Day, I. J., Staras, K., and Serpell, L. C. (2016) A critical role for the self-assembly of Amyloid-β1-42 in neurodegeneration. *Sci. Rep.* **6**, 1–13

29. Colletier, J.-P., Laganowsky, A., Landau, M., Zhao, M., Soriaga, A. B., Goldschmidt, L., Flot, D., Cascio, D., Sawaya, M. R., and Eisenberg, D. (2011) Molecular basis for amyloid- polymorphism. *Proc. Natl. Acad. Sci.* **108**, 16938–16943

30. Lührs, T., Ritter, C., Adrian, M., Riek-Loher, D., Bohrmann, B., Döbeli, H., Schubert, D., and Riek, R. (2005) 3D structure of Alzheimer's amyloid-beta(1-42) fibrils. *Proc. Natl. Acad. Sci. U. S. A.* **102**, 17342–17347

31. Colvin, M. T., Silvers, R., Ni, Q. Z., Can, T. V., Sergeyev, I., Rosay, M., Donovan, K. J., Michael, B., Wall, J., Linse, S., and Griffin, R. G. (2016) Atomic Resolution Structure of Monomorphic Aβ 42 Amyloid Fibrils. *J. Am. Chem. Soc.* **138**, 9663–9674

32. Qiang, W., Yau, W.-M., Luo, Y., Mattson, M. P., and Tycko, R. (2012) Antiparallel -sheet architecture in Iowa-mutant -amyloid fibrils. *Proc. Natl. Acad. Sci.* **109**, 4443–4448

33. Huber, M., Ovchinnikova, O. Y. u, Schütz, A. K., Glockshuber, R., Meier, B. H., and Böckmann, A. (2015) Solid-state NMR sequential assignment of Osaka-mutant amyloid-beta (Aβ1-40 E22Δ) fibrils. *Biomol. NMR Assign.* **9**, 7–14

34. Wälti, M. A., Ravotti, F., Arai, H., Glabe, C. G., Wall, J. S., Böckmann, A., Güntert, P., Meier, B. H., and Riek, R. (2016) Atomic-resolution structure of a disease-relevant Aβ(1-42) amyloid fibril. *Proc. Natl. Acad. Sci. U. S. A.* **113**, E4976-84

35. Van Nostrand, W. E., Melchor, J. P., Cho, H. S., Greenberg, S. M., and Rebeck, G. W. (2001) Pathogenic Effects of D23N Iowa Mutant Amyloid β-Protein. *J. Biol. Chem.* **276**, 32860–32866

36. Tay, W. M., Huang, D., Rosenberry, T. L., and Paravastu, A. K. (2013) The Alzheimer's amyloid-β(1-42) peptide forms off-pathway oligomers and fibrils that are distinguished structurally by intermolecular organization. *J. Mol. Biol.* **425**, 2494–2508

37. Laganowsky, A., Liu, C., Sawaya, M. R., Whitelegge, J. P., Park, J., Zhao, M., Pensalfini, A., Soriaga, A. B., Landau, M., Teng, P. K., Cascio, D., Glabe, C., and Eisenberg, D. (2012) Atomic view of a toxic amyloid small oligomer. *Science*. **335**, 1228–31

38. Sarkar, B., Mithu, V. S., Chandra, B., Mandal, A., Chandrakesan, M., Bhowmik, D., Madhu, P. K., and Maiti, S. (2014) Significant Structural Differences between Transient Amyloid-β Oligomers and Less-Toxic Fibrils in Regions Known To Harbor Familial Alzheimer's Mutations. *Angew. Chem. Int. Ed.* 10.1002/anie.201402636

39. Krotee, P., Griner, S. L., Sawaya, M. R., Cascio, D., Rodriguez, J. A., Shi, D., Philipp, S., Murray, K., Saelices, L., Lee, J., Seidler, P., Glabe, C. G., Jiang, L., Gonen, T., and Eisenberg, D. S. (2018) Common fibrillar spines of amyloid-β and human islet amyloid polypeptide revealed by microelectron diffraction and structure-based inhibitors. *J. Biol. Chem.* 10.1074/jbc.M117.806109

40. Colletier, J.-P., Laganowsky, A., Landau, M., Zhao, M., Soriaga, A. B., Goldschmidt, L., Flot, D., Cascio, D., Sawaya, M. R., and Eisenberg, D. (2011) Molecular basis for amyloid-beta polymorphism. *Proc. Natl. Acad. Sci. U. S. A.* **108**, 16938–43

41. Tycko, R., Sciarretta, K. L., Orgel, J. P. R. O., and Meredith, S. C. (2009) Evidence for novel β-sheet structures in Iowa mutant β-amyloid fibrils. *Biochemistry*. **48**, 6072–6084

42. Liu, C., Zhao, M., Jiang, L., Cheng, P.-N., Park, J., Sawaya, M. R., Pensalfini, A., Gou, D., Berk, A. J., Glabe, C. G., Nowick, J., and Eisenberg, D. (2012) Out-of-register β-sheets suggest a pathway to toxic amyloid aggregates. *Proc. Natl. Acad. Sci. U. S. A.* **109**, 20913–8

43. Sun, Y., Ge, X., Xing, Y., Wang, B., and Ding, F. (2018) β-barrel Oligomers as Common Intermediates of Peptides Self-Assembling into Cross-β Aggregates. *Sci. Rep.* **8**, 10353

44. Sievers, S. A., Karanicolas, J., Chang, H. W., Zhao, A., Jiang, L., Zirafi, O., Stevens, J. T., Münch, J., Baker, D., and Eisenberg, D. (2011) Structure-based design of non-natural amino-acid inhibitors of amyloid fibril formation. *Nature*. **475**, 96–100

45. Seidler, P. M., Boyer, D. R., Rodriguez, J. A., Sawaya, M. R., Cascio, D., Murray, K., Gonen, T., and Eisenberg, D. S. (2018) Structure-based inhibitors of tau aggregation. *Nat. Chem.* **10**, 170–176

46. Saelices, L., Johnson, L. M., Liang, W. Y., Sawaya, M. R., Cascio, D., Ruchala, P., Whitelegge, J., Jiang, L., Riek, R., and Eisenberg, D. S. (2015) Uncovering the mechanism of aggregation of human transthyretin. *J. Biol. Chem.* **290**, 28932–28943

47. Soragni, A., Janzen, D. M., Johnson, L. M., Lindgren, A. G., Thai-Quynh Nguyen, A., Tiourin, E., Soriaga, A. B., Lu, J., Jiang, L., Faull, K. F., Pellegrini, M., Memarzadeh, S., and Eisenberg, D. S. (2016) A Designed Inhibitor of p53 Aggregation Rescues p53 Tumor Suppression in Ovarian Carcinomas. *Cancer Cell.* **29**, 90–103

48. Krotee, P., Griner, S. L., Sawaya, M. R., Cascio, D., Rodriguez, J. A., Shi, D., Philipp, S., Murray, K., Saelices, L., Lee, J., Seidler, P., Glabe, C. G., Jiang, L., Gonen, T., and Eisenberg, D. S. (2018) Common fibrillar spines of amyloid-β and human islet amyloid polypeptide revealed by microelectron diffraction and structure-based inhibitors. *J. Biol. Chem.* **293**, 2888–2902

49. Olmsted, J. B., Carlson, K., Klebe, R., Ruddle, F., and Rosenbaum, J. (1970) Isolation of microtubule protein from cultured mouse neuroblastoma cells. *Proc. Natl. Acad. Sci. U. S. A.* **65**, 129–136

50. Mosmann, T. (1983) Rapid colorimetric assay for cellular growth and survival: application to proliferation and cytotoxicity assays. *J. Immunol. Methods.* **65**, 55–63

51. Liu, Y., Peterson, D. A., Kimura, H., and Schubert, D. (1997) Mechanism of cellular 3-(4,5-dimethylthiazol-2-yl)-2,5- diphenyltetrazolium bromide (MTT) reduction. *J. Neurochem.* **6**, 581–593

52. Hatami, A., Albay, R., Monjazeb, S., Milton, S., and Glabe, C. (2014) Monoclonal antibodies against A??42 fibrils distinguish multiple aggregation state polymorphisms in vitro and in Alzheimer disease brain. *J. Biol. Chem.* **289**, 32131–32143

53. Manuscript, A., Iii, G. E., Salvadores, N., Shahnawaz, M., Soto, C., May, A., Responsible, B., Tatarnikova, O. G., Orlov, M. A., Bobkova, N. V, Chen, G., Xu, T., Yan, Y., Zhou, Y., Jiang, Y., Melcher, K., Xu, H. E., Baughman, H. E. R., Clouser, A. F., Klevit, R. E., Nath, A., Vasconcelos, B., Cosmin, I., Arjan, S., Matthew, B., Wang, P., Vanoosthuyse, A., Kolen, K. Van, Verheyen, A., Kienlen, P., Jean, C., Octave, N., Baatsen, P., and Moechars, D. (2017) Heterotypic seeding of Tau fibrillization by pre - aggregated Abeta provides potent seeds for prion - like seeding and propagation of Tau - pathology in vivo. *Acta Neuropathol.* **131**, 1327–1334

54. Kfoury, N., Holmes, B. B., Jiang, H., Holtzman, D. M., and Diamond, M. I. (2012) Trans-cellular propagation of Tau aggregation by fibrillar species. *J. Biol. Chem.* **287**, 19440–19451

55. Sawaya, M. R., Sambashivan, S., Nelson, R., Ivanova, M. I., Sievers, S. A., Apostol, M. I., Thompson, M. J., Balbirnie, M., Wiltzius, J. J. W., McFarlane, H. T., Madsen, A. Ø., Riekel, C., and Eisenberg, D. (2007) Atomic structures of amyloid cross-β spines reveal varied steric zippers. *Nature.* **447**, 453

56. Fitzpatrick, A. W. P., Falcon, B., He, S., Murzin, A. G., Murshudov, G., Garringer, H. J., Crowther, R. A., Ghetti, B., Goedert, M., and Scheres, S. H. W. (2017) Cryo-EM structures of tau filaments from Alzheimer's disease. *Nature.* **547**, 185

57. Falcon, B., Zhang, W., Schweighauser, M., Murzin, A. G., Vidal, R., Garringer, H. J., Ghetti, B., Scheres, S. H. W., and Goedert, M. (2018) Tau filaments from multiple cases of sporadic and inherited Alzheimer ' s disease adopt a common fold. *Acta Neuropathol.* **136**, 699–708

58. Lazo, N. D., Grant, M. A., Condron, M. C., Rigby, A. C., and Teplow, D. B. (2009) On the nucleation of amyloid β-protein monomer folding. *Protein Sci.* **14**, 1581–1596

59. Krone, M. G., Baumketner, A., Bernstein, S. L., Wyttenbach, T., Lazo, N. D., Teplow, D. B., Bowers, M. T., and Shea, J. (2008) Effects of Familial Alzheimer's Disease Mutations on the Folding Nucleation of the Amyloid β-Protein. *J. Mol. Biol.* **381**, 221–228

60. Chong, S.-H., Yim, J., and Ham, S. (2013) Structural heterogeneity in familial Alzheimer's disease mutants of amyloid-beta peptides. *Mol. BioSyst. Mol. BioSyst.* **9**, 997–1003

61. Kirschner, D. A., Abraham, C., and Selkoe, D. J. (1986) X-ray diffraction from intraneuronal paired helical filaments and extraneuronal amyloid fibers in Alzheimer disease indicates cross-beta conformation. *Proc. Natl. Acad. Sci.* **83**, 503–507

62. Sanders, D. W., Kaufman, S. K., DeVos, S. L., Sharma, A. M., Mirbaha, H., Li, A., Barker, S. J., Foley, A. C., Thorpe, J. R., Serpell, L. C., Miller, T. M., Grinberg, L. T., Seeley, W. W., and Diamond, M. I. (2014) Distinct tau prion strains propagate in cells and mice and define different tauopathies. *Neuron.* **82**, 1271–1288

63. Shi, D., Nannenga, B. L., de la Cruz, M. J., Liu, J., Sawtelle, S., Calero, G., Reyes, F. E., Hattne, J., and Gonen, T. (2016) The collection of MicroED data for macromolecular crystallography. *Nat. Protoc.* **11**, 895–904

64. Hattne, J., Reyes, F. E., Nannenga, B. L., Shi, D., de la Cruz, M. J., Leslie, A. G. W., and Gonen, T. (2015) MicroED data collection and processing. *Acta Crystallogr. Sect. A Found. Adv.* **71**, 353–360

65. Nannenga, B. L., Shi, D., Leslie, A. G. W., and Gonen, T. (2014) High-resolution structure determination by continuous-rotation data collection in MicroED. *Nat. Methods.* **11**, 1–5

66. Kabsch, W. (2010) XDS. *Acta Crystallogr. D. Biol. Crystallogr.* **66**, 125–32

67. McCoy, A. J. (2007) Solving structures of protein complexes by molecular replacement with Phaser. *Acta Crystallogr. D. Biol. Crystallogr.* **63**, 32–41

68. Emsley, P., and Cowtan, K. (2004) Coot: model-building tools for molecular graphics. *Acta Crystallogr. D. Biol. Crystallogr.* **60**, 2126–32

69. McCoy, A. J., Grosse-Kunstleve, R. W., Storoni, L. C., and Read, R. J. (2005) Likelihood-enhanced fast translation functions. *Acta Crystallogr. D. Biol. Crystallogr.* **61**, 458–64

70. Collaborative Computational Project Number 4 (1994) The CCP4 suite: programs for protein crystallography. *Acta Crystallogr. D. Biol. Crystallogr.* **50**, 760–763

71. Lee, B., and Richards, F. M. (1971) The interpretation of protein structures: Estimation of static accessibility. *J. Mol. Biol.* 10.1016/0022-2836(71)90324-X

72. Connolly, M. L. (1983) Solvent-accessible surfaces of proteins and nucleic acids. *Science.* **221**, 709–13

73. Lawrence, M. C., and Colman, P. M. (1993) Shape complementarity at protein-protein interfaces. *J. Mol. Biol.* **93**, 946–950

74. Richards, F. M. (1977) Areas, volumes, packing, and protein structure. *Annu. Rev. Biophys. Bioeng.* **5**, 151–176

75. Sievers, S. A., Karanicolas, J., Chang, H. W., Zhao, A., Jiang, L., Zirafi, O., Stevens, J. T., Münch, J., Baker, D., and Eisenberg, D. (2011) Structure-based design of non-natural

amino-acid inhibitors of amyloid fibril formation. *Nature*. **475**, 96–100

76. Kyte, J., and Doolittle, R. F. (1982) A simple method for displaying the hydropathic character of a protein. *J. Mol. Biol.* **157**, 105–132

77. Krotee, P., Rodriguez, J. A., Sawaya, M. R., Cascio, D., Reyes, F. E., Shi, D., Hattne, J., Nannenga, B. L., Oskarsson, M. E., Philipp, S., Griner, S., Jiang, L., Glabe, C. G., Westermark, G. T., Gonen, T., and Eisenberg, D. S. (2017) Atomic structures of fibrillar segments of hIAPP suggest tightly mated β-sheets are important for cytotoxicity. *Elife*. 10.7554/eLife.19273

78. Eliceiri, K., Schneider, C. A., Rasband, W. S., and Eliceiri, K. W. (2012) NIH Image to ImageJ : 25 years of image analysis HISTORICAL commentary NIH Image to ImageJ : 25 years of image analysis. *Nat. Methods.* **9**, 671–675

79. Kaufman, S. K., Thomas, T. L., Del Tredici, K., Braak, H., and Diamond, M. I. (2017) Characterization of tau prion seeding activity and strains from formaldehyde-fixed tissue. *Acta Neuropathol. Commun.* **5**, 41

80. Kleffner, R., Cooper, S., Khatib, F., Flatten, J., Leaver-Fay, A., Baker, D., and Siegel, J. B. (2017) Foldit Standalone: a video game-derived protein structure manipulation interface using Rosetta. *Bioinformatics*. **33**, 2765–2767

81. Gremer L, Schölzel D, Schenk C, Reinartz E, Labahn J, Ravelli R, Tusche M, Lopez-Iglesias C, Hoyer W, Heise H, Willbold D, Schröder G. (2017) Fibril structure of amyloid-β (1–42) by cryo electron microscopy. Science 358, 116-119